12-2017

Transport of water and ions through single-walled armchair carbon nanotubes: A molecular dynamics study

Michelle Patricia Aranha
University of Tennessee, Knoxville, maranha@vols.utk.edu

To the Graduate Council:

I am submitting herewith a dissertation written by Michelle Patricia Aranha entitled "Transport of water and ions through single-walled armchair carbon nanotubes: A molecular dynamics study." I have examined the final electronic copy of this dissertation for form and content and recommend that it be accepted in partial fulfillment of the requirements for the degree of Doctor of Philosophy, with a major in Chemical Engineering.

Brian J. Edwards, Major Professor

We have read this dissertation and recommend its acceptance:

Steven M. Abel, Joshua Sangoro, Jerome Baudry

Accepted for the Council:
Carolyn R. Hodges

Vice Provost and Dean of the Graduate School

(Original signatures are on file with official student records.)

Transport of water and ions through single-walled armchair carbon nanotubes: A molecular dynamics study

A Dissertation Presented for the

Doctor of Philosophy

Degree

The University of Tennessee, Knoxville

Michelle Patricia Aranha

December 2017

Dedication

I would like to dedicate this dissertation to my family for their unconditional love, support and encouragement.

Acknowledgements

I would like to extend my sincerest thanks to my advisor, Dr. Brian J. Edwards for his contribution with helpful suggestions and guidance during the entire course of my graduate studies. He gave me the freedom and the confidence to pursue different aspects of the subject matter and I have learned much from him. I am also thankful to him for his patience for proofreading and for providing many valuable comments on my dissertation.

I am also deeply appreciative of the insightful critique that I received from my committee members - Dr. Jerome Baudry, Dr. Joshua Sangoro and Dr. Steve Abel during the proposal defense. My work and I have benefitted greatly from their recommendations and constructive feedback.

This work has been supported in part by the computational resources provided by the Extreme science and discovery environment program (XSEDE Project # CTS160032 and CTS160038), Oak Ridge Leadership Computing Facility (OLCF Project # NTI107) and the high-performance computing facilities (Newton and Beacon) at the University of Tennessee, Knoxville. I am thankful for the award of substantial computational time by these agencies that have made this work possible. I would also like to thank the University of Tennessee, Knoxville (UTK) for the Chancellor's fellowship, the funding from the Chemical and Biomolecular Engineering (CBE) Department as well as the recent generous scholarship from the Elsie L. Crenshaw foundation that have supported me financially.

I would like to thank the wonderful and kind people at the University of Tennessee, especially Rita and Amy at the CBE department who have helped me over the years with a number of administrative tasks and have thereby made things easier for me.

I consider myself privileged to have been a part of the Chemical Engineering Department at UTK; here I gained the unique opportunity of interacting with so many bright minds from all over the world and this has tremendously enriched my experience as a graduate student. Additionally, it has been a pleasure working in MRAIL office (Dougherty 306 A, B) for the last 4 and half years. I have fond memories of the discussions shared over many interesting topics with both current and past members and I have tremendously enjoyed being a part of the group. Hadi, Hanieh, Mahdy, Mouge, Amir, Reza, Travis, Bo, and Xiangui: it was fun getting to know you and your hard work and the dedication that you showed towards your research served as a constant source of inspiration to me.

I was extremely fortunate to have some exceptionally supportive women as my batchmates and friends: Diana, Zuania, Samantha, Nelly, and Samiksha. I could always count on them for being there when needed. I owe gratitude to my friend Dominik with whom I have shared many enjoyable conversations and delightful meals. I would like to thank my friends Abhinav, Mary and Fatemeh who are no longer in Knoxville but have nevertheless had a positive influence on me. I am thankful for the wonderful learning experience at the University of Tennessee, Knoxville and I will always cherish the memories from my time spent here.

To the people in my life who have always encouraged me and who make everything worthwhile: my mother, father, sister, and brother-in-law - Thank you for everything, I love you and I am indebted to you forever.

Abstract

The narrow hydrophobic interior of a carbon nanotube (CNT) poses a barrier to the transport of water and ions, and yet, unexpectedly, numerous experimental and simulation studies have confirmed fast water transport rates comparable to those seen in biological aquaporin channels. These outstanding features of high water permeability and high solute rejection of even dissolved ions that would typically require a lot of energy for separation in commercial processes makes carbon nanotubes an exciting candidate for desalination membranes. Extending ion exclusion beyond simple mechanical sieving by the inclusion of electrostatics via added functionality to the nanotube bears promise to not only reduce the energy requirement of the ion rejection process but to also lend the nanotube an added attribute of perm-selectivity.

Confinement of water and ions in the nanotube leads to unique structure, dynamics, and electrostatic effects, which manifest as a result of discreteness of molecules, ion-ion interactions, and ion-specific interactions at nanoscale confinements that are not accounted for in continuum-based transport equations. Using Molecular dynamics (MD), an attempt has been made to provide a detailed molecular-level understanding of the structure, dynamics, and energetic aspects of the permeation mechanism as functions of CNT pore sizes, external solution concentrations, the number and nature of charges on the CNT wall, and external electric fields. Ion transport and electrolyte rejection rates are calculated from long-timescale MD simulations for the cases studied herein, and these are compared to the predictions of continuum theory. Additionally, ion conduction rates are indirectly calculated as functions of the energy barriers that are obtained by using umbrella sampling and free energy perturbation methods. The feasibility of using the thermodynamically-derived Donnan theory to make realistic predictions of co-ion concentrations in charged CNT-based nanoporous membranes with diameters less than 3 nm is discussed.

Furthermore, the deviations from macroscopic ion transport predictions and their possible causes are highlighted.

It is hoped that this work, when taken in conjunction with experimental studies, will not only help to extend the general continuum-based transport equations to cover nanoscale transport phenomena but will also help to improve the MD force-fields to enable predictions with greater accuracy.

Table of Contents

List of Tables

List of Figures

Nomenclature

d = diameter of nanotube

e = electronic charge

g_{max} = Maximum ion conductance

h = Planck's constant

k_B = Boltzmann constant

u_i = ionic mobility

A = Helmholtz energy

C_s = Molar concentration of Reservoir

D_i =Diffusion coefficient of species 'i'

ΔG_{hyd}= Free energy of hydration

ΔG = Potential of mean force

H = Hamiltonian

J_i = z-dimensional flux of species 'i'

K_i = Equilibrium partition coefficient of species 'i'

L = Length of the CNT

N = Avogadro's number

P_i = Permeability coefficient of species 'i'

R = Gas constant

T = Temperature

X = molar concentration of fixed-charge based on aqeuous solution volume

γ_i = activity coefficients

λ_i = molar distribution coefficient(ion partition coefficient)

$\rho_e =$ local electric charge density

τ_{HB} =Hydrogen bond lifetime calculated from the forward rate constant

$\emptyset$ =electrostatic potential

ϵ =absolute permittivity

κ =inverse debye length

λ =coupling parameter (Free energy calculations)

ξ =Reaction coordination for PMF

Chapter 1. Introduction

Nanofluidic devices have typical sizes in the range of 1-100 nm[1] and find a wide variety of potential applications[2] in drug delivery[3], detection systems[4,5], diagnostic devices, and clean, energy-saving technologies such as novel membranes for desalination[6]. Some examples of high impact implementation of these types of devices that are commercialized today are lab-on-a-chip analytical instruments[7,8] and nanofluidic transistors[9-12]. Confinement in such devices of dimensions approaching the characteristic length scales of the fluid molecular constituents leads to transport phenomena that are distinct from those seen in the macroscopic regime. Fluid flow under nanoscale confinement is commonly encountered in biology, but the mechanism that facilitates the rapid movement of water across cell membranes was unexplained until as recently as 1992 when Agre and coworkers discovered the aquaporin, an integral membrane protein[13]. Despite being lined with hydrophobic residues, this protein forms a water channel having high water permeability, allowing water transport in a single file to the cell while blocking other charged solutes. Along with water permeation, ion transport, which is seen across lipid bilayers through plasma membranes also known as ion channels[14-16], is important for cell homeostasis. Examples of this in nature are not limited to the biological world: a class of fullerenes that shares many of the structural and functional features of biological channels is carbon nanotubes (CNTs). A recent review paper discusses a vast array of commercially available carbon nanotube applications[17].

1.1 Relevance and applicability

A carbon nanotube (CNT) can be viewed as a single sheet of graphene that has been rolled into a seamless cylinder. It has many unique properties, such as a high aspect ratio, high thermal and electrical conductivity, extremely high tensile strength on account of sp^2 bonding, and can be

chemically functionalized making it conducive to use in many new technologies[18]. The graphitic walls of the CNT are hydrophobic, almost frictionless, and the CNT diameter can be tuned to be comparable to that of a single molecule[19]. In spite of reduced dimensionality and hydrophobicity, computer simulations and experiments report water to readily enter the nanotube and, in the case of pressure driven flow, the flux observed is many orders of magnitude higher than that obtained from continuum calculations[20-24]. This property of high water flux with high selectivity is extremely conducive to desalination applications. High water flow rate, along with selective ion transport, is an important feature of ion channels in living organisms; however, experimental analysis to study ion channels is a real challenge as ion channels can degrade under experimental conditions, have dimensions of the order of few nanometers and possess non-uniform surfaces, and uneven charge distributions that make them a complex system to study. On the other hand, carbon nanotubes can be easily embedded into lipid membranes and hence can be used as simplified biomimetic devices to study water and ion transport at a nanoscopic level[25,26].

1.2 Water flow enhancement

The unconventional flow rates exhibited by CNTs have exciting implications in the field of ultrafiltration and nanofiltration. A popular approach[24] to explain the enhancement of flow is to replace the no-slip boundary condition with a slip-modified condition in the standard Navier-Stokes (NS) treatment of classical fluid mechanics applied to steady-state, pressure-driven, laminar flow through a cylinder. When subject to a pressure gradient, the radial velocity profile $u_{HP}(r)$ that develops is given by

$$u_{HP} = \frac{\Delta p_z R^2}{4\mu} \left(1 - \frac{r^2}{R}\right) \tag{1.1}$$

where R is the radius of the cylinder, μ is the fluid viscosity, and Δp_z is the applied pressure gradient. The volumetric flow rate can be obtained via integration of Eq. (1) as

$$Q_{HP} = 2\pi \int_0^R r\, u_{HP}\, dr = -\frac{\pi R^4 \Delta p_z}{8\mu} \tag{1.2}$$

which is the classical Hagen-Poiseuille (HP) Law. Under conditions of fluid slip at the wall, the no-slip boundary condition used in the derivation of Eq. (1) ($u_{HP}(R) = 0$) can be replaced with a slip-modified condition, $u_{slip}(R) = -L_s \frac{\partial u}{\partial r}|_{r=R}$, where L_s is the slip length. The slip-modified velocity (u_{slip}) and flow rate (Q_{slip}) are then derived as

$$u_{slip} = -\frac{R^2 \Delta p_z}{4\mu}\left(1 - \frac{r^2}{R^2} + \frac{2L_s}{R}\right) \tag{1.2}$$

$$Q_{slip} = Q_{HP}\left(1 + \frac{4L_s}{R}\right) \tag{1.4}$$

respectively. The order of magnitude of enhancement in flow is debated between available experimental and simulation studies[22-24], typically ranging from 1 to 2 orders of magnitude (as $L_s >> R$ and $\frac{4L_s}{R}$ ~ 10 - 100). Regardless, with significant progress in the low-cost production of aligned CNTs[27-29] whose diameters can be carefully controlled, CNTs provide great promise for the development of novel nanofluidic devices and membranes that can simultaneously increase throughput and reduce energy consumption.

1.3 Modification of structure and dynamics of water under confinement

The confinement of water in carbon nanotubes has been shown to produce some remarkable structural and dynamical features as compared to bulk water[30,31], which include a lower number of hydrogen bonds[32-34], increased lifetimes of hydrogen bonds[35], the layered structure of water under confinement[36], its reduced density and viscosity[37], and an increased proton mobility in 1-D water chains[38]. Water has unique properties and an understanding of the interactions between water and carbon nanotubes is key to the development of many new applications.

1.4 Ion transport

Highly efficient membranes should allow for large water flow rates with a precise degree of control over ion selectivity. Flow of water and ions in nanotubes can be achieved by application of an electric field, pressure difference, concentration gradient, uneven charge distribution, and/or osmotic pressure. The desired rate and selectivity of ion transport can be controlled by various means, such as varying the pore size, the ion concentration, the charge distribution, the density of charges, and via chemical functionalization. Simple ion-exclusion can be achieved via steric hindrance or the sieving mechanism when the diameter of the pore is smaller than that of the hydrated ion but still large enough to allow water molecules to translocate[39]. However, if one wishes to construct membranes of practical interest where appreciable flow rates are desired, the diameter of the CNT must exceed the size of the ion. In such cases, ion transport is usually tuned by a combination of sieving and an application of charges on the CNT surface. The various contributions to ion exclusion arise from sieving, electrostatic interaction of ions with charges and other ions that may be present in the system, the modification of the hydration shell of the ions, and the anisotropic dielectric of the membrane phase (which is quite different from the bulk phase). In the absence of well-known theories at the nanoscale and very limited experimental studies, it is quite a challenge to quantify the exact contributions and significance of each of these exclusion mechanisms to the total ion exclusion as a function of pore size, ion type, concentration of fixed-charges, and external solution concentration. Without the ability to predict characteristics and the extent of ion exclusion within carbon nanotubes, progress towards the rational design of nanofluidic devices employing them is impeded.

1.5 Predictive theories

At the continuum level, the theoretical framework to describe water and ion transport is provided by the coupled Navier-Stokes (NS) and Poisson-Nernst-Planck (PNP) equation. Major components of the solution to the ion transport equations in continuum theory is the distribution of ions and electric potential, which can be obtained from the Poisson-Boltzmann (PB) relation. However, these theories are based on a number of approximations that are justified at the continuum level to make the solutions tractable. Water, which is practically treated as an incompressible Newtonian fluid under ordinary conditions, has its flow commonly described by the Navier-Stokes (NS) equation of hydrodynamics. The NS equation for incompressible Newtonian fluids assumes the fluid to be a continuous isotropic medium having constant viscosity where the stress vector is directly proportional to the strain vector. At the nanoscale, however, especially at confinements below 1 nm, the fact that water is made up of discrete molecules cannot be ignored and the discrepancies in the observables for water, such as viscosity, fluid velocity, etc., between results obtained from both experiments and simulations and those acquired by theoretical calculations from classical fluid dynamics begin to appear.

The rate and extent of ion transport across membranes is influenced not only by the ion concentrations on the two sides of the membrane but also by the voltage (i.e., the electric potential) that exists across the membrane even in the absence of an applied electric current[40,41]. This electric potential always originates as a result of a net charge[42]. This excess charge could result from unequal ion concentrations between the solutes at the interfaces due to membrane selectivity to a particular ionic species on account of membrane fixed-charges or a diffusion potential caused by the dissimilar mobilities of ions inside the membrane. The tool for describing this potential and ion concentration distributions from a charged surface is the Poisson-Boltzmann equation. The PB

equation assumes the ions to be point charges and the dielectric to be spatially-uniform, structureless medium. It neglects the correlation between charges and disregards ion specific effects. In reality, ions are not point-like particles and steric effects must be included that depend on the effective ionic radius. Also, the assumption of a constant bulk dielectric is expected to break down close to surfaces, especially near hydrophobic surfaces where water ordering induces an electric dipole pointing towards the interface. Ion specificity is intimately connected to the Hoffmeister effect, namely, that the interaction between charged and neutral objects in aqueous media depends crucially on the ion type and not only on the electrolyte concentration. While simulation studies suggest that using the bulk dielectric is not a critical assumption and that neglecting the correlations between charges does not give any major error, one still cannot overlook the finite-size effects of the ion or its specificity at the nanoscale[43].

A simple comparison of the characteristic electrostatic length scales shown in Table 1-1 should make the problem of using continuum theory obvious. The table shows a comparison of the electrostatic length scales for 0.001 M, 0.1 M, and 1 M NaCl solutions in a (10,10) CNT with a diameter of 1.356 nm, length of 5 nm, and for a constant surface charge density of $\sum\sim 0.009\ e/nm^2$. The electrostatic length scales are comparable to the diameter of the nanotube and thus the assumptions of continuum theory will very likely breakdown at this scale.

Apart from the Poisson-Boltzmann equation[44], the ionic distributions inside the membrane phase can be predicted from statistical mechanics theories, such as the mean spherical approximation with the second virial coefficient and the hypernetted chain correlations[45,46]. Even with the added level of information and complexity, these theories do not perform any better than the more approximate PB equation. Therefore, a universal and tractable theory that provides a complete description of the ion concentration for any charge distribution, membrane geometry,

Table 1-1: Comparison of electrostatic length scales.

Type of electrostatic length	Equation	Value (nm)
Bjerrum Length (length below which electrostatic interactions dominate thermal effects)	$l_{B=}\ \frac{z^2e^2}{4\pi k_B T}$	0.67
Debye length (characterizes the length of the Electric Double Layer (EDL))	$\lambda = \sqrt{\frac{\varepsilon k_B T}{8\pi n e^2 z^2}} = \sqrt{\frac{\varepsilon k_B T}{2N_A e^2 I_c}}$ $= (8\pi l_B \rho_s)^{-(\frac{1}{2})}$	9.7, 0.97, 0.3
Gouy – Chapman length (distance from the wall where the electrostatic interaction of a single ion with the wall becomes of the order of thermal energy)	$l_c\ = \frac{1}{(2\pi \sum l_{B)}}$	2.4, 2.4, 2.4 ($\sum \sim 0.009\ e/nm^2$)
Dukhin length (scale below which surface conduction dominates over bulk)	$l_{Du} = \frac{\lvert\sum\rvert}{\rho_s}$	155.9, 1.56, 0.15598

and size, external solution concentration or type of electrolyte, and that takes into account the molecular nature of the solution inside a membrane, is still lacking. Even so, there exists an even more simplified expression than the Poisson-Boltzmann equation which ignores the effect of geometry and pore size, assumes homogeneous distribution of surface charges, and an ideal behavior of free ions in solution throughout the space - the Donnan theory[47,48]. This theory provides the equilibrium distribution of ions in the pore when a charged or selective membrane comes into contact with solutions of unequal concentrations. An exact solution for the transition from Poisson-Boltzmann theory to the Donnan model and their intrinsic linkage was shown by Dähnert et al[49]. The Donnan model has been found by some studies[50] to present a good starting point to predict co-ion exclusion trends in commercial membranes. Recently, Fornasiero et al.[51] have suggested that CNTs with negatively-charged functionalities show an ion exclusion phenomenon that is dominated by electrostatic interaction over steric effects, and that the ion rejection follows trends similar to that predicted by Donnan theory.

An added level of information in the statistical mechanics theory might yield better results but at the cost of increasing complexity of the solution; furthermore, molecular-level simulations are too computationally expensive to conduct for each and every case[42,52]. Nevertheless, a few prudent simulations cannot only point out the cause of deviations between simple macroscopic equations, such as the Donnan model, and observed potentials, but can also help to identify the coupling between various simulation conditions, such as nanotube diameter, ion size, ion charge density, external solution concentration, and fixed-charge concentration. Hence simulations could guide the development of governing equations that go beyond the known phenomenological coefficients to include information missing at the macroscopic scale such as finite-size effects, hydration effects, ion correlations, and the variation in the dielectric constant.

An approach that allows us to resolve water and ion transport at the microscopic level is molecular dynamics (MD) simulation. MD is a powerful tool, which explicitly calculates the motion of all particles in the system described by classical mechanics (i.e., Newton's equations of motion) and enables us to probe the structure, dynamics, and energetics of the species of interest. For the CNT based nanofluidic platforms that we are interested in, given a correct potential model, one can obtain an exact solution for the ion transport through sufficiently long molecular dynamics simulations. For processes near equilibrium, the local structure of water and ions under confinement (i.e., the distribution functions and coordination numbers of ions), and time correlation functions that provide dynamic properties, such as the diffusion coefficient and viscosity, can be easily determined from an MD simulation. Thermodynamic functions, such as Gibbs energy or the Helmholtz energy that cannot be directly measured in an MD simulation and cannot be expressed as a simple average of some function of coordinates and momenta[53,54], can be straightforwardly calculated by employing separate techniques, such as umbrella sampling[55] or free energy perturbation methods[56].

1.6 Objectives of this study

The objectives of this work are to present qualitative and quantitative information regarding the structure, dynamics, and energetics of the water and ions under confinement using molecular dynamics simulations and to use those results to shed light on ion permeation mechanisms in confined channels by taking into account the detailed structure of the CNT/electrolyte system and ion-specific interactions. We would also like to establish whether Donnan theory (which is obtained from a thermodynamic derivation) provides a sufficient description of co-ion exclusion from charged CNTs in contact with 1-1 electrolytes. With recent increases in available computational speed and power, we attempt to directly compare the ionic

fluxes calculated according to macroscopic theory equations to the results of long MD simulations for cases of passive transport under varying confinements in uncharged CNTs, through charged nanotubes having varying magnitudes of fixed-charges and external solution concentrations, and electric field-driven ionic fluxes. Our goal is to identify and explain the reasons for any observed deviations between macroscopic equations and the results of the MD simulations that may be used in development of transport equations governing nanoscale transport in the future.

To attain these goals, we adopt the following approach:

1. We first validate our description of the simulation model with CNT in bulk water against well-known experimental and simulation results via a thorough comparison of the water structure (radial distribution functions of water, hydrogen bonding structure, and axial density), dynamics (diffusion coefficients, hydrogen bond lifetimes), and energetics (hydrogen bond energies) under confinement. We then select a water model that can best reproduce the properties of real water that are required to simulate appropriately the physical problem under consideration.

2. We then use the validated model to explore water and ion permeation mechanisms through an uncharged CNT via a thorough study of the structure, dynamics, and energetics of the translocating solute (ion). We compare the structural features (molecular distributions, coordination numbers) and dynamical features (diffusion coefficients) for different pore sizes and electrolyte concentrations. The distinct boundary between the CNT and the bulk reservoir provides a barrier to ion translocation, and we can provide quantitative estimates of the barrier to the transport via single ion potential of mean force (PMF) studies. To ensure the validity and the quality of our PMF results, we also perform rigorous free energy perturbation studies (via the Bennett acceptance ratio method) to obtain ion solvation energy in bulk and under confinement in the CNT. This not only provides a quantitative estimate of the energy barrier for the ion to partition into the CNT, but also

allows for understanding the energy barrier in context of the structural changes taking place during the ion translocation process. Since ion permeation rates are intertwined with the free energy barriers for ion translocation, we also obtain transport coefficients for ions, such as ion permeability and maximum conductance.

3. We extend the simulations mentioned above to obtain pseudosteady-state fluxes through uncharged nanotubes and these fluxes can be compared to theoretical calculations from the Nernst-Planck equation.

4. Further, we study the modulation of ion concentrations in the nanotube through the application of charges. We explore the phenomena associated with ion exclusion through CNTs of different diameters as a function of the nature (discrete vs. partial), the distribution and strength of the charges, the external solution concentration, and the type of electrolyte. We then compare our results for co-ion concentration retained in the CNT with those of Donnan theory.

5. We study the passive transport of ions through charged nanotubes by obtaining pseudosteady-state fluxes through a nanotube having a fixed diameter by varying the fixed-charge concentration and the external solution concentration.

6. Finally, we apply electric fields to drive an ion flux through charged carbon nanotubes and present the results in context of Donnan exclusion and Nernst-Planck equations.

Our results can provide a microscopic framework and guide towards interpreting the experimental observables and help to serve a two-fold purpose: 1) the deviations observed between simulations and experimental studies can help improve force-fields that are commonly used in molecular simulations of such systems; 2) dissimilarities in the results of the MD simulations and the calculations from continuum-level transport equations can allow for a detailed molecular interpretation of the missing physical information in the continuum-level equations.

1.7 Organization of chapters

Even though there may be overlap in the methodology employed, we make an effort to organize the chapters containing results in such a way that they can be understood as separate works. The dissertation has two main parts: Part 1, which contains chapters 1-3, introduces the concepts, methods, and reviews the literature on this topic; Part 2, consisting of Chapters 4-9, presents a detailed analysis of the relevant transport processes through CNTs, especially those of ions through the nanotubes.

In Chapter 2, we provide details on the classical transport equations and theories related to species transport, molecular dynamics methods, and details pertaining to the calculation of structural features, the dynamic coefficients, ion solvation energies, and the free energy profiles of the permeation process.

Chapter 3 is a comprehensive review of the literature related to recent experimental, theoretical, and simulation-based research to describe structure, dynamics, and energetics of water and ion permeation mechanisms in CNTs. We give a brief account of the progress so far in theoretical and experimental studies, the disagreements between various studies, and a sampling of prototypes of the CNT-based applications developed to date.

Chapter 4 describes our analysis of the structure, dynamics, and energetics of water under varying degrees of confinement in carbon nanotubes. These studies helped validate our model and the methods that were later used for conducting comprehensive molecular dynamics studies of ion transport.

Chapter 5 discusses the ion uptake and the associated structure and dynamics of an electrolyte in charged sub-3 nm carbon nanotubes. In these studies, we observe preliminary evidence of Donnan-like ion adsorption isotherms.

In Chapter 6, we compare the flux from Fick's diffusion equation with the results of rigorous MD simulations for uncharged nanotubes with diameters of 2-3 nm. We also assess the validity of the continuum dynamics approach in describing transport in these nanopores.

Chapter 7 describes a comparison of the MD results of co-ion exclusion with the predictions of Donnan theory. The applicability of Donnan theory to describe co-ion exclusion is described in context of the results obtained from MD simulations and suggestions are made for improvement to the Donnan model.

In Chapter 8, we study the rejection of electrolytes on account of electrostatic interactions due to the addition of fixed-charges to the nanotube and the passive flux of electrolyte through these charged nanotubes. We demonstrate the controllability of ion flux by the modulation of the fixed-charges on the nanotube for different strengths of the high concentration reservoir

Lastly, in Chapter 9 we report the electric field-driven electrolyte flux trends obtained through a 3 nm diameter carbon nanotube with different magnitudes of fixed-charges that connects two reservoirs, one containing a strong electrolyte at high concentration and the other containing pure solvent (i.e., water).

We summarize the main findings and conclusions in Chapter 10.

Chapter 2. Theory and Methods

We use the molecular dynamics simulation package GROMACS to resolve ion conduction through CNTs. For efficient implementation, it is important to first have a good understanding of the theory governing macroscopic ion transport, molecular dynamics concepts, and the various analysis techniques that must be used with the simulation output data to obtain meaningful results of the properties of interest. We thus present in the following section certain aspects of the theory, methods, and analysis techniques that we used in our studies of ion transport.

2.1 Macroscopic theory

The transport of ions across an uncharged or charged membrane can be described by the continuum Nernst–Planck (NP) and Poisson-Boltzmann (PB) equations.

2.1.1 Poisson–Boltzmann theory

The Poisson-Boltzmann approach is one of the most widely used continuum-based methods to obtain the equilibrium distribution of mobile ions near a charged surface. Some examples of its applications are in obtaining the space-charge distribution at semiconductor junctions and semiconductor/electrolyte surfaces, as well as the distribution of ions around hydrophobic colloidal particles in electrolyte solutions. The surface may be a metal, an insulating solid, a synthetic polyelectrolyte, or a biological macromolecule with fixed-charges that result from dissociation reactions or by adsorption of charged species.

The Poisson relation for the potential and the space-charge distribution is given by

$$\nabla^2\phi = -\frac{\rho_e}{\epsilon} \tag{2.1}$$

Here, ϕ is the electrostatic potential (V), ρ_e is the volume space-charge density (C/m^3), and ϵ is the absolute permittivity (F/m). The volume space-charge density is given by

$$\rho_e = z_i F c_i$$

where z_i is the ion valence, F is the Faraday constant (C/mol), and c_i is the ion concentration (mol/m^3). If we assume that the ionic concentrations can be described by Boltzmann's statistics, we have

$$c_i = c_{i,bulk} \exp\left[\frac{-z_i F \phi}{RT}\right] \tag{2.2}$$

where R is the gas constant (J/mol/K) and T is the absolute temperature (K). The Poisson-Boltzmann relation for potentials that vary in only one direction is given by

$$\frac{d^2\phi(x)}{dx^2} = -\frac{1}{\epsilon}\sum_i z_i F c_{i,bulk} \exp\left[\frac{-z_i F \phi(x)}{RT}\right] \tag{2.3}$$

When a surface is positively charged, a positive potential develops at the surface and negative ions (counter-ions) accumulate while positively-charged ions (co-ions) deplete at the surface. The analytical solutions of the general non-linear Poisson-Boltzmann relation are known for a limited number of cases of planar geometries and cylindrically symmetric systems; i.e., for systems with simple boundary conditions. In most cases, general solutions are computationally intensive. For the case of a univalent symmetrical electrolyte, the PB equation simplifies to

$$\frac{d^2\phi(x)}{dx^2} = \frac{2zFc_{i,bulk}}{\epsilon} \sinh\left[\frac{zF\phi(x)}{RT}\right] \tag{2.4}$$

If the electrical potential is very small such that $\frac{zF\phi(x)}{k_B T} \ll 1$, we obtain the "Debye–Hückel approximation", which is the linearized version of the Poisson-Boltzmann equation that can be applied to symmetrical electrolytes. It is expressed as

$$\frac{d^2\phi(x)}{dx^2} = \kappa^2\phi(x) \tag{2.5}$$

where

$$\frac{1}{\kappa} = \lambda = \sqrt{\frac{\epsilon RT}{2c_{i,bulk}F^2z^2}} = \sqrt{\frac{\varepsilon k_B T}{2N_A e^2 I_c}} \tag{2.6}$$

$$Ic = \frac{1}{2}\sum c_i \, {z_i}^2 \tag{2.7}$$

$1/\kappa$ is also the characteristic Debye length, λ (m), that provides the thickness of the double layer, which is the distance over which the potential decays to $1/e$ of its value at $x = 0$, k_B is the Boltzmann constant, N_A is Avogadro's number, e is the elementary charge, and I_c is the ionic strength (mol/m^3). The Debye length (i.e., the charge screening length) decreases as the salt concentration increases.

The Poisson–Boltzmann relation suffers from limitations when used to describe ion concentrations in narrow membranes. The Poisson-Boltzmann theory (which is a mean-field description of the distribution of the potential and concentration) makes several assumptions and simplifications:

a. Uniform surface-charge density or constant surface potential, neglecting discreteness or non-homogeneity of the charges. This is equivalent to a mean-field approximation where the potential of mean force acting on each ion is the same as the mean potential in the Poisson equation.
b. Ions are treated as point charges.
c. The uniform dielectric is equal to the bulk dielectric for the charged space under consideration.

d. Ionic concentrations can be adequately described by Boltzmann statistics; i.e., the ion-ion correlations are neglected.

2.1.2 Donnan theory

Donnan equilibrium is applicable to perm-selective membranes that pose a restriction to the passage of one or several ionic species. This restriction or perm-selectivity might be a consequence of the presence of charges or steric effects where one of the ionic species may be of colloidal size. The fixed-charges may arise due to ionization of functional groups or because of the adsorption of ions of external origin when the membrane is immersed in an electrolyte solution. Donnan theory gives the ion concentration inside such a semi-permeable membrane that is in thermodynamic equilibrium with its external solution. We would like to investigate if the co-ion concentration or the excess salt concentration in charged CNTs that is obtained using an approximate theory like Donnan theory (which is a result of a thermodynamic derivation that does not consider the graininess of the system) is the same as that obtained from MD simulation.

Consider a charged membrane that is in equilibrium with an electrolyte solution, such that the fixed-charges are distributed uniformly. An electric potential difference is established between the membrane and the solution. For such a situation, Donnan equilibrium gives an expression for co-ion exclusion. Below, we present the formal derivation of the Donnan theory expression predicting the co-ion concentration within a charged membrane.

Ignoring the partial molar volume of ions, the electrochemical potential (J/mol) for ionic species '*i*' in external bulk solution is given by

$$\bar{\mu}_i^{bulk} = \mu_i^0 + RT\, lnc_i^{bulk} + z_i N_A e \phi_{bulk} \tag{2.8}$$

$$\bar{\mu}_i^{bulk} = \mu_i^0 + RT\, lnc_i^{bulk} + z_i F \phi_{bulk} \tag{2.9}$$

for cations

$$\bar{\mu}_{+}^{bulk} = \mu_{+}^{0} + RT\ lnc_{+}^{bulk} + z_{+}F\phi_{bulk} \tag{2.10}$$

and for anions

$$\bar{\mu}_{-}^{bulk} = \mu_{-}^{0} + RT\ lnc_{-}^{bulk} + z_{-}F\phi_{bulk} \tag{2.11}$$

where μ_i^0 is the chemical potential in the standard state (J/m^3), z_i is the ion valence, c_i^{bulk} is the bulk concentration of ion '*i*' (mol/m^3), *R* is the gas constant (J/mol/K), *T* is the absolute temperature (K), ϕ_{bulk} is the electrostatic potential of the bulk phase, *F* is the Faraday constant (C/mol), N_A is the Avogadro constant, and *e* is the elementary charge. For simplicity, we assume ideal solutions.

In a similar fashion, the electrochemical potential for an ion in the membrane at any location *x* from the membrane wall is given by

$$\bar{\mu}_{i}^{mem} = \mu_{i}^{0} + RT\ lnc_{i(x)}^{mem} + z_{i}F\phi(x) \tag{2.12}$$

such that for cations

$$\bar{\mu}_{+}^{mem} = \mu_{+}^{0} + RT\ lnc_{+(x)}^{mem} + z_{+}F\phi(x) \tag{2.13}$$

and for anions

$$\bar{\mu}_{-}^{mem} = \mu_{-}^{0} + RT\ lnc_{-(x)}^{mem} + z_{-}F\phi(x) \tag{2.14}$$

c_i^{mem} is the concentration of ion '*i*' in the membrane and $\phi(x)$ is the electrostatic potential in the membrane phase at location *x* from the membrane wall. If we subtract the electrochemical potential of the ion in the bulk phase from that in the membrane, we obtain the familiar Boltzmann relation:

$$c_{i(x)}^{mem} = c_i^{bulk} \exp \frac{(\bar{\mu}_i^{mem} - \bar{\mu}_i^{bulk} - (z_i F(\phi(x) - \phi_{bulk}))}{RT} \tag{2.15}$$

$$c_{i(x)}^{mem} = c_i^{bulk} \exp\left(\frac{(-\Delta\bar{\mu}_i^{ex} - z_i F\phi_{Don}(x))}{RT}\right) \tag{2.16}$$

$\Delta\bar{\mu}^{ex}$ is the difference in the excess chemical potential of ion '*i*' between the bulk phase and the membrane phase and $(\phi(x) - \phi_{bulk})$ = $\phi_{Don}(x)$ is the Donnan potential. At equilibrium, the electrochemical potential of each ion should be the same in both the membrane and the external solution,

$$\bar{\mu}_i^{mem} = \bar{\mu}_i^{bulk} \tag{2.17}$$

Thus,
$$\Delta\bar{\mu}_i^{ex} = 0 \tag{2.18}$$

$$c_{i(x)}^{mem} = c_i^{bulk} \exp\left(\frac{(-z_i F \phi_{Don}(x))}{RT}\right) \tag{2.19}$$

$$\phi_{Don}(x)) = (\phi(x) - \phi_{bulk}) = \frac{RT}{z_i F} ln(\frac{c_i^{bulk}}{c_{i(x)}^{mem}}) \tag{2.20}$$

such that for cations

$$(\phi(x) - \phi_{bulk}) = \frac{RT}{z_+ F} ln(\frac{c_+^{bulk}}{c_{+(x)}^{mem}}) \tag{2.21}$$

and for anions

$$(\phi(x) - \phi_{bulk}) = \frac{RT}{z_- F} ln(\frac{c_-^{bulk}}{c_{-(x)}^{mem}}) \tag{2.22}$$

Considering a univalent salt such as NaCl, the expression for cations is given as

$$(\phi(x) - \phi_{bulk}) = \frac{RT}{F} ln(\frac{c_+^{bulk}}{c_{+(x)}^{mem}}) \tag{2.23}$$

and for anions

$$(\phi(x) - \phi_{bulk}) = -\frac{RT}{F} ln\left(\frac{c_-^{bulk}}{c_{-(x)}^{mem}}\right) \tag{2.24}$$

Equating the right-hand sides

$$\frac{RT}{F} ln\left(\frac{c_{+}^{bulk}}{c_{+(x)}^{mem}}\right) = -\frac{RT}{F} ln\left(\frac{c_{-}^{bulk}}{c_{-(x)}^{mem}}\right) \tag{2.25}$$

$$\left(\frac{c_{+}^{bulk}}{c_{+(x)}^{mem}}\right) = \left(\frac{c_{-(x)}^{mem}}{c_{-}^{bulk}}\right) \tag{2.26}$$

$$c_{+}^{bulk} . c_{-}^{bulk} = c_{+(x)}^{mem} . c_{-(x)}^{mem} \tag{2.27}$$

$$c_{+(x)}^{mem} = c_s^2 / c_{-(x)}^{mem} \tag{2.28}$$

Here c_s is the concentration of the external solution.

From the electroneutrality assumption in a charged membrane we have

$$\sum_i z_i c_i^{mem} + \alpha c_{fixed} = 0 \tag{2.29}$$

where α is the valence of the fixed-charge. For a monovalent salt this becomes

$$c_{+(x)}^{mem} - c_{-(x)}^{mem} + \alpha c_{fixed} = 0 \tag{2.30}$$

For a positively-charged membrane with fixed-charge valence, α = 1, equation (2.30) can be rewritten as

$$c_{+(x)}^{mem} - c_{-(x)}^{mem} + c_{fixed} = 0 \tag{2.31}$$

$$c_{+(x)}^{mem} + c_{fixed} = c_{-(x)}^{mem} \tag{2.32}$$

Substituting for $c_{-(x)}^{mem}$ in equation (2.32) with the expression from equation (2.28), the co-ion concentration $c_{+(x)}^{mem}$ can be solved for

$$c_{+(x)}^{mem} - \frac{c_s^2}{c_{+(x)}^{mem}} + c_{fixed} = 0 \tag{2.33}$$

$$(c_{+(x)}^{mem})^2 + c_{fixed} . c_{+(x)}^{mem} - c_s^2 = 0 \tag{2.34}$$

$$c_{+(x)}^{mem} = \frac{1}{2}\left(\sqrt{(c_{fixed}^2 + 4c_s^2)} - c_{fixed}\right) \tag{2.35}$$

We can arrive at a similar expression for the co-ion concentration using negative fixed-charges, and thus we can generalize the expression for a monovalent salt as

$$c_{co-ion(x)}^{mem} = \frac{1}{2}\left(\sqrt{(c_{fixed}^2 + 4c_s^2)} - c_{fixed}\right) \tag{2.36}$$

Further, assuming uniform distribution of ions and potential (taking the mean field approach) the ion concentration can be given by an average concentration and the potential can be replaced by an average potential at any location. This is a good assumption in cases where the Debye length is comparable to the pore size.

For a more rigorous treatment, the external solution concentration can be replaced by the thermodynamic activities($a_{\mp} = \gamma_{\mp} c_{\mp}$). Here, $\gamma_{\mp}$ is the activity coefficient and these values are well-known for common electrolytes. Given just the external salt concentration and the immobile charge concentration, this simple expression gives the equilibrium co-ion concentration in the charged membranes without requiring a description of the properties of the membrane. The Donnan-exclusion that arises because of the Donnan potential refers to the exclusion of co-ions that have the same electrical charge as that of the fixed-charge and the preferential adsorption of the counter-ions that have the opposite electrical charge. This theory does not take into account the size of the ions or their ion specific nature.

2.1.3 **Nernst-Planck Equation**

The Nernst-Planck equation gives the ion flux that arises from diffusion (concentration gradient), migration (electric field driven), and convection (pressure drive) as

$$J_i = -D_i\left[\frac{d\overline{C}_\iota}{dx} + \overline{C}_\iota \frac{d\ ln\overline{\gamma}_\iota}{dx} + \frac{z_i F}{RT}\overline{C}_\iota \frac{d\overline{\emptyset}}{dx}\right] + u_i C_i \tag{2.37}$$

Here, J_i, D_i, $\overline{C}_\iota$, $\overline{\gamma}_\iota$, are the ion flux, diffusion coefficient, molar concentration, and activity coefficient of species *i*, respectively. $\overline{\emptyset}$ is the electric field, which may be internal (diffusion

potential as in the case of charged species having differing mobilities, or Donnan potential because of fixed membrane charges) or external (arising from an applied electric field), or a combination of both. When the potential is taken from the PB equation, the Nernst-Planck equation becomes the Poisson-Nernst-Planck equation.

2.2 Molecular dynamics

The microscopic features of transport are not accessible by macroscopic theory and are not sufficiently accessible by experiments. Here, the simulation of reasonably equilibrated and validated atomistic models provide great opportunities to gain a deeper insight into these microscopic features, which in turn can help with more knowledge-based development of membranes[57]. Gunsteren and Berendsen[58] elegantly elucidated the benefits of molecular modeling as a tool to understand and interpret experimental results, to obtain semi-quantitative estimates of experimental results, and to interpolate or extrapolate experimental data into regions that are difficult to access in the laboratory.

In order to understand what is happening at a molecular scale, one needs a mathematical model that gives a functional value; i.e., the potential energy for any given configuration of atoms. This potential energy function, also known as the force-field, contains the sum of all the bonded and non-bonded interactions between atoms. The molecular modeling begins with the construction of a structure file having information of the coordinates of all atoms in the system. The atoms in this file are arranged as realistically as statistically possible by avoiding overlaps between atoms. The atoms are considered spheres of some specific atomic radius that are obtained from parameterized force-fields and bear their atomic masses. The mechanical springs or torsion rods with spring constants related to, for example, experimentally known bond strengths, then describe the bonded interactions between atoms resulting in bonds, bond angles, and dihedral angles. The

Lennard–Jones (Pauli's repulsion + van der Waals' attraction) interactions and the Coulombic interaction give the short-range and the long-range contributions to the non-bonded potential. The sum of all these interactions provides the potential energy of the system. The typical structure of force field is

$$V(\bar{r_1}, \bar{r_2}, \ldots \bar{r_n}) = \sum_{Covalent\ bonds} K_b(l - l_0)^2 + \sum_{Bond\ angles} K_\theta(\theta - \theta_0)^2 + \sum_{Dihedral\ angles} K_\vartheta(1 + \cos(n\vartheta - \delta)) + \sum_{\substack{Non-bonded\\ interaction\\ (VDW+Coulomb)}} [\left(\frac{a_{ij}}{r_{ij}{}^{12}}\right) - \left(\frac{b_{ij}}{r_{ij}{}^{6}}\right) + \frac{q_i q_j}{\varepsilon r_{ij}}] \quad (2.38)$$

The parameters used in the description of the force field may be obtained by fitting a set of data calculated by quantum mechanics and/or determined experimentally. Ewald sum rules are generally used to calculate long-range electrostatics. The system can then be relaxed/optimized by a suitable energy minimization technique that changes the geometry of the system in order to relieve any unrealistic local tensions. This enables one to use a geometrically optimized system having the lowest potential energy.

One can perform MD simulations, which involves solving Newton's equations of motion for every atom investigated, by calculating the forces acting on each atom of the model via a gradient operation,

$$\bar{F_i} = -\frac{\partial V(\bar{r_1}, \bar{r_2}, \ldots \bar{r_n})}{\partial r_i} = m_i \frac{d^2 \bar{r_i}}{dt^2} \quad (2.39)$$

The starting velocities of all atoms are assigned via a Maxwell distribution given by the kinetic energy. The several thousand coupled differential equations of second-order can then be solved numerically in small time steps , Δt, via finite difference methods. The Verlet algorithm derived via Taylor expansion of the position $\bar{r_i}$ is commonly used in MD simulations because of its simplicity and stability:

$$\overline{r_i}(t + \Delta t) \cong 2r_i(t) - r_i(t - \Delta t) + \frac{F_i(t)}{m_i}\Delta t^2 \tag{2.40}$$

Considering the very fast oscillations of covalent bonds, Δt must be very short (of the order of 1 fs) to avoid numerical breakdown connected with problems of energy conservation. Furthermore, the limited model size demands the application of periodic boundary conditions to avoid extreme surface effects.

From the perspective of statistical mechanics, MD is simply a method of conformational sampling that yields average structural and thermodynamic properties of microscopic states (configurations)[59]. These microscopic states are distributed in accordance with a certain statistical ensemble, for example, the NVT ensemble, which is obtained by coupling to a thermal bath, or the NPT ensemble, which is obtained by coupling to both a thermal bath and a barostat. MD is not without its challenges, the main ones being the derivation of accurate force-fields for the molecular systems of interest and sampling the configuration space for all possible molecular conformations that will be populated by a molecular system in thermal equilibrium. The latter deals with predicting structural quantities of the system based on the confidence that the system has achieved thermal equilibrium and is in the lowest possible energy state.

2.2.1 Limitations of molecular dynamics

Quantum effects: Many dynamical events involve quantum-effects such as changes in chemical bonding, the presence of non-covalent intermediates and tunneling of protons or electrons. Classical MD cannot be used to model such phenomena. However, we need not concern ourselves with quantum effects since they are not relevant to our domain of flow of fluids through carbon nanotubes.

Reliability of interatomic potential: The results of the simulation will be realistic only if the potential energy function mimics the forces experienced by the real atoms. The current force-fields available, such as GROMOS, AMBER, and OPLS, have proven to be sufficiently accurate in terms of kinetic and thermodynamic properties derived by means of MD simulations for proteins and nucleic acids; however, there remains much room for improvement.

Time limitations and size limitation: Relevant timescales for observing the desired phenomena may extend over several nanoseconds to microseconds. However, the presence of significant fast motions limits the time-step in the numerical integration to about 1 fs, thus making the nanosecond timescale the current domain of standard MD simulations. For instance, MD simulations are currently limited to timescales of the order of 100 ns or a few μs even on massively parallel machines, while transport in biological ion channels takes place in the millisecond domain. While MD can evaluate certain thermodynamic and transport parameters, it cannot sufficiently resolve measurable current flow[60]. However, due to the development of specialized hardware and better parallelization algorithms, the speed of MD simulations and hence the accessible timescale is steadily increasing[61].

Size limitation*:* If the size of the MD cell is comparable to the correlation lengths of the spatial correlation functions of interest, the MD simulations are much less reliable[62]. This problem can be partially alleviated by a method known as finite-scaling, which consists of computing a physical property using several boxes with different sizes and then using a fitting procedure to find the most reliable estimate for the true physical quantity.

Breaking and formation of bonds: Classical MD does not capture breaking and formation of covalent bonds, but it may be possible to handle such reactive chemistry within a generalized MD framework with the recently developed force-field REAX-FF.

2.2.2 Avoiding errors

While the systematic errors that can be generated by the use of empirical potentials are difficult to quantify[63], we try to avoid common sources of user errors that can lead to artifacts like the unphysical flow of water in the absence of an external force to help improve the usefulness and reliability of our MD simulations[64,65]. Some of the common sources of error are listed below:

Use of simple cut-off implemented in GROMACS: A non-zero force may be produced at the cut-off by simple truncation of forces at the cut-off distance. While we use the Verlet scheme with a simple cut-off that has been implemented in GROMACS over the group scheme, we alleviate this problem of non-zero forces to some extent by increasing the cutoff distance within the range recommended by the parametrized force-field for the non-bonded interactions.

Neighbor list update frequency: It was shown recently that a protein membrane system may be particularly sensitive to the neighbor-list (NL) update frequency and that some interactions could be missing when the default GROMACs NL update frequency of 10 is used[66]. This came to our attention after we had conducted a majority of our simulations; we will thus conduct some tests in the near future to assess the sensitivity of the results to the neighbor list update frequency.

Treatment of charge groups: Care is taken to treat all the partially-charged carbon atoms as separate groups.

Use of reaction field: The more efficient Particle Mesh Ewald Summation technique[67,68] which takes into account that the dielectric of the medium (contains water and ions) is not homogeneous is used to treat electrostatics.

Use of Berendsen thermostat: The Berendsen weak-coupling thermostat can create an inhomogeneous temperature distribution that can generate net flow. We use the Berendsen

thermostat only for the initial relaxation of the system temperature; thereafter the velocity-rescale thermostat of GROMACS is used and the center-of-mass motion is removed at every time step.

Lorentz-Berthelot mixing rules as opposed to other rules: We use the geometric mean recommended by the OPLS force-field for cross-interaction terms.

Use of single-precision as opposed to double-precision: Use of single-precision is thought to give round-off errors (due to the difference in the number of significant digits presented in the decimal places; 7 digits for single precision as compared to 15 digits in double precision). We have tested results for both single and double-precision GROMACS builds with little difference in results between the two. We thus employed the less computationally expensive single-precision GROMACS build.

2.3 Analysis Techniques

2.3.1 Structural calculations

Radial distribution functions

Radial distribution functions provide a good understanding of the length scales to which structural correlations exist and also help to reveal differences in the local structure of water and ions induced by varying confinements, external charges, and concentrations of electrolyte. The radial distribution function is the ratio of the average number density at a distance *r* from any given atom to the number density at a distance *r* from an atom in an ideal gas at the same overall density. For confined cases where we are interested in the structuring of water and ions with respect to the CNT, we calculate the RDF around the center of mass of the CNT that runs parallel to the *z*-axis of the CNT. The RDFs obtained from MD can be compared directly with neutron scattering, X-ray scattering, or light scattering experiments of similar systems.

Coordination numbers

We study the equilibrium ion solvation structure in bulk and inside the CNT, which allows us to study the effect of confinement. Additionally, a comparison between coordination numbers of ions in bulk obtained from MD simulations and from experiments allows us to judge how well the force-field represents real ion solvation[69]. The first solvation shell coordination number is determined by integrating the radial distribution function to the first minima of the radial distribution profile of the water and ion. This is also the radius of the first coordination shell. This method is similar to counting the number of water molecules in the first hydration shell. The RDF is calculated from an average of several equilibrated simulation frames.

Water hydrogen bonding numbers

To compute the number of hydrogen bonds we have employed the following empirical geometric criterion[70,71]:

a. The donor-acceptor (*O - - - O*) distance, $r_{oo} \leq 0.35$ nm. This is roughly the value of the location of the first water solvation shell as visualized from the radial distribution function where the number of water molecules is slightly greater than 4.

b. The donor – acceptor angle (*O - - - OH*), $\theta \leq 30°$

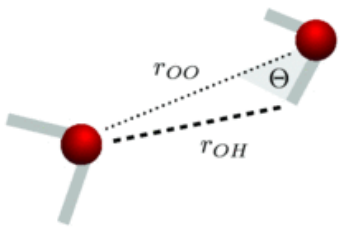

Figure 2-1: Geometrical criterion for hydrogen bonds

This empirical formulation comes from a minimally geometrically consistent criterion that was identified from statistical analysis of many protein structures. The geometrical definition of a hydrogen bond relies to some extent on cutoffs that are chosen with some degree of arbitrariness or, in general, are less restrictive. Other descriptions of hydrogen bonds include the energetic definition or the more recently introduced topological definitions. However, the evidence of these definitions successfully yielding accurate values for the number and distribution of hydrogen bonds is yet limited. For practical purposes, we apply the geometrical criterion for hydrogen bond definition. Moreover, the geometrical definition of the hydrogen bond, while providing a good representation of the directionality of the hydrogen bond, corresponds well with more sophisticated hydrogen bond definitions and allows us to easily compare our work with that of others[72].

2.3.2 Dynamics calculations

Diffusion coefficients

The diffusion coefficient can be calculated from the Einstein equation using the mean-squared displacements (MSD) of the species of interest. In normal or Fickian diffusion, the slope of the MSD curve is proportional to the diffusion coefficient. Each time step is used as a time origin to improve statistics, and different time intervals that are considered to be uncorrelated with the entire simulation are used to obtain statistically relevant values of the diffusion coefficient,

$$D = \lim_{t\to\infty} \frac{1}{2td} \langle |r_i(t) - r_i(0)|^2 \rangle \tag{2.41}$$

Here, $r_i(t)$ is the position of the i^{th} particle, d is the number of dimensions, and t is the time duration. We also obtained the diffusion coefficient from the integral of the velocity autocorrelation function using the Green-Kubo relation:

$$D = \frac{1}{Nd}\int_0^{\infty} \left\langle \sum_{i=1}^{N} v_i(t).\, v_i(0) \right\rangle dt \tag{2.42}$$

Here, *N* is the number of particles, and v_i is the velocity of the i^{th} particle.

Hydrogen bond lifetimes

There are two definitions that are commonly used to describe hydrogen bond lifetimes; mainly, uninterrupted hydrogen bond lifetimes and interrupted hydrogen bond lifetimes, which are outcomes of the history dependent and history independent forms of the correlation functions. The calculation of uninterrupted hydrogen bond lifetimes entails calculating the distribution of lifetimes by making a histogram of the number of hydrogen bonds that existed continuously from time '0' to time '*t*'. The calculation of uninterrupted (continuous) hydrogen bond lifetimes requires sampling at very short intervals and hence storing coordinates every few fs, requiring impractically large data storage without a guarantee of a good approximation[70].

We use the history independent definition of hydrogen bond lifetimes that allows for the formation and breaking of the hydrogen bonds; i.e, the interrupted hydrogen bond lifetimes. The hydrogen bond lifetimes are calculated according to the reactive flux method of Luzar and Chandler[73]. This involves calculating the hydrogen bond autocorrelation function

$$c(t) = \frac{\langle h(0)h(t)\rangle}{\langle h\rangle} \tag{2.43}$$

where $h(t) = 1$ if the tagged water pair is hydrogen bonded and is zero otherwise. Thus, $c(t)$ is the probability that a pair of water molecules is hydrogen bonded at time'*t*' given that they were bonded at $t = 0$. The reactive flux correlation function is given by

$$k(t) = -\frac{dc}{dt} = -\frac{\langle j(0)[1 - h(t)]\rangle}{\langle h\rangle} \tag{2.44}$$

where $j(0) = -\frac{dh}{dt}|_{t=0}$. On further partitioning of the function $k(t)$ to take into account whether or not a pair has moved apart after its bond is broken, the kinetics follows

$$k_{in}(t) = -\frac{\langle j(0)[1-h(t)]H(t)\rangle}{\langle h\rangle} = -\frac{dc}{dt} = kc(t) - k'n(t) \tag{2.45}$$

where $H(t) = 1$ if the donor-acceptor distance is less than 0.35 nm and it is zero otherwise. Furthermore, $n(t) = \int_0^t dt' k_{in}(t')$ is the probability at time *t* that a pair of initially bonded water molecules are now unbonded but remain separated by less than $r = 0.35$ nm. This type of kinetics results from a coupling of hydrogen bond population and diffusion. Here k and k' give the rate for breaking and forming of hydrogen bonds, which are obtained by fitting $k_{in}(t)$, $c(t)$, and $n(t)$ in the above equation. The average hydrogen bond lifetime is given by the inverse of the forward rate $1/k$.

2.3.3 Energetics

Hydrogen bond energies

Sheu et al.[74] calculated the hydrogen bond energies of peptides via a kinetic approach utilizing the forward rate constant of hydrogen bond lifetimes; this technique has been subsequently adapted to predict the activation energies in many recent works[70]. The specific rate constant in the Arrhenius form is

$$k = A\,exp\left(-\frac{E}{RT}\right) \tag{2.46}$$

$$\tau_{HB} = \frac{h}{k_B T} exp(\frac{\Delta G}{k_B T}) \tag{2.47}$$

Here, ΔG is the Gibbs free energy of activation, *A* is the prefactor, *h* is the Planck's constant, *T* is the temperature, and k_B is the Boltzmann constant.

Free energy of solvation of ions using the Bennett Acceptance Ratio method

The free energy barrier essentially governs the dynamics of water and ion transport through a CNT, and a discussion of water and ion transport would be incomplete without providing some insight into the energetics of ion permeation. The chemical potential (or the free energy) dictates how ions and water partition into a CNT membrane, and obtaining a reliable estimate of the free energy can help uncover the fundamental physical mechanisms of ion transport and quantify the barriers to ion transport through CNTs. Several approaches using a combination of MD simulations and numerical calculations centered on statistical mechanics have been proposed to calculate relative free energies; i.e., the energies between the two end-states of interest. These include the well-established and popular equilibrium techniques such as thermodynamic integration (TI)[75], free energy perturbation (FEP) methods[76], and the more recently proposed methods which are based on non-equilibrium work[77].

In order to calculate the solvation energy of the ions from MD simulations, we rely on the Bennett acceptance ratio (BAR) method, which is an improvement over the unidirectional FEP method. Several studies indicate that the BAR technique gives smaller errors as compared to the traditional FEP and TI approaches and has generally proved very useful in ligand binding studies for drug delivery[78]. It provides a practical and efficient strategy to calculate plausible values for the free energy difference while minimizing bias related errors associated with FEP. A rigorous derivation of the BAR method can be found in the 1976 paper by Bennett[79]. This technique has been implemented in GROMACS [80] and can be used via a staging scheme employing multiple lambda values, which will be discussed later. We focus here on general aspects of the BAR method and its practical implementation in simulations.

The BAR method to calculate the free energy of hydration (ΔG_{hyd}) involves decoupling the solute molecule (in the present case, the ion) from its environment, and since free energy is a state function, we can calculate the free energy difference between the end states (the ion coupled with the solution and with all the interactions between the ion and the solvent switched off) without worrying about constructing an actual physical process. As such, it is called an alchemical transformation where the interactions between the solute and the solvent can be switched off using a coupling parameter λ. We define a parameter-dependent Hamiltonian,

$$H(\Gamma, \lambda) = \sum_{i}^{N} \frac{p_i^2}{2m_i} + U(x_{i,} \dots, x_{N;}\ \lambda) \tag{2.48}$$

One can connect the Hamiltonians of the initial and end states

$$H(\lambda_i) = (1 - \lambda_i)H_0 + \lambda_i H_1 = H_0 + \lambda_i \Delta H \tag{2.49}$$

There needs to be significant overlap between the two end-states sampled since the free energy difference calculated relates to the point where the free energy difference probability distributions of the two states intersect. Thus λ values can be successively changed from 0 to 1 in several steps, ensuring proper sampling of all states important to the free energy calculation. The Hamiltonian of the state is given by the sum of the potential and kinetic energies; however, the kinetic energy terms are separable and the free energy calculations boils down to the calculation of the potential energy terms.

The potential energy (U) between two states is expressed as a linear function of the coupling parameter λ, where $0 \leq \lambda \leq 1$:

$$U(\lambda_i) = (1 - \lambda_i)U_0 + \lambda_i U_1 \tag{2.50}$$

From the FEP theory, which forms the basis and the limiting case of the BAR method, the free energy is given by

$$\exp(-\beta\Delta G) = \langle(exp(-\beta\Delta U)\rangle_0^{eq} \tag{2.51}$$

$$\Delta G = -\frac{1}{\beta}\ln\frac{1}{N}\sum_{i=1}^{N}\exp[-\beta\Delta U(\Gamma_i)] \tag{2.52}$$

$$\Delta G = -\frac{1}{\beta}\sum_{i=1}^{n}\ln\langle\exp(-\beta\Delta\lambda_i\Delta U)\rangle \tag{2.53}$$

Here, β is the reciprocal temperature. The free energy difference is calculated during the transformation of the molecule while having its interaction with the solvent turned off; i.e., its potential energy transitions between that of the initial and final states by modulation of the λ parameter between 0 and 1. This is done in two steps: first by having its Coulombic interactions with its surrounding linearly scaled to zero, and then by switching off the van der Waals interaction using a soft-core scheme. Since the chemical composition of the end-states of interest differ on account of the solute being completely decoupled from the solvent, their Hamiltonians will differ significantly, and to ensure sufficient overlap between configurational spaces, a number of intermediate λ values may be chosen to achieve the transformation between the end-states. Thus the overall change is split into a series of smaller perturbations and is achieved by performing a number of simulations at different λ values where a number of staging windows are chosen such that energy difference distributions at subsequent λ values overlap.

In the BAR method, instead of perturbing directly from state A to B, two intermediate perturbations to an intermediate state R are performed. The intermediate state is to be determined self-consistently in a post-processing step. The advantage of using GROMACS is that this intermediate step calculation is done on the fly during the simulation and the free energy difference

output is accompanied by the uncertainty in the calculation. We follow the best practices and methods given in several excellent papers in order to avoid errors associated with under sampling in free energy calculations[75-86].

Potential of mean force calculation from umbrella sampling

Umbrella sampling gives an estimate of the PMF or the free energy along a reaction coordinate, which in our case is the ion translocating from the bulk state to the interior of the CNT. Provided good sampling and convergence, these should agree well with the values obtained from the difference in solvation energies of the ion in the CNT and in bulk. Prior to Torrie and Valleau[55] introducing umbrella sampling, the conventional technique to calculate the free energy difference was numerical integration, following the determination of some derivative of the free energy at a series of state points connecting the state or system of interest to one with a known free energy. The umbrella sampling technique is briefly described here:

$$Q = \sum_j \exp\left(-\frac{U_j}{k_B T}\right) \tag{2.54}$$

Q is the canonical partition function, U_j is the potential energy states of the ensemble

$$A_i = -k_B T \ln Q_i \tag{2.55}$$

$$A - A_0 = -k_B T \ln Q + k_B T \ln Q_0 = -k_B T \ln\left(\frac{Q}{Q_0}\right) = -k_B T \ln(P) \tag{2.56}$$

P is the probability density, A_0 is the reference state free energy, which is zero:

$$\frac{A}{k_B T} - \frac{A_0}{k_b T} = -ln\left\langle \exp\left(-\frac{U}{k_B T} + \frac{U_0}{k_B T}\right)\right\rangle = -ln\langle \exp(-\Delta U^*)\rangle_0 \tag{2.57}$$

$\langle \quad \rangle_0$ denotes the ensemble average over a canonical ensemble of reference systems and U^* is the reduced energy $\frac{U}{k_B T}$. The same set of equations can be transformed into a continuous ensemble.

The form of the energy landscape determines the ergodicity of the system. Many systems are non-ergodic; i.e., some regions of the configurational space are not sampled because of the timescale of the simulation due to the high potential energy states or high-energy barriers that separate the regions of interest. Thus, adequate sampling of all regions of the configurational space is required for estimating an accurate value of the free energy. The free energy of a state is proportional to the probability distribution of states of interest. On running a MD or a MC simulation long enough, if the probability distribution of all regions along the reaction coordinate can be obtained, one can easily estimate the free energy. However, the probability distribution converges slowly, owing to the barriers along the *x* direction. Thus, umbrella sampling by itself may not be useful. A bias in the form of a harmonic potential may be introduced to enhance sampling in the unfavorable regions of the configurational space. The weighted histogram method (WHAM) introduced by Kumar et al.[87] is generally applied as an extension of Umbrella sampling of a biased simulation. The WHAM method corrects the biased probability distribution to finally yield an unbiased probability distribution of the correct physical system.

Next we discuss an implementation of the umbrella sampling scheme for our systems. Since the ions travel mainly along the *z*-axis of the CNT, a suitable reaction coordinate would be one that connects the *z* coordinate of some point of the reservoir at the entrance of the CNT with the *z* coordinate of some point of the reservoir at the exit of the CNT, along which the PMF must be determined. To avoid poor sampling along the reaction coordinate, the Hamiltonian is biased by addition of an umbrella potential term of a harmonic form that restrains the potential in the configuration of the system to z' value:

$$U(z') = \frac{1}{2}k'(z - z')^2 \tag{2.58}$$

The potential of mean force that can be obtained through umbrella sampling using MD simulations gives a quantitative estimate of the energetic cost of ion transport through CNTs. The PMF profile that consists of peaks, minima, and flat regions gives us an idea of the energy landscape that the ion must traverse while translocating through the CNT.

The PMF is obtained by the integration of the mean force acting on the ion that is at position z',

$$PMF(z) = -\int_{z_{ref}}^{z} f_z\,(x, y, z' = 0)dz' \tag{2.59}$$

z_{ref} is the reference point in bulk where the PMF is taken as zero. For a very dilute system, the potential of mean force may be taken as the intermolecular force between two molecules as they are not affected by the rest of the molecules in the system. In other words, for very low densities, the potential that provides the mean force acting on a molecule is the intermolecular potential. However, it is easy to see that in a dense system this is not the case. Calculation of free energies provides us with a quantitative value that can be compared directly with experimental data and can help in the improvement of force-fields.

Quantities derived from energy profiles

Marrink and Berendsen provided a theoretical derivation of permeation-related properties, such as permeability coefficients, the partition coefficients, the maximum conductance that could be computed directly from the potential of mean force calculation, and local diffusion coefficients of permeating species[88].

a. Permeability coefficients

The permeability coefficient of species 'i' expressed in terms of the potential of mean force ($\Delta G(z)$) and the local diffusion coefficient $D_i(z)$ of species 'i' is given by[89]

$$P_i = \left(\int_{z_1}^{z_2} \frac{\exp(\Delta G(z)/RT)}{D_i(z)} dz \right)^{-1} = \frac{K_i \times D_{eff}}{L} \tag{2.60}$$

where the permeability coefficient is in m/s. Knowing the PMF and the local diffusion coefficient, one can easily estimate the permeability coefficient. Unlike biological membranes, the CNT membranes that we study are quite homogeneous and thus the diffusion coefficient inside the membrane to the first approximation can considered as independent of the *z*-position. This is also further demonstrated by the flatness of the free energy profile inside the CNT as opposed to that inside lipid bilayers where the free energy profile has a triangular form with a well-defined peak[90]. The CNTs (d =1.356 nm – 3 nm) that we study are also almost twice the thickness of the lipid membranes, which makes the boundary effects less important.

b. Partition coefficients

The equilibrium partition coefficient is given by[90]

$$K_i = \frac{1}{L} \int_{z_1}^{z_2} \exp\left(-\frac{\Delta G(z)}{k_B T} \right) dz \tag{2.61}$$

c. Maximum conductance

Assuming single-ion occupancy, which is likely only for very narrow membranes and low reservoir concentrations, the maximum single channel ion conductance can be estimated from an expression given by Roux et al.[89]

$$g_{max} = \frac{q^2}{k_B T L^2} \langle D(z)^{-1} \exp\left(\frac{\Delta G(z)}{k_B T} \right) \rangle^{-1} \langle \exp\left(-\frac{\Delta G(z)}{k_B T} \right) \rangle^{-1} \tag{2.62}$$

d. Specific conductance

The expression given by Vorobyov et al.[90] for specific conductance given is

$$G_i = tG_m = \frac{N_A C q^2 P_i}{k_B T} \tag{2.63}$$

where N_A is Avogadro's number, q is the ionic charge in coulombs, C is the concentration in mol/m^3, k_B is Boltzmann constant in J/K, T is the temperature in K and G_i is the specific conductance in S/m^2.

Chapter 3. Literature review

Sumio Iijima in 1991 reported[91] the preparation of a new type of finite carbon structure consisting of needle-like tubes, produced using an arc-discharge evaporation method, which we today know as carbon nanotubes (CNTs). These new hollow graphitic tubules of nanometer dimensions stimulated almost immediate interest in their unique structural[92], optical, electronic[93], mechanical, and thermal properties[94]. Chemical vapor deposition[95] and laser ablation techniques[96] have since become popular methods of producing carbon nanotubes. The unique physical properties and potential applications of carbon nanotubes in commercial nanofluidic applications, as well as their functionality as tools to test quantum mechanics and model biological systems, encourage a large amount of new research even today.

3.1 Structure and properties of carbon nanotubes

A carbon nanotube is a seamless cylindrical sheet of graphene whose diameter is so small and its aspect ratio (diameter vs. length) is so great that it can be considered from the electronic point of view as a one-dimensional structure[97]. A nanotube may consist of one (single-walled) or more concentric seamless cylindrical shells of graphene sheets (multi-walled). Each carbon atom is bonded to three neighboring carbon atoms through sp^2 hybridization. A single-walled CNT (SWCNT) has an inner diameter of

$$d_{in} = \left(\frac{a}{\pi}\right)\sqrt{n^2 + m^2 + nm} - 2r_c \qquad (1)$$

where a is the lattice parameter of graphene with value of 0.25 nm, n,m are chiral indices, and r_c is the Van der Waals radius of the carbon atoms (0.17 nm).

CNTs can be metallic or semiconducting. depending on their chirality[98]. They exhibit ballistic transport of electrons[99], are good conductors of heat[100], and have stiffness values higher than steel[101].

3.2 Studies on confinement and transport of water through carbon nanotubes

One would not expect water to enter a narrow hydrophobic carbon nanotube[102]; however, MD simulations that showed spontaneous and continuous filling of non-polar (6,6) CNTs with a one-dimensional ordered chain of water molecules were first reported by Hummer, Rasaiah, and Noworyta in 2001[19]. It was observed that water moved through the nanotube in a highly correlated single-file manner maintaining a chain of hydrogen bonds. Water within the (6,6) nanotube moved in bursts— Hummer et al. reported an average of about 17 water molecules pass through the tube each nanosecond, with occasional peaks of about 30 molecules ns^{-1}.

Theoretical predictions of a one-dimensional continuous-time random walk (CTRW) of the entire train of water molecules in the pore were also shown to quantitatively reproduce the important features of the transport of water molecules through a carbon nanotube as found in the MD simulations[20]. These features included the bursts of unidirectional pulses, the typical time durations and intervals between the pulses, the distribution of the number of particles translocated during a pulse, the lifetimes in the channel for molecules that either traverse the channel or return back into the initial reservoir, and the passage and return probabilities for molecules that enter the channel[20]. Jing-Yuan et al[103] investigated the length dependence of flow measurements through CNTs and found that the flow of water decreases as the length of the tube is increased according to a fast power-law decay ($L^{-2,-3}$) in contrast to the slower power-law decay (~ $1/L$) found by Berezhkovskii and Hummer[20] using the CTRW model. A similar fast power-law decay was also

reported by Guo et al.[104], who suggested an exponential decay for longer CNTs that was independent of the pressure or the applied electric-field.

The key to these unique features of water transport through a (6,6) CNT was thought to reside in the energetics of hydrogen bonding. If water molecules enter the nanotube, they each lose on average two out of their four hydrogen bonds. This would be expected to be too high an energetic cost to allow the water to enter. However, fluctuations in the number of hydrogen bonds per water molecule in the bulk aqueous phase result in a significant fraction of water molecules that are incompletely hydrogen-bonded, and thus have a low binding energy. This class of water molecules is not present within the nanotube, which provides enough difference in the chemical potential to drive water into the tube where the water is shielded from fluctuations.

Gordillo and Marti reported a distortion of the hydrogen bond network due to confinement; specifically, a decrease in the average number of hydrogen bonds as compared to their bulk counterpart. In the most extreme case of (6,6) tube, the number of H-bonds was found to be half of that in bulk water. They also noted a layered structure of water inside the CNTs based on the density profiles[32]. An examination of the structural properties of water in the interface external to the CNT using MD simulations also revealed a characteristic layering of the water radial density profile and a significant decrease in the number of hydrogen bonds of water surrounding the CNT[105]. Werder et al. calibrated potentials of water to recover the macroscopic contact angle of 86° (non-wetting behavior) of a water droplet on graphite, and, using these potentials, they found a layered structure of water near the walls and a lower number of average hydrogen bonds of water inside the CNT[106].

Koga et al. investigated dimensionally-confined phase transitions of water in CNTs and found that under severe confinement and subjected to high axial pressures, water can exhibit a

first-order freezing transition to hexagonal and heptagonal ice nanotubes, and a continuous phase transformation into solid-like square or pentagonal ice nanotubes that depend on the diameter of the nanotube[30]. Even though MD-related force-fields are criticized for accuracy, more recently, Kumar et al.[31] demonstrated experimentally that similar to the observations of MD, the phase transitions of confined water in CNTs are extremely diameter-dependent and freezing transitions as high as 138 °C for 1.05 nm metallic SWNTs were observed, close to the range of enthalpy stabilized, ice-like water as predicted by MD simulations[107]. Based on their observation of axial diffusion coefficients and radial molecular distributions of water confined in tubes of different diameters, Mashl et al. reported that at a certain critical diameter of 0.86 nm, water forms ice-like hexagonal structures with distinctive hydrogen bonding that makes it practically immobilized inside the nanotube[108].

The single-file hydrogen-bonded water wires in highly-confined nanopores form ideal proton conduction wires displaying fast proton transport as compared to proton transport in bulk water; this has potential applications in fuel cells[38]. Zhu and Schulten[109] noted that in pristine nanotubes, water dipoles adopt a single orientation along the tube axis with a low flipping rate between the two possible alignments. Surface-charge modifications can induce a bipolar ordering of water in nanotubes similar to that previously observed in biological water channels.

Osmotic water transport through carbon nanotube membranes was studied by Kalra et al.[21] where an osmotic force drives water from a pure water compartment through a hexagonally-packed carbon nanotube membrane to a salt solution compartment. Majumdar et al. showed through experiments that pressure-driven liquid flow through a membrane composed of an array of aligned carbon nanotubes is four to five orders of magnitude faster than predictions from conventional fluid-flow theory[22]. Holt et al. reported water flow measurements though micro-fabricated

membranes with aligned CNTs as pores that exceeded the hydrodynamic predictions by more than three orders of magnitude[23]. These flows were comparable to flow rates extrapolated from molecular dynamics simulations. Aluru et al. related the enhanced flow of water in CNTs to a velocity jump in the depletion region where the water concentration is less than 5% of the bulk value and a weak hydrogen bonding within the depletion region due to the free OH bonds[110]. Thomas and McGaughey[111] simulated pressure-driven flow through CNTs and obtained a flow enhancement that was the same order of magnitude as the experimental results of Holt et al.[23] but many orders of magnitude lower than reported by Majumdar. He suggested that by using a slip-modified boundary condition, the flow through the CNT could be completely described by Hagen-Poiseuille's equation and that the large enhancements previously reported in experiments of Majumdar et al. were a miscalculation of the available flow or are the presence of an uncontrolled external driving force[24].

Striolo simulated water confined in infinitely long CNTs and argued that long lasting hydrogen bonds were responsible for the ballistic transport of water when observed for durations of up to 500 ps, and that the trajectories are essentially Fickian when time scales in excess of 500 ps are taken into consideration[112]. Gong et al. reported molecular dynamics simulations in which charge-induced ordering of water leads to spontaneous and continuous unidirectional flow through a carbon nanotube that connects two reservoirs[64]. However, Karttunen et al.[65] pointed out that the flow was an artifact caused by the three charges being treated as a single charge group in GROMACS, and that when the three charges are treated separately, no flow is observed. Thus even though simulations are an invaluable tool, one must exercise caution while using accepted protocols since a small number of errors have since been discovered in them.

3.3 Ion transport through carbon nanotubes

It was recognized early on that carbon nanotubes can be used as selectivity filters[113]. Sun and Crooks made the first attempt at experimentally studying mass transport phenomena through single-pore multi-walled nanotubes of 150 nm diameter by probing the transport rates of polystyrene particles (100 nm - 60 nm)[114]. If CNTs are to be used as selectivity filters, this membrane separation application will require alignment of the tubes[115-118] into a defect-free, mechanically strong membrane, where each tube spans the complete thickness of the membrane and the tube mouths are open at the faces of the membrane. Ion flux can be enhanced by augmenting diffusive transport across the membrane with electrophoresis, electro-osmosis, or via the application of pressure. Miller et al. showed that electro-osmotic flow can be driven across template-prepared carbon nanotube membranes (outside diameter ~ 300 nm) and the rate and direction of flow can be controlled by changing the magnitude and the sign of the transmembrane current[119]. However, in order to have ion channel mimetic carbon nanotubes or to have them behave like molecular sieves, the diameter of the nanotube should be only a few nanometers, which is still very challenging to fabricate.

Uncharged pores and graphene slits have been proposed as a means of selective ion transport based on differential dehydration energies[120]. Hinds et al. fabricated an array of aligned CNTs (diameter ~ 6 nm -10 nm) that were incorporated into a polymer film, and thus obtained a well-ordered nanoporous membrane structure to study transport. They were able to demonstrate molecular gating by functionalizing the tips of the CNTs[121]. Theoretical modeling of ionic distribution and transport in silica nanotubes, 30 nm in diameter, suggested that when the diameter is smaller than the Debye length, a unipolar solution of counterions is created within the nanotube and the co-ions are electrostatically repelled[122].

Qiao et al. studied electrolytic transport through modified carbon nanotubes of diameter ~ 1.08 nm via MD simulations and found that application of partial charges on the rim atoms and an external electric field significantly increased ion occupancy[123]. They found that the adsorption behavior of the Na+ and Cl- counterions on a charged CNT was very different even though the magnitude of charge on the tube was the same and possibly depended on the size of the counterion, the local electrostatic interactions between the ion-water, ion-charged surface atoms, and on the external electric field. Such a difference gives rise to an atypical dependence of electro-osmotic transport on the surface charge that cannot be predicted by the conventional continuum theories[123]. They also observed that the application of partial charges on a (16,16) CNT and the application of an external electric field significantly increased ion occupancy as compared to the occupancy in an uncharged tube.

Molecular dynamic studies showing spontaneous encapsulation and electrophoretic transport of RNA[124] and selective partitioning of DNA in CNTs[125], which were also demonstrated by experiments[126], have also been reported. With an emphasis on the potential applications in micro/nano total analysis systems, Hyun et al.[127] demonstrated ion separation using a Y-junction carbon nanotube.

Aqueous electrolytes have an advantage of lower impedance and high power resulting from the low viscosity of the brine; however, they have received less attention as supercapacitors compared to ionic liquids or molten salts. The primary disadvantage of an aqueous electrolyte supercapacitor is the limitation of the electric potential to ~1 V. Wander and Shuford[128] elucidated the potential of electrolytes as supercapacitors by trying to understand ion transport dynamics using molecular dynamic simulations.

The electrical double layer (EDL) is a specific charge distribution at the solid-liquid interface where the fixed surface charges on the CNT are compensated by mobile counter-ions in the solution. The thickness of the electrostatic screening zone depends on the ionic concentration and can vary from less than 1 nm at high ionic strengths to a few tens of nanometers at low ionic strengths. In the case of nanometer-sized apertures, the EDL can represent a significant fraction of the total volume. Plecis et al.[129] called the counter-ion enrichment and exclusion of co-ions due to electrostatic interactions with surface charges as the exclusion-enrichment effect (EEE). They investigated the consequence of passive transport of charged species through a Pyrex nano-slit. By measuring the flux of the charged fluorescent dye through the slit, they found it possible to investigate the quantitative changes in the nano-slit permeability when the EDL thickness increases. At high ionic strengths, the instantaneous flux is proportional to the geometrical cross section. As the EDL thickness increases, the effective cross section through which anions can diffuse is reduced, resulting in a lower effective flux. For cationic species, the enrichment effect at low ionic strength increases the number of cations in the nano-slit that can be transported by diffusion. This was the first experimental or simulation work to give quantitative results for EEE and its consequences on perm-selectivity. While this experiment was conducted in a Pyrex nano-slit, the concept is applicable to nanoporous materials and could be applied to charged carbon nanotubes.

Fornaseiro et al.[51] investigated ion transport through sub-2-nm aligned carbon nanotube platform, which had negatively charged groups at the opening. Using pressure-driven filtration experiments and capillary electrophoresis analysis of the feed and permeate, they were able to quantify ion exclusion in these membranes as a function of solution strength, pH, and ion valence. Their trends strongly supported a Donnan-type rejection mechanism, dominated by electrostatic

interactions between fixed membrane charges and mobile ions, whereas steric and hydrodynamic effects appeared to be less important. They did point out, however, that although their results provide insight into the nature of ion transport, it was unclear if continuum models could be rigorously applied to sub-2-nm pores.

Liu et al.[130] fabricated a device consisting of a single-walled carbon nanotube that spanned a barrier between two fluid reservoirs through which electrophoretic transport of a small single-strand DNA was studied. They found the transport to be marked by large transient increases in ion current, which they attributed to electro-osmotic flow arising from the trapped charge on a metallic CNT. Pang et al. reported unusually high ionic conductance through nanotubes and similar results were described by Choi et al.[131], who reported a similar five-fold enhancement in stochastic ion transport rates for single-walled carbon nanotube ($d = 1.6$ nm). They observed a scaling of the ion transport rate with the cation type and reported on pore blocking trends. They assign these scaling trends to the changes in the hydration shell.

More recent work includes those by Secchi et al.[132] and Amiri et al.[133]. Secchi et al.[132] performed experimental studies on measurement of ion transport and current fluctuations inside CNTs (r = 3.5 nm - 35 nm). They found that the conductance exhibits a power-law behavior (with an exponent close to 1/3) at low salinity, as opposed to the constant surface conductance found in similar-sized boron nitride tubes. They rationalized this power-law scaling of conductance in terms of a salinity-dependent surface charge, which they accounted for based on hydroxide adsorption at the hydrophobic carbon surface. Amiri et al.[133] conducted experimental studies on ion conductance through individual single-walled carbon nanotubes that had negatively-charged carboxylate groups at the entrance as a function of solution concentration and type of cation. They found a preferential cation conductance with a diameter dependence and quantified ion

conductance based on the Gouy-Chapman theory. There are several other studies and reviews[134-139] on ion transport and partitioning through CNTs that also discuss the concepts and the possible applications of CNT based devices as molecular sieves and energy storage devices.

Chapter 4. The general features of the structure and dynamics of water in single-walled carbon nanotubes

4.1 Introduction

Evidence of biological water channels that permit fast and selective transport of water while blocking the transport of other solutes was given by Agre in 1992[13] for which he was later awarded the Nobel prize. Since then there has been tremendous interest among biophysicists concerning the dissimilarities in the structure and the transport of water under confinement in biological channels and that under macroscopic conditions[140]. In 2002, Hummer et al.[19] reported the results of Molecular Dynamics (MD) simulations conducted on a (6,6) CNT (d = 0.8 nm) wherein water could infiltrate a hydrophobic single-walled carbon nanotube (SWCNT) that was as narrow as an aquaporin channel. These studies hinted that the anomalous transport features of the water in biological channels were not unique to the domain of naturally occurring biological membranes but could be reproduced in artificial nanoscale membranes. Preceding the studies of Hummer, Koga et al.[30] and Gordillo et al.[32] using molecular dynamics had looked into the structure of water that was artificially introduced into nanotubes and reported on phase transitions (solidification) and excluded volume effects under confinement. Buoyed by this new discovery of the spontaneous filling of a nanotube with water molecules[19], a large number of molecular dynamics[105,141-144] and Monte Carlo (MC) simulations[145,146] using different water models were performed in great detail by various groups to look into the structure and dynamics of water. These results consistently showed striking long-range density fluctuations of unexpected magnitude, the lowering of the average number of hydrogen bonds as compared to bulk water, alignment of the OH bonds of water molecules along the nanotube axis, rotation of water molecules around the OH-bonds, and reduced diffusion coefficients.

Amongst the first experimental studies to report on the nature of water in carbon nanotubes was an X-ray diffraction study conducted by Maniwa et al.[147] in which they reported on water adsorption inside SWCNT bundles (d ~ 1.35 nm – 1.38 nm) where the liquid-like water transforms into a new solid form; i.e., into ice-nanotubes at 235 K. Another early direct experimental observation of water filling in nanotubes with confinements corresponding to up to 10 molecular layers was reported by Naguib et al.[148] They demonstrated a method to fill 2 nm – 5 nm diameter multi-walled CNTs with an aqueous fluid and perform in situ high-resolution TEM measurements. Finally, the structure and dynamics characteristics described by MD were first confirmed by Kolesnikov et al.[149] in 2004 using neutron diffractions (ND) and inelastic neutron scattering (INS) experiments of 1.5 nm diameter and 10 nm length SWCNT.

In this chapter, we describe the MD simulation results for the structure and dynamics of water under confinements in CNT diameters of 0.8 nm to 3 nm. Molecular dynamics simulations of a CNT in a TIP4P water bath were carried out using GROMACS 4.6.1 molecular dynamics package. In order to compare our results of water under confinement with existing studies, the structure and dynamics characteristics in terms of the radial and axial distributions functions of water, the average number of hydrogen bonds, and water self-diffusion coefficients were determined. This study not only helped us understand the changes taking place in water under confinement but also helped to validate our method and model that were later used for conducting comprehensive molecular dynamics studies of water and ion transport through single-walled carbon nanotubes for a variety of different cases of confinements, solution concentrations, surface charges, and electric fields, which are described in the latter chapters of this dissertation.

4.2 Computational Methodology

We performed MD simulations of water confined inside ten 5 nm long single-walled armchair CNTs with diameters ranging from 0.8 nm -3 nm. Additional simulations were performed by using just the water-filled CNT (without the external bath) from Figure 4-1 and by applying periodic boundary conditions to mimic an infinitely long CNT. The CNT atoms are modeled as uncharged Lennard-Jones atoms using the parameters for sp^2 carbon of benzene (OPLS_147) of the OPLS – AA[150] force-fields. The carbon atoms are held fixed during the course of the simulation using a harmonic restraining potential with a force constant of 10,000 KJ/mol/nm^2 to restrict their translational and rotational motion in the water bath. The TIP4P water model (see Figure 4-2) was chosen because of its more accurate representation of the phase diagram of water, the reproduction of the O-O peaks in the radial distribution function, and, most importantly, because the OPLS-AA force-field was developed entirely with TIP4P water. Water molecules are represented by the rigid four-site TIP4P empirical model having partial positive charges at the two hydrogen atoms, a Lennard-Jones interaction centered at the uncharged oxygen atom and an additional charge site, M, which is located on the bisector of the HOH angle. The LINCS algorithm is used to keep the water molecules rigid, thereby allowing for longer integration time steps. The Lennard-Jones parameters of cross-interaction are calculated based on the geometric mean for both σ and ϵ. The different MD parameters that were used for water and carbon are given in Tables 4-1, 4-2, and 4-3. Periodic boundary conditions are applied in all three directions. Particle Mesh Ewald summation was used for electrostatics in 3D periodic systems and the non-bonded interactions were truncated at a distance of 1 nm.

The CNT is solvated in a pre-equilibrated (300K, 1 bar) water bath and the water molecules inside the tube are removed to permit water to naturally enter the tube during the course of the

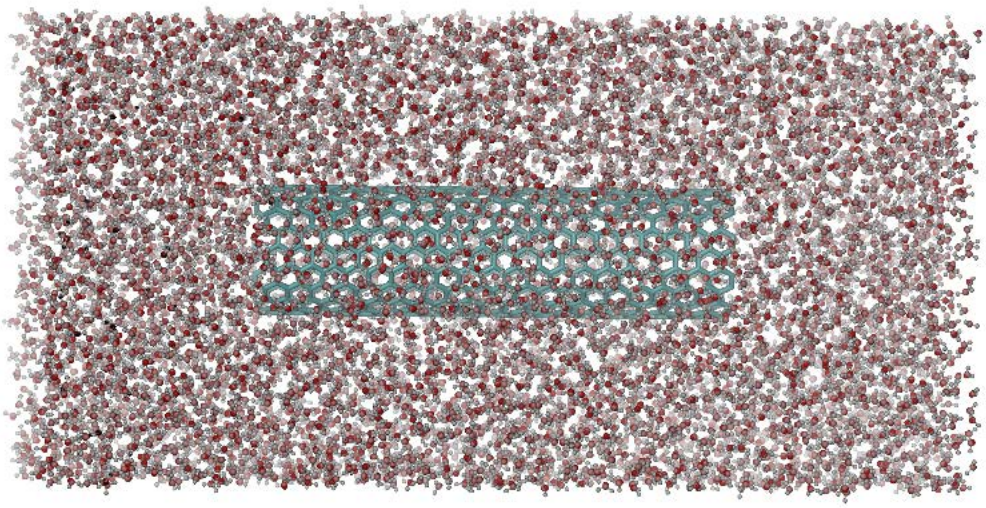

Figure 4-1: Snapshot of the initial configuration for a (10,10) CNT in bulk TIP4P water with view parallel to pore axis.

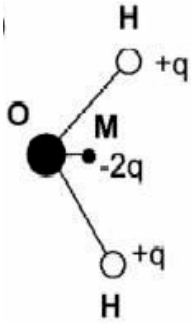

Figure 4-2: TIP4P water model.

Table 4-1: TIP4P parameters.

$d_{OH}(nm)$	$d_{OM}(nm)$	$H-O-H(°)$	$\sigma_{OO}\,(nm)$	$\epsilon_{OO}(\frac{KJ}{mol})$	$q_H\,(e)$	$q_M\,(e)$
0.09572	0.01546	104.52	0.3154	0.6485	0.52	$-2q_H$

Table 4-2: CNT parameters.

$q_M\,(e)$	$\sigma_{CC}\,(nm)$	$\epsilon_{CC}(\frac{KJ}{mol})$	$m(au)$
0	0.355	0.29288	12.011

Table 4-3: Carbon-Water interaction parameters.

$\sigma_{CO}\,(nm)$	$\epsilon_{CO}(\frac{KJ}{mol})$
0.3346	0.4358

simulation. This allows us to obtain the natural density of water inside the carbon nanotube. Energy minimization by the steepest descent method is carried out to remove any unphysical overlaps between atoms. The initial velocities of the atoms are assigned according to a Maxwell distribution at a temperature of 300 K with a random seed generator, and the system is then equilibrated in an NVT ensemble at 300 K by coupling to a Berendsen thermostat with a coupling constant of 5 ps for 1 ns. This is followed by an NpT equilibration via coupling to a v–rescale thermostat[151] at 300 K and a Berendsen barostat or a Parrinello-Rahman barostat at 1 bar for 5 ns. Once the target temperature and pressure are attained, all simulation runs for accumulation of statistics are carried out in the NVT ensemble with the v-rescale thermostat, a leap frog (Verlet) integrator, and a time step of 1 fs. We use Visual Molecular Dynamics (VMD 1.9.1) to visualize the trajectory.

4.3 Results

We discuss the effect of confinement on the molecular distribution of water inside the CNT and on its transport characteristics.

4.3.1 Axial density distribution of water inside CNTs

The fluid structure within the nanotube can be characterized by the density profile of water. The axial density of water in the tube follows a significant wave-like pattern with minimum values at the openings for the smaller diameter tubes, namely (6,6) and (8,8), as shown in Figure 4-3a. The wave-like pattern suggests a unique arrangement of water molecules inside the CNT pointing to more ordered ice-like structures. There are significant valleys at the entrances and exits of the smallest diameter tubes, namely (6,6) and (8,8), indicating that considerable energy is required for water to enter the smaller diameter tubes. The fluctuations in the density of water along the CNT length are more or less uniform. The walls of the CNT are hydrophobic and not all the volume of the CNT is available to water; hence the average density of water in the CNT as shown in Figure 4-3b is lower than the bulk value and is seen to increase as the diameter of the tube increases. It can also be seen that the average density of water (Figure 4-3b) inside the CNT increases sharply from the (6,6) to the (8,8) CNT and more slowly thereafter for increasing tube diameters.

4.3.2 Radial density distribution

The oxygen atom was used to characterize the radial density distribution of water in the CNT since the oxygen atom is quite close to the actual center of mass of the molecule[152]. The distribution profiles of water molecules in the CNT was found by using the cylindrical radial distribution function by calculating the ratio of the local density of water $\rho(r)$ to the average density of the system, ρ. The local densities are calculated by dividing the space inside the CNT

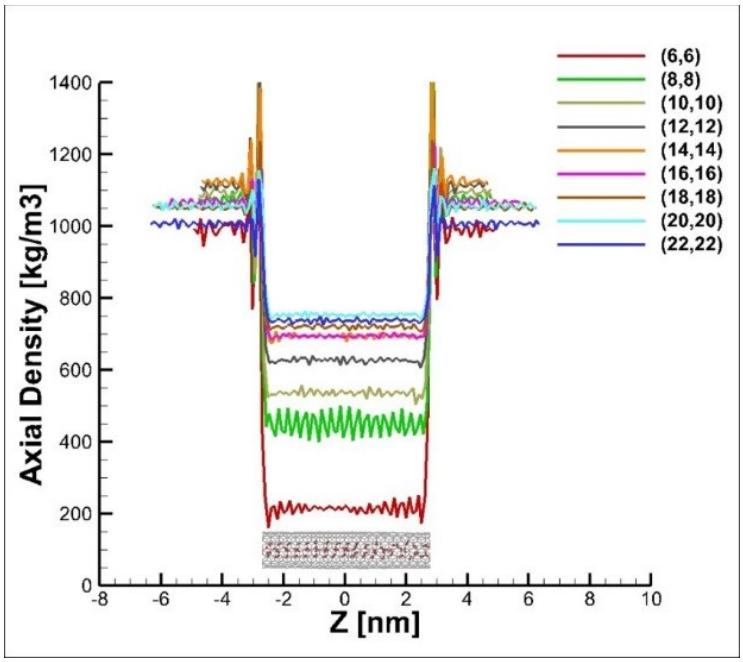

(a)

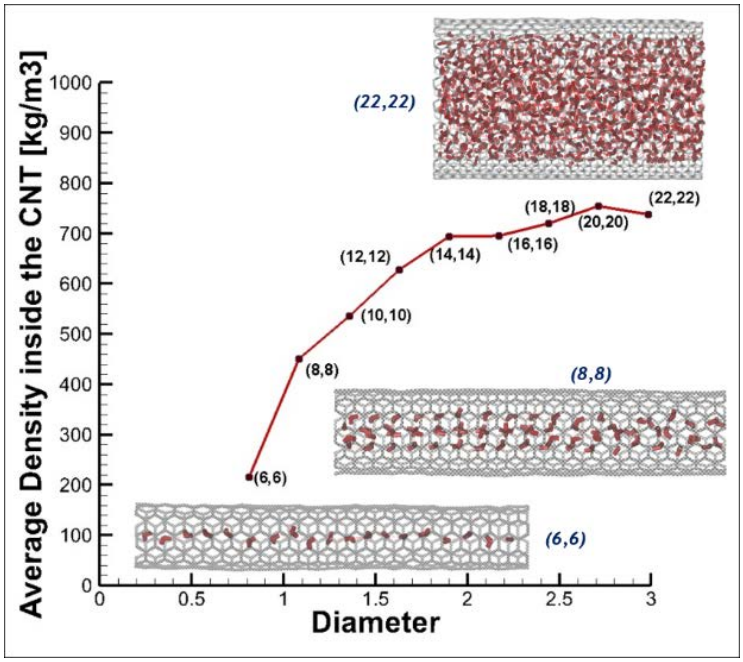

(b)

Figure 4-3: (a) Water density distribution along the nanotube axis; (b) average density of water in the tube.

into a number of cylindrical shells and taking the statistical average of the density for each shell.

The distribution of water inside is not uniform in the radial direction but more ordered, forming ice-like structures according to ice rules[103]. As reported by Hummer et al.[19], we also find that water molecules form a single-file hydrogen-bonded structure in the (6,6) CNT. This is represented by a single peak at the center of the tube, as shown in Figure 4-4. For the (8,8) CNT, water molecules appear to form a square net-like layer with water molecules present only near the wall and none at the center. For the (10,10) tube, there is a cylindrical shell surrounding a single-file of water. As the diameter of the CNT is increased, the number of ordered water molecular layers increases, which is evident from the increasing number of peaks in the radial density distribution. There are noticeable 3rd and 4th peaks for (14,14), (15,15), (16,16), and (18,18), (20,20), and (22,22) tubes. respectively (Figures 4-5 and 4-6). The width of the peaks also increases with the CNT diameter, indicating that water molecules are more ordered in smaller diameter tubes. The distance between the peaks (4, 3.4, and 2.8 for (8,8), (10,10), and (12,12), respectively, in Figure 4-4) is also greater than the r_{oo} distance of the first maximum of the bulk TIP4P water of 2.76 nm, as shown in Figure 4-7[150], and gradually approaches the value of the first maximum as the diameter increases. As the diameter increases further (see Figure 4-5), it can be seen that significant layering is still observed near the walls of the CNT; however, as we move towards the center of the tube, one can see the magnitude of the peaks diminishing with increasing diameter, thus signaling an approach to bulk behavior at the center. If we probe the structure of water in even larger diameter tubes, as shown Figure 4-6, we see that ordered structure of water in the CNTs becomes less obvious and more disordered at the center, with layering observed only close to the walls.

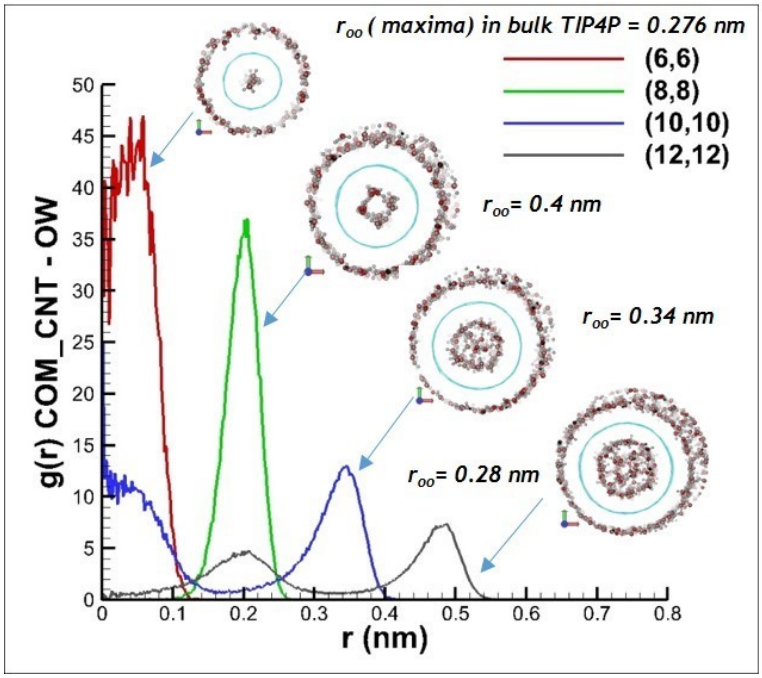

Figure 4-4: Radial density distribution of water in CNTs (6,6), (8,8), (10,10), (12,12).

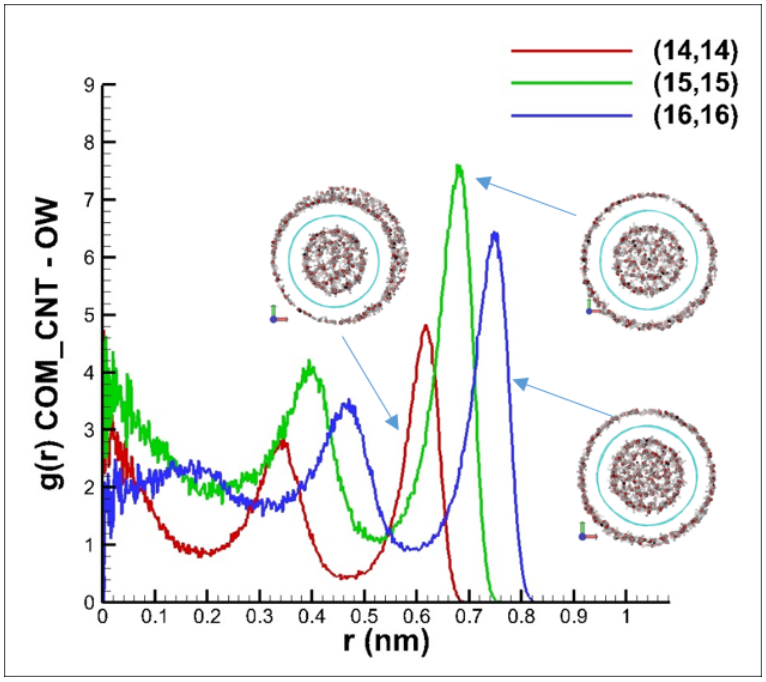

Figure 4-5: Radial density distribution of water in CNTs (14,14), (15,15), (16,16).

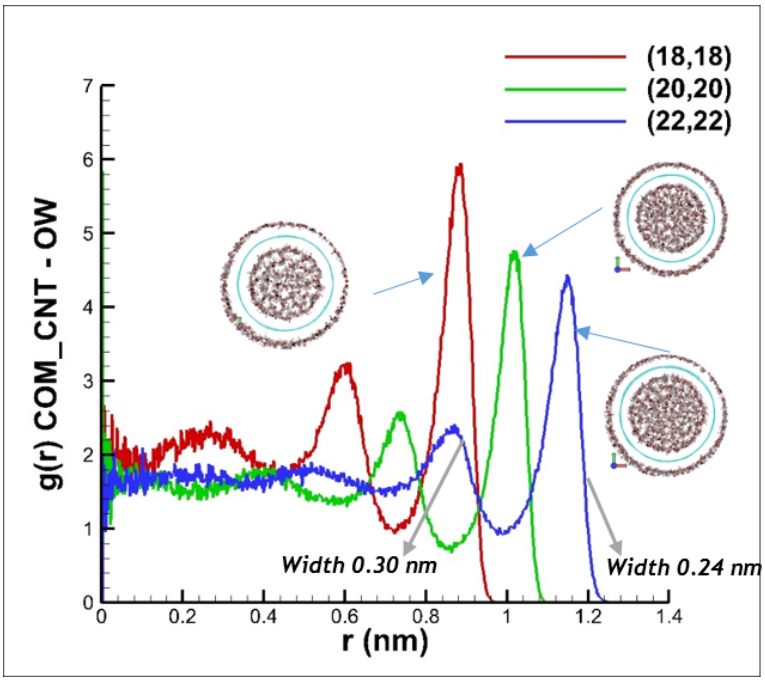

Figure 4-6: Radial density distribution of water in CNTs (18,18), (20,20), (22,22).

Table 6.5: Values for the O···O RDF (rigid models).†

Refs.	SPC [98]	SPCE [98]	TIP4P [95]	RWK2 [945]	ST2 [85]	Expt. [966]
T(K)	308	306	298	300	283	298
ρ	0.970	0.998	0.999	1.000	0.997	0.997
r_{M1}	2.77	2.75	2.76	2.75	2.84	2.87
g_{M1}	2.78	2.96	3.00	2.95	3.16	3.10
r_{m1}	3.55	3.31	3.37	3.35	3.53	3.31
g_{m1}	0.90	0.84	0.82	0.85	0.68	0.73
r_{M2}	4.58	4.64	4.42	4.41	4.65	4.50
g_{M2}	1.09	1.14	1.13	1.09	1.18	1.14

†See also tables in Ref. [77]. ρ: Density, g/cm^3.
r_{M1}: Position of the first maximum in Å.
g_{M1}: Intensity of the first maximum.
r_{m1}: Position of the first minimum in Å.
g_{m1}: Intensity of the first minimum.
r_{M2}: Position of the second maximum in Å.
g_{M2}: Intensity of the second maximum.

Figure 4-7: Values for the O...O RDF (rigid water models).

4.3.3 Diffusivity and hydrogen bonds

We measured the self-diffusivity of water in the CNTs and compared it with bulk values. The diffusivity of water in CNTs is anisotropic as compared to that in bulk water. This is due to the fact that the motion of water is severely limited in the radial direction as compared to the axial direction. Figure 4-8 gives an account of the average diffusivity of different water models under varying degrees of confinement[153] in CNTs. It is also known that different models of water under confinement yield different values of diffusivity, but this is to be expected on account of the difference in bulk water diffusivity coming from a comparison of different water models[154] as shown in Table 4-4.

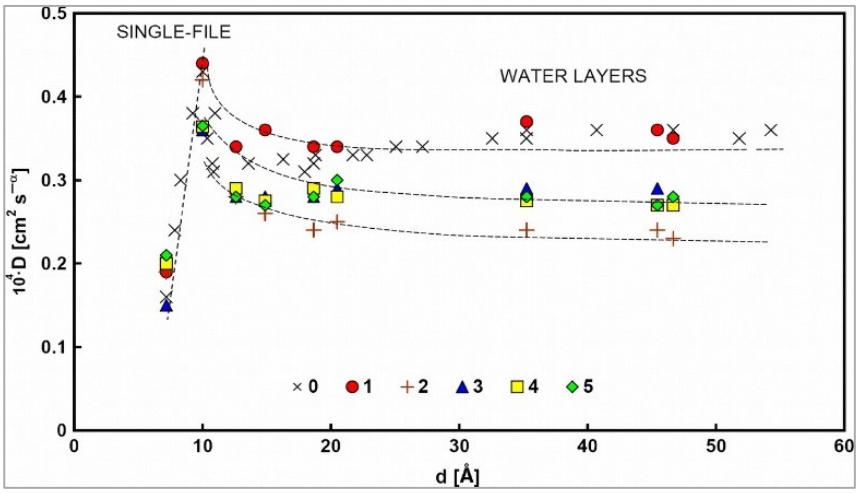

Water models simulated legend

Group	Water Model	Nanotube
0	TIP3P	Rigid
1	TIP3P	Flexible
2	SPC/E	Rigid
3	TIP3P flexible	Rigid
4	SPC flexible	Rigid
5	SPC flexible	Flexible

Figure 4-8: Average self-diffusivity coefficient D vs nanotube diameter calculated with various models.

Table 4-4: Computed properties of liquid water models at 298 K at and 1 bar for different water models.

Model	ρ (g/cm3)	$10^5\kappa_T$ (MPa−1)	10^5 α_p (K^{-1})	Cp (cal/mol/K)	$\Delta_v H$ (kcal/mol)	ε	Bulk diffusivity $10^9 D$ (m^2/s)
TIP4P	1.001	59	44	20	10.65	52	3.9
TIP5P	0.999	40.5	63	29	10.46	82	2.6
TIP4P/Ew	0.9954	48.1	33	19.2(21.4)	10.58(11.76)	63.4	2.44
TIP4P/2005	0.9979	46.5	28	18.9(21.1)	10.89(11.99)	60	2.08
Expt	0.9971	45.8	25.6	18	10.52	78.4	2.27

In the case of the finite CNTs, we use the Einstein equation (Eq. 4.1) to calculate the axial diffusion coefficients of water under confinement:

$$D = \lim_{t\to\infty} \frac{1}{2td} \langle |r(t) - r(0)|^2 \rangle \tag{4.1}$$

Here, $r(t)$ is the position of the center of the mass of the molecules, *d* is the number of dimensions, and *t* is time. For the case of infinite CNTs, we calculate the diffusion coefficients using the Einstein equation and the Green-Kubo relation (Eq. 4.2), which utilizes the time integral of the velocity autocorrelation function:

$$D = \frac{1}{Nd} \int_0^\infty \left\langle \sum_{i=1}^{N} v_i(t).v_i(0) \right\rangle dt \tag{4.2}$$

Here, N is the number of water molecules and v_i is the velocity of the i^{th} water molecule. By analyzing the mean-squared displacements, we can understand the mechanism of diffusion in these narrow carbon nanotubes and try to recognize some of the factors that affect the observed diffusivity.

Case 1: Finite CNTs

Figure 4-9 shows the axial diffusion coefficient of water as a function of CNT diameter obtained assuming that Fickian diffusion is valid in the narrow CNTs. Quite low values for the diffusion coefficient are obtained in the narrowest tubes, with the calculated diffusion coefficient being especially low in the (8,8) CNT. As the tube diameter increases, the diffusion coefficient can be seen to slowly approach the bulk diffusivity of TIP4P water (3.9×10^{-5} cm^2/sec).

Fickian diffusion occurs only when molecules pass each other randomly in the direction of flow; however, this may not be possible when molecules are confined in long narrow tubes such as in the (6,6) or the (8,8) CNT. When water molecules are confined in a narrow, one-dimensional channel, they are prevented from passing each other and the diffusion that develops could be of a single-file nature or of a ballistic nature where the confined water molecules move in a highly

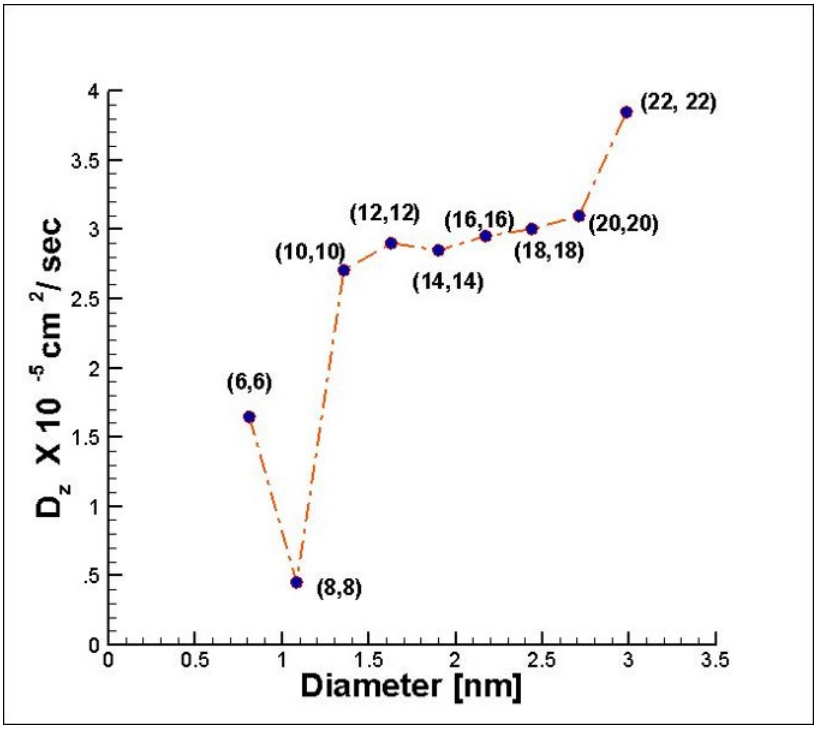

Figure 4-9: Diffusion coefficients of water in CNTs assuming Fickian diffusion.

coordinated fashion. The nature of the mean-squared displacements expected for these different diffusion mechanisms is shown in Figure 4-10. Deviations from Fickian diffusion may be seen due to pore–fluid interactions, pore size, or pore connectivity[112].

Diffusion in a one-dimensional interacting particle system with excluded mutual passage is known as single-file diffusion. In the (6,6) CNT ($d = 0.81$ nm) (Figure 4-11), we can observe from the trajectories of individual water molecules that they cross each other inside the CNT and strongly resemble the motion of molecules diffusing in a single file. The key feature of single-file diffusion is that the typical mean-squared displacement of molecules scales as $t^{1/2}$ rather than *t* as in normal diffusion. We calculate the exponent of time 'α' (Table 4-5) from a log – log plot of MSD vs time in order to verify if we have single-file diffusion in the (6,6) CNT. This calculation yields sub-diffusive 'α' values of ~ 0.8 for the narrowest CNTs (6,6) and (8,8) and normal 'α' values close to 1 for the wider tubes. We must, however, point out that water molecules inside the finite CNT that we utilize have short lifetimes, which may affect our results. To overcome the problem of limited lifetimes of water molecules in finite CNTs, we make use of CNTs that are connected to each other from end-to-end in a periodic simulation box. The results from those studies are presented next.

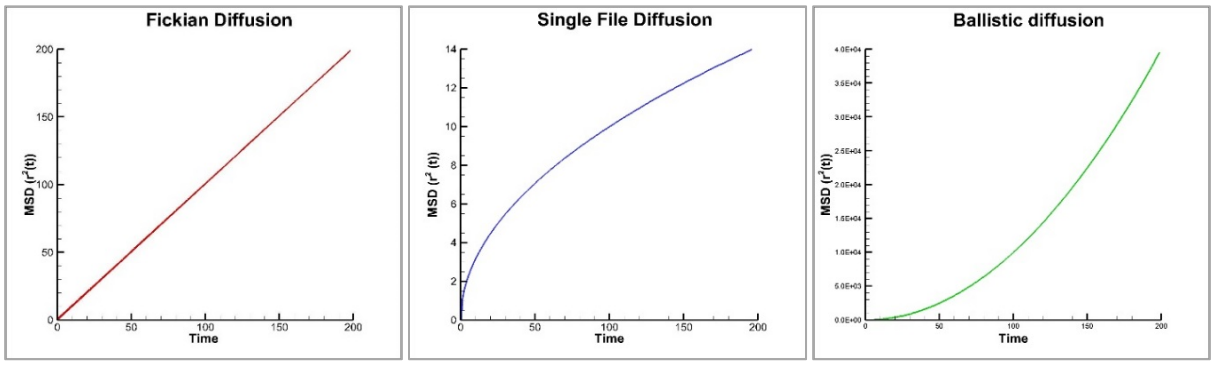

Figure 4-10: Types of diffusion.

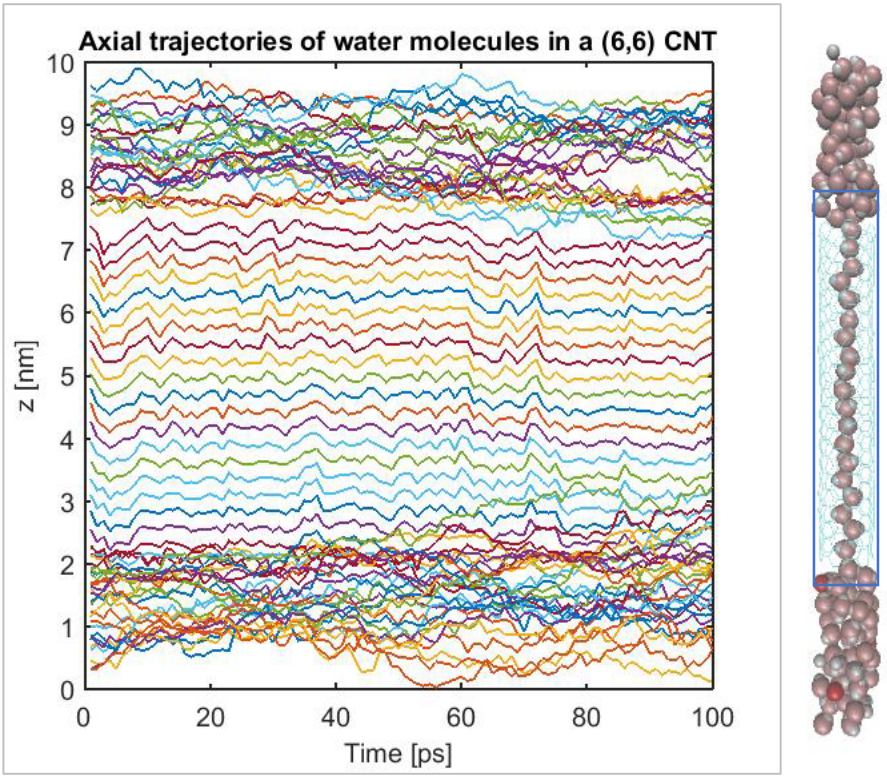

Figure 4-11: *z*-dimensional trajectories of water molecules in a (6,6) CNT for 100 ps.

Table 4-5: Model: log MSD = α log t + intercept.

CNT	α
(6, 6)	0.8193 (0.8168, 0.8219)
(8, 8)	0.8715 (0.8668, 0.8762)
(10, 10)	0.9017 (0.8997, 0.9038)
(12, 12)	0.9161 (0.9132, 0.919)
(14, 14)	0.9287 (0.927, 0.9304)
(15, 15)	0.9298 (0.9268, 0.9328)
(16, 16)	0.9494 (0.9491,0.9497)
(18,18)	0.9428 (0.9402, 0.9454)
(20, 20)	0.9594 (0.958, 0.9608)
(22, 22)	0.9533 (0.9502, 0.9565)

The values within the parenthesis represent the 95% confidence intervals.

Case 2: CNTs connected end-to-end (Infinite CNTs)

Figures 4-12 and 4-13 depict the logarithmic plot of the axial MSD of water molecules inside the CNT versus time and the axial diffusion coefficient in the CNTs (R = 10 – 22) obtained via the Einstein relation. The representative visual guide lines for Fickian (solid), single-file (dashed), and ballistic diffusion mechanisms (dotted-dashed) are also shown in black in Figure 4-12. We do not observe ballistic diffusion for the long timescales (30 ns) shown here. We observe a clear Fickian diffusion mechanism for water molecules inside CNTs with chiralities (R) ranging from 10-22; i.e. in the diameter range of 1.356 nm - 2.983 nm. The diffusion mechanism appears apparently Fickian for most of the duration of the simulation even in the smaller diameter (6,6) and (8,8) tubes (see Figure 4-12). The data shown here were collected every 1 ps for 30 ns. Perhaps femtosecond data collection might clarify the short time behavior of water confined in (6,6) and (8,8) CNTs.

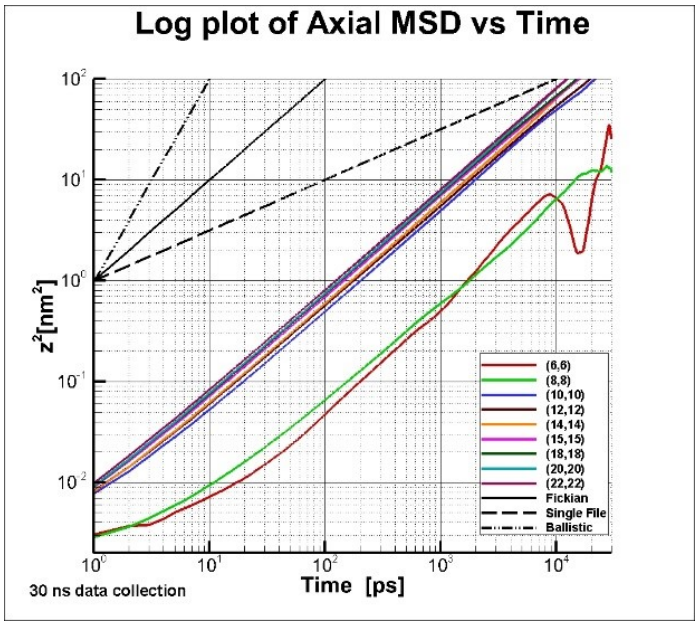

Figure 4-12: Log plot of MSD vs. time in infinite CNTs.

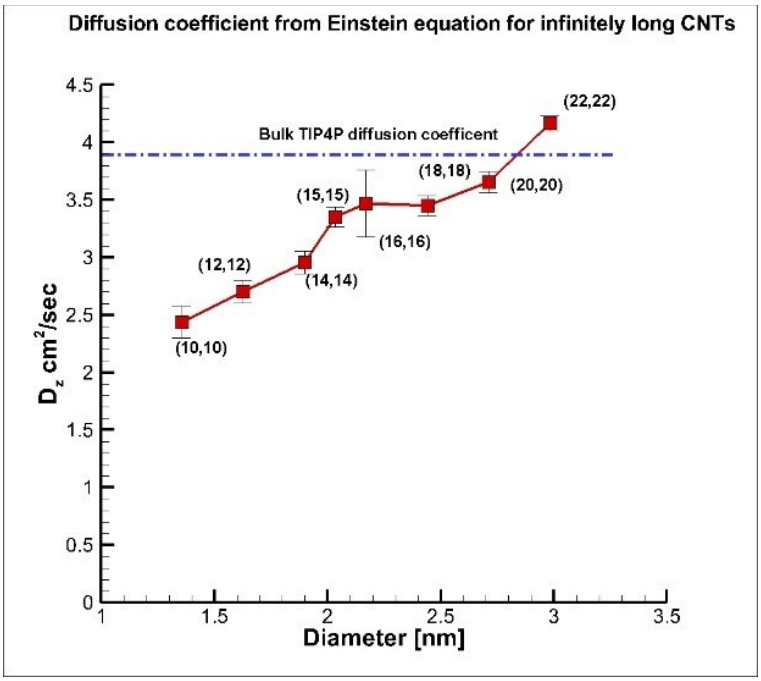

Figure 4-13: Axial diffusion coefficient of water from the Einstein relation (CNTs connected via periodic boundary conditions).

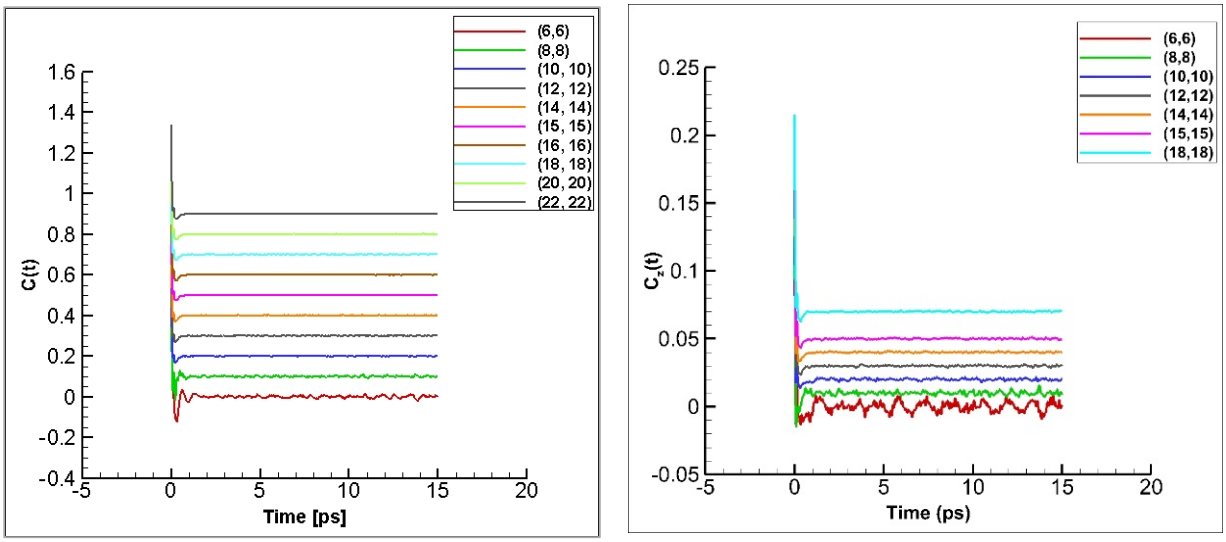

(a) **(b)**

Figure 4-14: (a) Overall velocity autocorrelation of water molecules in the CNT; (b) axial velocity autocorrelation of water molecules in CNT

The curves have been shifted on the *y*-axis for better visual inspection of the autocorrelation function.

We extend the simulation for 500 ps using a 0.5 fs time step and output the data at every time step to obtain an estimate of the axial diffusion coefficient using the velocity autocorrelation. It can be seen clearly that in a relatively short period the axial velocity autocorrelation (Figure 4-14b) converges to around zero from its initial value for the larger diameter tubes ($R \geq 10$). However, the same is not true for the smallest diameter tubes (6,6) and (8,8), where the fluctuations around zero are quite large, especially for water confined in the (6,6) tube. The overall velocity autocorrelation (Figure 4-14a) shows a smaller amount of fluctuations around the zero value for all tubes; however, the fluctuations in the (6,6) CNT are perceptibly higher than those seen in the wider tubes.

We show the overall diffusion coefficient of water in the CNTs calculated from the Green–Kubo relation in Figure 4-15. The overall diffusion coefficient values for all the diameter cases, as

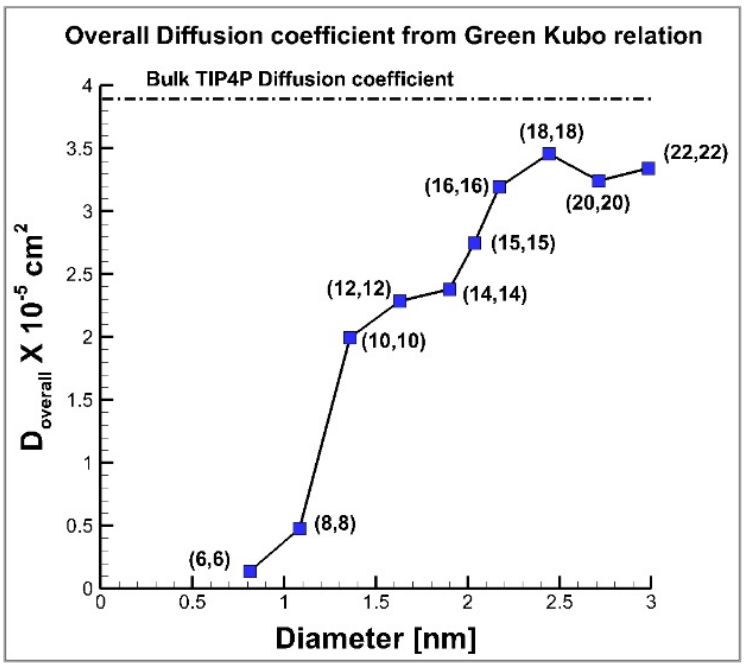

Figure 17

Figure 4-15: Overall diffusion coefficient from the Green-Kubo relation.

expected, are lower than the axial diffusion coefficient and we observe an increase in diffusion as the diameter increases and the confinement decreases.

At this point we would like to end our investigation into identifying the diffusive behavior of water under extreme confinements such as that seen in (6,6) and (8,8) CNTs. This is beyond the scope of our studies, but there do exist some studies conducted mainly by Striolo[112], Alexiaidis et al.[153], and Mukherjee et al.[155,156] that have studied water diffusion under these high confinements in detail and under different loading conditions that can help shed some light on the diffusion mechanism. While some debate still exists about the mode of diffusion of water in these tubes, we recount the main results of those studies.

Striolo[112] investigated diffusion of water in infinitely long CNTs of diameter 1.08 nm and found that water diffuses via a ballistic mode for up to 500 ps, which then changes to Fickian diffusion. Alexiadis et al.[153] did not find a distinct, long period of ballistic diffusion, which they ascribed to using a higher density than Striolo, where clusters have no space to perform coordinated ballistic motion. They showed that the diffusion mechanism is mainly Fickian with 'α' in $D \propto \left(\frac{|z(t)-z(0)|^2}{t^{\alpha}}\right)$ varying between 0.8 and 1[157]. Mukherjee et al.[158] found the behavior similar to that observed by Striolo, where they observed an initial phase of ballistic diffusion followed by a Fickian one in a long simulation run. For the very narrow diameter tubes investigated, they argued that hydrogen bonds lead to a strong correlated motion similar to the ballistic mode $(|z(t) - z(0)|^2 \propto t^2)$, but at the same time the quasi one-dimensional structure gives rise to single-file diffusion $\left(|z(t) - z(0)|^2 \propto t^{1/2}\right)$, resulting in an apparent Fickian diffusivity. Thus, bulk and confined water share the same macroscopic diffusion mode in finite length tubes.

The spatial pattern and fluctuations of hydrogen bonds of water characterize its structure and dynamics, and many of its distinctive properties are ascribed to hydrogen bonding[159,73]. The

distribution of hydrogen bond lifetimes provides a complementary view of hydrogen bond dynamics and hence the dynamics of water[73]. Thus, logically, we next proceed to discuss the diffusion coefficient as a function of modification of hydrogen bonding under confinement.

Usually, H-bonds are determined according to some geometric criteria:

1) The distance between the oxygen of both molecules has to be smaller than a certain threshold value R_{OO}.
2) The distance between the oxygen of the acceptor molecule and the hydrogen of the donor has to be lower than a certain threshold value R_{OH}
3) The bond angle between the O-O direction and the molecular O-H direction of the donor, where H is the hydrogen which forms the bond, has to be lower than a certain threshold value θ.

We use the second and third criteria to determine the H–bonds with $R_{OH} = 0.35\ nm$ and $\theta = 30^{\circ}$. The average number of hydrogen bonds of water in the nanotube is shown in Figure 4-16. In the (8,8) tube, we observe a sharp increase in the number of hydrogen bonds and also a more open ordered structure for water in the (8,8) CNT (see the radial density and the axial density profiles). One of the important differences between liquid water and ice is the number of hydrogen bonds. The average number of hydrogen bonds of solid ice is higher (4) than that for liquid water (3.5) and it also is energetically more favorable. Another notable feature of solid ice is that it has a more open structure as compared to liquid water. Both these features are comparable to that found for water confined in an (8,8) CNT; hence, we have a reduced ice-like mobility for water under confinement in (8,8) CNTs (see Figure 4-9). The effect of geometrical confinement slowly diminishes as the tube diameter increases, and we observe that the diffusion coefficient approaches bulk values for larger diameter tubes.

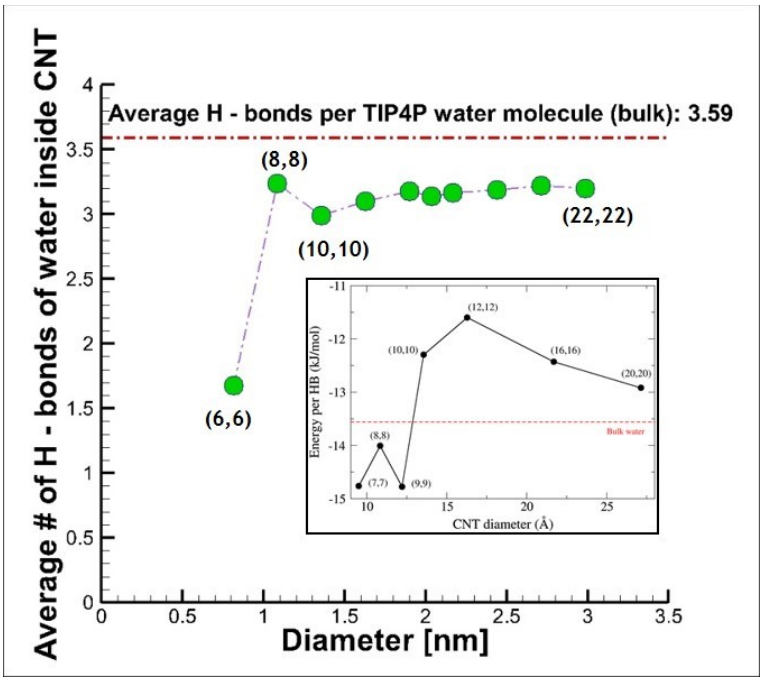

Figure 4-16: Average number of hydrogen bonds per water molecule as a function of CNT diameter.

We have obtained the donor (intramolecular oxygen) --- hydrogen (intramolecular hydrogen) --- acceptor (intermolecular oxygen) angle distribution, the donor (oxygen)-acceptor (oxygen) distance distribution, average numbers, lifetimes and energies of hydrogen bonds for different tube diameters and different conditions of surface charge and ions (Figures 4-17 to 4-19). These additional simulations were conducted on CNTs that are connected end-to-end and help us study the hydrogen bond structure and dynamics as a function of pore size, nature of the surface charge (discrete vs. partial), and surface charge signs and magnitudes. The interrupted or the intermittent hydrogen bond lifetimes calculated by the reactive flux method of Luzar et al.[73] are shown in Figure 4-19a. Sampling was done every 10 fs. Wider tubes have shorter hydrogen bond correlation times, while narrower tubes have longer relaxation times. These results are consistent with those obtained by other studies[160], which showed that even though the number and the lifetimes of hydrogen bonds that are continuously bonded are low under confinement, the

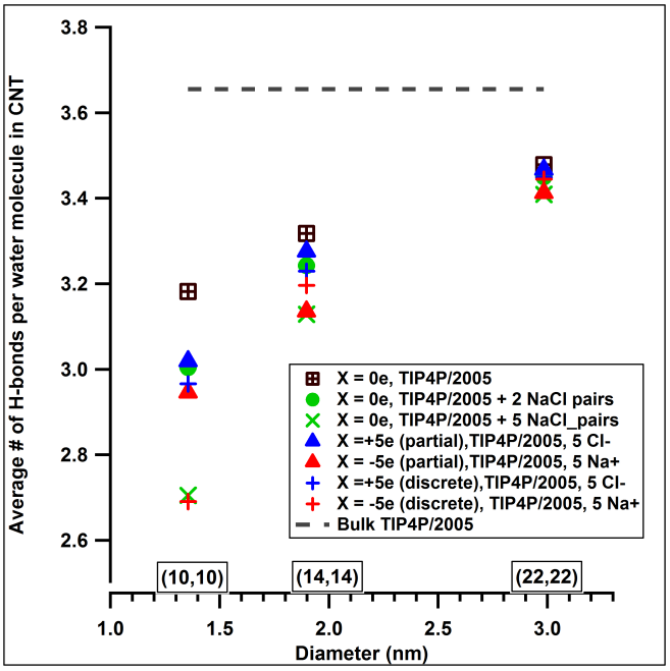

Figure 4-17: Average number of hydrogen bonds.

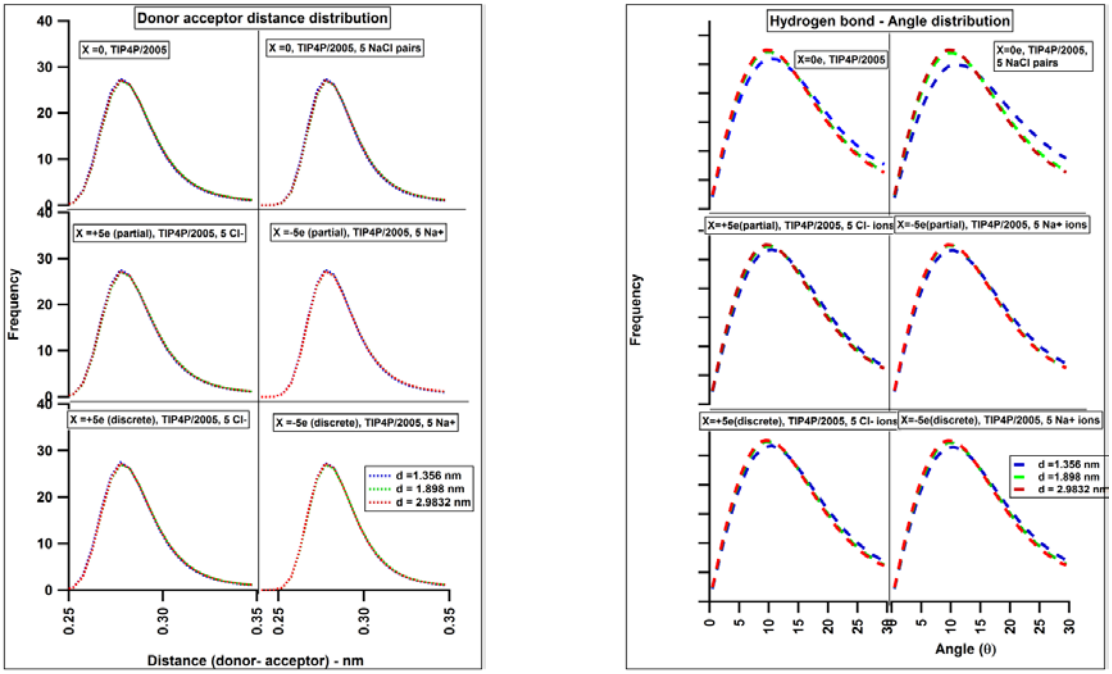

(a) **(b)**

Figure 4-18: (a) Hydrogen bond donor-acceptor distance distribution; (b) hydrogen bond angle distribution.

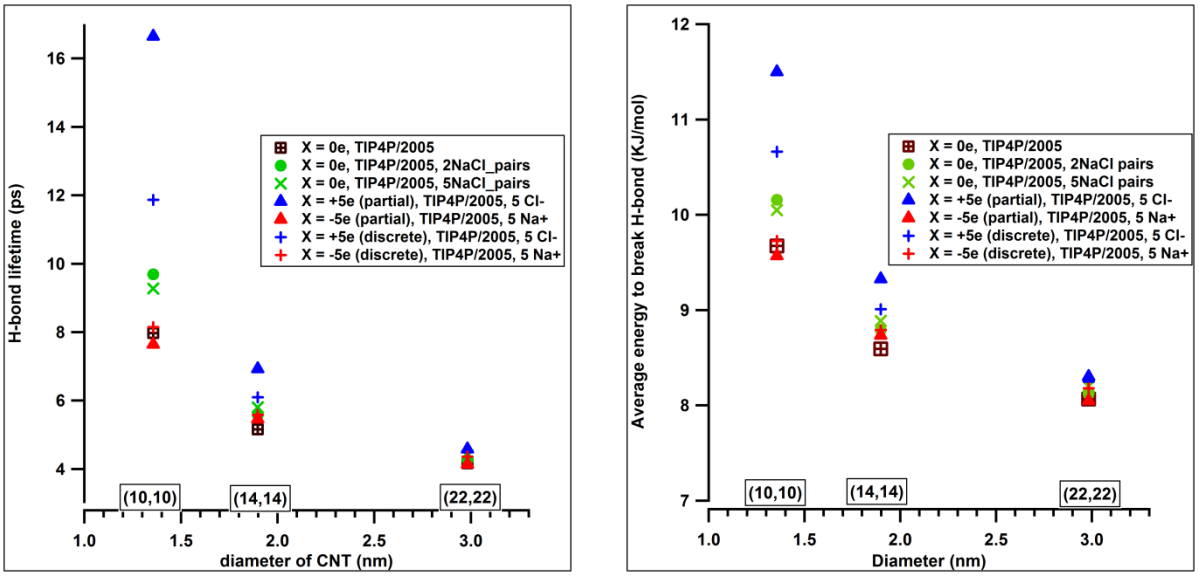

(a) **(b)**

Figure 4-19: (a) Hydrogen bond lifetimes; (b) hydrogen bond energies.

intermittent hydrogen bond correlation function $C_{HB}(t)$ of water decays more slowly under confinement than in bulk. Thus while hydrogen bonds inside the tube have a shorter lifetime as compared to bulk water, they remain in each other's vicinity and cause the bonds to reform easily which contributes to long correlation times. The mobility of water is associated with the relaxation times of hydrogen bonds, and long correlation times in narrow carbon tubes suggests correlated or concerted motion of water molecules.

We next look into the spatial diffusion of water in CNTs; i.e., the diffusion of water near the walls and that at the center of the tube. There have been disputes about the spatial variation of the diffusion coefficient of water in CNTs. While Liu et al.[161] claim that diffusion of the outer shell water SPC molecules is much slower than that of the inner shell (TINKER package), Farimani et al.[162] obtained the opposite result with a slight enhancement in the axial diffusivity at the walls using SPC/E water and GROMACS. Our results with TIP4P water and GROMACS, as shown in

Figure 4-20, agree more with the results of Farimani et al.[162] A possible explanation given by them was the probable depletion of hydrogen bonds, the weak carbon–water interactions, and water orientation near the surface of the CNT.

4.3.4 Water permeation in finite CNTs

Figure 4-21 details the number of permeation events taking place within the CNT. In the case of the (6,6) CNT, one can see unidirectional bursts of water in a particular direction with the flux reversing direction after some time. In the (8,8) CNT, water is clearly immobilized with no occurrence of positive or negative flux. One can observe equilibrium in the net flux of water for all wider tubes with the number of water passages from left to right equaling the number of passages from right to left.

4.3.5 Water transport through a (6,6) CNT ($d = 0.81$ nm)

Berezkhovskii and Hummer[20] used a continuous-time random-walk (CTRW) model to describe concerted transport through channels densely filled with molecules in a single-file arrangement. The CTRW was found to quantitatively reproduce the important features of transport of water molecules through the (6,6) carbon nanotube, namely, the bursts of unidirectional pulses. Similar to the works of Zhu and Schulten, who also used the CTRW model of Berezhkovskii and Hummer [163], we calculate the parameter "k"; i.e., the hopping rate (a hop is the translocation of the water molecule by a distance equal to the separation of adjacent water molecules). We then use the hopping rate to get a prediction of the number of permeation events and compare it to the total number of permeation events that we observe in the simulation. (A permeation event is defined as a water molecule entering from one end of the CNT and exiting the other.) The results are shown in Table 4-6.

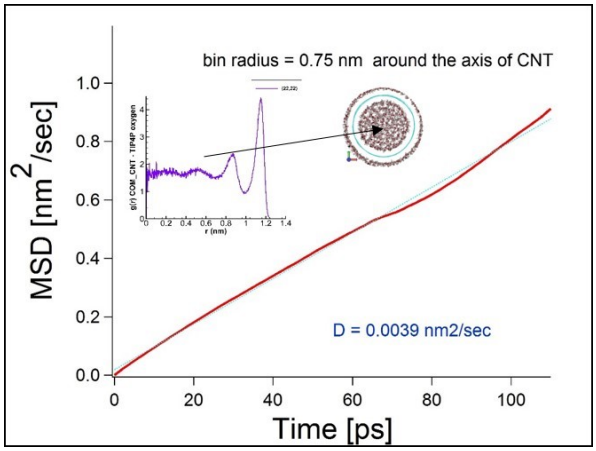

(a)

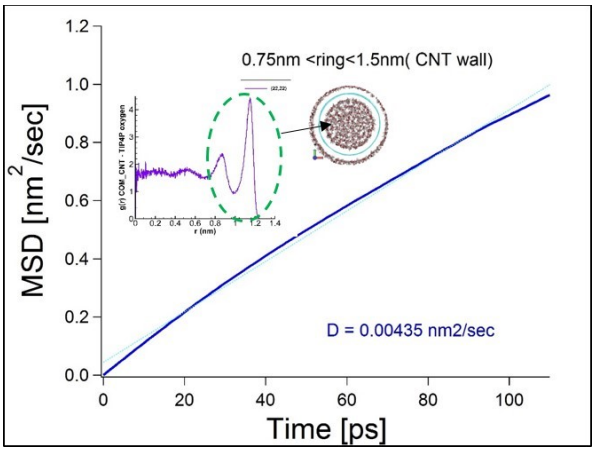

(b)

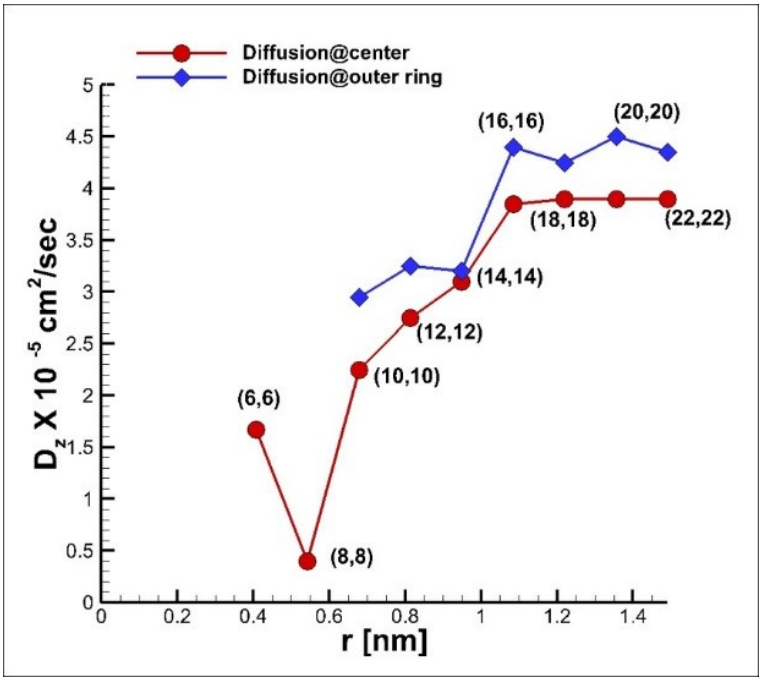

(c)

Figure 4-20: (a) axial diffusion coefficient of water in the cylindrical region at the center of the (22,22) CNT; (b) axial diffusion coefficient of water in the annular region near the walls of the (22,22) CNT; (c) spatial diffusion coefficient of TIP4P water confined in CNTs of different diameters.

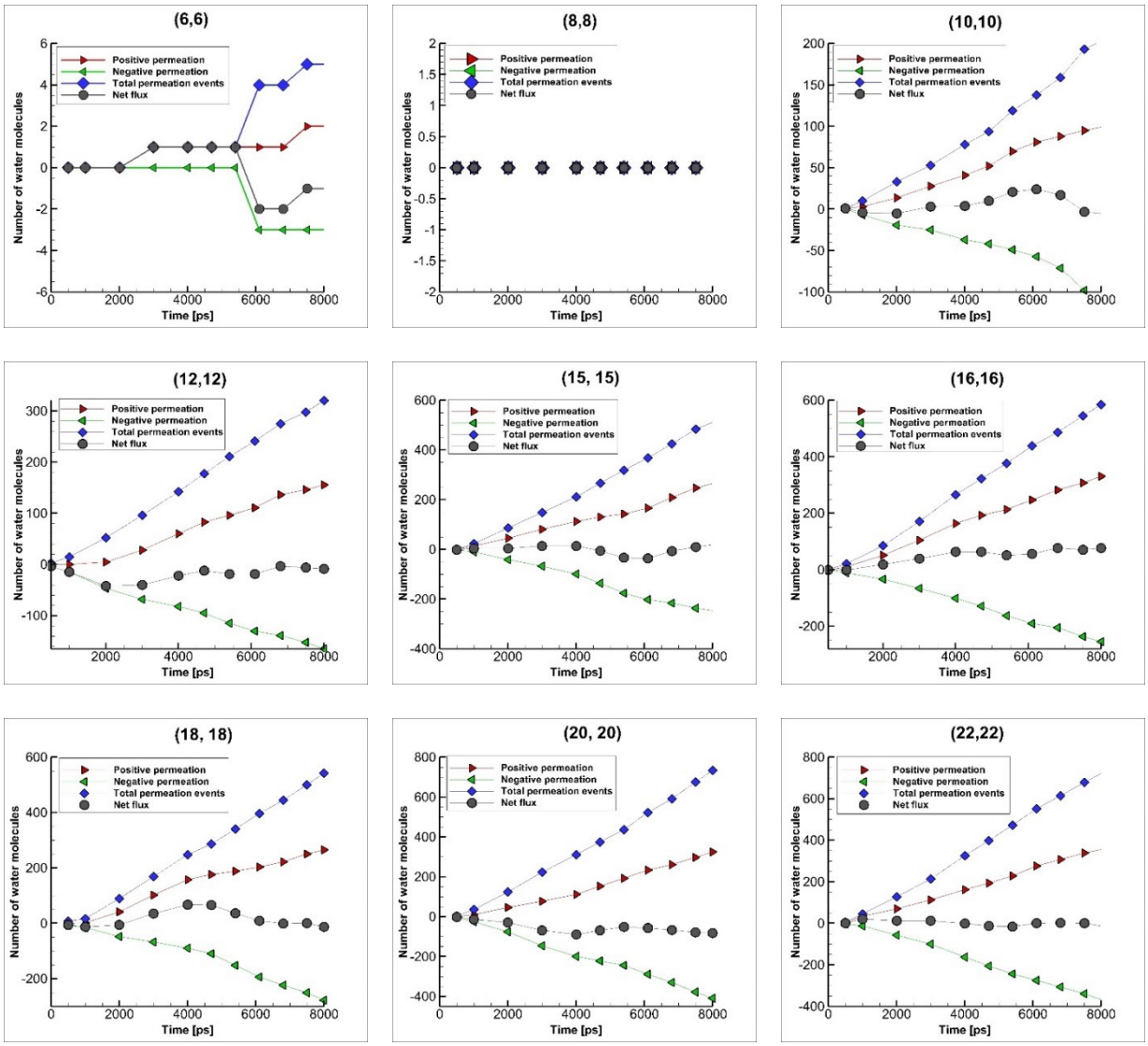

Figure 4-21: Number of permeation events in CNTs of different diameters with time.

Number of permeation events from left to right (red), Number of permeation events from right to left (green), Net flux (grey) i.e. the number of permeation events from left to right – number of permeation events from right to left, Total number of permeation events (blue) i.e number of permeation events from left to right + number of permeation events from right to left.

Table 4-6: Permeation events in a (6,6) CNT using CTRW model of Berezkhovskii and Hummer.

D_z (nm^2/ps)	Force Field	Water Model	Tube length (nm)	Bidirectional hopping rate (CTRW model) k (ps^{-1})	Unidirectional hopping rate k_0 (ps^{-1})	hopping time $\tau = 1/k$	Total number of permeation events predicted (CTRW model) p (no/ns)	Total Permeation events observed from trajectory p(no/ns)
0.00165 **(This work)**	OPLS-AA	TIP4P	5	0.048	0.024	20.83	2.44	0.625
0.00091[163]	CHARMM	SPC	1.34	0.027	0.0135	37	4.5	5.9
Garde et al.[21]	AMBER	TIP3P	4.5	0.050	0.025	20	7	5.8
Berezhkovskii[20]	AMBER	CTRW model	1.34	-	-	13	7	7.1

The number of permeation events from the CTRW model is

$$p = \frac{2k_0}{N+1} = \frac{k}{N+1} \tag{4.3}$$

$$k = 2D/a^2 \tag{4.4}$$

Here, $k_0 = k/2$ is the unidirectional hopping rate, N is the number of water molecules in the CNT (19), a is distance between water molecules (0.26 nm), $k = 2D/a^2$ (Bidirectional hopping rate), D is the one-dimensional diffusion coefficient and is calculated from the mean-squared displacements of water molecules in the CNTs. (For simplicity, we use D that was calculated assuming Fickian diffusion.)

The difference in the values of the hopping times between different studies may be due to differences in the force fields and different water models used[163]. The number of permeation events

that we observe during the 8 ns of data collection through a single 5 nm CNT is in the same range as the CTRW model. However, deviations have been observed from the predictions of the CTRW model by Li Jing-Yuan et al.[103] and Guo et al.[104], who found water permeability to decay with nanotube length. As a note for future investigations intending to study water transport through (6,6) CNTs, we would like to suggest recording of the permeation events through several bundles of aligned (6,6) CNTs for long durations to help alleviate the problem of good averaging.

4.4 Conclusions

We have studied the effect of confinement on the structure and dynamics of TIP4P water confined in narrow carbon nanotubes using molecular dynamics simulations. Water assumes an ordered configuration inside sub-3nm diameter nanotubes with structures varying from single chain-like in the narrowest (6,6) nanotubes, square ice-like net in the (8,8) tubes, and layered arrangement near the walls and bulk-like behavior at the center of the tube in the case of larger diameter tubes.

The results for the axial diffusion coefficient of water in finite CNTs indicated a Fickian diffusion mechanism for water confined in CNT with chiralities $R \geq 10 - 22$. In the narrowest tubes, i.e., (6,6) and (8,8), the diffusion appears apparently Fickian at long durations even though the trajectories strongly resemble single-file diffusion. Visualization of the trajectories of water molecules inside the smallest diameter (6,6) tubes shows that the water molecules transport collectively as a single object, which could be a subject of future detailed investigations. The axial diffusion coefficient shows a non-monotonic increase as the diameter increases with water being almost immobile in the (8,8) tubes. A possible reason for the extremely slow diffusion of water in the (8,8) tubes could be the ice-like hydrogen-bonded structure of water. We found water permeability in the (6,6) CNTs to be within the range yet slightly lower than that predicted by the

CTRW. Results for hydrogen-bond structure, dynamics, and energetics were also provided for different degrees of confinements. Under confinement, we find a reduced number of hydrogen bonds as compared to bulk. These bonds, however, have longer lifetimes and the lifetimes decay with increasing tube diameters.

We have tried to present a comprehensive molecular scale picture of the structure and dynamics of water confined in nanotubes of diameters between 0.8 nm - 3 nm. We consider the results of this study as validation of our simulation model and as a foundation for the studies described in the subsequent chapters.

Chapter 5. Ion uptake and the associated structure and dynamics of an electrolyte in charged sub-3 nm carbon nanotubes

5.1 Introduction

The significant enhancement in water flow at much lower applied pressures, as well as an opportunity for ion selectivity and high ionic conductivity through carbon nanotubes (CNTs), make them attractive candidates for numerous applications such as fuel cells, electrodialysis, capacitive deionization, and water purification technologies. With a view to providing a foundation for future investigations of selective ion transport under confinement through nanotubes with fixed-charge groups, we have conducted these relatively short molecular dynamics (MD) simulations lasting between 15-30 ns of charged nanotubes in contact with electrolyte solutions, which nevertheless provide a significant glimpse into the characteristics of ion uptake in charged CNTs.

In this study, we report the results of the preliminary MD-based investigations into the ion sorption phenomena taking place in single-walled armchair nanotubes that have uniformly distributed immobile charges. These fixed-charges mimic ionizable functional groups, such as those found in polymer ion exchange membranes. Our system consists of a single CNT between two baths of electrolytes, with one of the compartments containing pure solvent. We test the extent of co-ion and counter-ion sorption for different electrolyte solutions (NaCl, LiCl, and CsCl) with a common anion in three different diameter nanotubes (1.36 nm, 1.9 nm, and 3 nm) by varying the concentration of the fixed-charges, the sign of the fixed-charges, and the solution strength of the high concentration reservoir.

5.2 Methods

The simulation system and the cases simulated are shown in Figure 5-1 and Table 5-1, respectively. For each electrolyte type, the combination of nanotube diameter, fixed-charge concentration, fixed-charge sign, and external solution concentration resulted in 36 different simulation cases and a corresponding number of simulation runs of a typical duration of 15-30 ns. The charges on the nanotube were distributed as partial charges and the molar concentrations of the fixed-charges were calculated on the basis of the aqueous solution volume. The system was overall electroneutral; i.e., for the net charge applied on the CNT, the corresponding number of ions of the same sign as that on the CNT were deleted before the start of the simulation. In the case

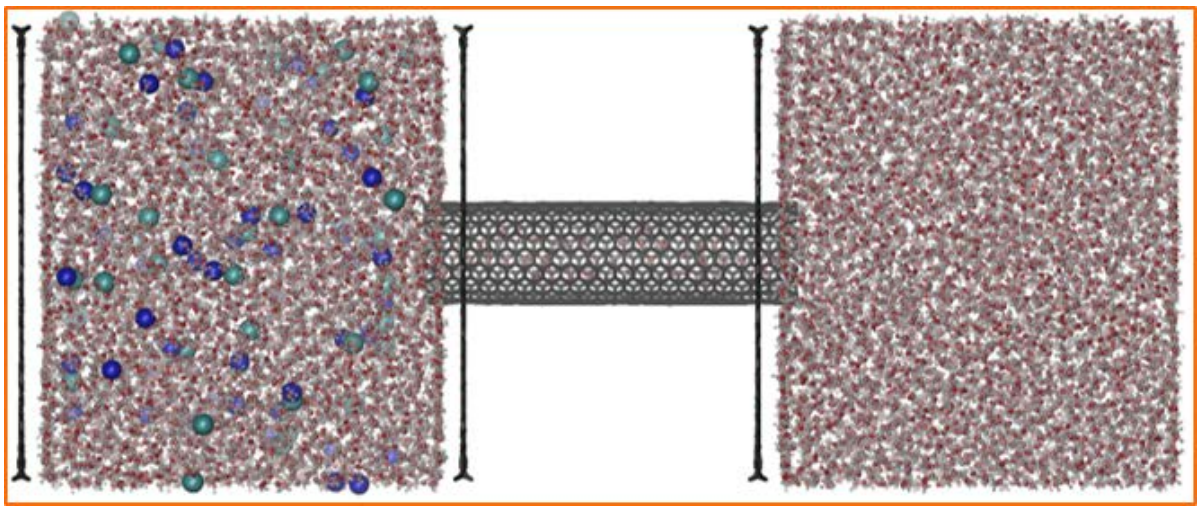

Figure 5-1: Schematic illustration of the simulated system: carbon atoms (black), TIP4P/2005 water molecules (red), sodium ions (blue), chloride ions (green). The nanotube has partial charges distributed on each carbon atom.

Table 5-1: The nanotube diameters, the molar fixed-charge concentrations, and the solution strength of the high concentration reservoir that made up the various simulation cases.

Cases				
CNT diameter (nm)/ CNT chirality (R,R)	**1.35 (10,10)**	**1.9 (14,14)**	**3 (22,22)**	
Fixed-charge (M), X (+/-)	**0.35**	**1**	**2**	
External solution concentration, Cs (M)	**0.05**	**0.1**	**0.4**	**1**

of the NaCl electrolyte, we tested the ion concentration in the nanotube for all magnitudes and signs of the fixed-charge shown in Table 5-1, whereas in the case of LiCl and CsCl, we only report the results for the case of a uniformly-distributed negative fixed-charge of 2 M.

The atoms of the CNT and graphene sheets were modeled as uncharged Lennard-Jones particles using parameters for the sp^2 carbon of benzene in the OPLS-AA force field. The carbon atoms of the CNT and graphene were held fixed during the course of the simulations using a harmonic restraining potential with a force constant of 10,000 kJ/mol/nm^2 to restrict their translational and rotational motion. The TIP4P/2005 water model was chosen because of its more accurate representation of the phase diagram, the reproduction of the O-O peaks in the radial distribution functions, and, most importantly, because the OPLS-AA force-field was developed entirely with the TIP4P class of water models. The LINCS algorithm was used to keep the water molecules rigid, thereby allowing for longer integration time steps. The Lennard-Jones parameters of cross interactions were calculated on the basis of the geometric means for both σ and ϵ. Periodic boundary conditions were applied in all three directions. Particle Mesh Ewald Summation was used for electrostatics in the 3D periodic systems and the non-bonded interactions were truncated at a distance of 1.2 nm. Energy minimization by the steepest descent method was carried out to

remove any unphysical overlaps between atoms. Once the target temperature was attained, all simulation runs required for accumulation of statistics were carried out using the GROMACS MD package in the NVT ensemble with the v-rescale thermostat, a leap frog (Verlet) integrator, and a time step of 1 fs. In the following study, X denotes the fixed-charge concentration (M) and Cs is the solution strength of the upstream reservoir (M).

5.3 Results

5.3.1 Ion uptake

While the transport processes taking place are decidedly non-equilibrium, it is reasonable to assume a local equilibrium in the counter-ion and co-ion concentrations in the nanotube over the duration of long simulations. We show the measured average counter-ion, co-ion, and effective fixed-charge concentrations obtained from simulations with different strengths of sodium-chloride solution in the upstream high concentration reservoir in Figures 5-2a and b. We observe similar behavior in both cation and anion exchange type nanotubes; i.e., for any fixed-charge concentration and CNT size, the co-ion rejection worsens with increasing external solution concentration. For instance, in the case of the (22,22) CNT with 0.35 M negative fixed-charge concentration (Figure 5-2a), the co-ion is completely rejected when the external solution concentration is 0.05 M or 0.1 M and starts to show a finite concentration that increases as the external reservoir concentration is increased to 0.4 M and 1 M. This is evidence of a Donnan-type rejection mechanism, where, for a given fixed-charge concentration, the ion rejection improves with decreasing concentration of the external solution. At the charged CNT surface in contact with the external electrolyte solution, an equilibrium (Donnan equilibrium) is established, which leads to a discontinuity in both ion concentration and potential. For a clearer understanding of Donnan-type ion sorption trends, and in order to draw attention to the similarity of our results to the Donnan

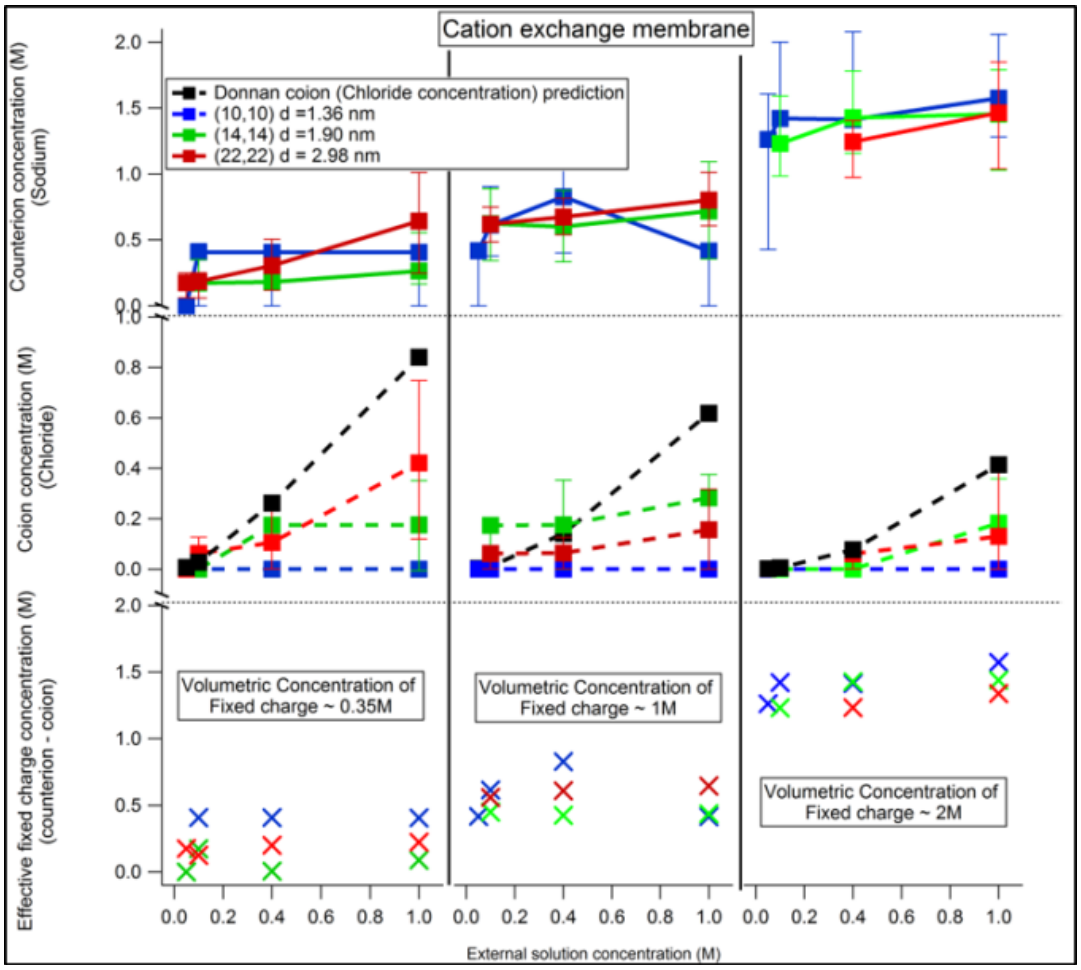

(a)

Figure 5-2: Counter-ion concentration, co-ion concentration, and effective fixed-charge concentration (ordinates) in negatively-charged (cation-type exchanger: (a)) and positively-charged (anion-type exchanger: (b)) nanotubes as functions of the external solution concentration (abscissas).

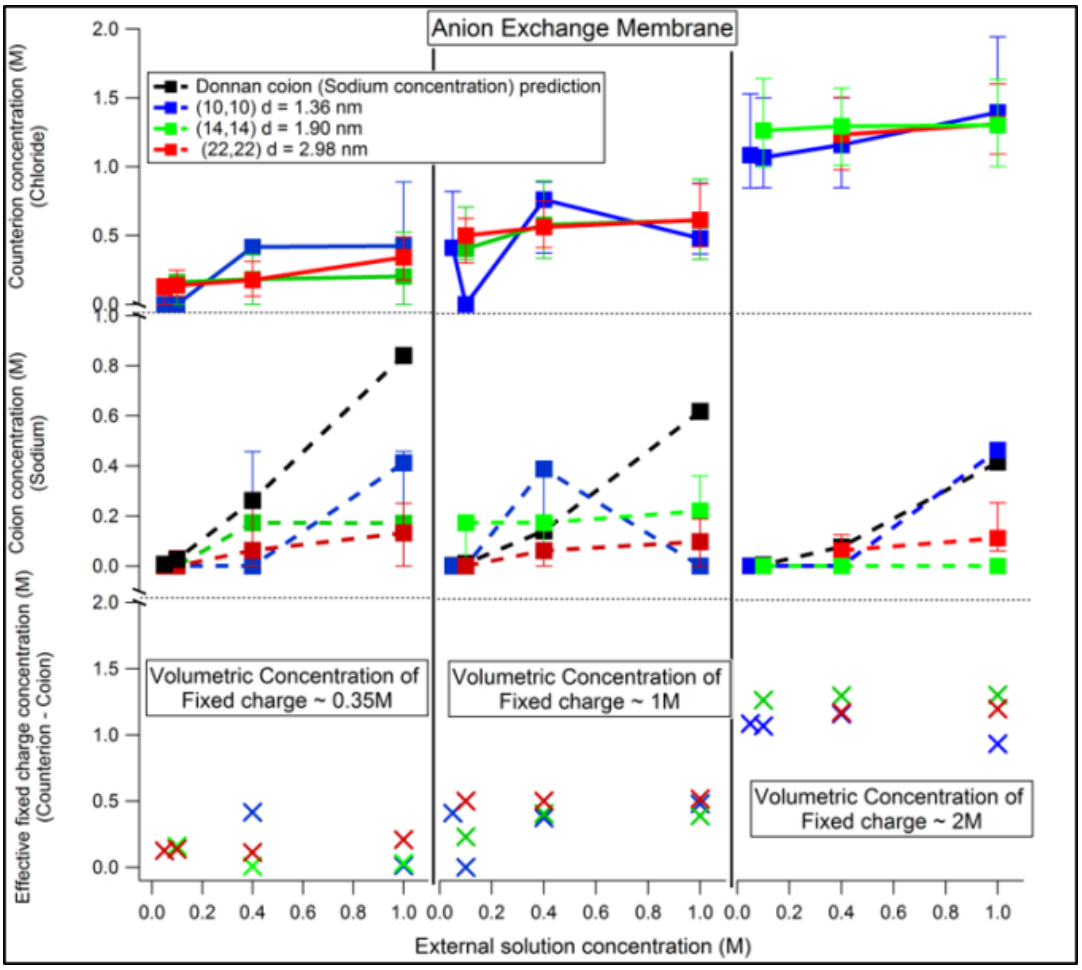

(b)

In both Figs. (a) and (b), the average counter-ion, co-ion, and effective fixed-charge results for the last 5 ns of the simulations are shown in the top, middle and bottom panels, respectively. In each of the figures, results are shown for the magnitude of fixed-charge being increased from left to right. Thus, each of the Figs. (a) and (b) is divided into primarily three parts (by dividing the abscissa) based on the magnitude of the fixed-charge on the nanotube. The left, middle and right sections correspond to cases of fixed-charges of about 0.35 M, 1 M, and 2 M, respectively. The results for ion concentrations in the (10,10), (14,14), and (22,22) CNTs are shown in blue, green, and red, respectively. The error bars show the maximum and minimum concentrations observed during data collection. The predictions from Donnan theory for the co-ion concentration in the charged nanotube at the various conditions of external solution and fixed-charge concentration are shown by the black trace. These predicted values are calculated for equal concentrations of sodium-chloride solution in both reservoirs.

ion exclusion mechanism, we show an example of a typical Donnan exclusion governed ion uptake isotherm in Figure 5-3[164] where chloride co-ions are rejected from a negatively-charged CNT in favor of sodium counter-ions. Another obvious characteristic is the increasing co-ion concentration with increasing external solution concentration with the preservation of local electroneutrality at all times.

There is no solute in Reservoir 2 (the low concentration reservoir) at the start of the simulation; thus a Donnan potential is absent at the interface of the CNT and Reservoir 2. Because of the neglect of the gradient that may be present in the co-ion concentration profile, the black trace in Figure 5-2a and b shows overestimated values of co-ion concentrations. While the measured co-ion concentrations are lower than those of the Donnan predictions, it is hard to

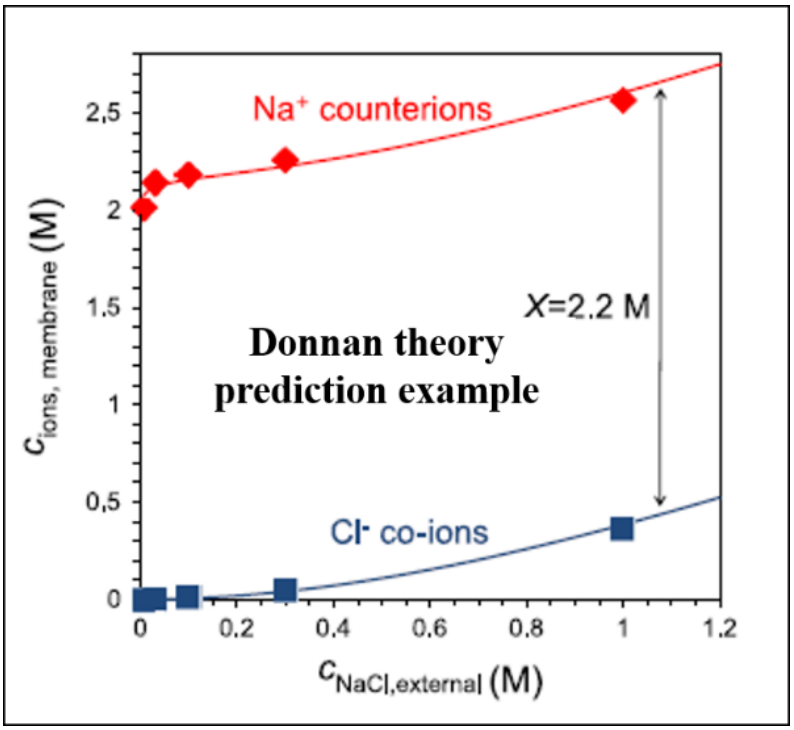

Figure 3

Figure 5-3: A typical Donnan exclusion-based ion uptake isotherm as a function of external solution concentration for a fixed-charge $X = 2.2$ M.

estimate the extent to which the Donnan theory prediction value that is shown in Figure 5-2 is overestimated without a guess for the extent of ion exclusion due to steric hindrance.

Increasing the amount of fixed-charge should result in poor co-ion concentration in the CNTs, which is most visible in the case of the (22,22) negatively-charged CNTs (Figure 5-2a, middle section, red trace). From the error bars, it appears that the sodium counter-ions are absorbed to a slightly greater extent than the chloride counter-ions. This seems reasonable because of the smaller hydration shell and greater charge density of sodium ions as compared to the chloride ions.

We find a deviation from local electroneutrality in the CNT over the timescales of the simulation. In some studies, deviations from local electroneutrality have been suspected to be a consequence of Manning counter-ion condensation in the cases of densely charged surfaces. For monovalent electrolytes, counter-ion condensation occurs when the distance between fixed-charges is less than the Bjerrum length[165]. Even though we have closely spaced charges that might satisfy the condition for Manning condensation, a visual inspection in VMD does not show any counter-ion condensation on the low surface-charge density nanotube that has smeared partial charges. Nevertheless, we provide the governing equation i.e., equation (5.1) for the modified Donnan model[165] that takes into account counter-ion condensation and show the co-ion concentration values predicted from this counter-ion condensation theory alongside those predicted by the ideal Donnan model in Table 5-2.

$$(X + C_{coion})(C_{coion})\frac{\left(\left(\frac{X}{\xi C_{coion}}\right) + 1\right)}{\left(\left(\frac{X}{C_{coion}}\right) + 1\right)}\exp\left(-\frac{\frac{X}{C_{coion}}}{\frac{X}{C_{coion}} + 2\xi}\right) = (\gamma_{\pm}^{2})\ C_{\infty}^{2} \qquad (5.1)$$

In this modified Donnan expression (equation 5.1), X is the fixed-charge concentration (M), C_{coion} is the co-ion concentration (M), C_{∞} is the external solution concentration (M), and a_{∞} is the external solution activity. Furthermore, ξ is the Manning parameter (linear charge density) =

Table 5-2: Comparison of ideal Donnan theory predictions with modified Donnan theory that takes into account counter-ion condensation. The predicted values are calculated two ways: first by taking into account the external solution concentrations, and second, using external solution activities.

Fixed-charge, X = 2 M				
External solution concentration (activity coeff)	**Donnan co-ion prediction (with external solution concentration)**	**Donnan co-ion prediction with external solution activities**	**Modified Donnan with ξ = 5, with external solution concentration, ion concentration in membrane**	**Modified Donnan with ξ = 5, with external solution activity, ion concentration in membrane**
0.05 (0.82)	0.0012	0.0008	0.0153	0.0153
0.1 (0.778)	0.0049	0.0030	0.0496	0.0496
0.4 (0.681)	0.0770	0.0364	0.328	0.2025
1 (0.657)	0.4142	0.1965	0.9122	0.5739
Fixed-charge, X ~ 1 M				
External solution concentration (activity coeff)	**Donnan co-ion prediction (with external solution concentration)**	**Donnan co-ion prediction with external solution activities**	**Modified Donnan with ξ = 5, with external solution concentration, ion concentration in membrane**	**Modified Donnan with ξ = 5, external solution activity, ion concentration in membrane**
0.05 (0.82)	0.0028	0.0019	0.0248	0.0248
0.1 (0.778)	0.0113	0.0069	0.0678	0.0678
0.4 (0.681)	0.1559	0.0782	0.3573	0.2321
1 (0.657)	0.6555	0.3529	0.9534	0.6119
Fixed-charge, X ~ 0.35 M				
External solution concentration (activity coeff)	**Donnan co-ion prediction (with external solution concentration)**	**Donnan co-ion prediction with external solution activities**	**Modified Donnan with ξ = 5, with external solution concentration, ion concentration in membrane**	**Modified Donnan with ξ = 5, with external solution activity, ion concentration in membrane**
0.05 (0.82)	0.0101	0.0068	0.0377	0.0377
0.1 (0.778)	0.0365	0.0232	0.0858	0.0858
0.4 (0.681)	0.2986	0.1785	0.3835	0.2564
1 (0.657)	0.8884	0.5491	0.9829	0.6402

$\frac{\lambda_B}{b} = \frac{e^2}{4\pi\epsilon kTb}$, where b is the distance between charges, λ_B is the Bjerrum length (0.7 nm), and γ is the activity coefficient.

The co-ion concentration within the membrane (in terms of external solution concentration) from ideal Donnan theory is

$$C_{coion} = \frac{1}{2}\left(\sqrt{(X^2 + 2C_\infty^2)} - X\right) \tag{5.2}$$

or in terms of external solution activity,

$$C_{coion} = \frac{1}{2}\left(\sqrt{(X^2 + 2a_\infty^2)} - X\right) \tag{5.3}$$

The most important result of the modified Donnan theory with counter-ion condensation from Table 5-2 is the greater co-ion concentration predicted in the charged membrane as compared to ideal Donnan theory. It would be interesting to test this phenomenon by adding discrete charges that are closely spaced to each other, which could be a subject of future investigations.

We would like to comment here on the limitations posed by these short simulations, which might prove useful for any future MD simulations of similar systems. The sequence of equilibration times required for good averages of counter-ion and co-ion concentrations in charged nanotubes are as follows:

a) X = 0.35 M > 1 M > 2 M
b) Cs = 0.05 M > 0.1 M > 0.4 M > 1 M
c) d = 1.356 nm > 1.9 nm > 3 nm

Thus, in the case where X = 0.35 M, Cs = 0.05 M, and d = 1.356 nm, very long equilibration times are required to obtain good averages of counter-ion and co-ion concentrations within the nanotube. The averages for co-ion and counter-ion concentrations for the narrowest diameter CNT with low fixed-charge concentration at low external solution concentration thus suffers from the limited duration of the simulation. The fastest equilibration is achieved in the (22,22) CNT in

contact with a 1 M sodium-chloride solution. In an upcoming chapter, we will study this case in more detail where we can extrapolate those results to some extent to the smaller diameter tubes.

Donnan theory neglects the size or the specific nature of the ions and only considers the valence of the ions. In Figure 5-4, we compare the sorption trends of different ions with the same valence and try to identify if the neglect of ion specific effects (such as their hydration energy) in Donnan theory is justified. The sequence for the ionic radii is as follows: Li (0.60 Å) < Na (1.02 Å) < Cs (1.73Å), whereas for the hydrated radius it is Li (1.95 Å) < Na (2.43 Å) < Cs (3.07Å). The hydrated radius of lithium is 3 times its ionic radius, whereas that of the cesium ion is less than twice its hydrated radius. It is thus evident that lithium has a high hydration energy (strongly hydrated) while cesium has the lowest hydration energy of the three. Hydration has an important effect on the charge density of the ion, and by consequence the extent to which fixed-charges can influence their sorption.

For a counter-ion to enter the narrow confines of a nanotube, the ion must shed some of its hydration shell water. To do so, it must experience a sufficient driving force via its electrochemical potential (RTln Cs) and the electrostatic (Coulombic) potential to compensate for this change in its hydration energy. For the cases studied and shown in Figure 5-4, the fixed negative charge is held constant at 2 M; thus the only variable for the ion is the external solution concentration. For strongly hydrated lithium ions at low external solution concentrations, the driving force is not enough to push the ion into the tube. Thus for the time scales of our simulation, at low external solution concentrations, we observe low lithium counter-ion concentrations in the narrowest (10,10) CNT. As the external solution strength and the diameter of the tube are increased, a greater number of lithium ions can enter the nanotube with less of an energy penalty from partial shedding of their hydration shell.

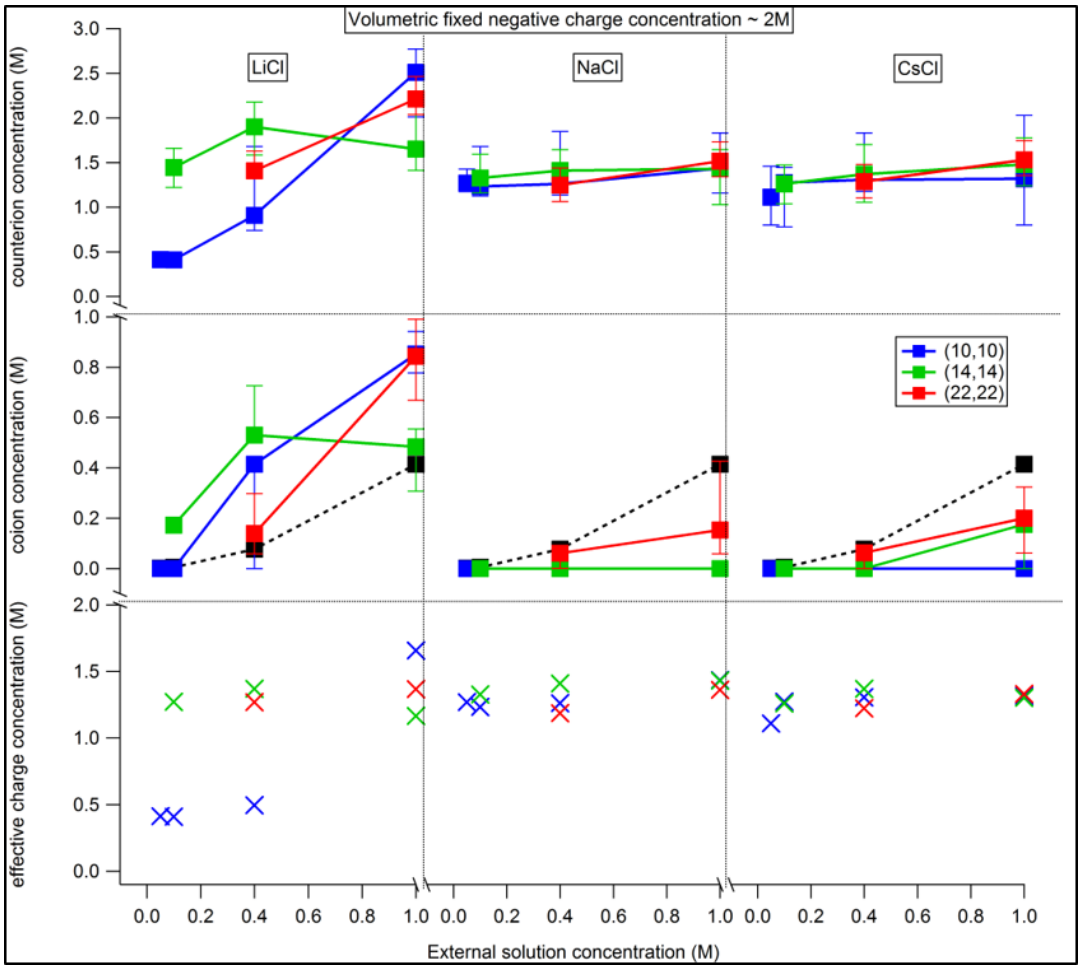

Figure 5-4: The counter-ion and co-ion concentrations in nanotubes as functions of the external solution concentration at a fixed negative charge of 2 M for different monovalent electrolyte solutions (LiCl, NaCl, and CsCl) in Reservoir 1.

The sodium and cesium ions are weakly hydrated as compared to lithium ions and are absorbed by the negatively-charged CNTs to almost the same extent at all external solution concentrations. This almost constant concentration of Na and Cs counter-ions at all external solution concentrations implies a saturation in the number of counter-ions that can be accommodated inside the nanotube. The trends show strong interactions between lithium cations-chloride anions under confinement as compared to between sodium–chloride or between cesium–chloride; i.e., this strong interaction in the case of lithium-chloride results in partially un-dissociated electrolyte inside the nanotube.

5.3.2 Structure and dynamics of water and ions

Tuning the interactions between the carbon and the electrolyte via fixed-charges can result in different interfacial structures that can be exploited for specific applications. Using these MD simulations in which we have employed a classical force field, we present a brief analysis of the interfacial interactions between the aqueous salt solution and the charged carbon nanotube and their corresponding influence on the structure and dynamics characteristics of the confined aqueous solution.

Radial density profiles

The final structure that water and ions assume inside a charged carbon nanotube is a consequence of various competing interactions between the different species—see Figure 5-5a. We can clearly see that water retains its layered structure under confinement in the presence of ions in a charged CNT. From Figure 5-5b, one can see that sodium and lithium ions can approach the wall more closely based on their smaller diameters and their charges; however, the strength of the water oxygen-carbon interaction is much stronger than the ion–carbon interaction. Moreover,

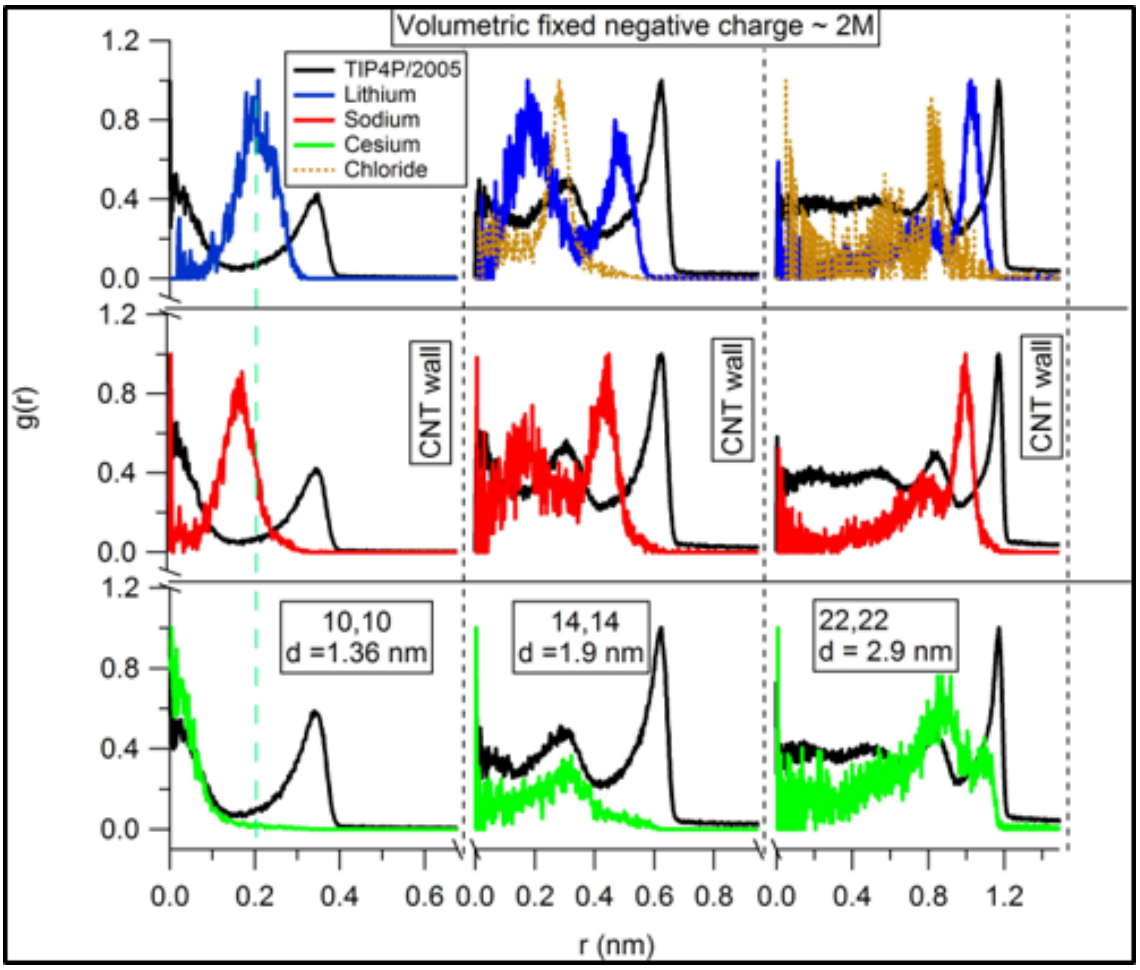

(a)

Figure 5-5: Radial density profiles of different cations and water in a CNT (a) for the case of a negative fixed-charge of 2 M and Reservoir 1 concentration of 0.4 M; (b) shows the interaction potential between carbon-water or carbon-ion as a function distance

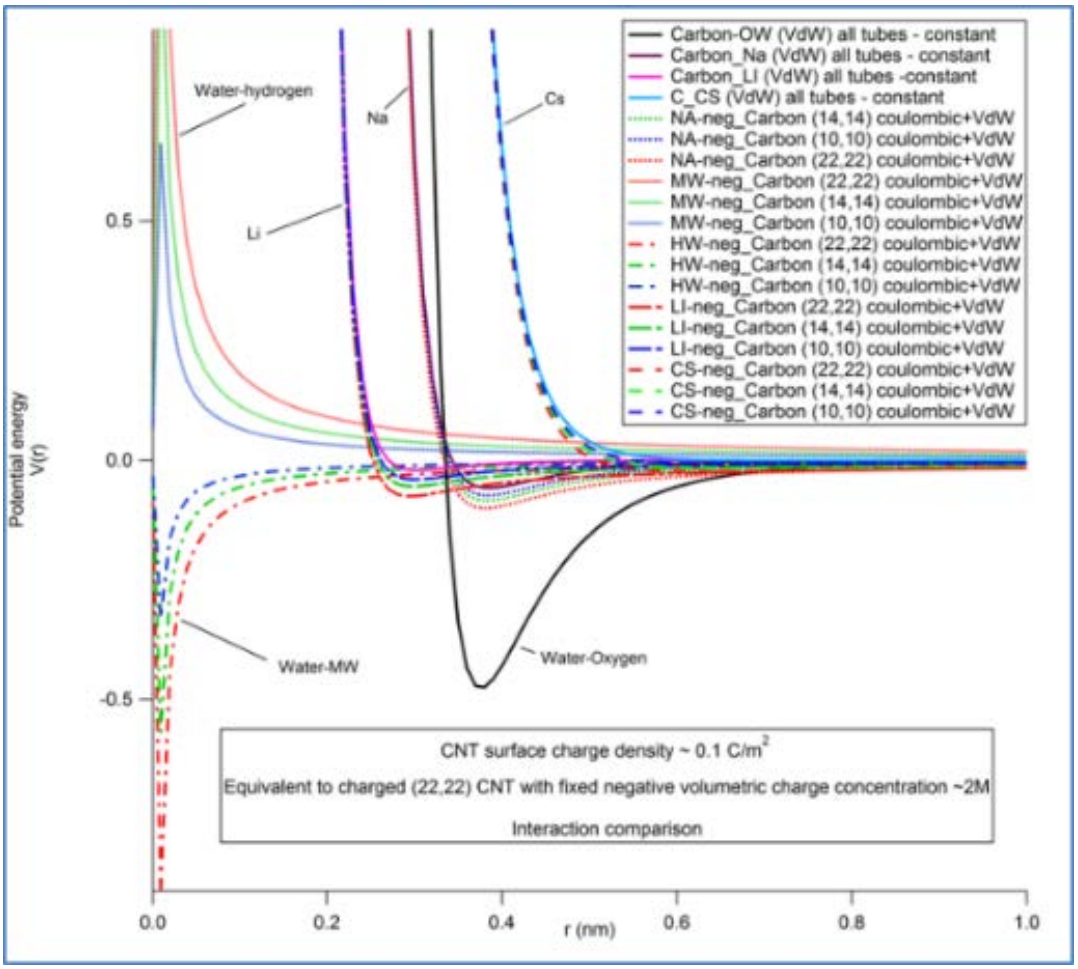

(b)

The fixed-charge concentration of 2 M resulted in the following surface charge densities in the (10,10), (1414), (22,22) nanotubes, respectively: 0.022 C/m^2, 0.062 C/m^2, 0.1 C/m^2. The abcissa is divided into 3 sections showing the density profiles for the cations in the (10,10), (14,14), and (22,22) cases, respectively. The ordinate is also divided into 3 sections: the top, middle, and bottom panels depict the density profiles for lithium (blue), sodium (red) and cesium (green) ions. The water density profiles are shown in black. For this specific case of fixed-charge concentration and external solution concentration, the chloride co-ion is mostly rejected when sodium or cesium are counter-ions; however, chloride ions are present in appreciable amounts with lithium counter-ions, and are shown the top panel in yellow.

the interaction of ions with water is more favorable than the interaction of the ion with the nanotube. Therefore, even in the case of negatively-charged CNTs with weak partial charges, we do not have contact adsorbed ions, and there always exists a layer of water between the ions and the nanotube surface. The small size of the hydrated lithium ion allows it to approach the carbon atoms more closely, whereas the peak for the cesium ion is seen to be shifted away to the center in the (10,10) CNT, which has the lowest surface-charge density. As the surface-charge density increases, the ions are observed to move closer to the wall on account of their increased interaction with the charged CNT. For the tube with the highest surface-charge density, we expect a decrease in the cation solvation near the wall.

Figure 5-6 shows the changes in the ionic structure for a counter-ion compared to its structure in an uncharged nanotube. Studies of ion structure in between uncharged graphene slits have shown that ions occupy the positions between the water layers to facilitate hydration without significantly disrupting the layering in the system[166]. In larger diameter charged CNTs, there is a visible increase in the height of the counter-ion peak closest to the wall and also in the degree of approach of the counter-ion to the charged nanotube surface. We find that addition of positive charges tends to influence the position of the peak for the chloride ions closest to the wall, whereas the addition of negative charges has barely any effect on the position of the corresponding peak for sodium ions. The addition of charges leads to a squeezing of water out of the layer closest to the wall to accommodate a greater number of counter-ions; this effect is visible in the narrowing of the water layer closest to the wall.

The results shown so far were for the cases in which the CNT had partial charges. In Figure 5-7, one can observe the changes in the radial density profiles for ions in a (14,14) CNT with discrete charges. Sodium (with a high charge density) behaves like a contact-adsorbed ion by

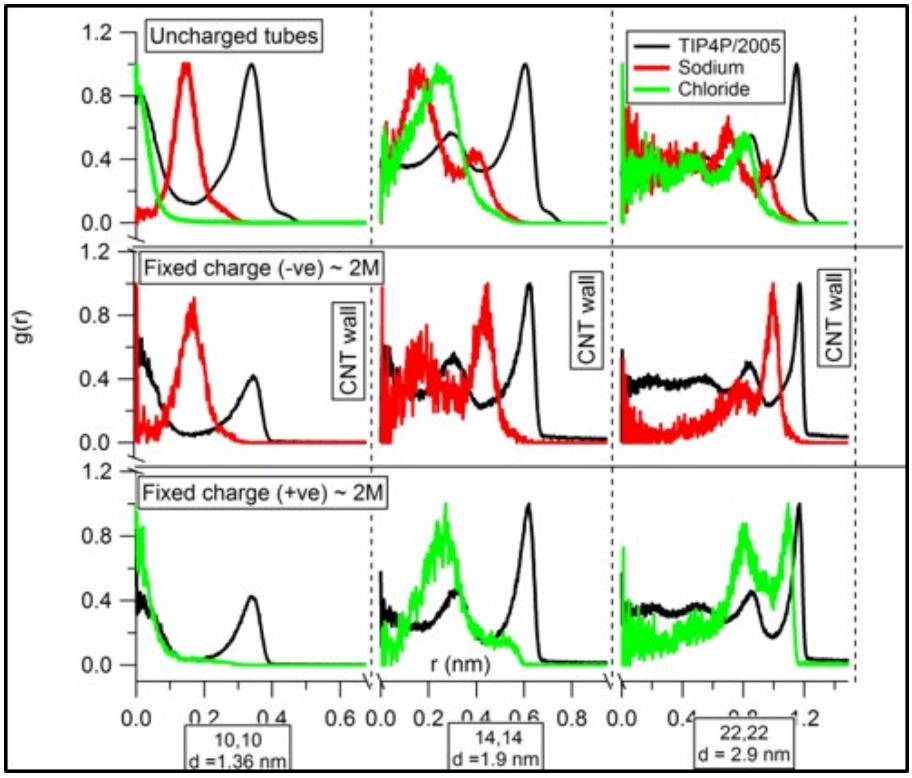

Figure 5-6: Ion density profiles in uncharged (top), negatively-charged (middle), and positively-charged nanotubes (bottom) in (10,10), (14,14), and (22,22) CNTs.

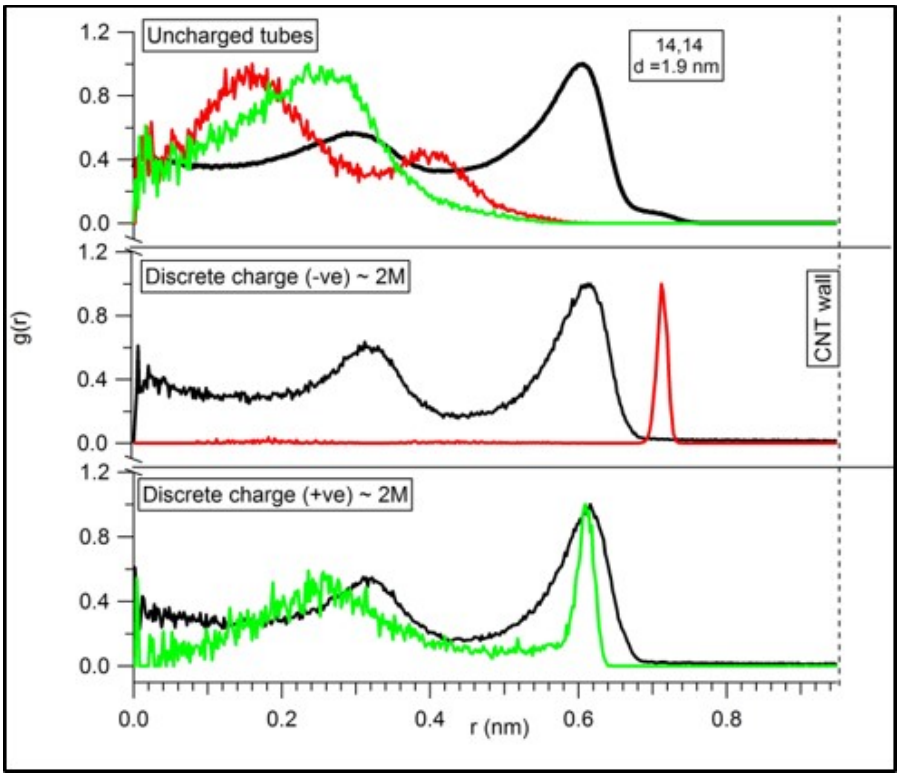

Figure 5-7: Counter-ion density profiles in a (14,14) CNT with discrete charges (middle and bottom panels). For comparison, ion density profiles in an uncharged CNT are shown in the top panel.

approaching the CNT at a distance closer than the first layer of water. The larger size of the chloride ion results in its lower charge density and it occupies a position within the water layer closest to the wall.

Coordination numbers in the first hydration shell for sodium and chloride ions

The ion-water radial distribution functions (RDFs) inside charged and uncharged nanotubes are integrated to the first minima to obtain the ion-water first hydration shell coordination numbers, which are shown in Figures 5-8a and b. Although we have not shown the ion-water radial profiles here, we would like to point out that the peak positions in the ion–water RDF in bulk and under confinement in uncharged nanotubes are the same. The reported first shell hydration number values for sodium are between 4-6 and for chloride are between 5-8[167]. In

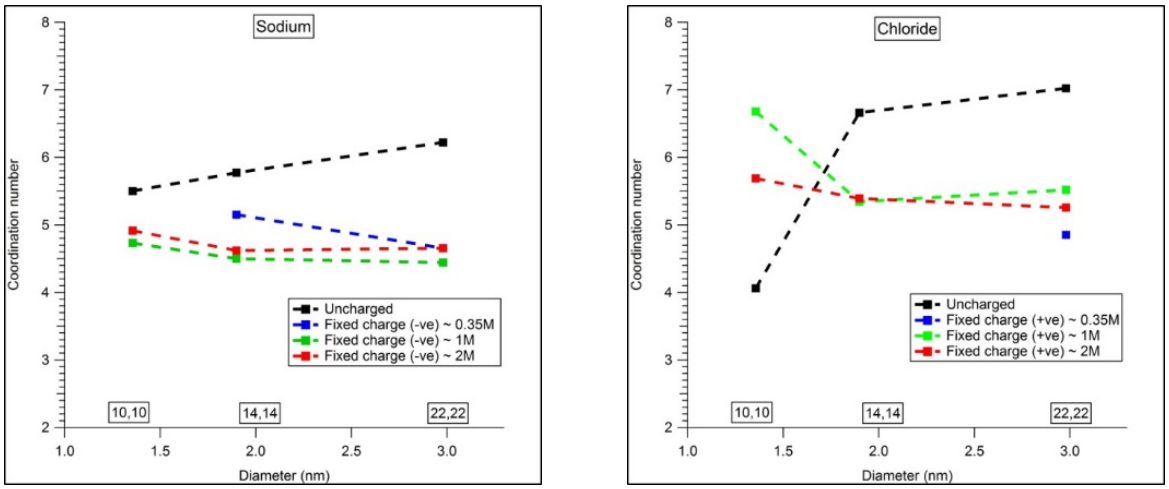

(a) **(b)**

Figure 5-8: Sodium (a) and chloride (b) coordination number in uncharged and charged CNTs at various values of fixed-charge concentration: 0.35 M (blue), 1 M (green), and 2 M (red).

uncharged CNTs, the depletion of water from the first hydration shell is significant only under the highest confinement; i.e., in the case of the (10,10) CNT. In the uncharged (10,10) CNT, the loose chloride hydration shell is perturbed to a greater extent than the sodium hydration shell. Sodium and chloride ions follow expected trends in uncharged CNTs where the first hydration shell coordination numbers decrease with increasing confinements. Our results of coordination numbers for ions in uncharged nanotubes are also consistent with observations from previous studies which showed that smaller ions with tighter hydration shells were not perturbed to the extent of decreasing hydration for the confinements considered here[167]. It seems that the presence of charges tends to squeeze the water nearer to the CNT walls, making fewer water molecules available to the ions near the charged surfaces and thus causing an overall decrease in their hydration numbers.

The coordination number of ions could decrease with increasing solution concentration owing to excess precipitated ions that are incompletely hydrated, and in the case of charged CNTs, the counter-ion hydration number could decrease from contact adsorption. While we observe an

overall decrease in the hydration numbers of ions in charged CNTs, we do not observe a substantial change in the hydration numbers of ions with increasing fixed-charge concentration. This happens because even though we increase the CNT fixed-charge concentration (which is uniformly distributed as partial charges on each atom of the nanotube), the surface-charge density does not increase by a significant amount to cause a counter-ion contact adsorption (see Table 5-3).

An unexpected result is observed for chloride ions near positively-charged walls in the (10,10) CNT: it appears that the addition of charges enhances the coordination of chloride in the positively-charged (10,10) CNT. A possible explanation for this is that, because of the size of the ion and its hydration shell, chloride ions face a steep energetic penalty in order to enter the uncharged (10,10) CNT, which has a radius of 0.678 nm. When positive charges are applied to the (10,10) CNT, this energetic penalty disappears and the hydration of chloride ions inside the CNT improves.

Table 5-3: Nanotube surface charge densities for the various fixed-charge concentrations.

CNT	$X = 0.35$ **M**	$X = 1$ **M**	$X = 2$ **M**
	C/m²	**C/m²**	**C/m²**
(10,10)	0.0075 ($\pm$1e)	0.022 ($\pm$3e)	0.038 ($\pm$5e)
(14,14)	0.01 ($\pm$2e)	0.026 ($\pm$5e)	0.06181($\pm$12e)
(22,22)	0.017 ($\pm$5e)	0.015($\pm$15e)	0.102 ($\pm$30e)

Hydrogen bonds

The results for the average number of hydrogen bonds per water molecule in the CNT for the various cases of fixed-charge, external solution concentration, and tube diameter are shown in Figures 5-9a-c. The modification in the number of hydrogen bonds represents a change in the structure of water as compared to the bulk structure. Bulk TIP4P/2005 has 3.66 hydrogen bonds per water molecule. It has been shown previously that confinement causes a reduction in the number of hydrogen bonds (N_{HB} = 3.2 ~ (14,14) and N_{HB} = 3.3 ~ (22,22)). The addition of sodium and chloride ions further alters the structure of water. We find that in most cases the number of hydrogen bonds inside the positively-charged CNT (which has a higher number of chloride ions) is higher than the corresponding number in negatively-charged tubes (which have a higher number of sodium counter-ions). These changes in the hydrogen bonding are probably caused by the structure making or breaking properties of the respective ions. From the results shown in Figures 5-9a-c, it appears that chloride ions tend to enhance the water structure by increasing the number of hydrogen bonds, whereas sodium ions tend to disrupt the water structure in nanotubes by decreasing the number of hydrogen bonds.

Similar trends can be seen in Figures 5-10a and b, where for a given fixed-charge concentration and external solution concentration, we observe a lower number of hydrogen bonds in negatively-charged tubes (sodium counter-ions) as compared to positively-charged tubes (chloride counter-ions).

5.3.3 Dynamics

Diffusion coefficient of water in charged nanotubes

We have previously seen that the water self-diffusion coefficient depends on the degree of confinement; thus its value is lower in the CNT than in bulk water (2.3×10^{-5} cm^2/s for TIP4P/2005

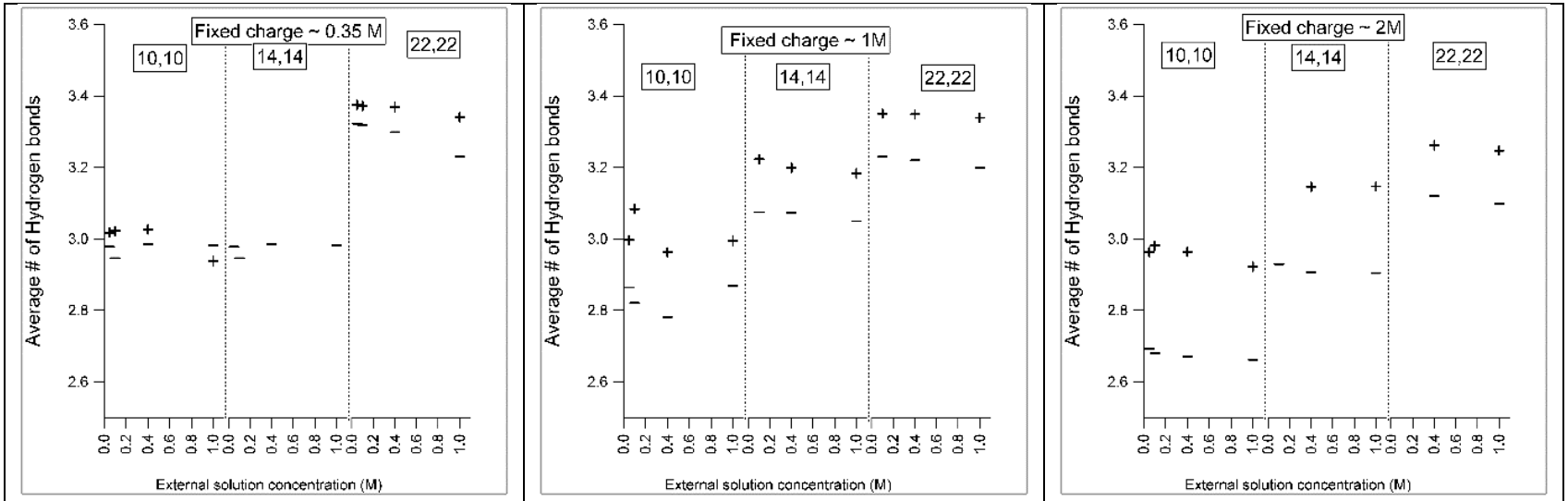

Figure 5-9: The average number of hydrogen bonds for magnitudes of fixed-charge *X* = 0.35 M, 1 M, and 2 M, respectively. The + and – markers represent the average number of hydrogen bonds in positively- and negatively-charged CNTs, respectively

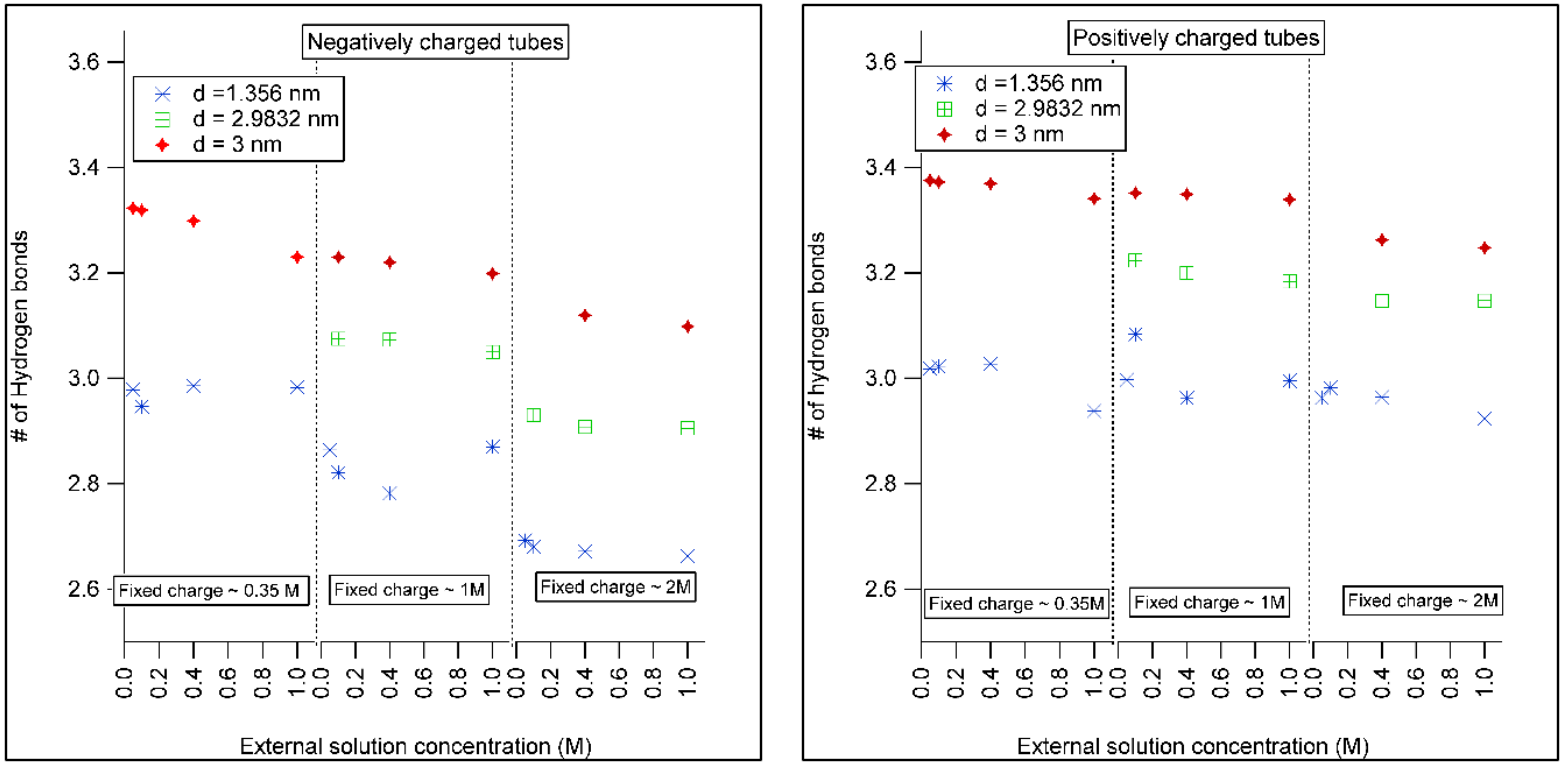

(a) **(b)**

Figure 5-10: The number of hydrogen bonds in positively-charged and negatively-charged tubes, respectively.

bulk water). The presence of ions disrupts the structure of water in the nanotube and in turn affects the dynamics of the water molecules—see Figure 5-10 and Figure 5-11. Some water in the nanotube is present as bound water, which is the water in mostly the first hydration shell of the ions. Increasing the fixed-charge concentration increases the number of counter-ions present in the nanotube and subsequently causes an increase in the quantity of bound water. This can result in a decrease in the diffusion coefficient of water. The presence of ions also has an effect on the hydrogen-bond lifetimes and numbers. Ions with a high charge density, such as sodium, are often called structure-breakers; i.e., they disrupt the hydrogen bonding structure by decreasing the number of hydrogen bonds and also by decreasing the lifetimes of the hydrogen bonds. On the other hand, chloride ions tend to keep the hydrogen bonding structure intact and increase the lifetimes of the hydrogen bonds. This has an immediate effect on the diffusion coefficient of water, where the presence of chloride ions (with their H-bond preserving nature) tends to slow down the mobility of water molecules, as seen in Figure 5-11b. The opposing effects of the decreased mobility of water, owing to a fraction of it being present as bound water in the hydration shell of sodium, and the structure breaking characteristics of sodium (which has a tendency to increase the movement of water) cause the change in the diffusion coefficient associated with the increasing presence of sodium ions in negatively-charged tubes to be minimal (see Figure 5-11a).

5.4 Conclusions

Counter-ion and co-ion sorption trends were simulated for the various combinations of diameters, fixed-charge concentrations, and external solution concentrations. We found that the co-ion exclusion trends strongly resemble the Donnan ion uptake isotherms. The inclusion of fixed-charges on the nanotube can help increase selectivity beyond simple steric effects. We have also shown the effect that the addition of fixed-charges has on the structure and dynamics of the

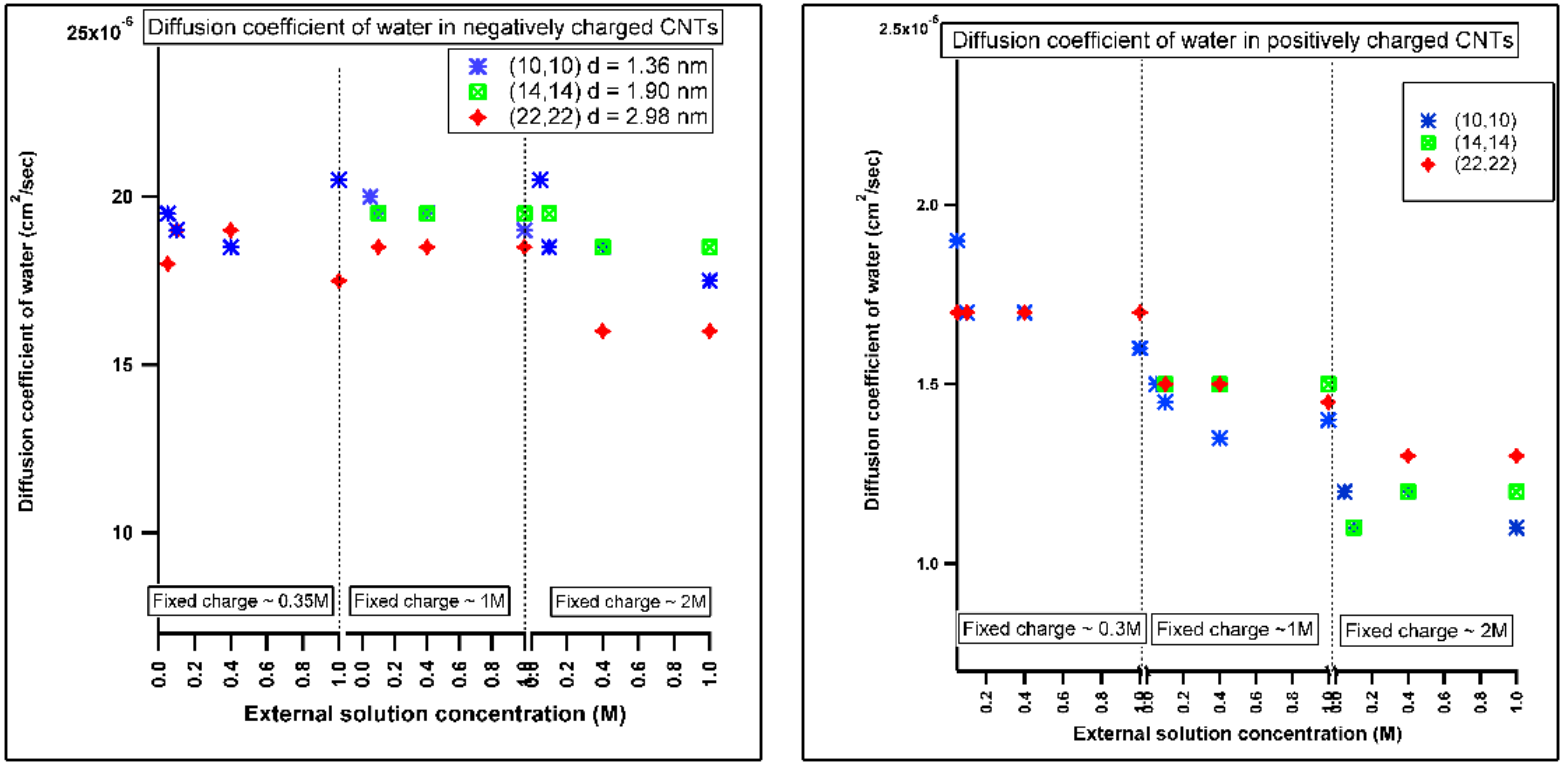

(a) **(b)**

Figure 5-11: The diffusion coefficient of water in negatively-charged (a) and positively-charged CNTs (b), respectively.

electrolyte in the nanotube. The trends obtained for coordination numbers, hydrogen bonding, and diffusion coefficients of water under various conditions of fixed-charge and external solution concentrations serve as a foundation for a further detailed investigation of ion transport through nanotubes that is described in Chapters 6-9.

Chapter 6. Pseudosteady-state diffusion of aqueous sodium chloride through uncharged carbon nanotubes

6.1 Introduction

The description of ion transport through nanoconfined media is an open problem and the development of new theories and accurate molecular models to explain the associated transport phenomena qualitatively and quantitatively is crucial to progress in the field of nanofluidics. Some of the applications proposed that involve ion transport through nanoporous media are ion exchangers[168,169], desalination membranes[169], filters[51], sensors[170,171], lab-on-chip devices[172], transistors[173], and, more recently, innovative means of energy harvesting using reverse electro-dialysis[174]. Narrow biological ion channels exhibit large water permeation rates with high selectivity and are responsible for cell regulation. Ion permeation and transport processes in these biological water-filled pores (ion channels) and functionalized semi-synthetic pores (gramicidin, alamethicin) are quite complex owing to their inhomogeneous pore structure with varying cross sections and functional groups (for selectivity), as well as the stochastic nature of the opening and closing of the pores.

Various theories have attempted to explain ion transport in biological pores via transient interfacial ion-pairing, formation of transient pores and the associated gating mechanism[16] (pore-mediated transport), ion-induced defect permeation[90], or as a combination of these methods[175]. On the other hand, artificial pores, such as functionalized carbon nanotubes (CNTs), have extremely simple morphologies and bear functional resemblance to biological pores in exhibiting fast water transport with ion selectivity. CNTs, with their well-defined pore size and structure, have thus emerged as both a simplified and mechanically stable model for biological pores and as one of the most promising materials for commercial nanofluidic applications.

One of the obstacles in effectively using carbon nanotubes in nanofluidic systems is the difficulty encountered in accurately predicting the ionic flux through them. This challenge has two aspects: first, the absence of any unified nanoscale theories to predict ion flux; second, the lack of a proper understanding whether the use of continuum equations to predict ion flux through simple structures, such as nanotubes with pore sizes of a few nanometers, is even justified. The latter has to do with the difficulty that nanoscale systems pose to experiments in testing the limitations of various empirical laws. To understand the current state-of-the-art in the field of nanofluidics concerned with the utilization of carbon nanotubes, one may refer to several excellent literature reviews provided by Daiguji[176], Bocquet[177], Schoch et al.[1], and Guo et al.[178]

Although exact force fields describing the correct potential functions that include electronic polarizability for water molecules and ions are not available, a number of simulation studies have previously demonstrated the spontaneous filling of water in the narrow hydrophobic nanotubes[19], fast water transport rates[179], and the ordered structure of water in nanotubes, all of which have been subsequently validated by experiments[22,23,31,33,180]. While a number of molecular dynamics (MD) simulation studies employing osmotically or pressure-driven carbon nanotube-based systems have shown water transport rates through nanotubes to be comparable to biological membranes[6,21,111], similar studies on ion conduction have been limited. The problem is especially magnified when it comes to studying concentration gradient-driven diffusive ion flux, which is due to two main contributing factors. First, the stochastic nature and extremely long timescales of simulations required for observing ion conduction in CNTs with pore sizes less than 1 nm makes MD ineffective without the use of large external forces, such as pressure or electric fields. Second, the decreasing concentration in the feed reservoir and diminishing concentration gradient that makes attaining a steady-state diffusive flux quite difficult.

In dilute environments and under extreme confinement ($d < 1$ nm; d is the CNT diameter), instead of employing fully atomistic MD simulations for long durations, one dimensional potential of mean force (PMF) calculations have achieved semi-quantitative success in predicting the permeation rate in biological channels[181]. For larger pore sizes that can accommodate more than one ion in a moderate to highly concentrated environment, the case is more complicated since one must consider multi-ion PMFs. To accelerate ion conduction and to mitigate the problem of long simulation times required to achieve sufficient ion permeation, some studies utilize either a pressure-driven[182] or an electric field-induced ionic current[183]. In many cases, the electric field used is much higher than the dielectric breakdown voltage of water. To overcome the second limitation of depleting concentration in the feed reservoir, some well-known techniques are available, such as dual control volume grand canonical molecular dynamics (DCV-GCMD)[184,185] and a new elegant simulation protocol described by Kutzner et al.[186] that restores the gradients; however, the widespread adoption of these techniques has not yet occurred.

This study focuses on the passive diffusion of ions through uncharged nanotubes with pore sizes in the range of 2-3 nm that are at the limit of the continuum approximation where bulk-like features are almost restored. When it comes to maintaining concentration gradients to observe steady-state diffusion, we use a simplistic approach by employing volumetrically large reservoirs of unequal concentrations and a high concentration gradient that enables us to observe a pseudosteady-state at the given concentration gradient on a timescale that is accessible to MD simulations.

Membrane theories based on refinements of the Nernst-Planck equation, such as the homogenous or position-dependent versions of the solubility-diffusion model[90,187] or ideas based on the theory of rate processes[188], are often used to explain the permeation mechanism and the

consequent ionic flux through mesoporous (2 nm > d > 50 nm) and nanoporous (d < 2 nm)[189] materials. From the analysis of 100s of nanoseconds of MD trajectories of the simulated ions, we were able to compare the unidirectional flow of ions with continuum dynamics equations and assess this simplest of scenarios using a generalized Fick's law, which might prove to be an adequate constitutive equation to obtain the ionic flux in this special case. In a previous study, it was shown that CNTs with diameters greater than 1 nm can easily accommodate an ion with very little energetic penalty, thus implying that ions can easily partition themselves into nanotubes[39]. Through our study, we analyze the extent of ion partitioning as a function of CNT diameter. This is the first step toward building the most general description of the multi-component mass transfer through nano-confined spaces, and the results reported here are among one of the first molecular dynamics simulation studies to investigate ion fluxes through different nanometer-sized pores using only a concentration gradient and in the absence of large external forces. Through this study, we will provide a complete account for the confinement-induced structural, dynamical, and energetic differences from bulk conditions that lead to a deviation of ion flux from continuum predictions.

In the first part of this article, the theory of species transport through membranes will be discussed, followed by a description of the details of the computational methods used in our study of ion fluxes and the determination of free energies of ions in bulk and under confinement. This is followed by the comparison of the steady-state flux through CNTs with that obtained from a continuum assumption of Fick's law and a discussion of the apparent deviation between continuum theory and simulation results. The aim of this paper is ultimately to develop a simple and straightforward description of ion transport for uncharged homogeneous pores that can relate

experimentally accessible quantities, such as fluxes, with the diameter of the pores and the external solution concentration.

6.2 Theory

Ion migration in continuum theory is described by the Nernst-Planck equation as an electro-diffusion process that takes into account the contributions from diffusion (concentration gradient), migration (electric field), and convection (hydrodynamic velocity). Without convection, the 1D species transport through membranes is given by

$$J_i = -D_i \left[\frac{d\overline{C}_\iota}{dx} + \overline{C}_\iota \frac{d\ ln\overline{\gamma}_\iota}{dx} + \frac{z_i F}{RT} \overline{C}_\iota \frac{d\overline{\emptyset}}{dx} \right] \tag{6.1}$$

where J_i, D_i , $\overline{C}_\iota$, $\overline{\gamma}_\iota$, are the ion flux, diffusion coefficient, molar concentration, and activity coefficient of species *i*, respectively. $\overline{\emptyset}$ is the electric field, which may be internal (diffusion potential as in the case of charged species having differing mobilities or Donnan potential because of fixed membrane charges) or external (arising from an applied electric field), or a combination of both. However, it is essentially irrelevant whether the field is generated by an external source or by diffusion in the system since the individual ion has no means of knowing the origin of the electric field[190].

The current density for an ideal solution is given by

$$i = F \sum_{i=1}^{n} z_i J_i = -F \sum_{i=1}^{n} z_i D_i \frac{d\overline{C}_\iota}{dx} - \frac{z_i^2 F^2}{RT} \sum_{i=1}^{n} D_i \overline{C}_\iota \frac{d\overline{\emptyset}}{dx} = 0 \tag{6.2}$$

The first term on the right side is the diffusion-controlled current that arises from the diffusion potential, which is also called the liquid junction potential, and the second term is the ohmic current due to the electric field. Rearranging the terms,

$$\nabla \emptyset = -\frac{i}{k_e} - \frac{F}{k_e}\sum_{i=1}^{n} z_i D_i \nabla C_i \tag{6.3}$$

where

$$k_e = \frac{F^2}{RT}\sum_{i=1}^{n} z_i^2 D_i\, C_i \tag{6.4}$$

In bulk solution, the electrostatic potential is zero; for a neutral pore of length L with no fixed-charges and no external electric field, the first term on the right side (the ohmic potential) vanishes. The second term on the right side is the diffusion potential, and it arises from a combination of ion concentration gradients and unequal ion diffusivities. It can be expressed as

$$\nabla \emptyset_{diff} = -\frac{F}{k_e}\sum_{i=1}^{n} z_i D_i \nabla C_i \tag{6.5}$$

For a univalent salt, assuming electroneutrality ($\bar{C}_+ = \bar{C}_- = C_s$), this is written as

$$\frac{d\emptyset_{diff}}{dz} = \left(\frac{D_- - D_+}{D_- + D_+}\right)\frac{RT}{F}\frac{d\ lnC_s}{dz} \tag{6.6}$$

$$\Delta \emptyset_{diff} = \left(\frac{D_- - D_+}{D_- + D_+}\right)\frac{RT}{F} ln\frac{C_0}{C_L} \tag{6.7}$$

where C_0 and C_L are the concentrations at the entrance and exit of the pore. It is clear fom the above expression that the diffusion potential vanishes for a small concentration gradient or when the anion and cation diffusivities are closely matched. The diffusivities of sodium and chloride ions in dilute sodium-chloride solution using the TIP4P/2005 water model and OPLS-AA parameters for sodium and chloride are calculated as 0.9×10^{-5} cm^2/s and 1.33×10^{-5} cm^2/s, respectively. Assuming a large concentration gradient, $C_0 = 1$ M and $C_L = 0.05$ M, the diffusion potential amounts to 15 mV.

It is evident that local electroneutrality is not a necessary condition, especially under nanoconfinement, whenever the ions have widely differing diffusion coefficients. An expression derived by Deen[191] allows us to estimate the deviation from electroneutrality under nanoconfinement for channel length L:

$$|C_+ - C_-| \sim \frac{\varepsilon RT}{F^2 L^2}\left(\frac{C_0}{C_L}\right)^2 \tag{6.8}$$

For the concentrations stated above at the tube entrance and exit, and assuming a separation (L) of 5 nm, the concentration difference can be as high as 3 M. However, ion pairing is observed in the CNT, which is made possible by the low dielectric medium and greater interaction between cations and anions, this effectively mitigates the concentration difference under nanoscale confinement.

The diffusion coefficients of sodium and chloride ions are interdependent so as to satisfy the condition of local electroneutrality; these are replaced by an effective or apparent diffusivity for a 1:1 electrolyte:

$$D_s = \frac{(z_+ - z_-)D_+ D_-}{z_+ D_+ - z_- D_-} \tag{6.9}$$

For NaCl in bulk TIP4P/2005 water, the apparent diffusion coefficient is 1.07×10^{-5} cm^2/s. In the absence of any external fields and under a negligible diffusion potential, the ionic flux is mostly governed by the conservation equations of a neutral solute; i.e., Fick's diffusion equation. In the present treatment, we neglect the diffusion potential and assess the validity of the concentration gradient-dependent Fick's equation as a first approximation to describe the ion flux through an uncharged CNT.

6.3 Computational methods

Model system

The system consists of an uncharged armchair single-walled carbon nanotube embedded between two graphene sheets that are in contact with two reservoirs, one containing sodium chloride solution and the other containing water (see Figure 6-1). The reservoirs are bounded by graphene walls. We considered four pore sizes with diameters of 1.9 nm (14,14), 2.4 nm (18,18), 2.7 nm (20,20), and 3 nm (22,22), which form single pores of 5 nm length and constant cross section. To obtain the water-filled CNT that is used as a starting structure in the simulation system, the CNT is solvated in a pre-equilibrated (300 K, 1 bar) water bath and the water molecules inside the tube are removed to permit water to naturally enter the tube during the course of the simulation. This allows us to obtain the natural density of water inside the carbon nanotube, which in all cases

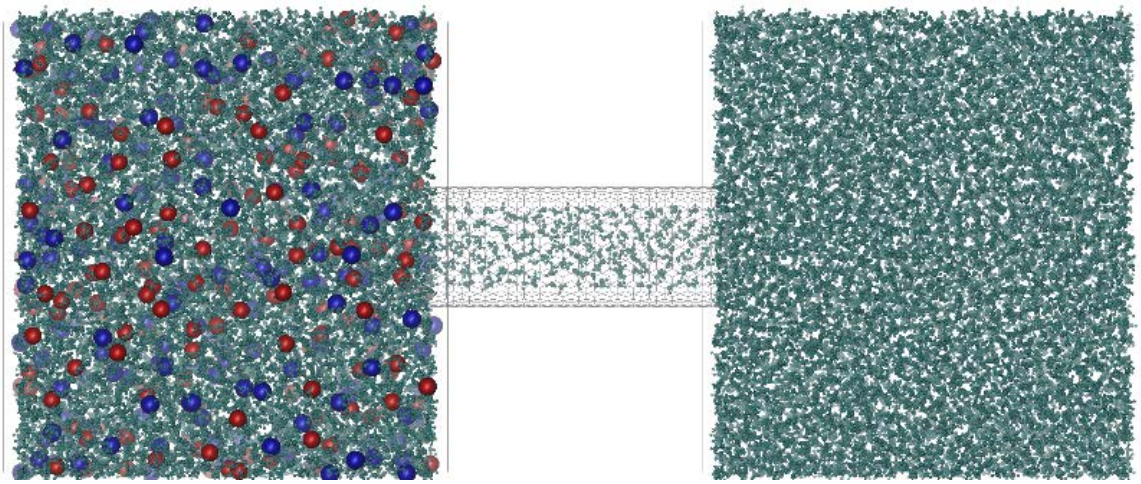

Figure 6-1: Schematic illustration of the side view of the uncharged CNT/reservoir system in studies of concentration gradient-driven electrolyte flux: sodium ions (red), chloride ions (blue), TIP4P/2005 water molecules (cyan), and the CNT (black).

is slightly lower than the bulk density. The two reservoirs also contain pre-equilibrated water at 300 K and 1 bar. Reservoir 1 is solvated with ions by removing water molecules and adding the requisite number of ions to build the concentration to 1 M (~208-280 pairs of ions in 11000-15000 TIP4P/2005 water molecules), whereas Reservoir 2 contains only water molecules. The concentration of Reservoir 1 is 7 times the physiological concentration and the corresponding Debye length at 1 M concentration is 0.3 nm. We use a high solute concentration in Reservoir 1 to obtain a faster response that justifies the use of the steady-state approximation at the MD timescale. No solute (Na^+ or Cl^-) is present in the nanotube at the beginning of the simulation. The dimensions of the simulation box are $7.3 \times 7.3 \times 18$ nm for the (14,14), (18,18) and (20,20) cases and $8.3 \times 8.3 \times 18$ nm for (22, 22) case.

Simulation details

The atoms of the CNT and graphene sheets were modeled as uncharged Lennard-Jones particles using parameters for the sp2 carbon of benzene in the OPLS-AA force field. The carbon atoms of the CNT and graphene were held fixed during the course of the simulations using a harmonic restraining potential with a force constant of 10,000 kJ/mol/nm^2 to restrict their translational and rotational motion. The TIP4P/2005[154] water model was chosen because of its more accurate representation of the phase diagram, the reproduction of the O-O peaks in the radial distribution functions, and, most importantly, because the OPLS-AA force-field was developed entirely with the TIP4P class of water models. The LINCS algorithm was used to keep the water molecules rigid, thereby allowing for longer integration time steps. The Lennard-Jones parameters of cross interactions were calculated on the basis of the geometric means for both σ and ϵ. The LJ interaction parameters are summarized in Table 6-1. Periodic boundary conditions were applied in all three directions. Particle Mesh Ewald Summation was used for electrostatics in the 3D periodic

systems and the non-bonded interactions were truncated at a distance of 1.2 nm. Energy minimization by the steepest descent method was carried out to remove any unphysical overlaps between atoms. The initial velocities of the atoms were assigned according to a Maxwell distribution at a temperature of 300 K with a random seed generator, and the system was then equilibrated in an NVT ensemble at 300 K by coupling to a v-rescale thermostat with a coupling constant of 5 ps for 1 ns. Once the target temperature was attained, all simulation runs required for accumulation of statistics were carried out using the GROMACS MD package in the NVT ensemble with the v-rescale thermostat, a leap frog (Verlet) integrator, and a time step of 1 fs. The lengths of the four simulation runs to attain a steady state ranged from 100 ns for the largest tube diameter to 400 ns for the smallest tube diameter. We used Visual Molecular Dynamics (VMD 1.9.1) to visualize the simulation trajectories.

Table 6-1: Lennard-Jones parameters used in the simulations.

Atom type (i)	σ_{ii} (nm)	ϵ_{ii} (kJ/mol)	Charge (q)
Ion			
Na^+	0.3304	0.016	+1
Cl^-	0.4417	0.4928	-1
Nanotube and walls			
C	0.355	0.29288	0
Water model (TIP4P/2005)			
O	0.3159	0.7749	0
H	0	0	0.5564
M	0	0	-1.1128
d_{OH} = 0.09572 nm, d_{OM} = 0.01546, ∠HOH = 104.52			

The preset concentration gradient gives rise to ionic fluxes, and the simulations were continued until the concentration in Reservoir 1 dropped to about 0.9 M, by which point a reasonable steady-state flux toward Reservoir 2 was established for a relatively small decrease of the concentration gradient. Forward osmosis of water is absent; i.e., there can be no net movement of water from Reservoir 2 to Reservoir 1 as the rigid graphene sheets do not allow the volume of compartment 1 to expand. In the absence of an external applied electric field or convection, the gradients that might exist arise from a combination of concentration difference and diffusion potential, with the concentration gradient being the predominant driving force. We assume that the pores in the periodic images do not interact with each other. This is a good assumption since the density of the pores in the plane is sufficiently low so that any interaction between pore images can be neglected. The system is overall electrically neutral and at a stationary state. The pore offers the ions a hydrophobic (albeit water-filled) pathway to the low concentration reservoir, and because of the relatively large aspect ratio ($L/d > 1$), only conduction in the z-direction is important.

Free energy calculations

The energy barriers in transporting an ion from bulk through the membrane were evaluated by using two different methods by simulations carried out in GROMACS; i.e., the 1D Potential of Mean Force (PMF) using umbrella sampling simulations and the Bennett Acceptance Ratio (BAR), which is a refinement of the free energy perturbation technique. References detailing the concepts, methodology, and implementation of the BAR and PMF methods can be found in several excellent articles[86,192,193]. In the umbrella sampling simulation, we begin with a CNT in bulk solution where the ion is held initially at 0.5 nm from the tube entrance. A counter ion is added to the simulation box outside the CNT to maintain overall electroneutrality. This system is

equilibrated by holding the ion fixed at the tube entrance for 1 ns. The reaction coordinate (ξ) is chosen along the z-axis (axial direction) of the CNT. To generate the trajectory for umbrella sampling, the position restraints are removed and a single Steered Molecular Dynamics simulation is performed where the ion is pulled a distance of 6 nm, translocating it through the entire length of the CNT. A spring constant of 1,000 kJ $mol^{-1}nm^{-2}$ and a pull rate of 0.01 nm ps^{-1} (0.1 Å ps^{-1}) were applied. A total of 100-150 windows were used per umbrella sampling simulation with a symmetric distribution of sampling windows; thus the adjacent windows have a spacing of 0.04-0.06 nm. Each window was equilibrated for 300 ps, followed by 500-1000 ps of data collection. The unbiased PMF was computed with the Weighted Histogram Analysis Method (WHAM), using Grossfield's code[194].

In the BAR method, to obtain the free energy of an ion in a particular state (i.e., in bulk or under confinement in the CNT), we first need to create a reversible thermodynamic pathway to allow the alchemical transition of the ion from fully interacting (with all interactions between ion and environment switched on) to a completely decoupled state (all interactions between ion and environment switched off). The decoupling of interactions of the ion is accomplished in two steps: first the Coulombic interactions are switched off, followed by the switching off of the van der Waals interactions. The Hamiltonian of a given state can be expressed as a linear combination of its neighboring states, which are functions of the coupling parameter, λ. The coupling parameter defines the degree to which the ion is interacting with its surrounding:

$$H(\lambda) = (1 - \lambda)H_0 + \lambda H_1 \tag{6.10}$$

When $\lambda = 1$, all interactions are turned on, whereas $\lambda = 0$ indicates that all interactions are switched off. We used 20 successive coupling parameters in steps of $\Delta\lambda = 0.05$ for turning off both the Coulombic and the van der Waals interactions. The soft-core potential was used to

circumvent the singularity problem of linear scaling[195]. The free energy difference between states can be obtained from its expression in terms of energy difference of simulated systems as

$$\Delta G = -\frac{1}{\beta}\sum_{i=1}^{n} \ln \langle \exp(-\beta \Delta\lambda_i \Delta H) \rangle \tag{6.11}$$

where $\beta = k_B T$ and n is the number of coupling steps. Since the kinetic energy terms of the Hamiltonian are separable, the free energy calculation reduces to

$$\Delta G = -\frac{1}{\beta}\sum_{i=1}^{n} \ln \langle \exp(-\beta \Delta\lambda_i \Delta U) \rangle \tag{6.12}$$

$$\Delta G_{bulk-conf} = \Delta G_{bulk} - \Delta G_{conf} \tag{6.13}$$

The relative free energy difference of ion transfer from bulk to the interior of the nanotube ($\Delta G_{bulk-conf}$) can be obtained from the difference of the free energies of ions in the bulk state and under varying degrees of confinement. For properly converged PMF and BAR simulations, the magnitudes of the energy barrier to transport an ion from the bulk state through the CNT obtained via both methods are equivalent.

Simulations at alchemical intermediate states were implemented in parallel with the stochastic dynamics integrator. For each λ, the equilibration lasted 50 ps and the production runs persisted for 300 ps. After the simulations were completed, we extracted the free energy difference from the output data using the GROMACS BAR tool to obtain the solvation free energy (ΔG_{bulk}) and the free energy of the ion under confinement (ΔG_{conf}).

6.4 Results and discussion

Figure 6-2 presents snapshots from the MD simulations taken under steady-state conditions at random time steps. At steady-state, the CNTs are filled with water containing a small number

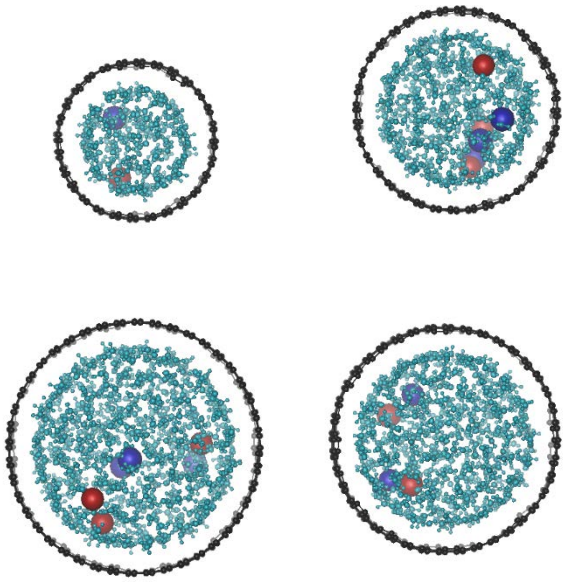

Figure 6-2: Carbon nanotubes (black) of various diameters filled with water molecules (cyan), sodium ions (red), and chloride ions (blue). Clockwise from top left are snapshots of the axial view of (14,14), (18,18), (20,20), and (22,22) CNTs during typical simulations.

of sodium and chloride ions, as determined by the external reservoir concentrations and the diameter of the CNT. There is a depletion shell between the fluid and the solid nanotube walls that results from the hydrophobic nature of the carbon-water energetic interaction, as commonly observed in many similar MD simulation studies[110,142]. As the diameter of the CNT increases, the depletion zone becomes a smaller portion of the overall CNT volume, and the water within the tube takes on more bulk-like characteristics. Figure 6-2 also illustrates that the CNT pore sizes used in the simulations are accessible to more than a single file of water and ions. The diameters of the pores (including the excluded volume) are 1.9 nm, 2.4 nm, 2.7 nm, and 3.0 nm for the (14,14), (18,18), (20,20), and (22,22) CNTs, respectively.

The area of the pore that is used in the determining the flux and densities of the species is calculated on the basis of their respective effective diameters of 1.56 nm, 2.06 nm, 2.36 nm, and

2.64 nm, which excludes the empty inner shell boundary of the hydrophobic carbon atoms. The smallest nanotube diameter employed here is 3 to 4 times the effective pore size of typical ion channels and is about the size of an OmpF porin at its widest cross section. Table 6-2 shows a comparison of the effective diameter of nanotubes used in this study with typical pore sizes of biological channels.

Table 6-2: Comparison of the effective diameter of nanotubes used in this study with the diameters of typical biological channels.

Channel type	Effective Diameter (nm)
CNTs used in the simulation	
14,14	1.56
18,18	2.06
20,20	2.36
22,22	2.64
Ion channels	
MthK (K-channels)[84]	0.53-0.59
Kv1.2/2.1(K-channels)[84]	0.45-0.52
NavAb selectivity filter (sodium channel)[196]	0.46
Nicotine acetylcholine receptor channel[85]	2 (water filled central pore region)
L-type calcium channels[197]	0.6
Semi-synthetic ion channels	
Gramicidin[76,79]	0.2-0.3
Porin	
OmpF[198]	2 (β barrel) 0.7 (constriction)

6.4.1 Electrolyte flux

Figure 6-3 shows the increase in the number of ions in Reservoir 2 with time, which is the cumulative amount of ions that has diffused from Reservoir 1 to Reservoir 2. After an initial induction period, which decreases as the CNT diameter increases (i.e., as the local conditions become more bulk-like), the number of ions passing through the channel increases in a roughly linear fashion with time, especially for the largest CNT. Figure 6-4 displays the instantaneous ionic fluxes vs. time, where again the induction period is particularly evident for small diameter tubes.

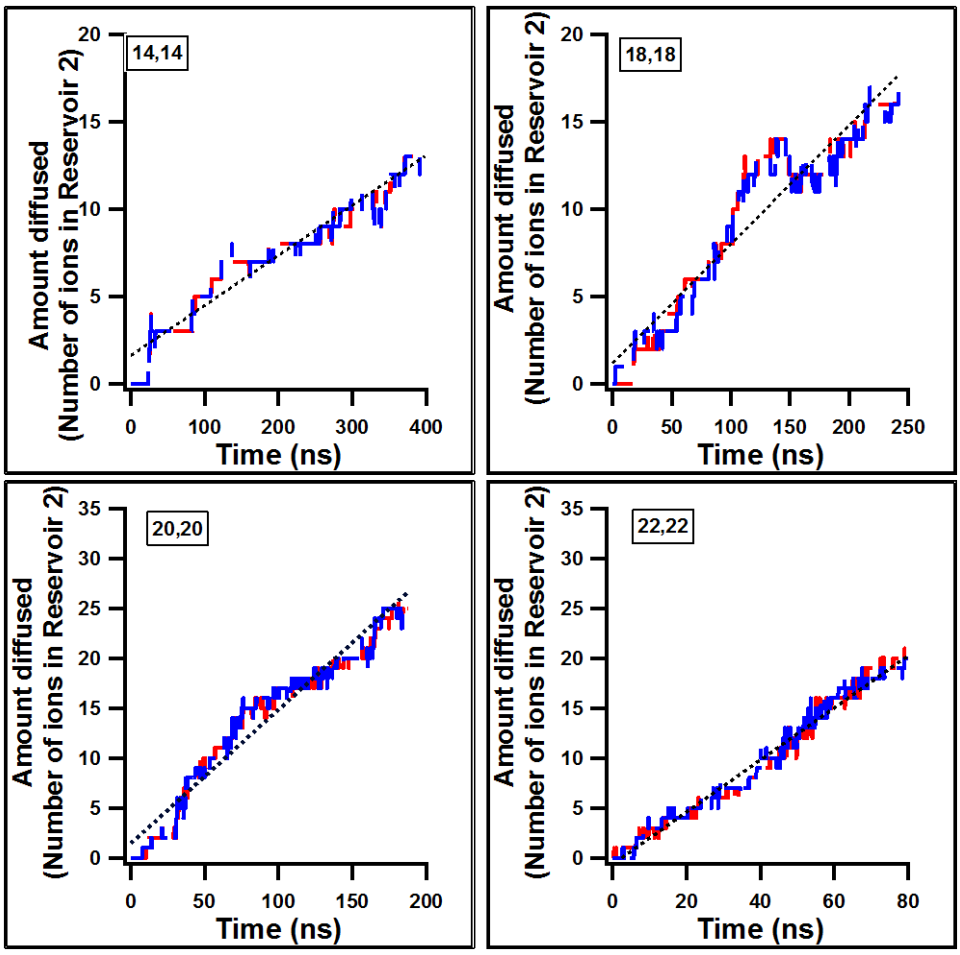

Figure 6-3: Amount of ion diffused as a function of time.

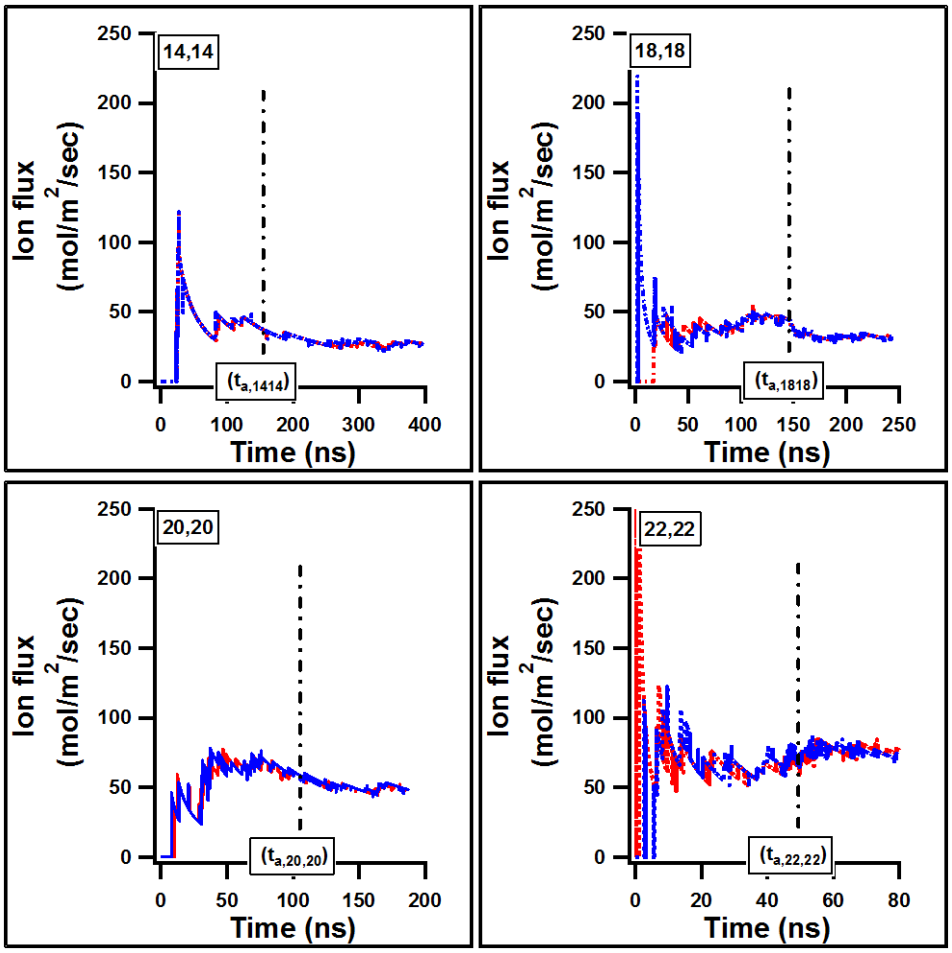

Figure 6-4: Ionic flux through uncharged tubes vs. time.

The reservoir volumes are rather large, so that during the course of the simulation, the concentration in the two reservoirs does not change appreciably in the time that it takes for a statistically-sufficient number of ions to traverse the membrane. This establishes a pseudosteady-state at the resulting concentration gradient, as can be seen from the instantaneous fluxes even in the transient diffusion systems examined herein. A steady-state flux does not result instantaneously from the imposition of the concentration gradients, and the relaxation time (or the lag time) indicates how fast a pseudosteady-state can result from an instantaneously applied concentration gradient. Similar to its macroscopic counterpart, the relaxation time (t_a), indicated in Figure 6-4,

is the time in which the flux approaches to within 3% of its steady-state value[190]; i.e., the standard deviation in flux is less than 3% of the average flux recorded at the end of the simulation. Calculated values for these relaxation times are 150 ns, 140 ns, 110 ns, and 50 ns for the four CNTs ranging from the smallest diameter to the largest, indicating a decreasing trend in t_a as more bulk-like conditions are approached. The relaxation time obtained for each of the CNT simulation systems is greater than the timescale ($t_{a,cont} = 0.42\frac{L^2}{D} \sim 10.5$ ns) predicted for species with diffusion coefficient (D) permeating through mesoscopic and macroscopic continuum systems of length, L. The induction period needed for the observable flux to be recorded and the relaxation time for pseudosteady-state to be achieved are greatest in the smallest diameter case. Contrary to the relaxation time in a macroscopic system being independent of the diameter, we observe a definite diameter dependence. If we assume the validity of the time-scaling equation cited above, the diffusion coefficient of the ions must possess an additional term for the diameter dependence that accounts for the larger lag times since all the CNTs considered herein have equal lengths (5 nm).

Once the diffusion barrier is passed (i.e., after the accumulated simulation time is greater than the relaxation time), the system can be described using Fick's law: an almost linear increase (dotted lines) in the concentration of ions in Reservoir 2 is observed (Figure 6-3). This allows for calculation of the steady-state flux from the slope of the linear part of Figure 6-3:

$$J_s = \frac{slope}{N_A \times A_s} \tag{6.14}$$

where J_s, N_A, and A_s are the ionic flux of species *S*, Avogadro's number, and the cross sectional area of the nanotube available for transport. The steady-state fluxes summarized in Table 6-3 are statistically equivalent for both ions, effectively increasing in magnitude as the CNT diameter

Table 6-3: Steady-state ion transport characteristics through the CNTs of various diameters. The numbers in parentheses indicate values calculated from continuum flux theory; these are provided for comparison with those obtained via MD simulation.

Case	Transport rate # of ions/s (10^7) Na^+, Cl^-	Ionic current (pA) Na^+, Cl^-	Ionic flux (mol/m^2/s) Na^+, Cl^-	Deviation in flux (%)
1.89 nm (14,14)	3.28, 3.33 (23.0)	5.25, 5.33 (36.8)	28.67, 29.16	87
2.44 nm (18,18)	6.48, 6.54 (38.90)	10.37, 10.46 (62.64)	33.3, 33.6	84
2.71 nm (20,20)	13.5, 13.47 (52.64)	21.6, 21.6 (84.22)	51.3, 51.2	76
2.98 nm (22,22)	25.17, 24.84 (65.89)	40.2, 39.74 (105.44)	76.4, 75.4	62
Fick's equation	-	-	200	0

increases. These range from about 28 mol m^{-2} s^{-1} for the smallest diameter tube (14,14) to roughly 75 mol m^{-2} s^{-1} for the (22,22) nanotube. Nevertheless, even for the largest CNT, the ionic flux is lower than the theoretical value based on Fickian diffusion at the macroscale (200 mol m^{-2} s^{-1}). The ion transport rates observed (~10^7 ion/s) are quite high, and are comparable to the transport rates observed through biological channels. However, similarly-sized biological ion channels are able to pump 10^7 ion/s at lower concentration gradients of 10 mM. For the pore sizes considered in this study, the diameter-dependent flux is clearly nonlinear and rapidly approaches the bulk value for larger diameter CNTs (Figure 6-5).

An estimate of the percentage depreciation of flux compared to the continuum diffusion equation as a function of the diameter is also presented in Table 6-3, which is calculated as

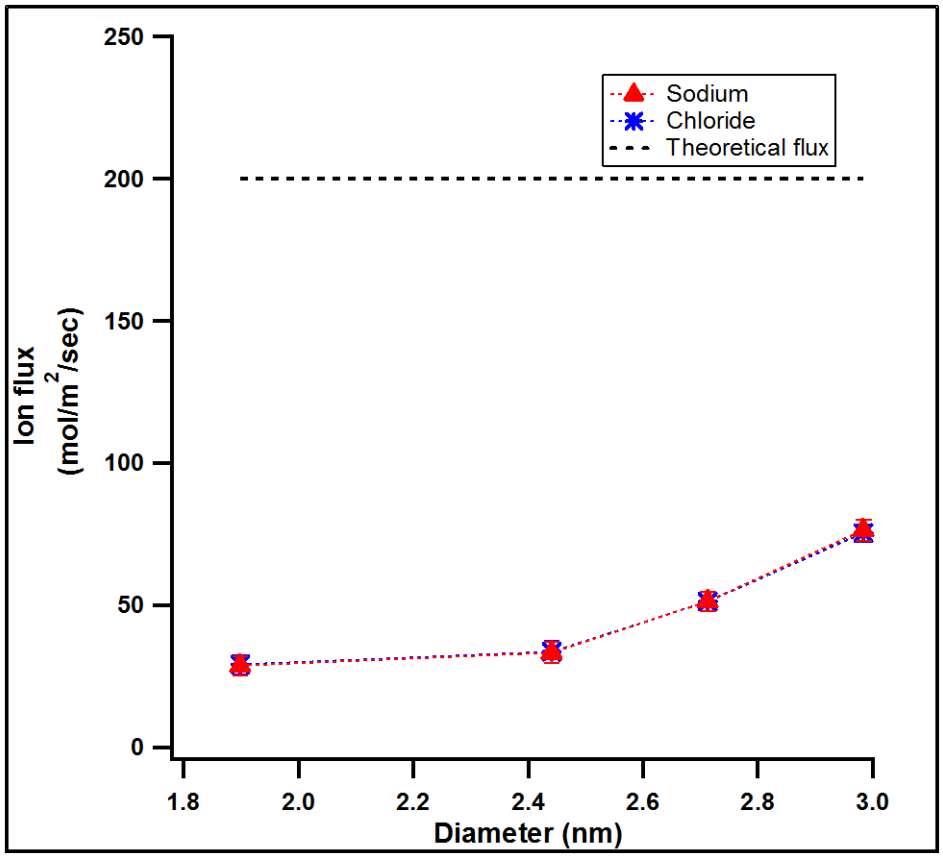

Figure 6-5: Average steady state sodium and chloride ion fluxes as functions of CNT diameter compared to the theoretical flux based on continuum Fick's law.

$$Deviation = \frac{J_{s,Fick} - J_{s,MD}}{J_{s,Fick}} \times 100 \tag{6.15}$$

These deviations range from 87% for the (14,14) CNT to 62% for the (22,22) CNT. The steady-state fluxes that we obtain for sodium and chloride ions overlap, and we do not observe selectivity of cation or anion at the temperature and pressure state point of the MD simulations.

If we assume negligible diffusion potential and that Fick's equation is a valid representation of transport, we can estimate the effective diffusion coefficients of the ions in the membrane from the ratio of the flux and the concentration gradient:

$$D_s = -\frac{J_s L}{C_L - C_0} \tag{6.16}$$

The diffusion coefficients of ions in the CNTs obtained in the above manner are 0.13 nm^2/ns, 0.165 nm^2/ns, 0.24 nm^2/ns, 0.385 nm^2/ns for the (14,14), (18,18), (20,20), and (22,22) CNTs, respectively, assuming Fickian diffusive behavior is followed at the steady-state concentration gradient and that the partition coefficient is unity. These values are very low relative to the bulk diffusion coefficient (1.07 nm^2/s), reflecting the constraining effects or the partitioning effects of the confining nanotubes that must be taken into account.

In order to clarify the origin of this apparently anomalous deviation from bulk-like behavior, we need to determine if the inclusion of the diffusion potential is important. Furthermore, the flux obtained from Fick's equation depends on the boundary conditions that define the concentration at the entrance and exit of the tube, as well as the particular value of the diffusion coefficient of the ions in the nanotube. In the following subsection, we carry out equilibrium molecular dynamics of a CNT between two symmetrical 1 M sodium-chloride reservoirs to probe the actual diffusion coefficients of the ions within the CNT; i.e., we calculate the diffusion coefficients of the sodium and chloride ions by applying Einstein's equation to the mean-squared displacement data (provided that they prove to vary in a linear fashion). We can then calculate the diffusion coefficients of the ions in the membrane to see if the Fickian limit is achieved and also verify if our initial assumption concerning the boundary conditions is indeed correct.

6.4.2 Effect of diffusion coefficients

To confirm that ions in the nanotube follow a Fickian diffusion mechanism, we study the scaling behavior of the *z*-dimensional mean-squared displacement (MSD) of the ions with time in the absence of any systematic forces; i.e., in an equilibrium setting with symmetric reservoir

concentrations of 1 M NaCl on both sides of the CNT. These MSD data vs. time are displayed in Figures 6-6a-d. MSD calculation is initiated for each ion every time it enters the nanotube and concludes when it exits from either end. If a particular ion reenters the nanotube after it has exited, it is treated as a new particle. Consequently, the statistics obtained for short-lived particles (ones that enter and exit quickly) is greater than those for long-lived particles because these situations occur more frequently. The MSDs were developed over multiple simulation time blocks, spaced periodically throughout the entire course of the simulation. Because of the limited lifetime over which the ions reside within the nanotube, we display the MSD over a 500 ps period for which reasonable statistics can be obtained. As evident from all of the figures, the MSDs of all confined ions increase linearly with time, indicating normal-mode or Fickian-type diffusion. For the largest tube diameter, which has an average occupancy of 10-12 ions of each species at any instant in time, the behavior is distinctly linear and extremely precise. These results are in agreement with the expectation that if the pore system is statistically uniform, the simple Fickian model will be directly applicable[199].

The nature of the MSD indicates a homogeneous diffusion coefficient inside the nanotube, which can be calculated using the Einstein relation,

$$< |z(t) - z(0)|^2 > = \ 2Dt \qquad 6.17$$

The axial diffusion coefficients of the ions in the (14,14), (18,18), (20,20), and (22,22) CNTs are shown in Figure 6-7 and the numerical values are collected in Table 6-4. These values are lower than the corresponding bulk values at 1 M concentration. A recent simulation study[200] reported that ions confined in neutral nanochannels of effective width of 0.36 - 1.26 nm tend to diffuse faster (along the graphene surfaces) than those in bulk solution, which was attributed to the relatively smaller concentration in confined spaces and the solvophobic nature of graphene surfaces. On the contrary, we

observe a suppressed diffusion coefficient of ions in the CNT as compared to 1 M bulk solution of sodium chloride. We also observe a diminished difference between the diffusion coefficients of the sodium and chloride ions in the nanotube as compared to when the ions are in bulk solution.

Based on the values of the diffusion coefficient of ions under confinement, we obtain values for the diffusion potential of 0 mV, 4.8 mV, 5.1 mV, and 2 mV for (14,14), (18,18), (20,20), and (22,22) CNTs, respectively. These diffusion potential values are very small to have a significant effect on the overall flux, making the assumption of Fickian diffusion-dominated flux reliable. Using Eq. (6.9) to obtain the effective diffusion coefficient of the ions for the different cases given in Table 6-4, we recalculate the theoretical flux from Fick's equation by taking into account the actual diffusion coefficient of the ions in the membrane as opposed to the bulk diffusioncoefficients. Figure 6-8 depicts the improved agreement between the recalculated theoretical flux and the flux obtained from the MD simulations.

6.4.3 Effect of boundary conditions

The imposed concentration gradient can be interpreted from the axial density profile, which enables estimation of the ionic flux. It is possible to extract the concentration profiles (Figures 6-9a, b) of sodium ions, chloride ions, and water molecules in the simulation box along the *z*-direction. The densities are obtained initially by dividing the simulation box into square slices of bin spacing of 0.1 nm. The volume considered for computing the densities in the nanotube region between the graphene sheets is taken as the actual volume accessible to water and ions in this region; i.e., the cylindrically binned nanotube volume instead of the volume of the square slice. The density of water inside the CNT is slightly lower than the bulk density and approaches bulk density as the pore size is increased. Layering in the densities of water and ions is seen near the

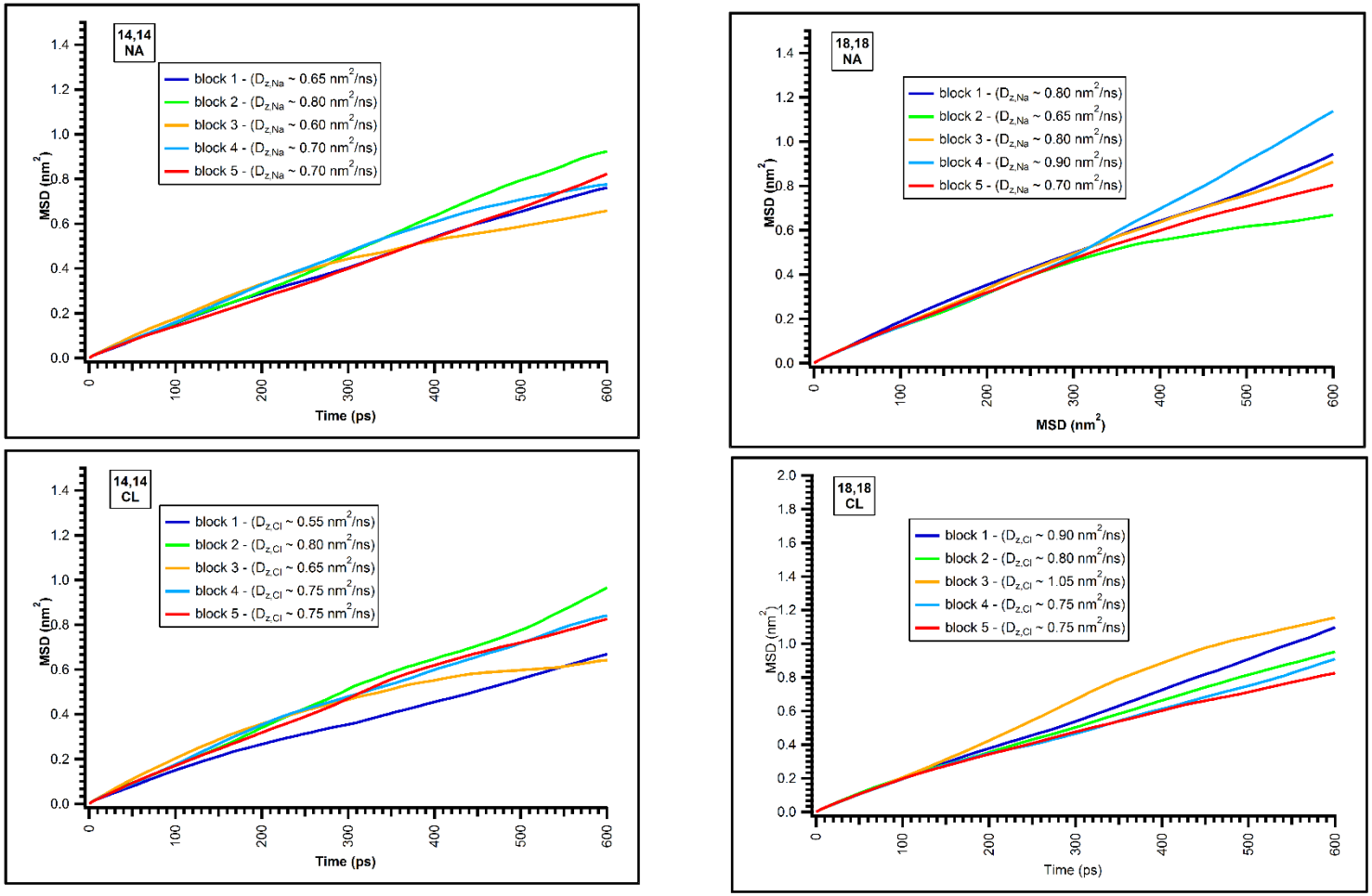

(a) **(b)**

Figure 6-6: Mean-squared displacements of ions in the nanotubes vs time corresponding to data from (14,14), (18,18), (20,20), and (22,22).

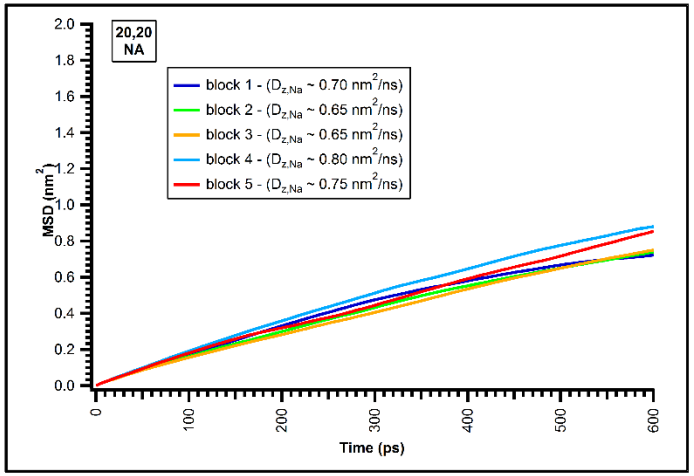

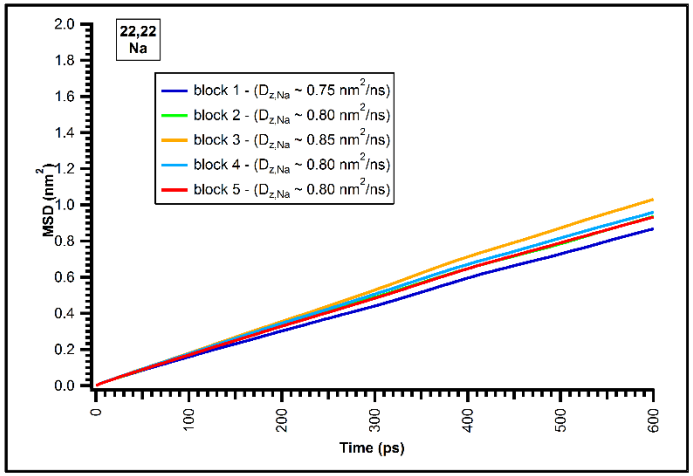

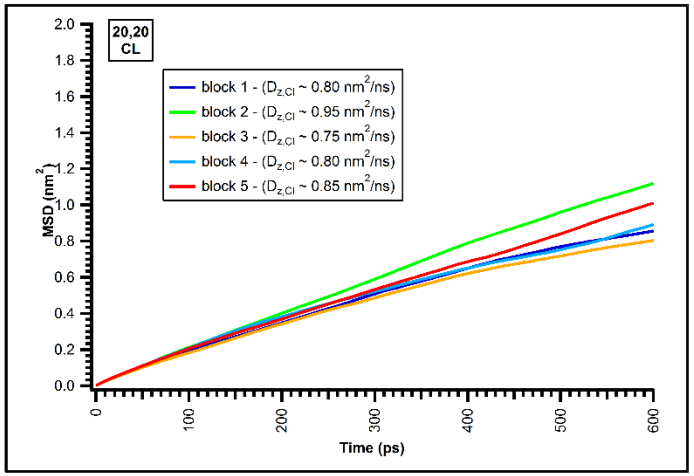

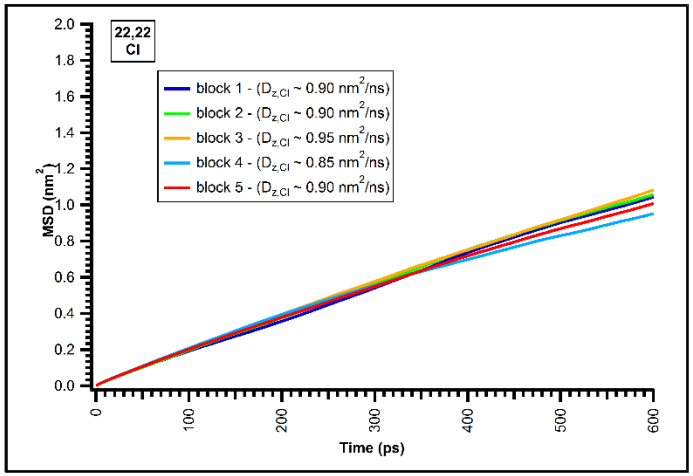

(c) **(d)**

In each figure, data for sodium ions are displayed in the top panel and for chlorine ions in the bottom panel. Data are presented in 5 blocks per plot, each block starting from a different time origin over the course of a simulation.

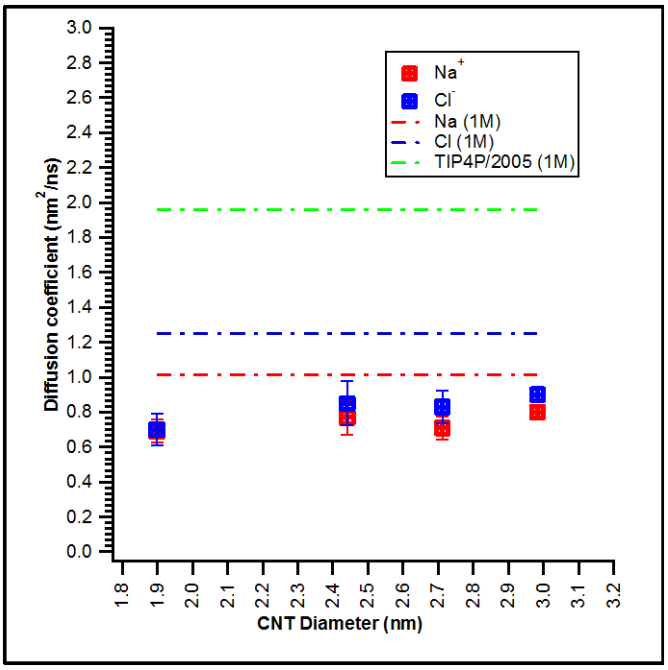

Figure 6-7: A comparison of the diffusion coefficients of ions in the nanotube with the corresponding bulk diffusion coefficients in 1 M solution; sodium (red), chloride (blue), water (green). The dashed lines (red, green, and blue) denote the bulk diffusion coefficients of the ions and water.

Table 6-4: Diffusion coefficients of ions in the nanotube calculated from the Einstein equation and the corresponding diffusion potentials for the concentration gradients in the simulations.

Diameter (nm)	Diffusion coefficient (nm^2/ns)		Effective diffusion coefficient (nm^2/ns)	Diffusion Potential (mV)
	Sodium	Chloride		
1.8984	0.65	0.65	0.65	0
2.44	0.75	0.85	0.79	4.8
2.712	0.7	0.8	0.75	5.1
2.89	0.8	0.85	0.82	2

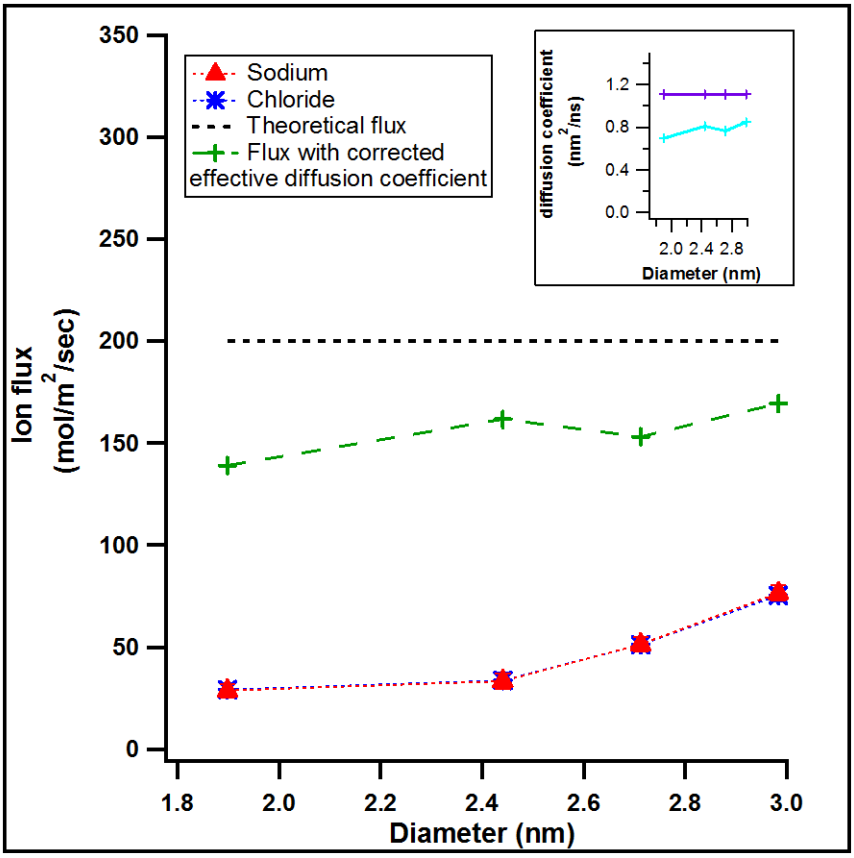

Figure 6-8: Ionic flux vs. diameter of the sodium (red) and chloride (blue) ions directly from the MD simulations compared to the continuum flux prediction corrected for the actual diffusion coefficients of the ions in the nanotube (green curve) and the uncorrected ionic flux prediction from continuum Fick's law with bulk values for diffusion coefficients (black).

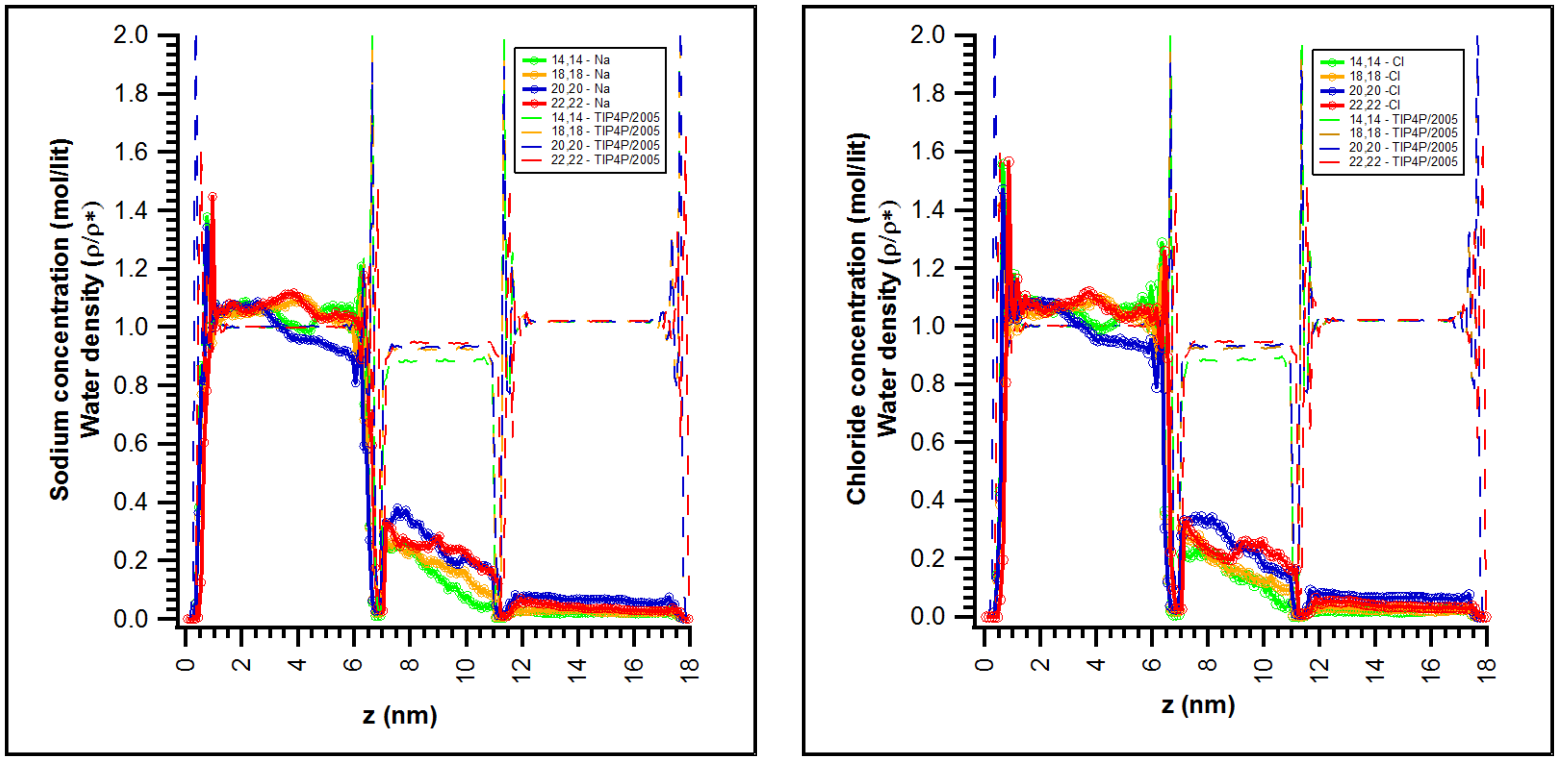

(a) **(b)**

Figure 6-9: The axial concentration profiles of sodium (9a) and chloride ions in the nanotubes (9b). The thick traces indicate the actual concentration of ions as functions of the *z*-position in the simulation box. The thin traces show the axial density profile of water normalized by the density of the bulk water, which is 1000 kg/m^3 or 56 mol/lit for TIP4P/2005

graphene surfaces and nanotube openings, which continue for about 1 nm (3.3 Debye lengths) from the graphene surface. The pore entrance-bulk interfacial region is a non-equilibrium region and will have an effect on the boundary conditions employed in the flux equation.

Concentration polarization, in which ions are accumulated at the upstream face of the membrane, is a common phenomenon in electric-field and pressure-driven flows. We do not observe any concentration polarization for this case of passive diffusion; however, there is a film-like diffusion boundary layer at the entrance of the CNT where the layered structure and the hydrophobic interactions cause the ion concentration at the tube entrance to decrease gradually from its bulk reservoir concentration (Figure 6-10). The thickness of this depletion region is less than 0.5 nm. Thus, there could exist an effective concentration gradient at the tube entrance that is lower than the value assumed initially in the theoretical calculation (i.e., the concentration of the bulk reservoir). This is one of the factors that could affect the rate of transport as it decreases the concentration gradient for ion transport. The concentration at the tube entrance is lower than the bulk concentration for all pore sizes. A close up of the ion concentration at the tube entrance (Fig. 6-10) shows that ion concentration in the wider pores is higher than that in the narrower pores. To match the bulk concentration (1 M), the number of ion pairs that would have to be accommodated within the (22,22) CNT is 15; however, we observe an average ion occupancy of 5-7. This non-ideality, where the concentration of the solute in the pore is lower than in the external solution, might be a consequence of ion solvation in the pore. We can make use of a molar distribution coefficient[190], $\lambda_s = C_{pore}/C_{bulk}$ (also sometimes written as the partition coefficient[201]), which takes into account this discontinuity in the concentration inside and outside the nanotube and rework the flux equation as:

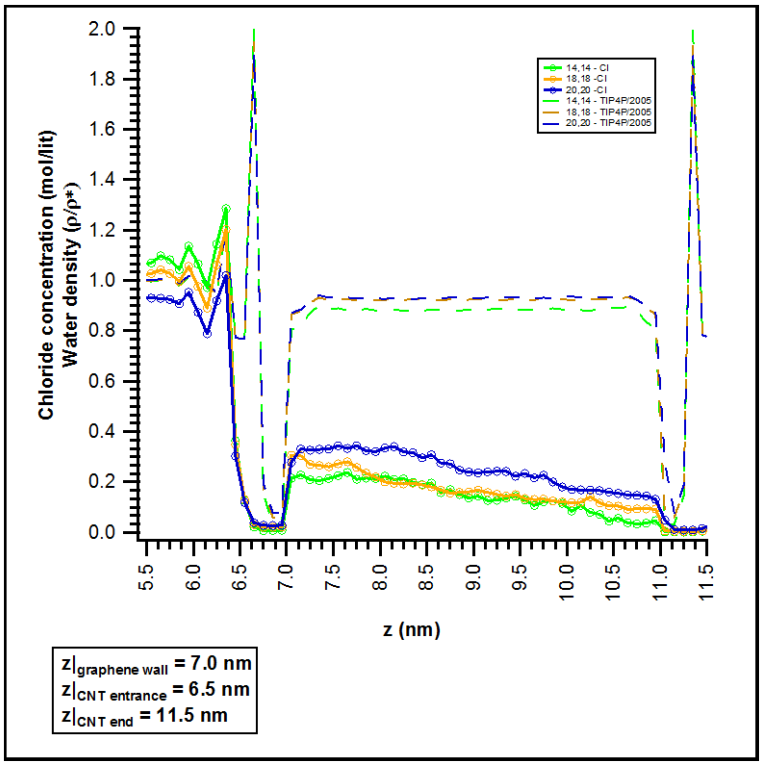

Figure 6-10: A close-up of the axial concentration profile near the tube entrance.

$$J_s = -D_s\lambda_s\left(\frac{dC}{dz}\right) = -D_s\lambda_s\frac{(C_L - C_0)}{L} \tag{6.18}$$

The partition coefficients that we obtain for the simulated cases vary between 0.35 and 0.5. We obtain λ_s from equilibrium simulations of the nanotube embedded between two reservoirs containing equal concentrations of sodium chloride solutions at 1 M. The values of λ_s thus obtained are 0.24, 0.41, 0.53, and 0.70 for (14,14), (18,18), (20,20), and (22,22) CNTs, respectively. The λ_s values that we obtained in all cases are comparable to some other studies of uncharged nanotubes[202] and graphene channels[201] employing sodium-chloride solution. The molar distribution coefficients obtained from the two cases (i.e., from reservoirs of equal concentration and from the cases studied herein by holding one of the reservoir fixed at 0 M) differ on account

concentrations), we plot the corrected theoretical flux and the actual flux obtained from MD in Figure 6-11.

We see a dramatic improvement in the agreement between the theoretical and the simulation values. Inserting the correct boundary conditions in Fick's equation gives us a better agreement between the simulation and the theoretical values. For the largest diameter tubes, namely, (20, 20) and (22, 22), the flux falls between the upper and the lower limits of the corrected theoretical value. The slight difference for the smaller diameter tubes may be related to the energy barriers that most likely affect the rate of transport. This modified equation is similar to a general mass transfer equation that takes into account permeability of the solute:

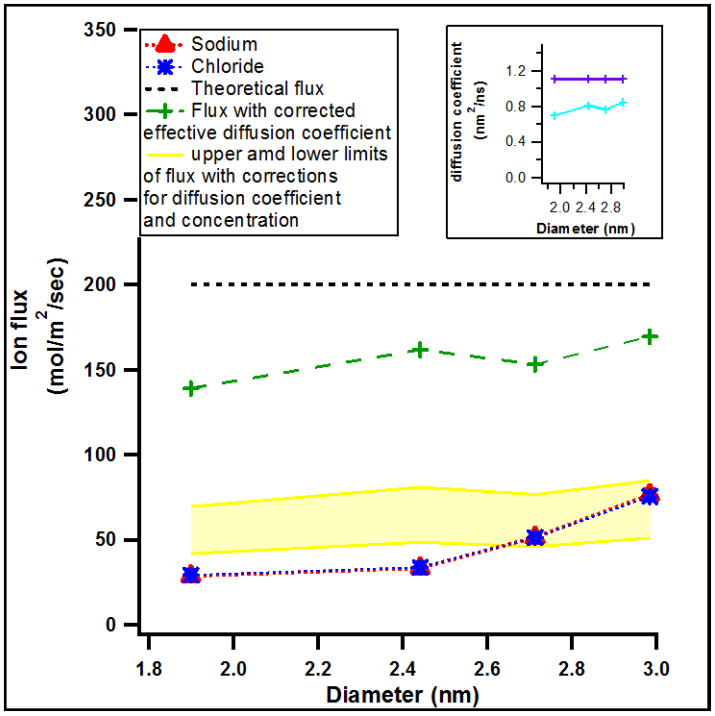

Figure 6-11: A comparison of the theoretical flux corrected to take into account ion partitioning and the actual effective diffusion coeffcients of the ions in the nanotube (yellow shaded region) with the actual sodium (red) and chloride (blue) ion fluxes obtained from MD simulations.

$$J_s = P\Delta C \tag{6.17}$$

where the permeability, $P = \frac{D_S \lambda_S}{L}$, has units of m/s.

It would also be worth investigating the phenomenon of ion saturation in nanopores, in which the flux plateaus as the concentration gradient is increased. We thus simulated additional cases with the largest diameter (22,22) CNT (d = 3 nm) under external solution concentrations of 0.4 M and 0.1 M. The axial concentration profiles for these cases are shown in Figure 6-12 and the normalized axial density profiles for these cases are shown in the inset. We see an external solution concentration independent drop in concentration at the entrance of the nanotube that is about 50% the bulk concentration for the various gradients simulated, indicating that the molar

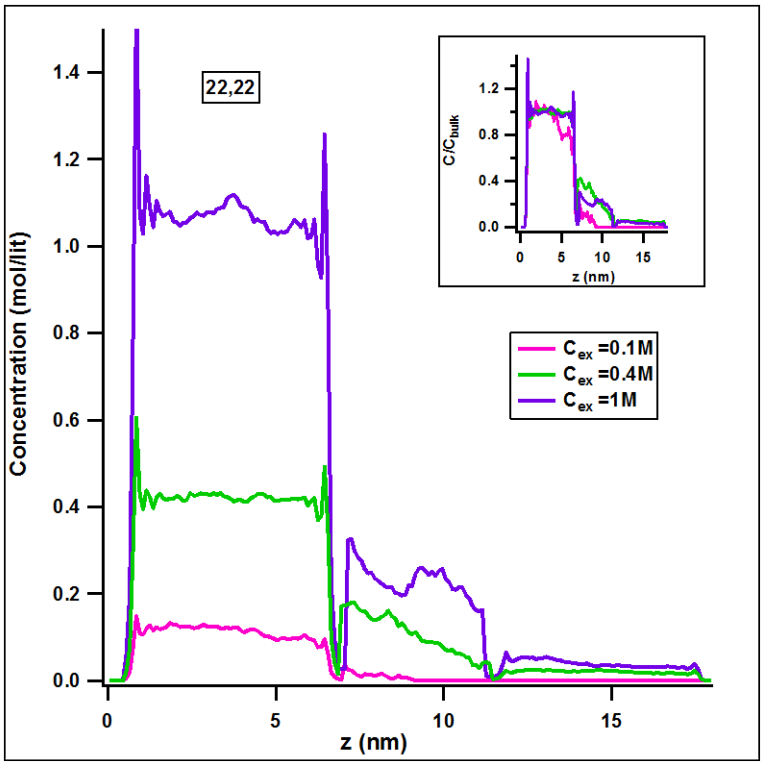

Figure 6-12: The axial concentration profiles of sodium ions for different concentration gradients in simulation systems employing a (22,22) CNT.

distribution coefficient for a particular diameter nanotube is independent of external solution concentration. When we plot the ion fluxes vs. external concentration (Figure 6-13), we observe a linear increase in the flux with the concentration gradient and we do not witness any plateau that would indicate ion saturation at higher concentrations. We thus do not believe that ion saturation in the (22,22) nanotube at 1 M external solution concentration is a cause for the low flux as compared to continuum theory predictions.

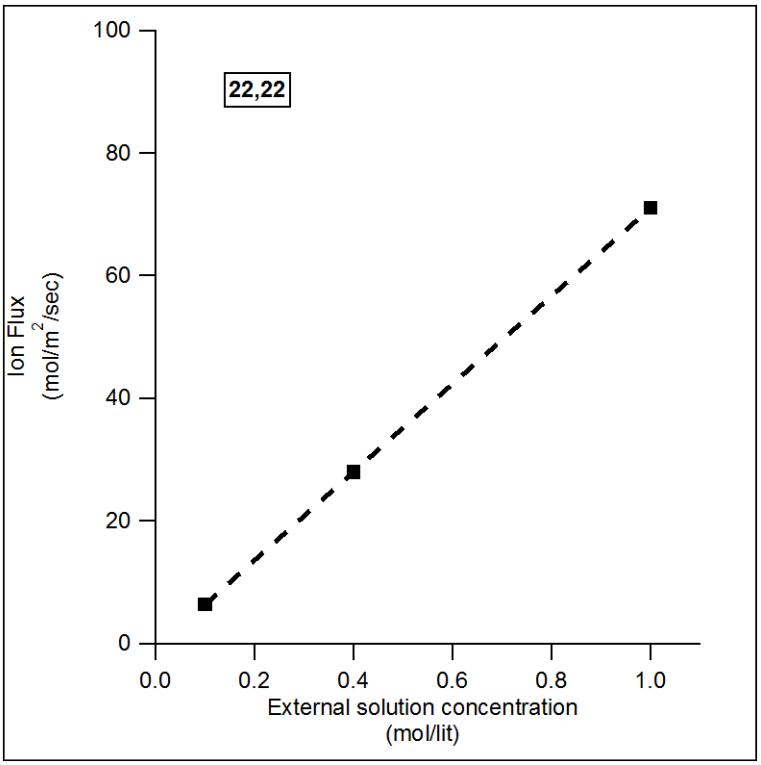

Figure 6-13: Ionic flux through a CNT with *d* = 3 nm as a function of the concentration gradient. Reservoir 1 has a finite concentration of sodium chloride solution while the concentration in Reservoir 2 is fixed at 0 M.

6.4.4 **Effect of energy barriers to transport**

The energetic barrier at the interface between the bulk and confinement zones is often associated with the dehydration of ions or the modification of the solvation shell, which is known to affect the rate of transport processes. We can calculate this free energy difference between the bulk reservoir and the interior of the CNT from MD simulations using the Bennett acceptance ratio (BAR) method, which is a free energy perturbation technique, as well as using the one-dimensional potential of mean force (PMF) profiles from umbrella sampling simulations. The calculations are conducted in an extremely dilute environment; i.e., only a single pair of ions is considered in the simulation box. The PMF profiles enable us to determine how the free energy profile varies as the ion enters from one end of the nanotube and exits from the other. Note, however, that these pores can hold more than one ion at a time; hence by neglecting the multi-ion interaction in these nanotubes, we provide only a simplistic approximation of the barrier to ion transport.

We determined the free energy of the anion and cation in bulk and under confinement using the BAR method (Figure 6-14). Experiments and simulation results give a wide range of ion solvation values in the bulk[203,204]; indeed, the bulk ion solvation values that we obtain with the OPLS-AA force-field and TIP4P/2005 water fall within this range. The relative free energy difference of the ions in bulk and under confinement from the BAR method is shown in Figure 6-15. There is a clear decreasing trend with increasing CNT diameter. Figure 6-15 clearly show how the energy barrier is a function of the tube diameter, and a further examination of the coordination shell of the ions reveals that, for a given pore size, the height of the barrier depends on the degree of modification of the coordination shell. The quality of these PMF profiles in Figure 6-16 is affected by the relatively short simulation time (500 ps - 1 ns) in each window; however, the energy

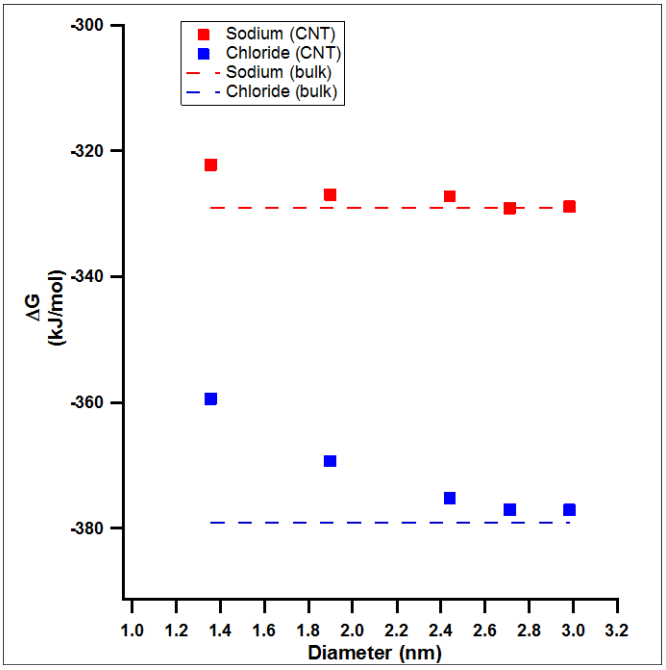

Figure 6-14: Free energy of the ions in bulk and under confinement computed using the BAR method.

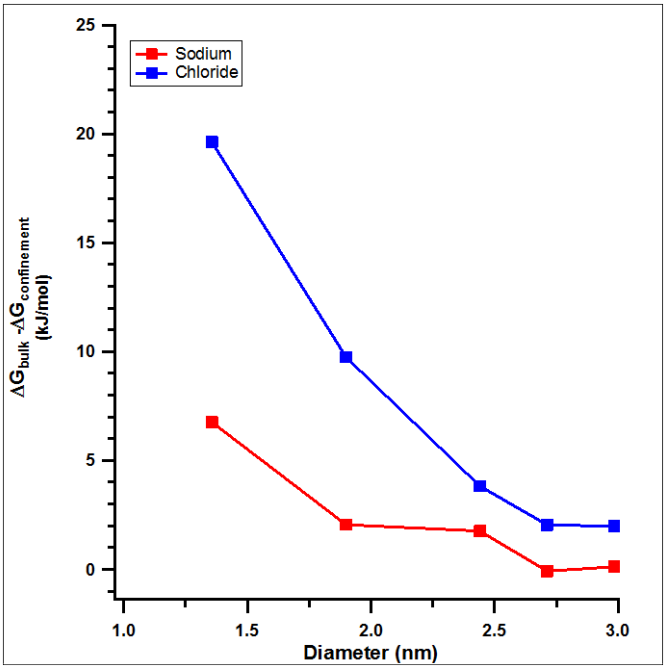

Figure 6-15: The free energy difference (BAR method) of ions between bulk and confinement as functions of CNT diameter.

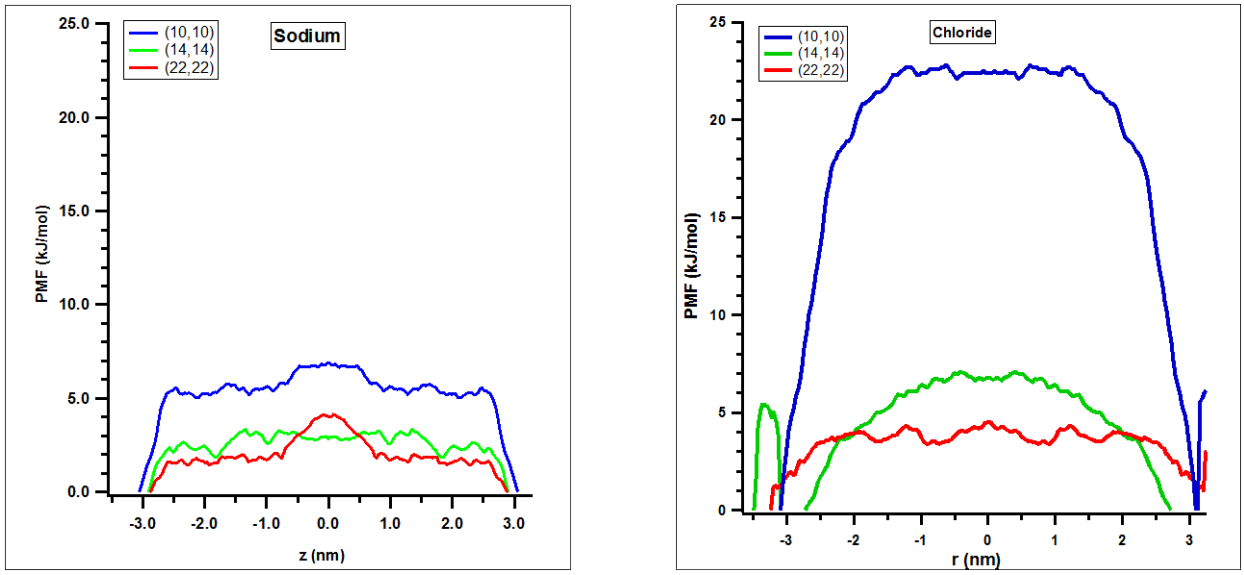

Figure 6-16: PMF profiles of cation (sodium) and anion (chloride) translocation from the bulk reservoir through the CNT.

barrier heights using umbrella sampling shown in Figure 6-16 and between the bulk reservoir and the center of the nanotube calculated using the BAR method (Figures 6-15) simulations are equivalent. The free energy difference is lower for the sodium cation as compared to the chloride anion in all cases as the nanotube prefers ions with a smaller solvated equivalent volume; this selectivity can be expected to increase with solution dilution. The difference in the excess free energy between bulk and confinement for cations and anions decreases as a function of tube diameter and becomes very small for the 3 nm diameter nanotube. There is a steep rise in the PMF profile at the entrance of the tube indicating an energetic penalty for an ion to partition from the bulk reservoir to the CNT. We also observe that the PMF profile of the translocating ion inside the CNT remains rather flat with small fluctuations. Thus the diffusion coefficient must vary very little with the position of the ion in the tube and must be equivalent to the average diffusion coefficient that we have calculated from the mean-squared displacement data. We have also shown the diameter dependence of the flux from the MD simulations and energy barrier from the BAR

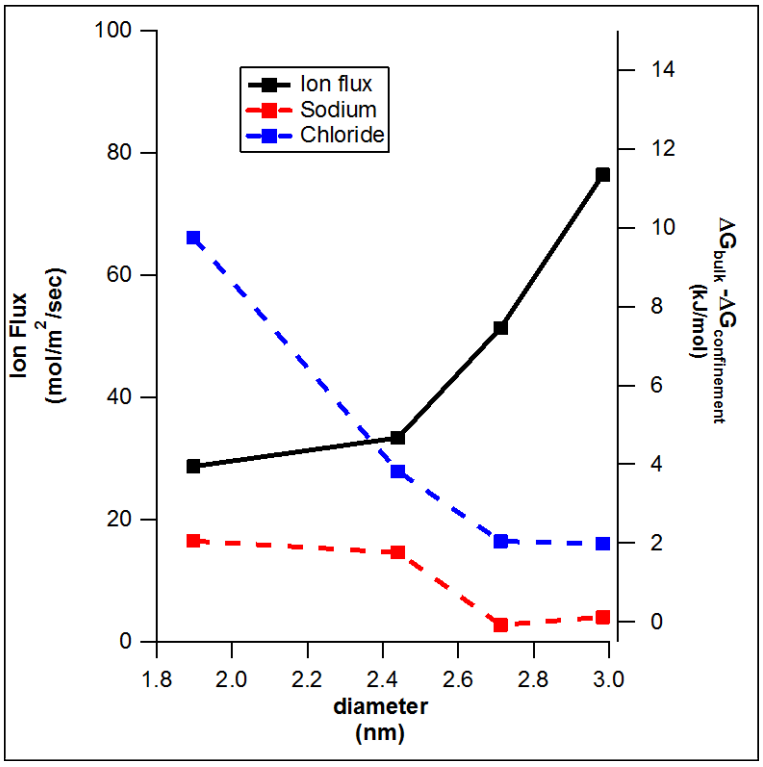

Figure 6-17: Comparison of ionic fluxes and energy barrier height vs. CNT diameter.

method, as displayed in Figure 6-17.

The single-ion PMF and the free energy perturbation calculation in a dilute environment provide a simplistic description of the energy barrier to transport that neglects the possibility of other ions being present in the tube, as well as their corresponding interactions. Increasing the external solution concentration should reduce these energy barriers (which are mostly steric in nature) to single-ion transport by providing a higher driving force for the ions to occupy the CNT volume. For a 1 M sodium-chloride solution, the electrochemical driving force provided by the concentration gradient is roughly estimated as -13 kJ/mol ($\Delta G = -RT \ln C_s$ = -13 kJ/mol). This should provide a sufficient driving force for sodium and chloride ions to permeate through the CNT with tube diameters greater than 1.89 nm (see Figure 6-15).

A more accurate representation of the energy barrier requires the inclusion of all interactions between ions that may be present in the system. The problem of single-ion PMFs is evident in the observation for the concentration gradient-driven ion fluxes for 2-3 nm diameter CNTs where we observe the ions travel in pairs maintaining local electroneutrality whenever possible. Indeed, even though the barriers for individual sodium and chloride ions are different, we do not witness any selectivity in the cases that we examined. Selectivity in uncharged pores is dominated by steric interactions and requires a higher degree of confinement and dilution to differentiate between ions based on their size and the binding energies of their hydration shells.

The Table 6-5 presents rough estimates of the transport-related quantities derived from the energy profiles of translocating ions (single ion PMF profiles). The quantities are calculated using equations (2.60), (2.61), (2.62) and (2.63). In calculating these values, the diffusion coefficient inside the CNT and the height of the energy barrier along the z-axis is considered to be constant.

6.4.5 Radial distribution functions and coordination shells

A major contributing factor to the energy barriers for ion transport is the modification of the hydration shells of the various ions. To examine these, we show the structure of the ions in bulk and under confinement through the ion-water radial distribution function in Figures 6-18 to 6-20. The radius of the first hydration shell can be obtained from the position of the first peak; Figure 6-20 shows very little change in the position of the radius of the first hydration shell in bulk and under confinement for both ions. From the narrower distribution of the first peak for the sodium-water radial distribution function (RDF) in both bulk and under confinement, it is apparent that the sodium-water bond is stronger than the chloride-water bond in their respective first hydration shells. In bulk, sodium has two and chloride has three visible peaks, which indicate the

Table 6-5: Quantities derived from the energy profiles

Sodium ion							
CNT (R,R)	**Diameter (nm)**	**Length (nm)**	**Diffusion coefficient X 10^{-9} (m^2/sec)**	**Permeability coefficients (m/s)**	**Partition coefficients**	**Maximum conductance (pS)**	**Specific conductance X 10^8 S/m^2**
10,10	1.35	5	0.65	0.017	0.09	161	0.437
14,14	1.9	5	0.65	0.067	0.45	161	2.51
18,18	2.2	5	0.75	0.067	0.45	185	2.51
20,20	2.6	5	0.70	0.14	1	173	5.21
22,22	3.0	5	0.85	0.17	1	210	6.33
Chloride ion							
CNT (R,R)	**Diameter (nm)**	**Length (nm)**	**Diffusion coefficient X 10^{-9} (m^2/sec)**	**Permeability coefficients (m/s)**	**Partition coefficients**	**Maximum conductance (pS)**	**Specific conductance X 10^8 S/m^2**
10,10	1.35	5	0.65	0.000043	0.00033	161	0.00159
14,14	1.9	5	0.65	0.00236	0.018	161	0.088
18,18	2.2	5	0.85	0.028	0.165	210	1.04
20,20	2.6	5	0.80	0.048	0.3	198	1.79
22,22	3.0	5	0.85	0.062	0.367	210	2.32

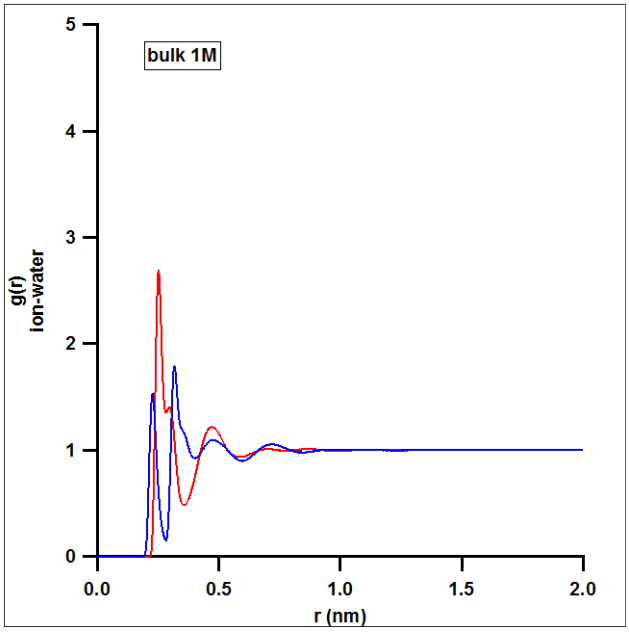

Figure 6-18: Sodium-water (red) and chloride-water (blue) radial distributions in bulk.

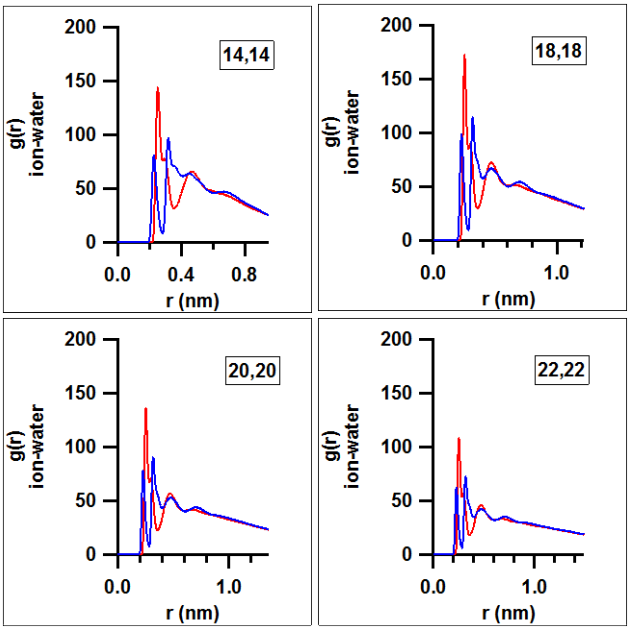

Figure 6-19: Sodium-water (red) and chloride-water (blue) radial distributions within the nanotubes (for comparison of peak heights).

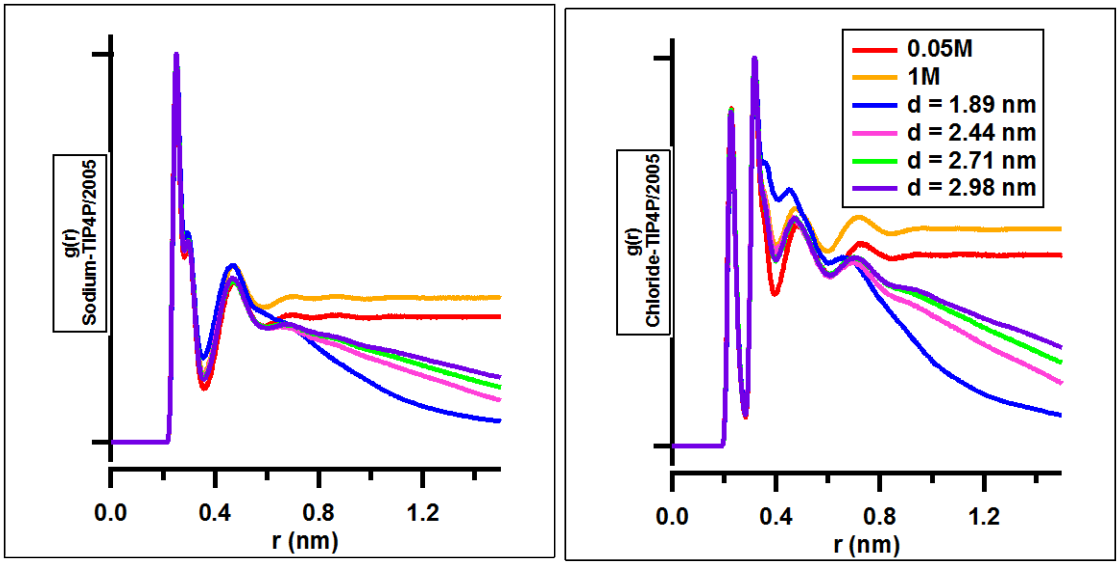

Figure 6-20: Ion–water distribution coefficients in bulk and under confinement (for comparison of peak positions).

number of hydration shells. Under confinement, the number of hydration shells for sodium remains more or less constant. The height of the sodium-water peak in the first hydration shell decreases from the smallest diameter tube to the largest diameter tube, which suggests a greater interaction and tighter distribution of water around sodium in the smallest diameter tube as compared to larger CNTs (see Figure 6-19). In chloride, the second and third peaks are barely discernible in the (14,14) CNT and gradually appear as diameter is increased. The third peak for chloride under confinement is shifted to the left and has much lower height as compared to bulk case. This RDF data imply that the structure of chloride under confinement is more severely affected relative to that of sodium.

Figure 6-21 shows the RDF of the water and ions around the CNT as a function of the distance from the CNT axis. There is clearly a higher degree of ordering of water and ions in the smallest diameter tubes as compared to that in the larger diameter tubes, where the layering is more

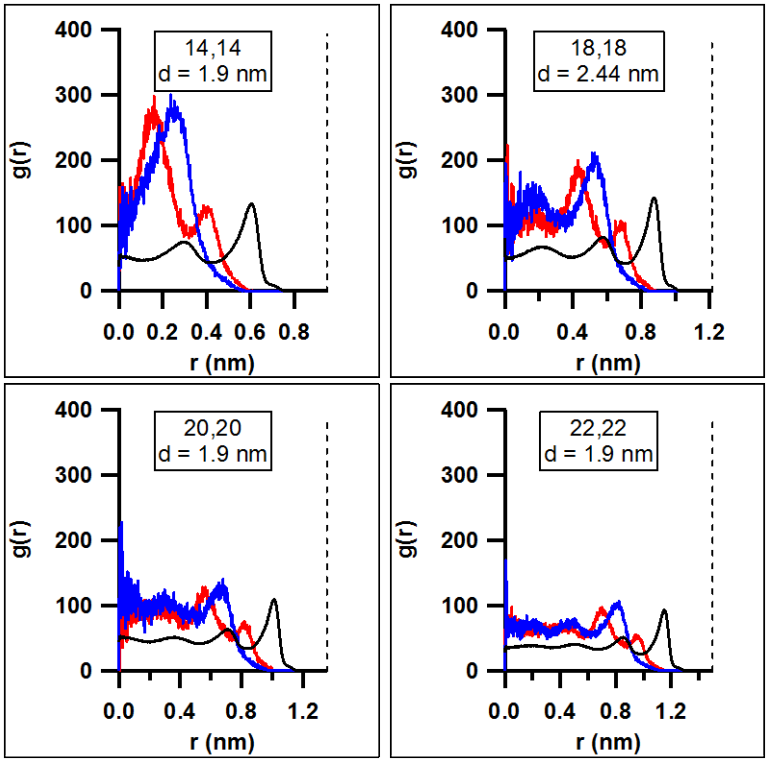

Figure 6-21: Radial distribution functions of the ions and water with respect to the *z*-axis of the CNT. The dotted lines designate the CNT wall position and the origin of the abscissa corresponds to the center of the nanotube.

prominent near the CNT walls and resembles a more bulk-like distribution at the center. This layering of sodium and chloride ions implies that not all locations inside the CNT are equally available to the ions and that some positions are more favored as compared to others. This might be an important factor that leads to a lower average occupancy inside the CNT and contributes to a lower partition coefficient.

The solvation shell coordination numbers are determined by integrating the radial distribution function to the corresponding minima of the radial distribution profiles of the water and ions. This is similar to counting the number of water molecules in each of the hydration shells. The results for the coordination numbers in each of the shells obtained are shown in Figure 6-22.

The first hydration shells for both anions and cations remains more or less intact for the CNT diameters studied. It is the second shell for sodium ions and the second and third shells for chloride ions that show a much greater degree of modification from their bulk values. This modification of the hydration shell under confinement has consequences for the hydration energy of the ions under confinement, which affects the transport rate.

The atomistic model employed herein neglects polarizability; non-polarizable models are known to over-structure the solvent[204]. This can lead to a lower molar distribution coefficient (lower partition coefficient), and hence a lower flux obtained in MD simulations. It would be very interesting to compare experimental flux results for similar diameter CNTs with the MD results to understand to what extent these force-fields can give accurate quantitative predictions of diffusive transport phenomena.

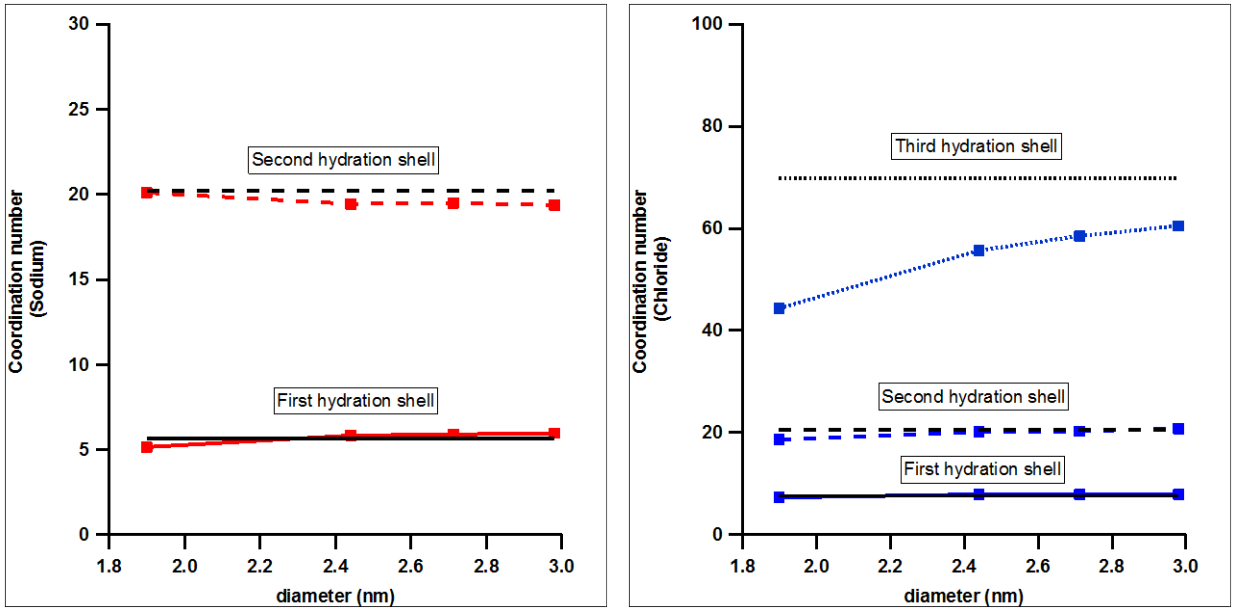

Figure 6-22: Coordination numbers of sodium and chloride ions in bulk and under confinement. Sodium ions (red), chloride ions (blue), and bulk hydration values of ions (black) of the respective hydration shells are represented by the dotted and dashed lines.

6.4.6 Ion residence times

Figure 6-23 shows the residence times for 1.9 nm, 2.4 nm, 2.7 nm, and 3 nm pores. The residence time was computed by counting the time an ion spends inside the nanotube within a time interval of 25 ns. When an ion left the interior of the nanotube and then returned, it was counted as a separate particle. The frequency of ions entering the pores for less than 200 ps is very high. There is no observance of residence time of one type of ion being longer than the other, thus showing no selectivity in transport. When it comes to short-lived particles, the frequency of sodium ions entering the narrow nanotubes is greater than that of the chloride ions; this expected since the

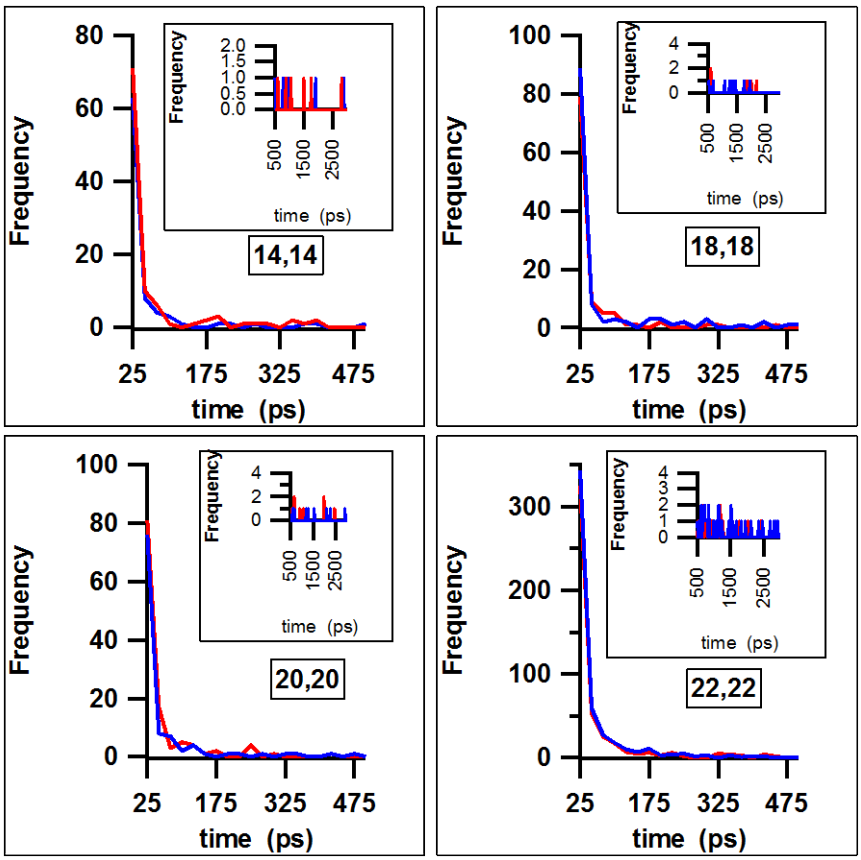

Figure 6-23: Ion residence times in the CNTs. The insets show plots for particles with long residence times in the corresponding nanotubes.

degree of modification of the first and subsequent hydration shells of sodium ions is less than that of chloride ions. This trend slowly changes as a greater number of chloride ions are seen to enter the larger diameter tubes (as compared to sodium ions) since the anion with the looser hydration shell can enter the tube more frequently. Thus, under a greater degree of confinement, one may expect to observe some selectivity for sodium over chloride.

6.4.7 Ion pairing

The lower than bulk liquid density and low dielectric causes ions to interact quite strongly with each other under confinement forming long-lived ion pairs as compared to bulk solutions, which diminishes the diffusion potential. These ion pairs are sometimes also called salt-bridges. Some instances of ions pairing are shown in the Figure 6-24, where one can see that, even under confinement, electroneutrality is maintained. From the trajectories for larger diameter tubes, we can see that the ion pairs are not constant, but that the ions exchange counter-ion partners several times under confinement. In the future, it would be interesting to study probability distribution of contact and solvent separated ion-pairs, the dynamic behavior of the exchanges between solvent separated and contact ion pairs, and the stability of these ion pairs under varying degrees of confinement.

6.4.8 Hydrogen bonding

Since solution dynamics are known to be affected by hydrogen bonding, we examined the extent of modification of the hydrogen bonds in aqueous solutions under confinement. Ions generally are disruptive to the water structure, which can be seen in the lowering of the average number of hydrogen bonds in bulk 1 M NaCl solution as compared to bulk TIP4P/2005 water.

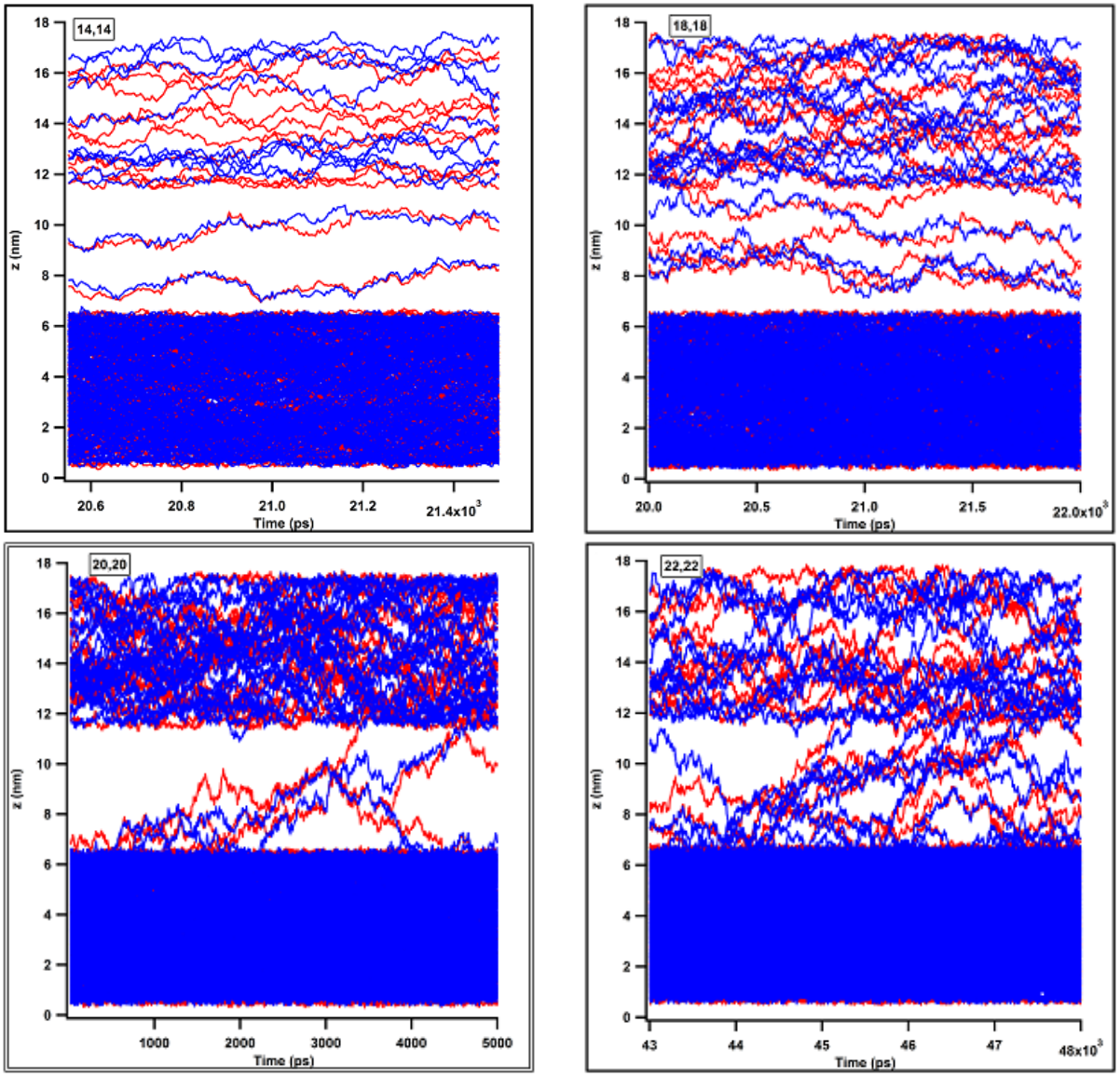

Figure 6-24: Instances of ion pairing/ ion clustering in uncharged CNTs.

Confinement of water in nanotubes is known to decrease the number of hydrogen bonds of the water molecules; confinement of water with ions further destroys the hydrogen-bond structure. However, the change in the number of hydrogen bonds with and without ions under confinement becomes less dramatic for the largest diameter tubes as compared to narrower tubes. This makes sense because in the smallest diameter CNT a significant amount of water is present in the form of hydration-shell water which augments the structure breaking effect induced by the ions. Whereas in the larger diameter tubes, the water in the hydration shell makes up a smaller fraction of the total water in the tube, thereby allowing the water structure to stay more or less intact with or without ions. These trends for hydrogen bonding are seen in Figure 6-25.

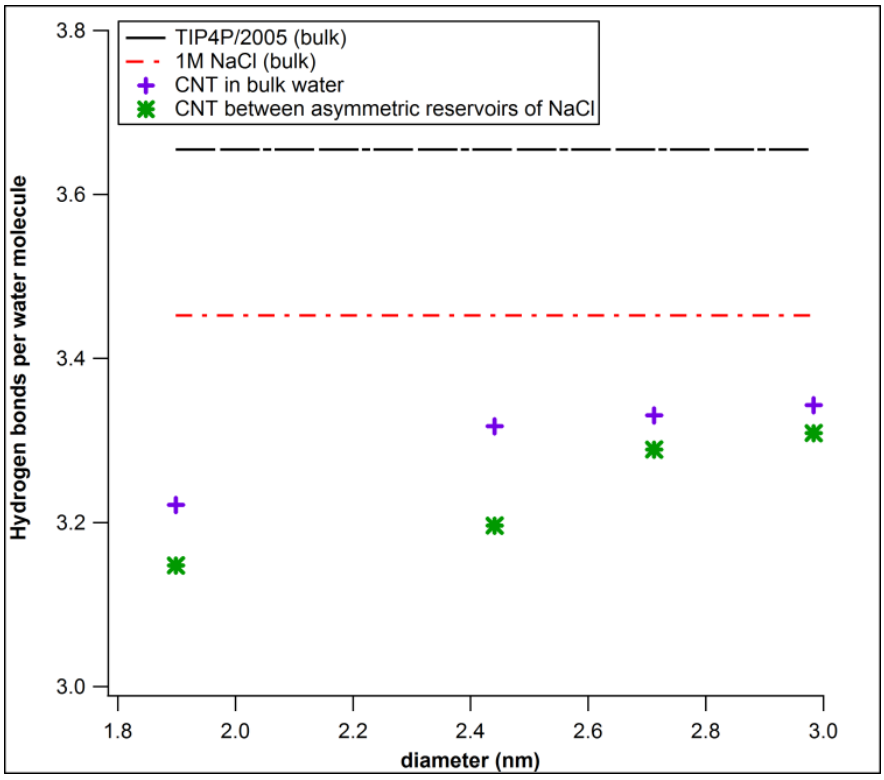

Figure 6-25: Hydrogen bond modification as a function of CNT diameter.

6.5 Conclusions

Understanding the nature of species transport through anisotropic media is of significant importance to the development of novel nanoscale fluidic devices, such as molecular filters, sensors, drug delivery systems, and other similar applications. Using 100s of nanoseconds of fully atomistic molecular dynamics simulations, we studied the steady-state fluxes of Na^+ and Cl^- ions through uncharged carbon nanotubes with diameters in the range of 2-3 nm in contact with two reservoirs, one of which contains high concentration sodium-chloride solution while the other contains pure solvent (i.e. water). By neglecting any electrical forces, we have compared the flux from Fick's diffusion equation with the results of rigorous MD simulations and have assessed the validity of continuum dynamics approach in describing transport in these nanopores.

Under confinement, we observed a much lower actual ionic flux when compared to the theoretical calculations, and these fluxes show progressively decreasing behavior as confinement increases whereas the free energy barrier relative to bulk water displays an increasing trend with greater degree of confinement. We reconcile the apparent discrepancy between the theoretical flux and that obtained from the simulations in terms of modified diffusion coefficients of the ions within the CNT, the concentration of the electrolyte at the tube entrance, and the energetic barriers present at the tube entrance, which collectively control and affect the overall rate of the transport process. We have thus found that continuum equations are valid for describing sodium and chloride ionic flux under a high concentration gradient through wide tubes of 3 nm diameter and above if one takes into account the modification of the diffusion coefficient in the membranes and the applicable partitioning coefficients. The saturation of ions in the nanotube, ion residence time, modification of the ionic hydration shell, coupling between ions, and the effect of ion pairing were also discussed in this chapter.

Chapter 7. A molecular dynamics study of electrolyte exclusion in charged carbon nanotubes via steric and electrostatic interactions: A comparison with Donnan theory

7.1 Introduction

Experimental and simulation studies[24] have shown that carbon nanotubes (CNTs) can permit high water fluxes through their hydrophobic cores at rates similar to those of ions channels[23] while maintaining ion selectivity via the incorporation of functional groups[121]. High water flux and salt rejection are essential features of nanofiltration and reverse osmosis membranes, which make the possible use of carbon nanotubes extremely attractive in this field. Ion exclusion in nanotubes is a function of steric hindrance, electrostatic exclusion, and dielectric exclusion; however, suitable empirical equations that connect these factors as functions of experimentally observable physical factors are lacking and hence quantitative predictions of ion exclusion are a challenge. In some cases, continuum theory may provides a sufficient constitutive equation to describe the relevant transport phenomena; for instance, some studies suggest that the Navier-Stokes equation gives a sufficient description of transport of water for confinements above 1 nm in dimension, provided that one uses the slip-modified boundary conditions[177]. In a similar manner, Daiguji[176] suggested that ion transport for confinements above 5 nm may also be described by continuum dynamics. Carbon nanotubes provide a simple model system wherein some of the simplifications of continuum theory, such as uniform charge distribution and uniform cross section, can be easily satisfied and hence can be used for testing the limits of validity of macroscopic equations when applied to nanometer-sized pores using long timescale molecular dynamics (MD) simulations. Long MD simulations of geometrically simple nanotubes helps us

obtain a tangible understanding of the ion exclusion mechanism in CNTs, which allows us to analyze the source of the differences in results obtained between continuum approaches and atomistic simulation results. This source of deviation between continuum and molecular dynamics approaches is the missing link to the development of robust empirical approaches and models required to predict transport phenomena at the nanoscale in many nano-confined systems.

A major component of the solution to ion transport equations in continuum theory is the distribution of ions and electric potential. In previous studies, Fornasiero et. al.[51] suggested a Donnan-type exclusion mechanism (a thermodynamic theory) to qualitatively describe ion exclusion in sub-2 nm functionalized nanotubes. The Donnan potential is a static potential that can arise from fixed-charges on the membrane, and the force with which the Donnan potential acts on an ion is proportional to the ionic charge. The absolute value of this force increases with dilution of the solution and with increasing molality of the fixed-charges. For a better understanding of ion equilibria in charged membranes, one can refer to some excellent texts that provide a most thorough discussion of the theory, models, and their underlying assumptions[189-191,205]. In this study, we provide a quantitative comparison of the co-ion concentration predicted by ideal Donnan theory to the results of MD simulation for different pore sizes and fixed-charge concentrations at a high external solution concentration.

Donnan theory provides the co-ion concentration in the charged pore in terms of very few factors: the fixed-charge concentration, the valences of the ions involved, and the external solution concentration. It neglects pore geometry, ion specificity, and ion partitioning owing to steric effects. The equations of a theory can reflect the effects of only those properties with which the model has been equipped[190]. In this spirit, we proceed to assess the usefulness and realism of the

ion exclusion description using Donnan theory at the nanoscale where the discreteness of the molecules and their correlations are unmistakable.

7.2 Theory

Donnan equilibrium occurs in perm-selective membranes that pose a restriction to the passage of one or several ionic species. This restriction or perm-selectivity might be a consequence of steric effects, where one of the ionic species may be of colloidal size, or due to the presence of charges. The fixed-charges may arise due to ionization of functional groups or as a result of adsorption of ions of external origin when the membrane is immersed in an electrolyte solution. Donnan theory describes the ion concentration inside such a semipermeable membrane that is in thermodynamic equilibrium with its external solution. We want to investigate whether the co-ion concentration or the excess salt concentration in charged CNTs that is obtained using an approximate theory like Donnan theory (which is a result of a thermodynamic derivation that does not take into account the graininess of the system) is the same as that obtained from MD simulation.

Consider a charged membrane that is in equilibrium with an electrolyte solution such that the fixed-charges are distributed uniformly on the pores of the membrane. An electric potential difference is established between the membrane and the solution. For such a situation, Donnan equilibrium gives an expression for co-ion exclusion. Below, we present the formal derivation of the Donnan theory expression for predicting the co-ion concentration within the charged membrane.

Ignoring the partial molar volumes of the ions, the electrochemical potential (J/mol) for ionic species i in external bulk solution is given by

$$\bar{\mu}_i^{bulk} = \mu_i^0 + RTlnc_i^{bulk} + z_i N_A e\phi_{bulk} \tag{7.1}$$

$$\bar{\mu}_i^{bulk} = \mu_i^0 + RTlnc_i^{bulk} + z_i F\phi_{bulk} \quad (7.2)$$

For cations,

$$\bar{\mu}_+^{bulk} = \mu_+^0 + RTlnc_+^{bulk} + z_+ F\phi_{bulk} \quad (7.3)$$

whereas for anions,

$$\bar{\mu}_-^{bulk} = \mu_-^0 + RTlnc_-^{bulk} + z_- F\phi_{bulk} \quad (7.4)$$

μ_i^0 is the chemical potential in the standard state, z_i is the ion valence, c_i^{bulk} is the bulk concentration of ion i (mol/m^3), R is the gas constant (J/mol/K), T is the absolute temperature (K), ϕ_{bulk} is the electrostatic potential of the bulk phase, F is the Faraday constant (C/mol), N_A is the Avogadro constant, and e is the elementary charge. For simplicity we assume ideal solution.

In a similar fashion, the electrochemical potential for an ion in the membrane at any location x from the membrane wall is given by

$$\bar{\mu}_i^{mem} = \mu_i^0 + RTlnc_{i(x)}^{mem} + z_i F\phi(x) \quad (7.5)$$

For cations,

$$\bar{\mu}_+^{mem} = \mu_+^0 + RTlnc_{+(x)}^{mem} + z_+ F\phi(x) \quad (7.6)$$

and for anions

$$\bar{\mu}_-^{mem} = \mu_-^0 + RTlnc_{-(x)}^{mem} + z_- F\phi(x) \quad (7.7)$$

c_i^{mem} is the concentration of ion i in the membrane, $\phi(x)$ is the electrostatic potential in the membrane phase at location x from the membrane wall. If we subtract the electrochemical potential of the ion in the bulk phase from that in the membrane, we obtain the familiar Boltzmann relation:

$$c_{i(x)}^{mem} = c_i^{bulk} \exp \frac{(\bar{\mu}_i^{mem} - \bar{\mu}_i^{bulk} - (z_i F(\phi(x) - \phi_{bulk}))}{RT} \quad (7.8)$$

$$c_{i(x)}^{mem} = c_i^{bulk} \exp\left(\frac{(-\Delta\bar{\mu}_i^{ex} - z_i F\phi_{Don}(x))}{RT}\right) \quad (7.9)$$

$\Delta\bar{\mu}^{ex}$ is the difference in the excess chemical potential of ion i between the bulk phase and the membrane phase, $(\phi(x) - \phi_{bulk}) = \phi_{Don}(x)$ is the Donnan potential. At equilibrium, the electrochemical potential of each ion should be the same in both the membrane and the external solution,

$$\bar{\mu}_i^{mem} = \bar{\mu}_i^{bulk} \tag{7.10}$$

Thus,
$$\Delta\bar{\mu}_i^{ex} = 0 \tag{7.11}$$

$$c_{i(x)}^{mem} = c_i^{bulk} \exp\left(\frac{(-z_i F \phi_{Don}(x))}{RT}\right) \tag{7.12}$$

$$\phi_{Don}(x)) = (\phi(x) - \phi_{bulk}) = \frac{RT}{z_i F} ln(\frac{c_i^{bulk}}{c_{i(x)}^{mem}}) \tag{7.13}$$

For cations,

$$(\phi(x) - \phi_{bulk}) = \frac{RT}{z_+ F} ln(\frac{c_+^{bulk}}{c_{+(x)}^{mem}}) \tag{7.14}$$

and for anions,

$$(\phi(x) - \phi_{bulk}) = \frac{RT}{z_- F} ln(\frac{c_-^{bulk}}{c_{-(x)}^{mem}}) \tag{7.15}$$

Considering a monovalent salt such as NaCl, the expression for cations is given as,

for cations,

$$(\phi(x) - \phi_{bulk}) = \frac{RT}{F} ln(\frac{c_+^{bulk}}{c_{+(x)}^{mem}}) \tag{7.16}$$

and for anions,

$$(\phi(x) - \phi_{bulk}) = -\frac{RT}{F} ln\left(\frac{c_-^{bulk}}{c_{-(x)}^{mem}}\right) \tag{7.17}$$

Equating the right-hand sides,

$$\frac{RT}{F} ln\left(\frac{c_+^{bulk}}{c_{+(x)}^{mem}}\right) = -\frac{RT}{F} ln\left(\frac{c_-^{bulk}}{c_{-(x)}^{mem}}\right) \tag{7.18}$$

$$\left(\frac{c_{+}^{bulk}}{c_{+(x)}^{mem}}\right) = \left(\frac{c_{-(x)}^{mem}}{c_{-}^{bulk}}\right) \tag{7.19}$$

$$c_{+}^{bulk} \times c_{-}^{bulk} = c_{+(x)}^{mem} \times c_{-(x)}^{mem} \tag{7.20}$$

$$c_{+(x)}^{mem} = c_s^2 / c_{-(x)}^{mem} \tag{7.21}$$

Here c_s is the concentration of the external solution.

From the electroneutrality assumption in a charged membrane, we have,

$$\sum_i z_i c_i^{mem} + \alpha c_{fixed} = 0 \tag{7.22}$$

where α is the valence of the fixed-charge. For a univalent salt this becomes

$$c_{+(x)}^{mem} - c_{-(x)}^{mem} + \alpha c_{fixed} = 0 \tag{7.23}$$

For a positively-charged membrane with fixed-charge valency, α ='1',

$$c_{+(x)}^{mem} - c_{-(x)}^{mem} + c_{fixed} = 0 \tag{7.24}$$

$$c_{+(x)}^{mem} + c_{fixed} = c_{-(x)}^{mem} \tag{7.25}$$

Substituting for $c_{-(x)}^{mem}$ from Eq. (21), the co-ion concentration is provided and solving for co-ion $c_{+(x)}^{mem}$,

$$c_{+(x)}^{mem} - \frac{c_s^2}{c_{+(x)}^{mem}} + c_{fixed} = 0 \tag{7.26}$$

$$(c_{+(x)}^{mem})^2 + c_{fixed} \cdot c_{+(x)}^{mem} - c_s^2 = 0 \tag{7.27}$$

Solving the quadratic equation, we obtain

$$c_{+(x)}^{mem} = \frac{1}{2}\left(\sqrt{(c_{fixed}^2 + 4c_s^2)} - c_{fixed}\right) \tag{7.28}$$

We can arrive at a similar expression for the co-ion concentration using negative fixed-charges, and thus we can generalize the expression for a monovalent salt as

$$c_{co-ion(x)}^{mem} = \frac{1}{2}\left(\sqrt{(c_{fixed}^2 + 4c_s^2)} - c_{fixed}\right) \tag{7.29}$$

Further, assuming a uniform distribution of ions and potential, taking the mean field approach, the ion concentration can be given by an average concentration and the potential replaced by an average potential at any location. This is a good assumption in cases where the Debye length is comparable to the pore size.

For a more rigorous treatment, the external solution concentration can be replaced by the thermodynamic activities ($a_{\mp} = \gamma_{\mp} c_{\mp}$). Here, $\gamma_{\mp}$ is the activity coefficient and these values are well-known for common electrolytes. Given just the external salt concentration and the immobile charge concentration, this simple expression provides the equilibrium co-ion concentration within the charged membrane without requiring a description of the properties of the membrane. The Donnan exclusion that arises because of the Donnan potential refers to the exclusion of co-ions that have the same electrical charge as that of the fixed-charge and the preferential adsorption of the counter-ions that have the opposite electrical charge. This theory does not take into account the size of the ions or their specific nature.

7.3 Computational methods

System details

The system consisted of a CNT embedded between two reservoirs containing solutions of equimolar concentrations (1 M) of a strong electrolyte sodium-chloride solution. The reservoirs were bounded by graphene sheets. The CNT diameters were 1.356 nm (10,10), 1.9 nm (14,14) and 3 nm (22,22). The 5 nm long CNTs were taken from separate NPT simulations (1 bar, 300 K) wherein water spontaneously entered the nanotubes enabling the water in the tube to attain its natural density. The reservoirs contain pre-equilibrated water at 1 bar and 300 K. The salt concentration of 1 M in the reservoirs was attained by replacing the requisite number of water molecules with the appropriate number of ions. Each reservoir thus contained about 11,000 water

molecules, 208 sodium ions, and 208 chloride ions. Every CNT atom bore a partial negative charge (which sometimes is referred to as a "smeared charge"), and the fixed-charge concentrations were calculated on the basis of the volume available to the solution; i.e., excluding the free volume of the shell neighboring the inner wall of the CNT due to the hydrophobicity of the carbon atoms. The negatively-charged carbon nanotube in this case behaves like a cation exchanger. To maintain overall electroneutrality, a number of chloride ions equal to the fixed-charge on the CNT were deleted. We also ran additional simulations of an uncharged CNT connecting 1 M sodium-chloride solutions as controls. The number of charges on the CNT in terms of the fixed-charge concentrations (mol/lit) and surface-charge densities (C/m^2) are summarized in Table 7-1. The system dimensions were 7.30 nm X 7.30 nm X 18 nm. An illustration of the simulation system is provided in Figure 7-1. Figure 7-2 shows the average axial density profiles of ions and water for uncharged CNTs that were obtained from the last 30 ns of the simulation duration. In the case of

Table 7-1: Charge density on the CNT in the various simulation runs.

CNT	**Fixed-charge**			
	0 M	**0.35 M**	**1 M**	**2 M**
	C/m^2	**C/m^2**	**C/m^2**	**C/m^2**
(10,10) $d = 1.36$ nm	0	0.007 (-1e)	0.015 (-3e)	0.030 (-5e)
(14,14) $d = 1.90$ nm	0	0.010 (-2e)	0.020 (-5e)	0.060 (-12e)
(22,22) $d = 2.98$ nm	0	0.010 (-5e)	0.050 (-15e)	0.100 (-30e)

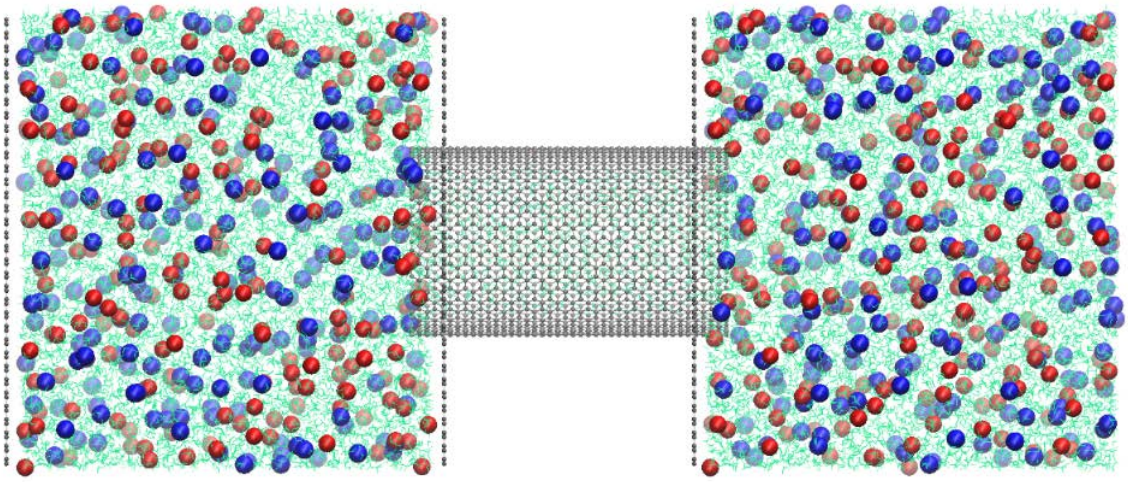

Reservoir 1 (1 M NaCl) **Reservoir 2 (1 M NaCl)**

Figure 7-1: Illustration of the simulation system for the (22,22) CNT. Sodium ions are colored red, chloride ions are blue, water molecules are green, and carbon atoms are black.

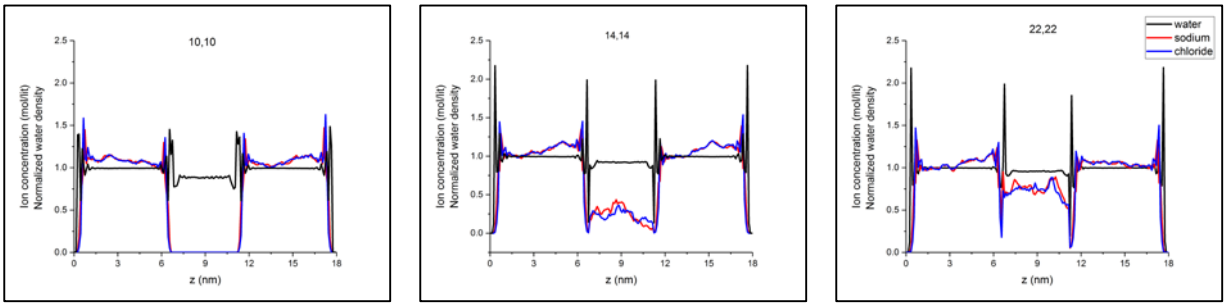

Figure 7-2: Equilibrium axial density profiles of water molecules (black), sodium ions (red) and chloride ions (blue) in the case of uncharged nanotubes after an initial equilibration time.

uncharged CNTs, no selectivity for cations or anions was observed and exclusion occurs due to both steric and ion solvation effects.

The carbon nanotube with the graphene sheets form a rigid structure and the internal volume of the CNT is fixed. Contrary to ion exchange resins and similar to zeolites, no swelling can occur in the nanotube. Water assumes a layered appearance under confinement and the amount of solvent that the nanotube can hold depends on the available internal volume; hence the number of water molecules and the density of water within the CNT increases with increasing diameter and gradually approaches the bulk density in the largest diameter tube, as can be seen in Figure 7-2.

7.4 Simulations method

The different pore sizes and different fixed-charge concentrations resulted in nine simulations runs of 60 ns. Additional simulation runs for the same duration were also performed for the case of the CNT with no charges. We used the TIP4P/2005 model to represent water. The parameters used in the simulation are from the OPLS –AA force-field; they are summarized in Table 7-2. The carbon atoms of the CNT and graphene sheets were held fixed during the course of the simulation using a harmonic restraining potential with a force constant of 10,000 kJ/mol/nm^2 to restrict their translational and rotational motion. The LINCS algorithm was used to keep the water molecules rigid, thereby allowing for longer integration time steps. The Lennard-Jones parameters of cross interactions were calculated on the basis of the geometric mean for both σ and ϵ. Periodic boundary conditions were applied in all three directions. Particle Mesh Ewald Summation was used for electrostatics in 3D periodic systems and the non-bonded interactions were truncated at a distance of 1.2 nm. Energy minimization by the steepest descent method was

Table 7-2: Parameters used in the simulations.

Atom type (i)	σ_{ii} (nm)	ϵ_{ii} (kJ/mol)	Charge (q)
Ion			
Na^+	0.3304	0.016	+1
Cl^-	0.4417	0.4928	-1
Nanotube and walls			
C	0.355	0.2929	(Fixed-charge dependent, refer to Table 7-1)
Water model (TIP4P/2005)			
O	0.3159	0.7749	0
H	0	0	0.5564
M	0	0	-1.1128
$d_{OH} = 0.09572$ nm, $d_{OM} = 0.01546$, $\angle$HOH = 104.52			

carried out to remove any unphysical overlaps between atoms. The initial velocities of the atoms were assigned according to a Maxwell distribution at a temperature of 300 K with a random seed generator, and the system was then equilibrated in an NVT ensemble at 300 K by coupling to a v-rescale thermostat with a coupling constant of 5 ps for 1 ns. Once the target temperature was attained, all simulation runs were performed for 60 ns each for accumulation of statistics, with the required analytics performed on only the final 30 ns of the total data collected. The simulations were carried out using GROMACS MD package in the NVT ensemble with the v-rescale thermostat, a leap frog (Verlet) integrator, and a time step of 1 fs.

7.5 Results and discussion

Before we delve into a comparison of the equilibrium co-ion concentration in charged nanotubes obtained via MD and Donnan theory, it would be informative to understand the position-dependent concentration of ions and the potential distribution inside the nanotube that dictate the extent to which ion uptake is affected by electrostatics at a given set of conditions of confinement, nanotube fixed-charge, and external solution concentrations. To accomplish this, we provide a comparison of the structure of ions near a charged surface revealed by the well-known macroscopic model (i.e., the Gouy-Chapman theory) and that obtained from molecular dynamics simulations of ions under varying degrees of confinement and fixed-charge in the nanotubes.

7.5.1 Ion concentration distribution in charged CNTs: Continuum theory and MD

Figures 7-3 show the concentration profiles and potential distributions according to the predictions of the Gouy–Chapman theory, which was calculated by assuming an effective point charge equal to the charge on the tube. Figures 7-4 show the ion distributions for various cases of fixed-charge concentrations and pore diameters calculated from the equilibrium MD simulation. In the Gouy-Chapman model, the electrostatic potential as a function of distance from the point charge source is given as

$$\emptyset(r) = \frac{q}{4\pi\varepsilon_0\varepsilon r}.e^{-r/\lambda_D} \tag{7.30}$$

and the ion concentrations are calculated as

$$C_r^{\pm} = C_{bulk}^{\pm}.e^{-z_{\pm}\emptyset(r)F/RT} \tag{7.31}$$

$\emptyset$ is the mean electrostatic potential detected at position r (m) from the charge (V), q is the charge (C), λ_D is the Debye length (m), ε_0 is the permittivity of vacuum (F/m), ε is the relative permittivity, $C_{bulk}^{\pm}$ is the bulk concentration of the cation or anion (mol/m^3), $C_r^{\pm}$ is the local

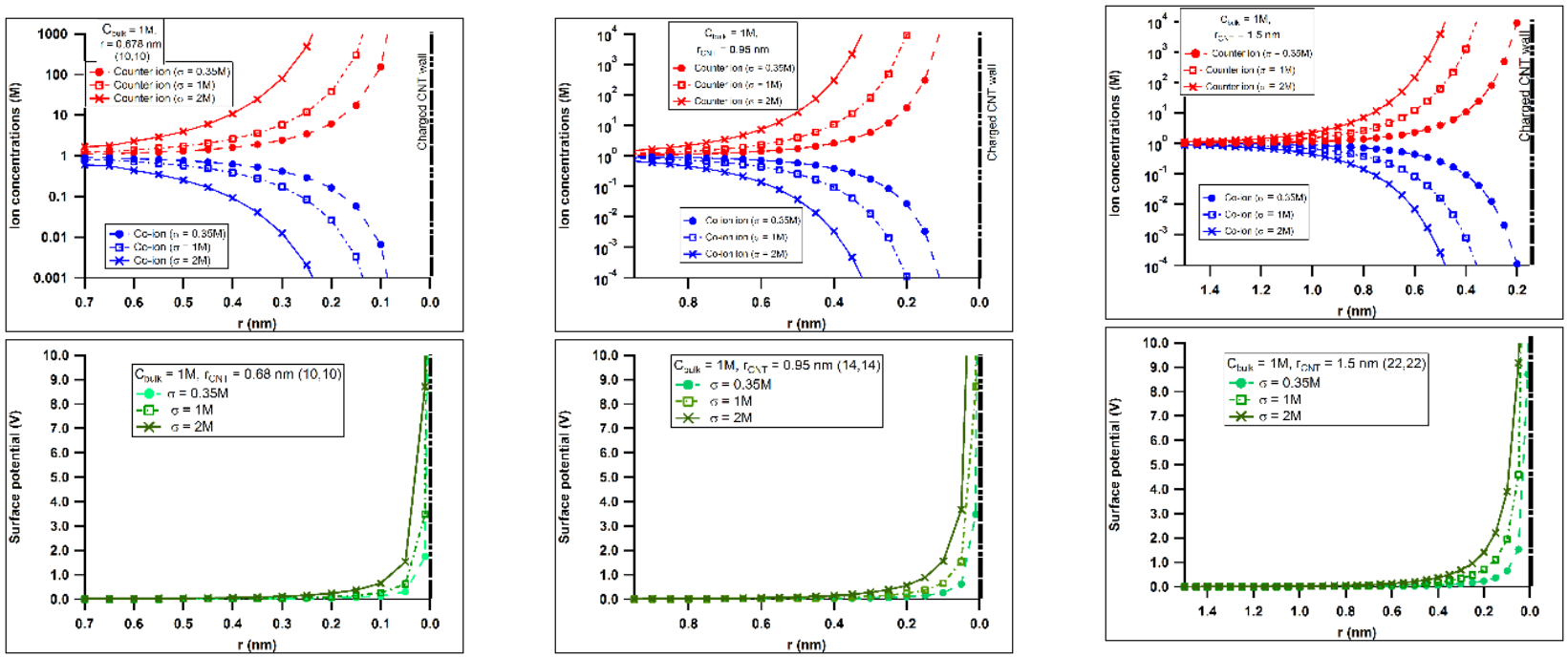

(a) (b) (c)

Figure 7-3: Local concentration of ions and the mean electrostatic potential from a charged surface from Gouy-Chapman theory.

The local concentrations of counter-ions and co-ions adjacent to a point source of charge according to the Boltzmann distribution (top panels) and the mean electrostatic potential as a function of distance *r* from a point charge source (bottom panels) according to the Gouy-Chapman theory in the absence of finite size effects. The point charge source coincides with the origin of the *x*-axis as designated by the dotted black line. The external solution concentration in all cases is 1M (Debye length, λ_D=0.3nm). In Figure 7a, the point charge *q* = -1e$^-$, -3e$^-$, -5e$^-$ and corresponds to the fixed-charge cases of 0.35 M, 1 M, and 2 M similar to the cases simulated for the (10,10) CNT. In Figure 7b, the point charge *q* = -2e$^-$, -5e$^-$, -12e$^-$ and corresponds to the fixed-charge cases of 0.35 M, 1 M, and 2 M similar to the cases simulated for the (14,14) CNT. In Figure 7c, the point charge *q* = -5e$^-$, -15e$^-$, -30e$^-$ and corresponds to the fixed-charge cases of 0.35 M, 1 M, and 2 M similar to the cases simulated for the (22,22) CN

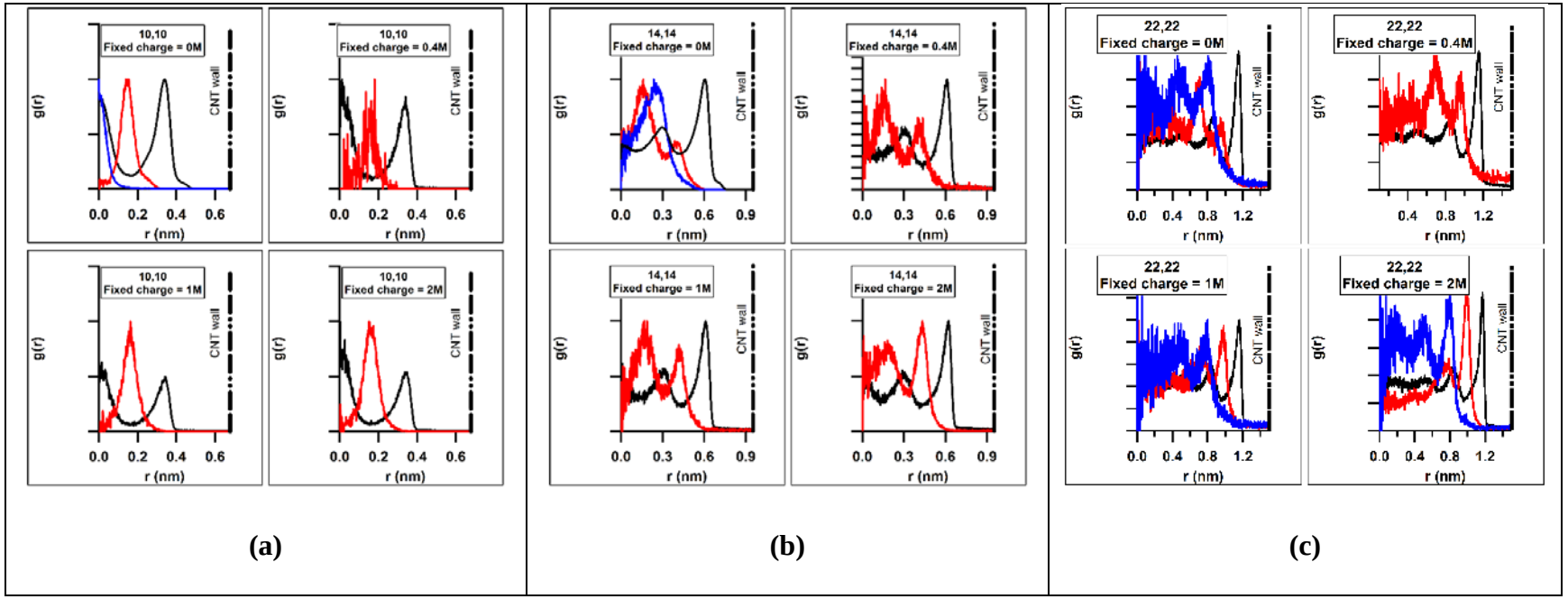

Figure 7-4: The non-smoothed radial distribution profiles of water and ions with respect to the *z*-axis of the nanotubes: (10,10), (14,14), and (22,22). The origin of the *x*-axis corresponds to the center of nanotube and the CNT walls are denoted by the dotted black lines. The RDF profiles are normalized by their maximum values. The sodium ion distribution is marked in red, the chloride ion distribution in blue, and the water RDF is black.

concentration of cation or anion at distance r from the from the charge (mol/m^3), $z_{\pm}$ is the valence of the cation or anion, F is the Faraday constant (C/mol), R is the gas constant (J/mol.K), and T is the absolute temperature (K). A comparison of Figures 7-3 and Figures 7-4 immediately shows that the packing of ions in charged CNTs deviates markedly from the predictions of Gouy-Chapman theory. In Figures7-3, we observe a smooth variation of the concentration from infinitely high concentration of cations at the negatively-charged wall to a concentration approaching bulk values for both cations and anions at the center of the largest diameter tube. For the various degrees of confinement (d =1.355 nm, 1.9 nm, and 3 nm), fixed-charge concentration (0.35 M, 1 M, and 2 M), and the external solution concentration (Cs =1 M) under consideration, the trend for counter-ion enrichment and co-ion depletion from the charge, which is also known as the electric double layer, is seen to exist at a distance of several times the Debye length. For the narrowest tube (10,10), the diffuse double layer persists into the center of the tube for all fixed-charge concentrations, which implies overlapping space-charge regions in this case. While the thickness of the electric double layer is several times the Debye length (0.30 nm) from the charged surface, the surface potential (as seen in the bottom panels) at a distance equal to the Debye length becomes a fraction of its value at the wall; more precisely, it becomes (1/e) times the potential at the charged wall.

A glimpse into the variation of the concentration of the ions in the nanotube and into the actual double-layer structure can be sought out through the radial distribution function (RDF) profiles of ions shown in Figures 7-4. While Gouy-chapman theory neglects the ion-ion correlations and has a smooth distribution showing counter-ion enrichment and co-ion depletion in the diffuse double layer, the effect of confinement leading to pronounced interactions with the carbon surface and ion-ion correlations is quite apparent from the RDF profiles of the ions in

nanotubes, which exhibit large oscillations in the density profiles. These correlations are quite strong under confinement for both charged and uncharged nanotubes, which is evident in the density fluctuations that continue to the center of the CNT. The magnitude of correlation-induced density fluctuations at the center of the tube increases with increasing degree of confinement, which can be seen in the decreasing density fluctuation at the center of the largest diameter tube (22,22) as compared to the smallest diameter tube (10,10).

RDF profiles in uncharged CNTs

Confinement and the specific interactions of the water and ions with the nanotube results in molecular restructuring close to the surface in a way that is very dissimilar to the bulk structure (see Figure 7-4a). The distance of closest approach of a molecule to the CNT surface depends on the degree of favorability of the interaction with the carbon surface atoms and the size of the approaching species. This difference in the interactions of water and ions with the carbon causes the distribution of water and ions close to the CNT wall to assume a layered arrangement with the water being closest to the CNT followed by the sodium and chloride ions. The bulk characteristics of water are regained at a distance of about 1 nm from the carbon surface; however, the fluctuations in densities persist for the charged ions owing to the long-range nature of the charged interactions. The number of peaks for sodium and chloride increase as the tube diameter increases, which corresponds to the fact that an increasing the number of ions can be accommodated in the larger diameters tubes. Ions prefer to be completely solvated; hence for sodium, if we compare the relative heights of the RDF peaks, the peak at the wall has a lower height compared to that of the second peak away from the wall (where sodium ion can be better solvated).

RDF profiles in charged CNTs

Increasing negative fixed-charge concentration results in a corresponding increase in the peak height for the sodium layer closest to the wall relative to the case when no charges are present on the tube (see Figure 7-4b-d). This effect is especially visible in the tubes that can accommodate more than one layer of sodium (in the (14,14) and (22,22) cases). The distance of closest approach to the charged CNT wall depends on the degree of favorability of the interaction with the carbon atoms of the CNT, size of the ion, and the charge density of the ion. Thus we can expect that a smaller sized, multivalent ion, or an ion with weak hydration shell would approach the charged CNT surface more closely. The result of the interaction of the ions with the smeared charges on the CNT wall is that the compact layer of the Gouy-chapman theory is missing and all we have is a diffuse double layer. Having discrete charges instead of smeared charges on the CNT wall may potentially modify the structure of the double layer by including a more compact layer of counter-ions near the charged CNT surface. We also observe that the cation enrichment in the first layer closest to the CNT wall is accompanied by a consistent depletion of water near the charged CNT. This can be witnessed in the marked reduction in the height of the peak representing the water concentration closest to the wall in the smallest diameter tube as the water is squeezed out from the layer closest to the wall to accommodate sodium counter-ions to balance the negative charge on the CNT. There is no obvious reduction in the height of the water peak closest to the charged wall in the two largest diameter CNTs; however, there is a narrowing of the water peak closest to the wall. The relative increase in the peak height of the second water layer in the larger diameter tubes also points to a loss of water in the layer closest to the wall as compared to the scenario of uncharged nanotubes. Very little useful information is obtained from the RDF profiles of the chloride anions in the charged tubes since their profiles resemble those of the uncharged CNTs.

Figures 7-5a-d provide the surface-charge densities of the nanotube and of the charge densities of ions in the monolayers adjacent to the wall for the case of the (22,22) CNT. This is equivalent to showing the integral capacitance at different inner core radii for the (22,22) CNT. Figures 4a-d have fixed-charges of 0 M, 0.35 M, 1 M, and 2 M, respectively, representing increasing surface potentials. In the case of the uncharged tube, the charge densities represent the ordering of ions according to their interactions under confinement, and the sums of the charge densities of both cations and anions are equal.

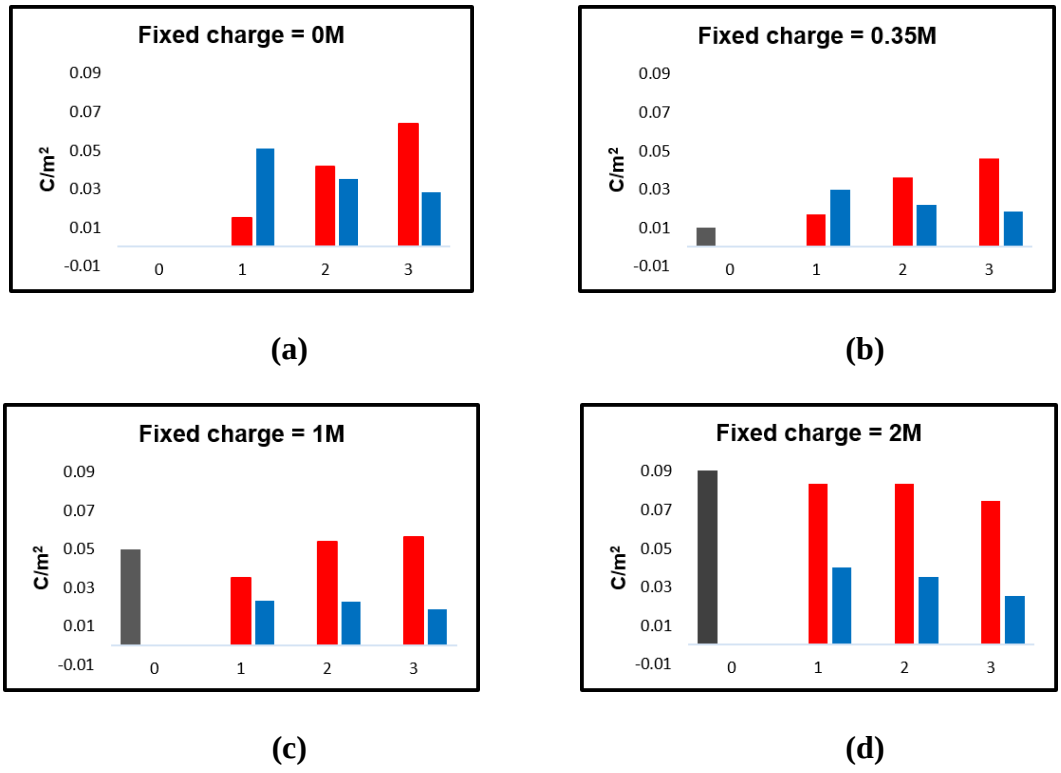

Figure 7-5: Charge density of the nanotube (per unit surface area) and the ions (per unit area of the cylindrical shell) in the 3 layers adjacent to the CNT surface in the (22,22) CNT at fixed-charge concentrations of 0 M (a), 0.35 M (b), 1 M (c), and 2 M (d). The magnitude of the fixed-charge density on the CNT (black), sodium counter-ion (red), and chloride co-ion (blue).

It is also evident that the ions retain their layered structure to the center of the tube, even in the largest diameter CNT. In the case of charged tubes, it is important to note that the field exerted by the surface potential decays to a small value at about 0.3 nm from the wall, which is the Debye length for the external solution concentration of 1 M. Thus most of the fixed-charge-ion interactions are screened at this distance, which makes the ions at the center of the tube follow a bulk-layered pattern. For the case with lowest fixed negative charge (0.35 M), the charge density at the wall, taken as the ratio of the charge to the surface area of the CNT, is clearly overcompensated by the adjacent layer of sodium counter-ions. This effect is sometimes called "overscreening"; we will follow a treatment demonstrated in planar electrodes by Fedorov et al.[206] to explain the phenomenon. The monolayer of counter-ions (0.6 nm away from the wall) thus possesses a net positive charge, which is in turn overcompensated by the next layer of chloride ions. The sum of the charge density of the first two layers of cations balances that of the anions in the first two layers and the charge on the wall, and at this point the field exerted by the surface potential for this case of low fixed-charge density has also decayed to a small value. This makes the ions at the center of the tube follow a bulk-layered pattern. In the case of charged tubes with low fixed-charge densities, the net cationic charge density exceeds the anionic charge density, in contrast to the uncharged cases, displaying a selectivity or an enrichment of counter-ions and depletion of co-ions, which is what is expected.

In the case of higher fixed-charges, 1 M and 2 M, no overscreening is observed. The ions in the first layer clearly cannot compensate for the fixed-charge on the tube, owing to the maximum admissible number of ions in the first layer, depending on their size and unfavorable partial desolvation for smeared charges. The effect of the surface potential causes the anions in the next layer to be excluded to some extent, although not completely. The next layer contains a much

higher number of cations than anions as compared to cases of low fixed-charge. In the layer farthest from the wall, the magnitude of the charge density closely resembles that of the bulk system.

7.5.2 Comparison of MD results with Donnan theory predictions

Figures 7-6a-c display the trends of counter-ion sorption and co-ion exclusion as a function of the magnitude of the fixed-charge on the nanotubes. Tables 7-3 and 7-4 summarize the results obtained from MD simulations and from Donnan theory for the average co-ion and counter-ion concentrations; i.e., the chloride and sodium ion concentrations in the negatively charged carbon nanotube.

Uncharged CNTs

a. Steric effects

Before discussing the sorption trends from Donnan theory and MD simulation, we investigate ion partitioning in the uncharged nanotubes. Steric effects are evident, with the (10,10) CNT completely excluding both the ions during the 60 ns simulation. The ratio of the concentration of a particular ion in the nanotube to the bulk solution concentration (i.e., the molar distribution coefficient) increases with increasing diameter. The distribution coefficients for both sodium and chloride ions are identical in the uncharged CNTs; the calculated values for the molar distribution coefficients averaged over the course of the simulation are 0, 0.25, and 0.80 for the (10,10), (14,14), and (22,22) cases, respectively.

Charged CNTs

b. Electrostatic effects

In the case of charged CNTs, the effects of counter-ion enrichment and co-ion exclusion are dictated by the extent to which the surface potential can influence the ions within the CNT. Regardless of the magnitude of the fixed-charge on the nanotube, for high external solutions and

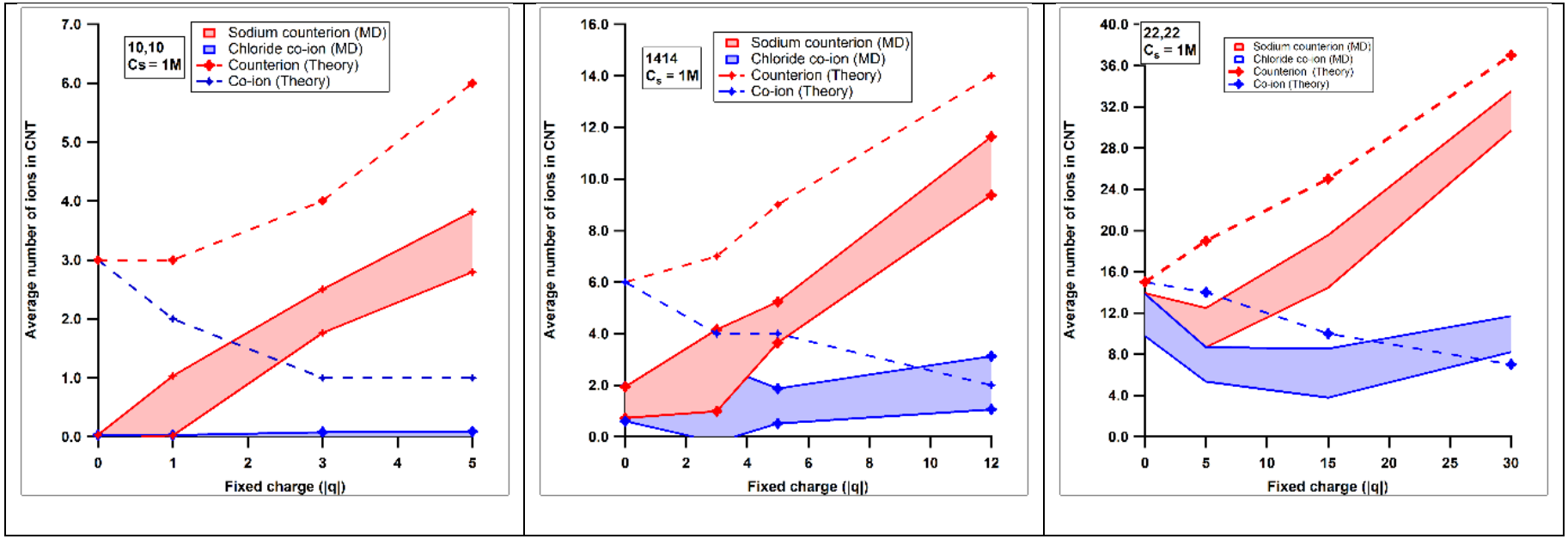

Figure 7-6: Comparison of MD results and Donnan theory predictions.

The shaded regions in red and blue show the average number of counter-ions (sodium) and co-ions (chloride) in the nanotubes within the standard deviation for the final 30 ns of data collection for the three CNT diameter cases (1.356 nm, 1.9 nm, and 3nm), each simulated with three negative fixed-charges (0.35 M, 1 M, and 2 M). The plots also show the case where fixed-charges are absent. The dotted red and blue lines are the predictions for counter-ions and co-ions, respectively, from Donnan theory.

Table 7-3: MD simulation results and Donnan theory predictions for co-ion concentrations in negatively-charged carbon nanotubes that are in contact with 1 M sodium-chloride solution.
The 3rd column shows the average co-ion concentration in the nanotube during the simulation (bold). The measurements of the minimum and maximum co-ion concentrations (italicized) observed during the simulations are given in parentheses below the average co-ion concentration. The standard deviation in the measured co-ion concentration is given in parentheses next to the average results for the co-ion concentration. The actual percentage rejection of co-ions from MD and the predicted rejection from Donnan theory are shown in columns 5 and 6, respectively.

Magnitude of Fixed-charge on nanotube (mol/lit)	CNT	Co-ion concentration (MD) (mol/lit)	Co-ion concentration (Donnan Theory) (mol/lit)	Co-ion Rejection from CNT (%) (MD)	Co-ion Rejection from CNT (%) (Donnan Theory)
0	**(10,10)** *(κa =2.26)*	**0** (0.011) *(0,0.379)*	1	100	0
0.35		**0** (0.009) *(0,0.379)*	0.82	100	18
1		**0** (0.027) *(0,0.379)*	0.56	100	44
2		**0** (0.03) *(0,0.379)*	0.40	100	60
0	**(14,14)** *(κa =3.16)*	**0.21** (0.11) *(0,0.66)*	1	79	0
0.35		**0.21** (0.25) *(0,0.82)*	0.77	79	23
1		**0.19** (0.11) *(0, 0.50)*	0.66	81	34
2		**0.34** (0.17) *(0, 0.66)*	0.40	66	60
0	**(22,22)** *(κa = 5)*	**0.69** (0.11) *(0.35, 1)*	1	31	0
0.35		**0.40** (0.09) *(0.11,0.70)*	0.86	60	14
1		**0.36** (0.14) *(0.06,0.70)*	0.64	64	36
2		**0.58** (0.10) *(0.30,0.87)*	0.44	42	56

Table 7-4: MD simulation results and Donnan theory predictions for counter-ion concentrations and the ratio of counter-ions to co-ions in negatively-charged carbon nanotubes.

The 3rd column shows the average counter-ion concentration in the nanotube during the simulation (bold). The measurements of the minimum and maximum counter-ion concentrations (italicized) observed during the simulations are given in parentheses below the average counter-ion concentration. The standard deviation in the measured counter-ion concentration is given in parentheses next to average results for the counter-ion concentration. The actual selectivity of counter-ions over co-ions (ratio of counter-ions to co-ions in the nanotubes) from MD and the predicted selectivity from Donnan theory are shown in columns 5 and 6, respectively.

Fixed-charge (mol/lit)	CNT	Counter-ion concentration (MD)	Counter-ion concentration (Donnan Theory)	Selectivity (Donnan theory)	Selectivity MD
0	**(10,10) r = 0.68 nm**	**0** (0.011) *(0, 0.0379)*	1	1	-
0.35		**0.2** (0.19) *(0, 0.76)*	1.23	1.5	-
1		**0.8** (0.14) *(0.379, 1.13)*	1.80	3.19	-
2		**1.25** (0.19) (0.76, 1.89)	2.46	6.04	-
0	**(14,14) r =0.95 nm**	**0.22** (0.10) *(0, 0.49)*	1	1	1.04
0.35		**0.43** (0.26) *(0.17, 1.32)*	1.293	1.67	2
1		**0.73** (0.13) *(0.33, 1.15)*	1.53	2.33	3.73
2		**1.74** (0.19) *(1.3, 2.3)*	2.49	6.21	5.018
0	**(22,22) r = 1.49 nm**	**0.74** (0.12) *(0.37, 1.17)*	1	1	1.07
0.35		**0.61** (0.11) *(0.23, 1)*	1.61	1.34	1.5
1		**1** (0.15) *(0.70, 1.34)*	1.55	2.41	2.76
2		**1.84** (0.11) *(1.5, 2.15)*	2.26	5.11	3.17

small Debye lengths, the effect of the surface potential is mostly limited to the first two layers closest to the wall. Thus the depletion or enrichment of ions in those two layers accounts for difference in the measured concentration of ions from the uncharged case.

i. Co-ion concentration: Co-ion exclusion from the nanotube increases with increasing confinement. In the narrowest tube, co-ions are completely excluded while also excluding some counter-ions from the nanotube due to steric effects. While Donnan theory predicts a decreasing co-ion concentration with increasing fixed-charge for a given external solution concentration, the trend in Figures 7-6b and c from the MD simulations shows a mild increase in the co-ion concentration at fixed-charges greater than 1 M. We have seen in the previous section that we do not have a uniform electrostatic potential over the pore volume owing to the high external solution concentration that results in mostly non-overlapping double layers, especially in the two largest diameter CNTs. Thus, even in charged nanotubes, the co-ions and counter-ions that occupy the location at the center of the largest diameter CNTs are governed less by the Donnan isotherm and are essentially absorbed as if the tube were uncharged.

ii. Counter-ion concentration: Figures 7-6a-c show that the sodium counter-ion concentration progressively increases with increasing negative fixed-charge on the tube, as expected, and approaches the total charge on the CNT except for a small decrease in the (22,22) CNT for a fixed-charge of 0.3 M. This deviation is very minor and can be reasoned by taking into account the limited timescale of the simulation. The predicted counter-ion concentration in the nanotube is calculated as the sum of the applied charge on the tube and the predicted co-ion concentration from Donnan theory. As co-ions in the nanotube are excluded to a greater degree, owing to the added effect of steric exclusion than that predicted by purely electrostatic repulsion of Donnan theory, a fewer number of counter-ions are required to balance the charge of the co-

ions in the nanotube. However, in the case of the maximum applied fixed-charge of 2 M on the tube, the co-ion concentration in the nanotube is close to the value predicted by Donnan theory; hence the counter-ions at the center of the nanotube are excluded mechanically via sieving.

iii. Electroneutrality: Donnan theory assumes local electroneutrality; i.e., at any instant, the number of fixed-charges on the tube is equivalent to the difference in the number of counter-ions and the number of co-ions. Local electroneutrality is not observed in the case of charged nanotubes; i.e., the difference in the number of counter-ions and co-ions does not equate to the fixed-charge on the tube.

iv. Rejection: Since the external solution concentration is 1 M, the co-ion distribution coefficient between membrane and the external solution is equal to the co-ion concentration in the nanotube. The effectiveness of ion exclusion from Donnan theory prediction and MD simulations (i.e., the percentage rejection, sometimes also called the exclusion coefficient) is obtained as

$$Rejection = \frac{C_s - \overline{C_s}}{C_s} \times 100 \tag{7.32}$$

where C_s and $\overline{C_s}$ are the concentrations of the free ions in the external solution and in the CNT, respectively. The free ions are essentially the co-ions that are absorbed without any electrostatic attraction to the fixed-charges. Donnan theory predicts an increase in the ion exclusion coefficient with increasing fixed-charge concentration. The ion exclusion coefficients (Tables 7-3 and 7-4) that we obtain for the two narrowest CNTs, (10,10) and (14,14), exceed the predictions of Donnan theory owing to a greater contribution from steric exclusion. In the wider (22,22) tubes, the trend of the ion exclusion coefficient shows a deviation from the trend predicted by Donnan theory for increasing fixed-charges; i.e., the ion rejection worsens at high fixed-charge number (2 M). In wide tubes, as the fixed-charge is increased, more counter-ions are absorbed to counterbalance the cumulative charge on the CNT. The electrostatic potential of the charged CNT is screened at a

distance equal to the Debye length from the wall (0.3 nm); hence more chloride ions are absorbed owing to their attraction to the sodium ions, thus causing the co-ion rejection to actually worsen in the largest tube diameter at the highest fixed-charge.

v. Selectivity

In Figure 7-7, we show a comparison of the selectivity obtained from Donnan theory and from MD simulations. We define selectivity as the ratio of the counter-ion concentration to the co-ion concentration. In an uncharged nanotube (fixed-charge of 0 M), both ions are equally permeable and the selectivity is unity. Donnan theory predicts an increasing trend in selectivity with increasing fixed-charge. By comparison, the selectivity trend obtained from MD grows quite slowly with increasing fixed-charges and the co-ion exclusion is worse in the (22,22) tube as compared to the (14,14) tube. This is because increasing selectivity with fixed-charge demands that the electrostatic potential of the wall influences the entire pore volume to cause counter-ion

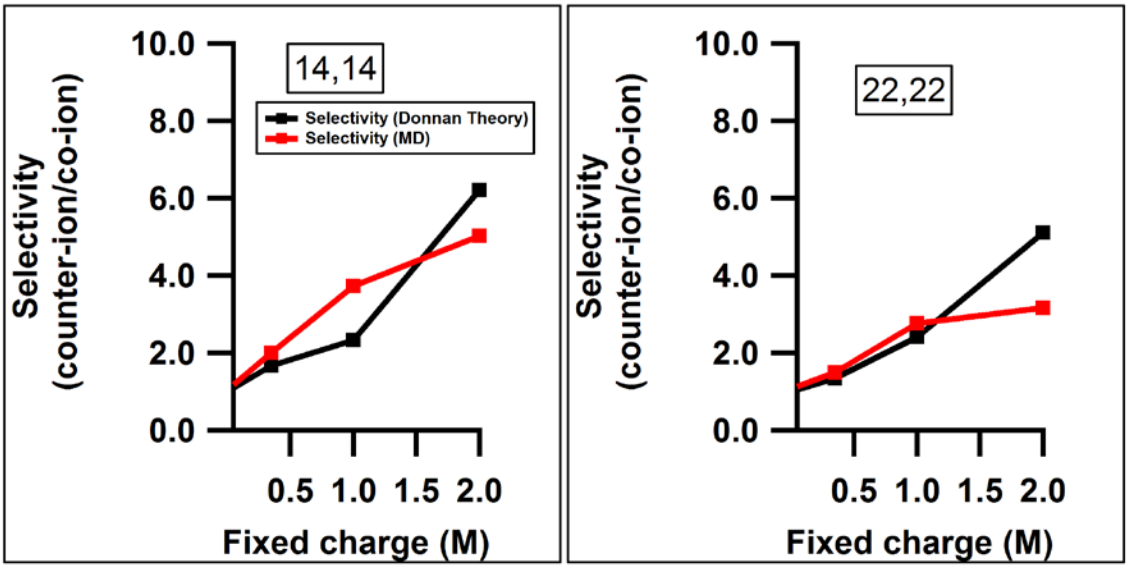

Figure 7-7: Selectivity as the ratio of the counter-ion to the co-ion concentrations in the (14,14) and (22,22) carbon nanotubes as functions of the fixed-charge on the tube.

enrichment and co-ion depletion. However, the counter-ions and co-ions are affected strongly by the wall potential only at distance equal to the Debye length from the wall. In the case of the nanotubes in contact with 1 M sodium-chloride solution, this distance is the annular region where the first two layers of sodium reside closest to the wall. The negative potential on the wall (irrespective of its magnitude) at high external solution concentrations influences the center of the nanotube to a much lesser extent, causing the central region to behave more like an uncharged pore. This central region makes up a significant volume of the (22,22) nanotube where the co-ions simply diffuse into the tube with minimal electrostatic repulsion from the wall potential. Thus instead of displaying a decreasing trend with fixed-charge, the number of co-ions absorbed into the CNT remains more or less the same irrespective of the charge on the (22,22) CNT. The counter-ions increase with fixed-charge, but the increase will be limited to the maximum permissible volume of the annular region close to the wall. This explains why the selectivity does not increase as per the Donnan trend. Better selectivity can be obtained when the radius of the nanotube is comparable to the Debye length; i.e., in the case of overlapping double layers. In this case, if the fixed-charge on the tube is high enough to validate the assumption of a uniform potential, the trends predicted by Donnan theory should be valid with even greater selectivity than that predicted by Donnan theory owing to additional effect of steric exclusion in nanometer-sized pores.

The trends of counter-ion and co-ion absorption in the different layers in the (22,22) CNT are shown in Figures 7-8a and b, respectively. It can be seen that the number of counter-ions in the first two layers closest to the wall increase with increasing fixed-charge, whereas their number stays more or less the same in the 3rd layer at the center of the nanotube for all fixed-charge values. In the layer closest to the wall, the maximum number co-ions can be found in the case of the uncharged tube. As the fixed-charge increases to 0.35 M and 1 M, the number of co-ions in the

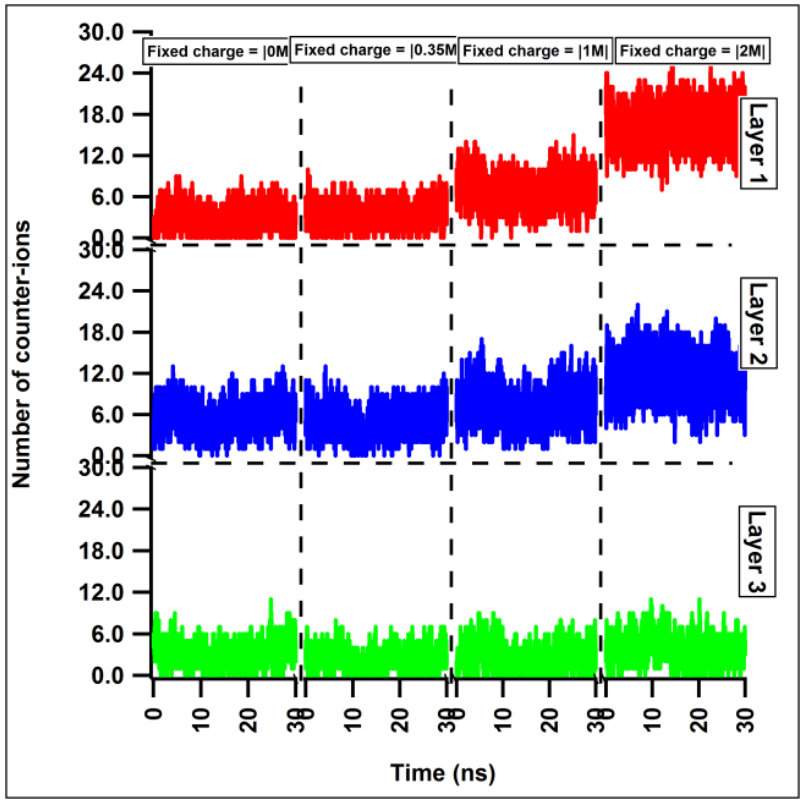

(a)

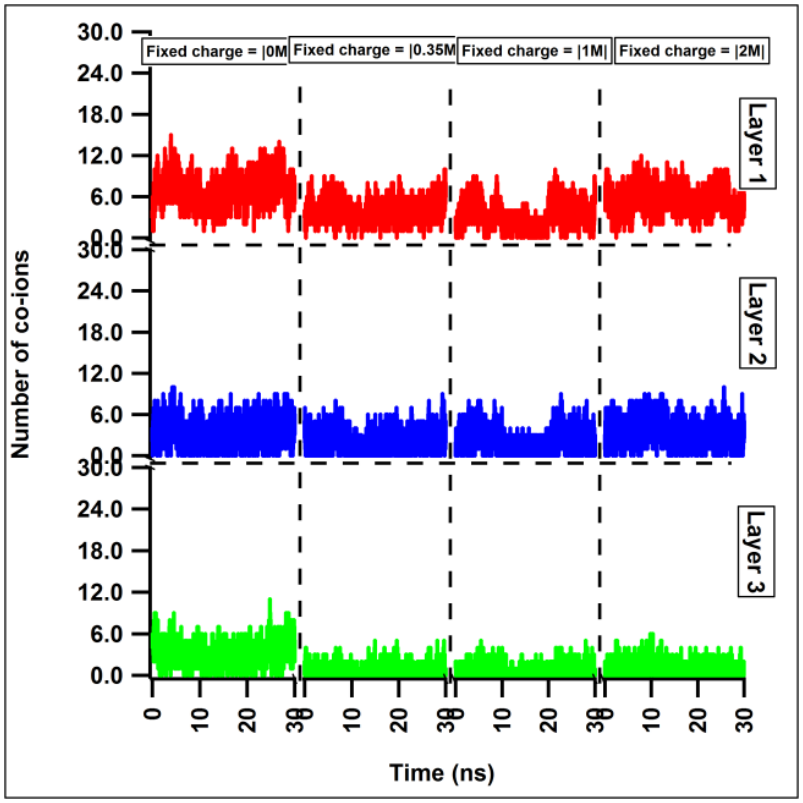

(b)

Figure 7-8: The number of counter-ions and co-ions in the layers adjacent to the wall. Layer 1 is the zone closest to the wall and layer 3 is the zone farthest from the wall making up the central section of the nanotube.

first layer can be seen to decrease as compared to the case of the uncharged CNT. However, the co-ions in the first layer show a slight increase at a fixed-charge of 2 M as compared to the lower fixed-charge cases, owing to charge screening and attraction to the sodium counter-ions in the nanotube. Irrespective of the magnitude of the fixed-charge on the CNT, the co-ion numbers in layer 2 and layer 3 remain more or less constant and close to their values in the uncharged CNT owing to the decaying surface potential in layers 2 and 3.

7.6 Conclusions

We have performed molecular dynamics simulations of carbon nanotubes in contact with reservoirs of sodium-chloride solution of equal concentrations to obtain the equilibrium concentration of counter-ions and co-ions within the uncharged and charged nanotubes of diameters in the range of 1.356 – 3 nm. The external solution concentration was fixed at 1 M (Debye length ~ 0.3 nm) and the charged nanotubes had uniformly distributed negative partial charges. The negative surface charges resulted in three fixed-charge concentrations based on aqueous solution volume of about 0.35 M, 1 M, and 2 M, which corresponds to weakly, moderately, and highly charged nanotubes. This simulation system allowed us to test the results of co-ion exclusion with Donnan theory. While some quantitative deviations from Donnan theory predictions are to be expected owing to the discrete nature of the solution and the finite sizes of the ions, we nevertheless can provide both a quantitative and qualitative comparison of the results of the MD simulations and Donnan theory.

In our simulations, owing to the use of high external solution concentrations, there exist non-overlapping double layers, which lead to a non-uniform potential over the pore volume and a decreasing ratio of thickness of the double layer to the pore radius with increasing pore radii. Two

of the primary assumptions of Donnan theory arising from the Boltzmann description of ion concentration distribution breakdown to some extent in our simulations. These assumptions are: 1) ions are point-like particles; 2) the existence of overlapping double layers leading to a uniform pore potential. The violation of the first assumption in our case clearly leads to higher co-ion exclusion, owing to steric effects, but does not affect the co-ion exclusion trend. The breakdown of the second assumption, owing to the use of high external solutions and wider pores, leads to deviation from the co-ion exclusion trend where the central region of the nanotube behaves increasingly like an uncharged pore with increasing tube diameter.

The counter-ions and co-ions are electrostatically attracted and repelled to a greater degree in the region close to the charged CNT and to a much lesser extent at the center of the tube. We believe that the MD trends will show better agreement with Donnan theory at low external solution concentrations and in all probability will show an enhancement in the co-ion exclusion beyond that predicted by Donnan theory. This enhancement in co-ion exclusion at low solution concentrations will stem mostly from the non-vanishing electrostatic potential at the center of the tube and from additional sieving due to the steric and unfavorable partial desolvation effects.

The equilibrium counter-ion and co-ion predictions are a consequence of the Boltzmann distribution, which does not capture the actual concentration profile of ions in the nanotube. Donnan theory makes no provisions for the inclusion of effects of ion-ion correlations that are evident in the layered arrangement of ions, even when they are very close to charged surfaces. This layered arrangement of ions does not decay quickly and continues to the center of even the wider tubes. This omission can make the actual co-ion exclusion trends deviate from Donnan theory.

Thus, while Donnan theory may be a good starting point to understand electrostatic ion exclusion and provides a simplified description of ion exclusion as compared to the more intricate Poisson-Boltzmann theory, it is important to recognize that without corrections for the finite size of the ions, ion–ion correlations, and the pore potential, this mean field theory is inadequate to describe accurately co-ion exclusion trends under confinement.

Chapter 8. Electrolyte diffusion through uniformly-charged carbon nanotubes

8.1 Introduction

We have previously seen that the rejection of electrolyte through uncharged carbon nanotubes is caused by sieving effects due to the modification of the solvation structure of the ions within the nanotube as well as a lower mobility of ions inside the nanotube. In this chapter, we analyze the rejection of electrolytes on account of electrostatic interactions due to the addition of fixed-charges to the nanotube. To do so, we simulate the passive transport of a sodium-chloride electrolyte through a uniformly-charged carbon nanotube (CNT) fixed between two reservoirs of unequal concentrations and study the one dimensional flux using molecular dynamics (MD) simulations spanning 100s of nanoseconds. Both the molarity of the high concentration reservoir and the magnitude of the fixed-charge applied to the CNT are varied, which allows us to modulate the strength of the electrostatic potential (also known as the Donnan Potential) and thus investigate its effect on electrolyte diffusion. We find that the rate of electrolyte diffusion from the high concentration reservoir to the low concentration reservoir is controlled by co-ion diffusion, which depends on the strength of the Donnan potential; this phenomenon is consistent with the description of ion transport through ion-exchange membranes[190].

8.2 Simulation method

The 3 nm diameter (22,22) and 5 nm long CNT used in this study consists of immobile negative partial charges that are uniformly distributed on its surface. The fixed-charge concentrations (calculated on the basis of aqueous solution volume) used are 0.35 M, 1 M, and 2 M, corresponding to net negative charges of -5e, -15e, and -30e, respectively. Reservoir 2 contains

pure solvent (TIP4P/2005 water). Reservoir 1 contains electrolyte solution of various concentrations, 0.1 M, 0.4 M, and 1 M. The rigid graphene walls prevent osmotic effects. The combination of fixed-charges and concentrations in Reservoir 1 resulted in nine simulated systems. The simulation box dimensions for all cases were 8.34 X 8.34 X 18.0 nm^3. The TIP4P/2005 water-filled reservoirs and the CNT containing water were equilibrated separately via NPT simulations (300 K, 1 bar) and were then combined to form the overall simulation system. The Reservoir 1 concentration is attained by simultaneously adding the requisite number of sodium and chloride ions and deleting an equal number of water molecules. The number of water molecules in each reservoir is about 11,000 and the number of sodium ions are 280, 112, and 28 for solutions corresponding to 1 M, 0.4 M, and 0.1 M in Reservoir 1. In order to maintain overall electroneutrality, the number of chloride ions in Reservoir 1 is less than the number of sodium ions by a value equal to the charge on the nanotube. The schematic of the system is similar to that shown in the chapter detailing the study of diffusion through uncharged nanotubes, which has been illustrated there (see Chapter 6, Section 6.3 Computational methods). For details of the MD simulation parameters used, the reader is referred to the chapter on diffusion of electrolytes through uncharged nanotubes. The simulations were conducted in the NVT ensemble (300 K) using GROMACS and the trajectories were visualized using VMD. Each simulation was run for at least 100 ns.

8.3 Theory

The driving forces for ion transport are the gradient of the chemical potential of the species, the gradient of the electrical potential, and the convection of the pore liquid. In the absence of convection owing to the rigid walls in our system, ion transport depends only on the diffusion flux and electric transference. The diffusive flux is

$$J_{i,_{diffusion}} = -D_i(\nabla C_i) \tag{8.1}$$

and the electric transference is

$$J_{i,_{ele}} = -\frac{D_i z_i C_i F}{RT}(\nabla \emptyset) \tag{8.2}$$

The total species flux is the sum of the two contributions

$$J_i = J_{i,_{diffusion}} + J_{i,_{ele}} \tag{8.3}$$

At steady state, several conditions must be met:

$$J_+ = -\bar{D}_+\left(\frac{d\bar{C}_+}{dx} + z_+\bar{C}_+\frac{F}{RT}\frac{d\varphi}{dx}\right) \tag{8.4}$$

$$J_- = -\bar{D}_-\left(\frac{d\bar{C}_-}{dx} + z_-\bar{C}_-\frac{F}{RT}\frac{d\varphi}{dx}\right) \tag{8.5}$$

$$z_+\bar{C}_+ + z_-\bar{C}_- + \alpha X = 0 \qquad \text{Electroneutrality} \tag{8.6}$$

$$z_+J_+ + z_-J_- = 0 \qquad \text{No electric current} \tag{8.7}$$

$$J_+, J_- = constant \qquad \text{Quasi-steady-state} \tag{8.8}$$

The subscripts + and – refer to the cation and anion and the overbars refer to the concentration within the nanotube. The large solution volume in the two compartments enables us to attain a quasi-steady-state for the 100 ns simulation during which the concentration of the two reservoirs does not change appreciably. At steady state, the flux does not change; however, some assumptions need to be made if Eq. (3) is to be used. It is assumed that interfacial resistance to diffusion is minimum, no mobile complexing agent acts as a carrier, and no anomalous diffusion (such as single-file motion) occurs. For our system, all of these assumptions are valid.

8.4 Results

In the following discussion of the results of our simulations, we use a nomenclature where 'X' is the molar concentration of the fixed-charge on the CNT and Cs is the concentration of

solution in Reservoir 1. To understand ion transport through charged carbon nanotubes systematically, we will first look only at the result (Figure 8-1) for the case of the nanotube with the maximum fixed negative charge (2 M) that is contact with Reservoir 1 having the highest external solution concentration (1 M) and compare it to the ion permeation results for an uncharged nanotube.

We have seen previously that the sodium and chloride ions are equally permeable through a 3 nm uncharged CNT, that electrolyte rejection is a consequence of reduced mobility in the nanotube and steric hindrance to the solvated ions, and lastly, that the electroneutrality condition leads to equal cation and anion fluxes through the CNT at all times during the

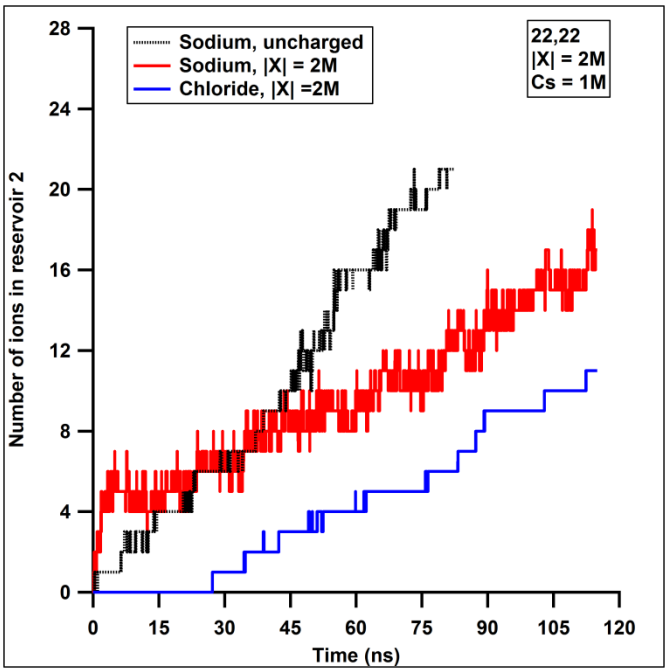

Figure 8-1: The number of cations (red) and anions (blue) that permeate through a nanotube bearing a uniformly-distributed (negative) fixed-charge (*X*) of 2 M strength. One end of the CNT is in contact with a reservoir containing an external solution concentration (*Cs*) of 1 M and the other end is in contact with pure water. The result for ion permeation through uncharged nanotubes for a similar setup is shown by the black trace for comparison.

simulation duration. Hence, for clarity we only show the sodium ion (black trace) permeation through the uncharged nanotube. In the uncharged case, the sodium ion flux is linear with time, and the permeation process is diffusion dominated. If we compare this with the case of the charged nanotube, we observe that the cation permeation increases rapidly in the first few nanoseconds, followed by the slowing down of the permeation process to a rate less than that seen in the uncharged nanotube. During this initial time period, the anions are completely excluded from the negatively-charged nanotube. After this initial spike in the cation permeation rate, both ion permeation rates become nearly equal, indicating the establishment of pseudosteady-state flux towards Reservoir 2. When $X = 2$ M, the CNT has a total charge of -30e uniformly distributed on it; however, the number of sodium counter-ions in the nanotube is insufficient to compensate this negative charge on the CNT during the initial period. A number of sodium ions travel down the concentration gradient (from Reservoir 1 to Reservoir 2) in proportion to the uncompensated charge in the CNT. This initial cation leakage to Reservoir 2 leads to a charge imbalance (excess positive charge) in Reservoir 2, which helps to depolarize the membrane of the uncompensated negative charge. Not all of the uncompensated negative charge on the CNT is balanced by the leakage of cations to Reservoir 2: some of the charge is balanced by an unequal distribution of cations and anions in Reservoir 1. Once Reservoir 2 attains the appropriate number of sodium ions required to depolarize the membrane, the initial spike in the sodium ion permeation stops and the diffusion of equal numbers of sodium and chloride down the concentration gradient begins. Since the nanotube is negatively charged, a number of chloride ions are repelled, leading to a much lower occupancy of chloride ions as compared to sodium counter-ions. A low occupancy of chloride ions implies lower anion flux, and since at steady state both cation and anions fluxes should be equal

(consequence of electroneutrality), the sodium ion flux in turn also decreases to the same rate as that of the chloride ions.

The fluxes depicted here in Figure 8-2 for the case of the charged CNT are calculated after the initial depolarization period by subtracting the number of sodium ions that leak into Reservoir 2 initially. After the depolarization period, the sodium and chloride fluxes are equal, and attain a value that is nearly half the value of the electrolyte flux for the case of uncharged nanotubes. This decrease in electrolyte flux as compared to the uncharged CNT can be further investigated in terms of diffusion coefficients, ion occupancies, and ion concentration gradients.

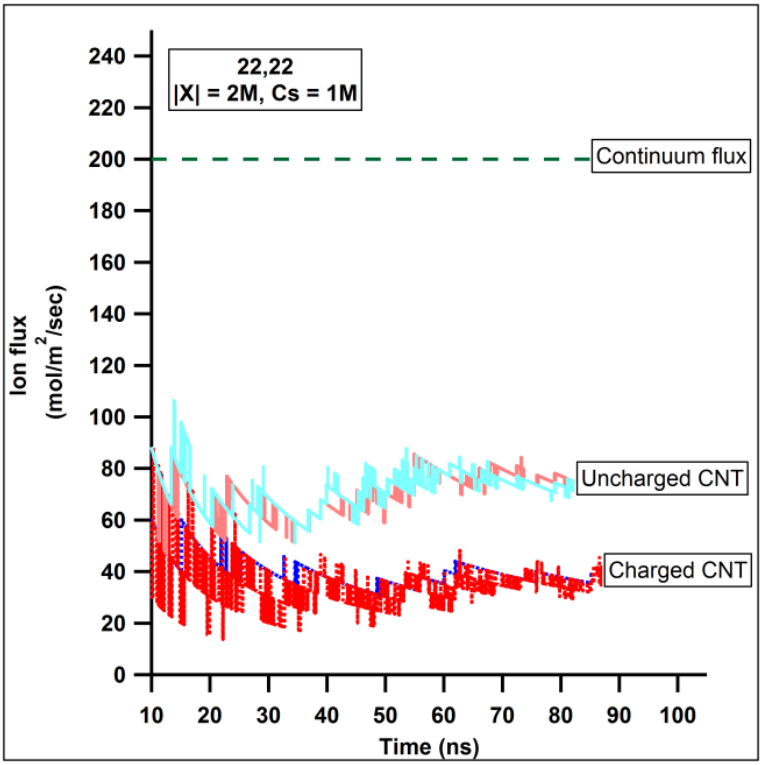

Figure 8-2: Sodium ion (red) and chloride ion fluxes (blue) for the case of charged and uncharged CNTs. The darker traces are for the case of the charged CNT (*X*=2 M, *Cs*=1 M) and the lighter traces are for the case of the uncharged CNT. The continuum flux assuming no ion partitioning from steric effects is shown by the dotted line.

In the case of the charged CNT in contact with 1 M sodium-chloride solution, the Debye length is 0.3 nm. Due to this screening limit, the ions away from the wall and at the center of the tube ($r = 5\lambda_D$) are mostly electroneutral and do not experience the electrostatic influence of the wall potential. The Donnan potential is not uniform over the pore volume; the effect of the Donnan potential for an anion at the center of the tube is minimal and its influence can be accounted for in the Nernst-Planck equation by a Donnan potential-dependent partition coefficient. The average chloride ion occupancy in the uncharged CNT is between 3-6 (standard deviation ≈ 1.4) and in the negatively-charged CNT is between 1-3 (standard deviation ≈ 1.3) (see Figure 8-3a). This decrease in anion occupancy in charged tubes mainly occurs because of anion repulsion near the charged CNT wall. The concentration profiles of the anions (Figure 8-3b) also show a similar result of lower anion density in the charged CNT as compared to the uncharged case. This poor partitioning of anions into the negatively-charged CNT leads to a lower concentration of the co-ion at the tube entrance and results in a lower driving force for the anion diffusion into Reservoir 2. Further, a plot of the mean-squared displacements of the anions and cations inside the charged CNT (see Figure 8-4) reveals lower diffusion coefficients for both cations and anions compared to their corresponding values in the uncharged CNT. The lowering of the counter-ion diffusion coefficient is due to lower mobility because of the attraction from the fixed-charges, whereas the lowering of the co-ion diffusion coefficient has to do with restricted mobility from the increased confinement in a smaller volume at the tube center because of repulsion near the wall.

The diffusion coefficient of the cation is slightly higher than that of the anion; this leads to diffusion potentials that can be calculated from

$$\emptyset(0) - \emptyset(L) = \left(\frac{D_- - D_+}{D_- + D_+}\right)\left(\frac{RT}{F}\right)\ln\left(\frac{C_0}{C_L}\right) \tag{9}$$

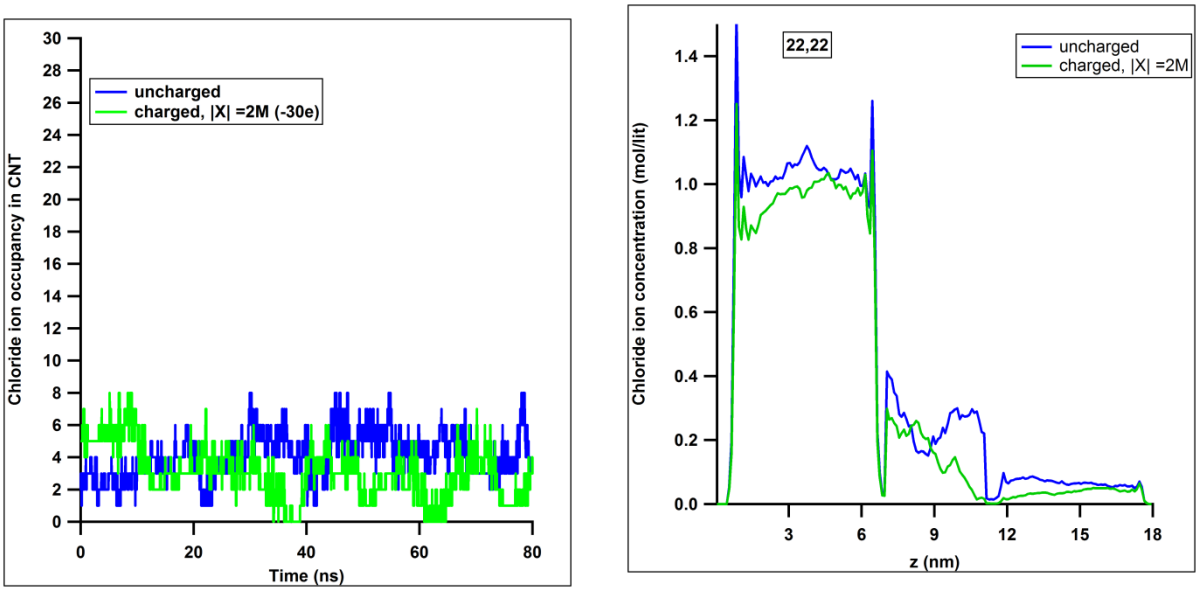

(a) (b)

Figure 8-3: Ion occupancy ((a); last 80 ns of data collection) and the axial concentration profiles ((b); last 30 ns of data collection) in the uncharged (blue) and charged CNTs (green).

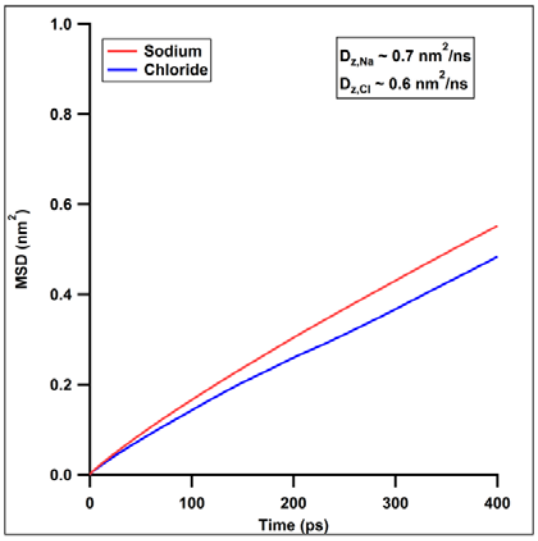

Figure 8-4: The mean-squared displacements of sodium (red) and chloride (blue) ions in the charged (22,22) CNT (*X*=2 M) for the last 50 ns of data collection.

The range of this diffusion potential is from -11.20mV at the beginning of the passage of chloride ions to Reservoir 2 to -4.5mV when the concentration in Reservoir 2 builds up to 0.1 M. This diffusion potential tends to speed up the chloride ion flux and slow down the sodium ion flux, until at steady state both fluxes assume the same value.

We can make a simple estimation of the unidirectional anion flux from the Nernst-Planck equation. We use two simplifying assumptions: the ion concentration gradient is linear and the electric field induced by the diffusion potential is uniform. In this case, the first assumption is perfectly reasonable, as can be visualized from the concentration profile of ions in the nanotube. The correctness of the second assumption can be surmised by the degree of correspondence of the flux estimate from the Nernst-Planck equation and from the simulation results. We make use of a diffusion potential assuming the concentration in Reservoir 2 is 0.05 M (≈ 14 ion pairs in Reservoir 2), which is close to the concentration of Reservoir 2 at the end of the simulation duration. The value for the diffusion potential at this concnetration of Reservoir 2 is -5.9 mV.

The Nernst-Planck equation for chloride ion transport takes the form inside the CNT of

$$J_{Cl} = -D_{Cl,CNT}\frac{(\lambda_m(C(L)-C(0))}{L} - \frac{D_{Cl,CNT}.z_{Cl}.F.C_{Cl,CNT_{entrance}}}{RT}\left(\frac{\emptyset_{diff}(L)-\emptyset_{diff}(0)}{L}\right) \quad (8.10)$$

Here 0 and L are the entrance and exit of the CNT and $\emptyset_{diff}$ is the diffusion potential. The contribution from the concentration gradient is 36 mol/m^2/s and from the diffusion potential is 8.3 mol/m^2/s, which together provide the total steady-state chloride co-ion flux as 44.1 mol/m^2/s. This estimate of ion flux from the Nernst-Plank equation without the explicit consideration of a Donnan potential but includes our estimate of the diffusion potential seems to agree well with the flux obtained from the MD simulations. The concentration gradient that is obtained graphically from Figure 3b takes into account the influence of the Donnan Potential on co-ion repulsion. For this

case of low Debye length, we thus find a predominantly diffusive flux for co-ions through the negatively-charged (22,22) CNT. In the case of sodium ions, we cannot simply neglect the Donnan potential by addition of a partition coefficient since the sodium ions are present in large numbers close to the charged wall (where the wall potential is not screened). Here,

$$J_{Na} = -D_{Na,CNT}\frac{(\lambda_m(C(L)-C(0))}{L} - \frac{D_{Na,CNT}.z_{Na}.F.C_{Na,CNT_{entrance}}}{RT}\left(\frac{\emptyset_{diff}(L)-\emptyset_{diff}(0)}{L}\right) \quad (8.11)$$

$$-\frac{D_{Na,CNT}.z_{Na}.F.C_{Na,CNT_{entrance}}}{RT}\left(\frac{\emptyset_{Donnan}(L)-\emptyset_{Donnan}(0)}{L}\right)$$

where, $\emptyset_{Donnan}(L) = \frac{RT}{zF}\ln(\frac{C_{Na,CNT(L)}}{C_{Na,Res2}})$ and $\emptyset_{Donnan}(0) = \frac{RT}{zF}\ln(\frac{C_{Na,CNT(0)}}{C_{Na,Res1}})$. Since we know the sodium ion flux from MD simulation, we can obtain a rough estimate of the membrane potential $[\emptyset_{Donnan}(L) - \emptyset_{Donnan}(0)]$ from the above equation.

Figures 8-5a and b show 5 ns long trajectories of the sodium and chloride ions that were inside the CNT at $t = 85$ ns. The first observations are that there are far more sodium ions inside the nanotube as compared to chloride ions and that the sodium ions approach the wall much more closely than the chloride ions. This close degree of approach to the charged wall can be seen in the radial spread of the sodium ions inside the nanotube as compared to that observed for chloride ions. The co-ions (i.e., the chloride ions) once out of the CNT tend to diffuse far from the nanotube entrance quickly, whereas a majority of sodium ions (counter-ions) crowd around the mouth of the nanotube for an appreciable amount of time even after exiting the nanotube. A careful cross examination of the r and z locations of ions at the instants of their exit from the nanotube shows that the ions exit the nanotube mostly from the center of the tube and much less frequently from a radial location near the walls. This is also supported by a visual inspection of the trajectories that were produced during the simulation in VMD. With these observations in mind, we can

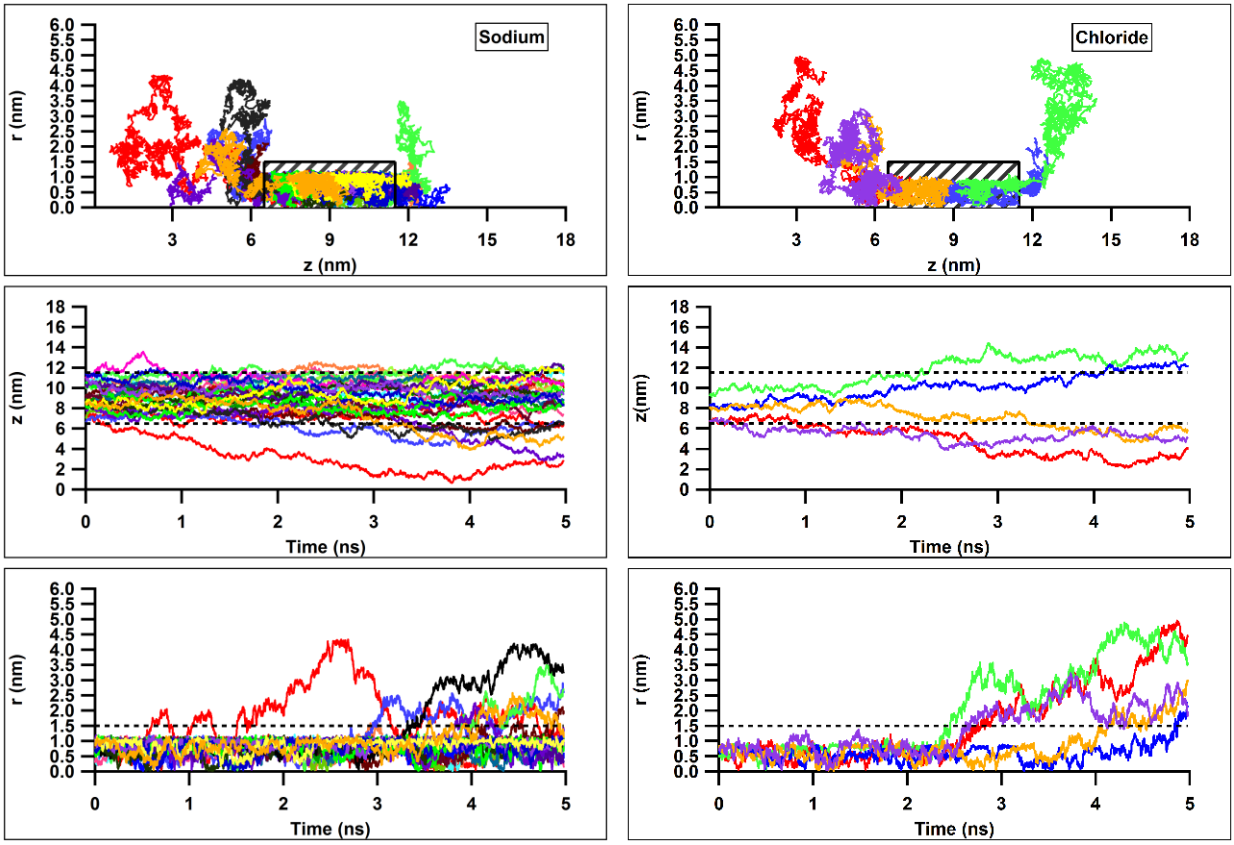

(a) **(b)**

Figure 8-5: The trajectories of diffusing sodium (a) and chloride (b) ions through the CNT in the radial and axial directions. In the topmost panels of figures (a) and (b), the patterned black box represents the radial and axial boundaries of the nanotube. The black dotted lines in the middle and bottom panels designate the axial and radial boundaries of the nanotube respectively.

examine the full suite of simulation results for all magnitudes of fixed-charge (X = 0.35 M, 1 M, 2 M) and Reservoir 1 concentrations (Cs = 0.1 M, 0.4 M, 1 M). Figure 8-6 shows the number of cation and anions that have translocated to Reservoir 2 as functions of time. In the simulations that we have conducted, the 3 nm diameter nanotube is permeable to both cations and anions but is more selective for cations owing to the negative partial charges on the pore. The co-ion permeation rate can be seen to be a clear function of the magnitude of the fixed-charge on the nanotube for all external solution concentrations. The permeation rate trend for chloride ions as a function of the magnitude of the fixed-charge for most cases is 0 M > 0.35 M > 1 M > 2 M. Both

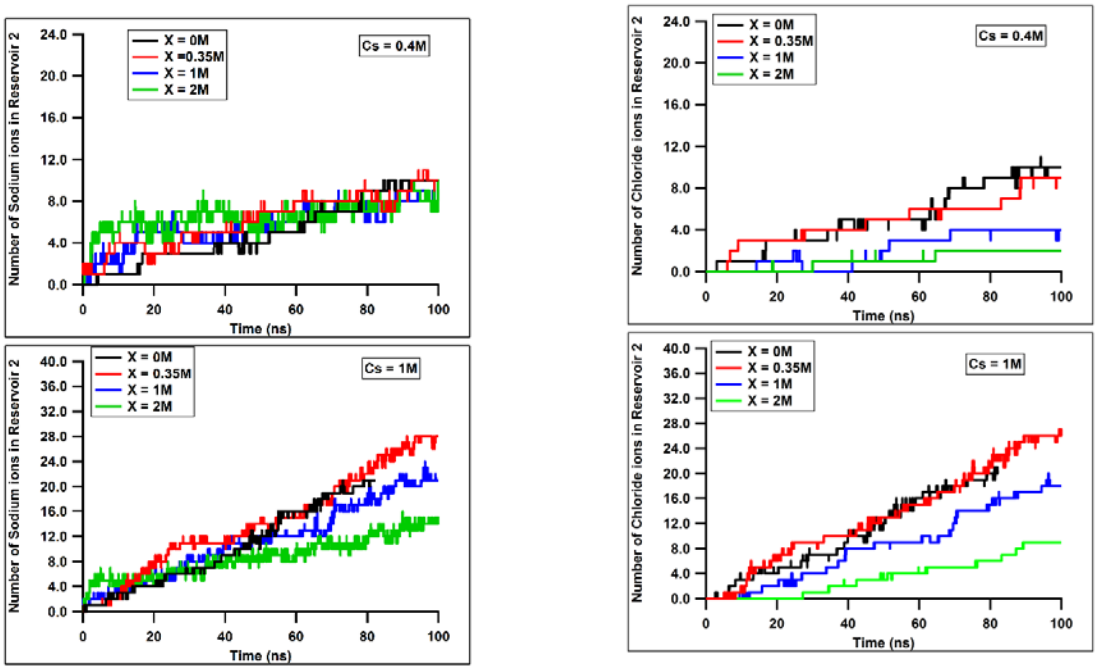

(a) **(b)**

Figure 8-6: The number of sodium ions (a) and chloride ions (b) that have diffused to Reservoir 2 during the simulation. The top and bottom panels show the ion diffusion for Reservoir 1 concentrations of 0.4 M and 1 M, respectively.

anion and cation flux decrease as the fixed-charge on the CNT is increased. Higher numbers of co-ions are excluded as the charge on the CNT is increased, and since electroneutrality must be maintained, the cations are also rejected, which decreases the flux of both the cations and anions to the same extent.

Figure 8-7 shows the cation leakage that occurs in the initial few nanoseconds of the simulation in order to depolarize the negatively-charged nanotube. The nanotube in all cases has fewer net positive charges inside the CNT than the negative charge on it. In Figure 8-8, we can see that for a particular magnitude of fixed-charge, the number of uncompensated charges increases slightly as the solution concentration decreases. At any particular solution concentration, the number of uncompensated charges increases as the magnitude of the fixed-charge is increased; however, a majority of this excess charge that is not accommodated inside the CNT leaks into the low concentration reservoir in the first few nanoseconds of the simulation and remains constant thereafter. The number of cations that leak is a function of the fixed-charge on the CNT; i.e., the tube with the highest fixed-charge number has the maximum number of ions that leak into Reservoir 2 (Figure 8-7a and b), whereas the tube with the lowest fixed-charge number has the least amount of ion leakage and the least amount of uncompensated charges. Not all of the uncompensated charges are balanced by the leakage of ions into Reservoir 2; some of it is balanced by leakage into Reservoir 1. Thus, while the whole system as such is electroneutral, there is charge imbalance in each of the compartments and within the nanotube that remains steady during the entire duration of the simulation—see Figure 8-8. In this figure, the sum of the excess positive charges in the two reservoirs is equal to the uncompensated negative charge on the CNT.

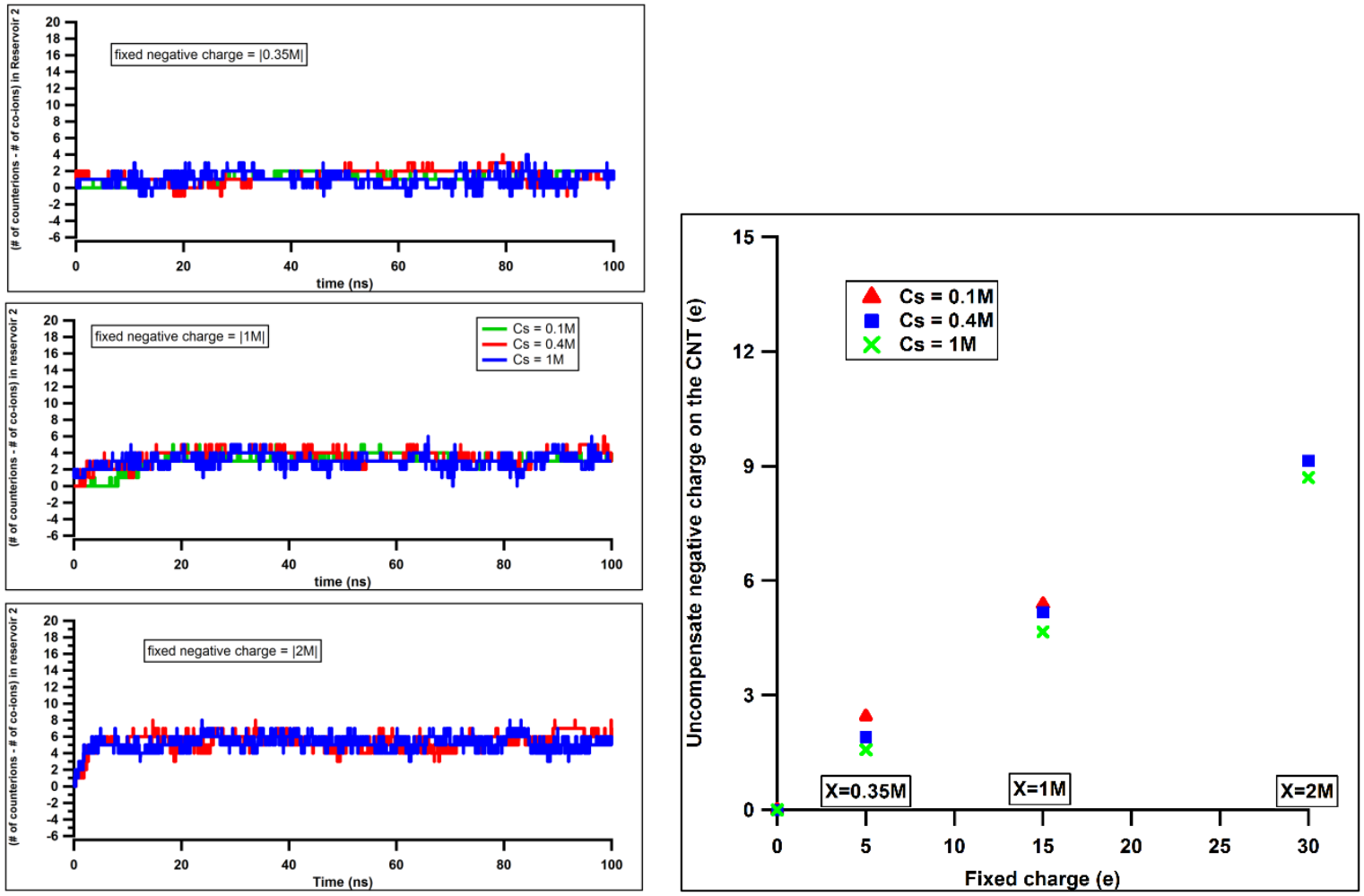

(a) **(b)**

Figure 8-7: Ion leakage at the beginning of the simulation that stays constant for the rest of the simulation duration (a), and the average uncompensated negative charge on the nanotube vs. applied fixed-charge for all concentrations of Reservoir 1 (b).

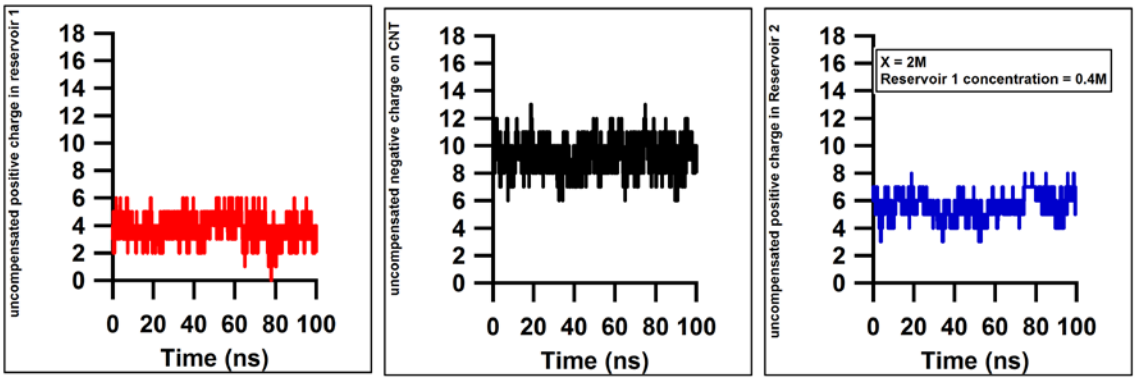

(a)

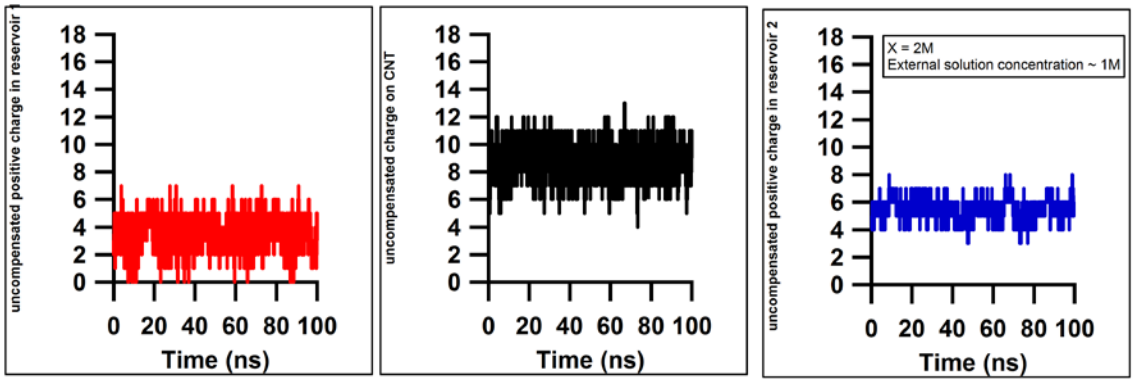

(b)

Figure 8-8: Temporal trends of the uncompensated negative charge on the CNT (black). The excess positive charge in Reservoir 1 (red) and excess positive charge in Reservoir 2 (blue) for the *X* =2 M, *Cs* = 0.4 M (a) and *X* =2 M, *Cs* =1 M (b).

Figure 8-9a shows the average steady-state fluxes of sodium and chloride ions from the left to the right side of the CNT, which are obtained after the initial depolarization period. If boundary layer diffusion or film diffusion is negligible, the co-ion flux is proportional to the diffusion coefficient of the ion in the CNT, its concentration in the nanotube, and is inversely proportional to the length of the nanotube. The concentration of the co-ion in the nanotube is expected to be smaller than that in Reservoir 1. When the fixed-charge number is high and the solution is dilute, the co-ion concentration should become very small owing to Donnan exclusion. We find that the electrolyte flux is consistent with this description, as can be seen in Figure 8-9a, where we observe a decreasing co-ion flux with increasing fixed-charge number for all concentrations of Reservoir 1. At steady state, the net current should be zero; i.e., the co-ion flux should equal the counter-ion flux to satisfy the electroneutrality condition. Thus, for a particular value of the concentration in Reservoir 1, we see a simultaneous decrease in the counter-ion flux with increasing fixed-charge number on the nanotube. More simply, the rate of electrolyte diffusion is controlled by the diffusion of the co-ion.

As stated above, the co-ion concentration in the nanotube decreases with increasing fixed-charge number; however, some non-idealities owing to additional steric effects and ion-ion interactions in the nanotube must be brought to attention. For X = 0 M and Cs = 1 M, the counter-ion and co-ion concentrations are equal to each and lower than the external solution concentration owing to the sieving action arising from unfavorable partial desolvation within the CNT. The concentration of sodium and chloride ions at the entrance of the nanotube for this uncharged CNT case is about 0.35 M. In the case where X = 0.35 M and Cs = 1 M, the counter-ion partitioning into the nanotube becomes more favorable owing to the electrostatic attraction, which causes some of the co-ions to be attracted by the counter-ions in the nanotube, thereby increasing their

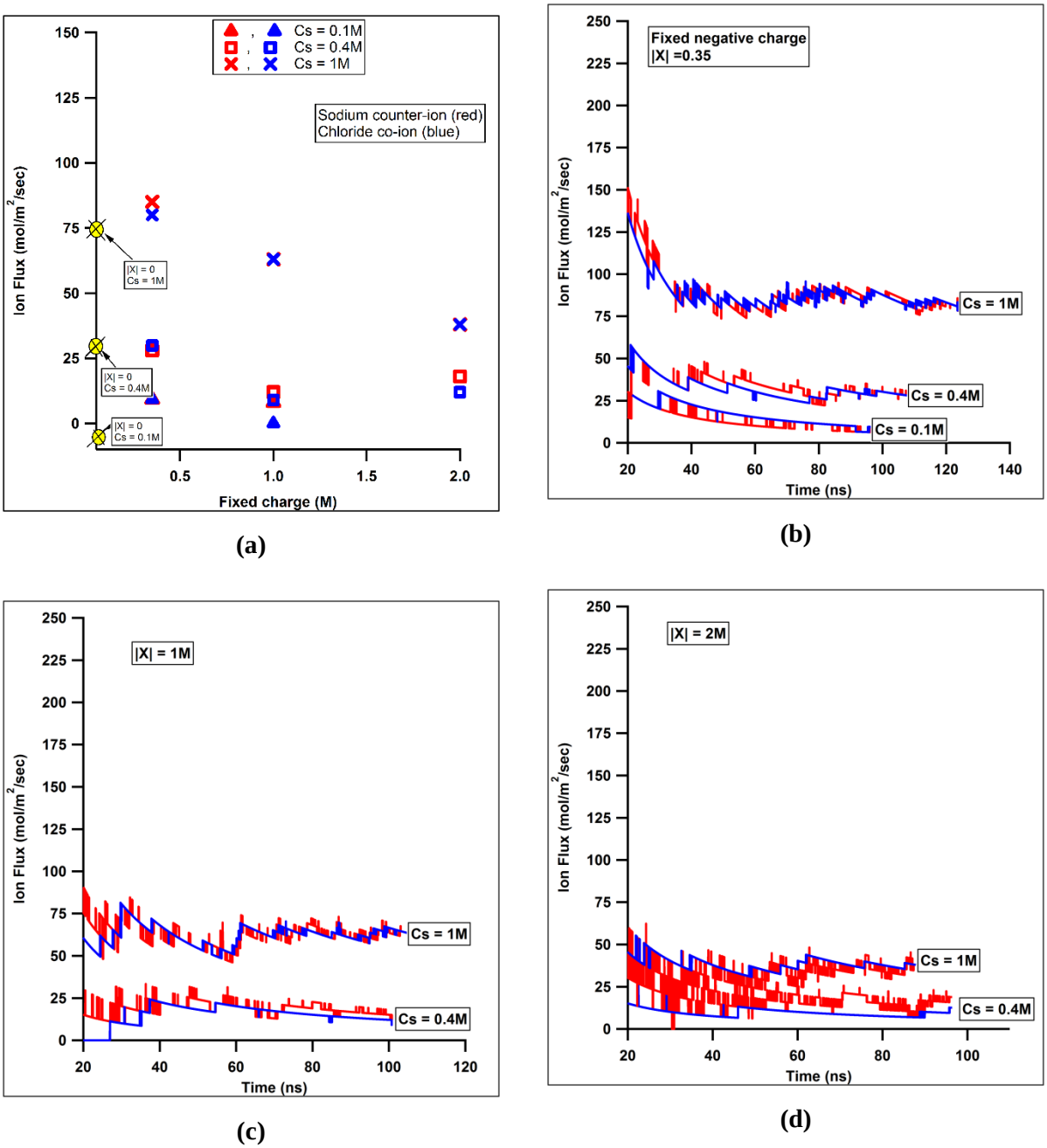

Figure 8-9: Electrolyte flux at all external solution concentrations vs. the fixed-charge on the nanotube (a). The ion flux through an uncharged CNT is indicated by the yellow circles. Instantaneous ion flux vs. time for the increasing magnitudes of fixed-charge: X = 0.35 M (b), 1 M (c), and 2 M (d).

concentration in the lightly charged CNT as compared to the uncharged case. The concentration of the chloride ions at the entrance in this case is about 0.4 M. This increase in the co-ion concentration in the lightly-charged nanotube has an effect of increasing the co-ion and counter-ion flux as compared to the corresponding flux through an uncharged tube at same external solution concentration of Reservoir 1.

Axial concentration profiles and Concentration polarization

Figures 8-10a-c show that regardless of the fixed-charge on the nanotube, concentration polarization is discernible only in the cases of low external solution concentration; i.e., when the Reservoir 1 concentration is about 0.1 M (top panels of Figures 8-10a and b). It is also seen to some extent in the case of high fixed-charge, $X = 2$ M, and when the reservoir concentration is 0.4 M. The co-ion concentration profile in the nanotube shows a gradient indicating that the co-ions will follow diffusive behavior within the CNT. In the case of low fixed-charge number, the counter-ions also display a gradient, indicating that some counter-ions behave as free ions. As the number of fixed-charges increases, a majority of the sodium ions behave like bound ions, and hence the gradient in the counter-ion concentration becomes less visible.

8.5 Conclusions

We have studied the steady-state fluxes through charged nanotubes having a pore size of 3 nm as functions of increasing external solution concentration of the upstream reservoir and increasing magnitude of the negative fixed-charge number on the CNT. In the case of charged CNTs, the electrolyte rejection and electrolyte flux depend on the fixed-charges on the nanotube that dictate the co-ion concentration within the nanotube. For a particular value of the upstream high concentration reservoir, a low fixed-charge results in high co-ion concentration in the nanotube and high electrolyte flux, whereas a high fixed-charge results in a low co-ion

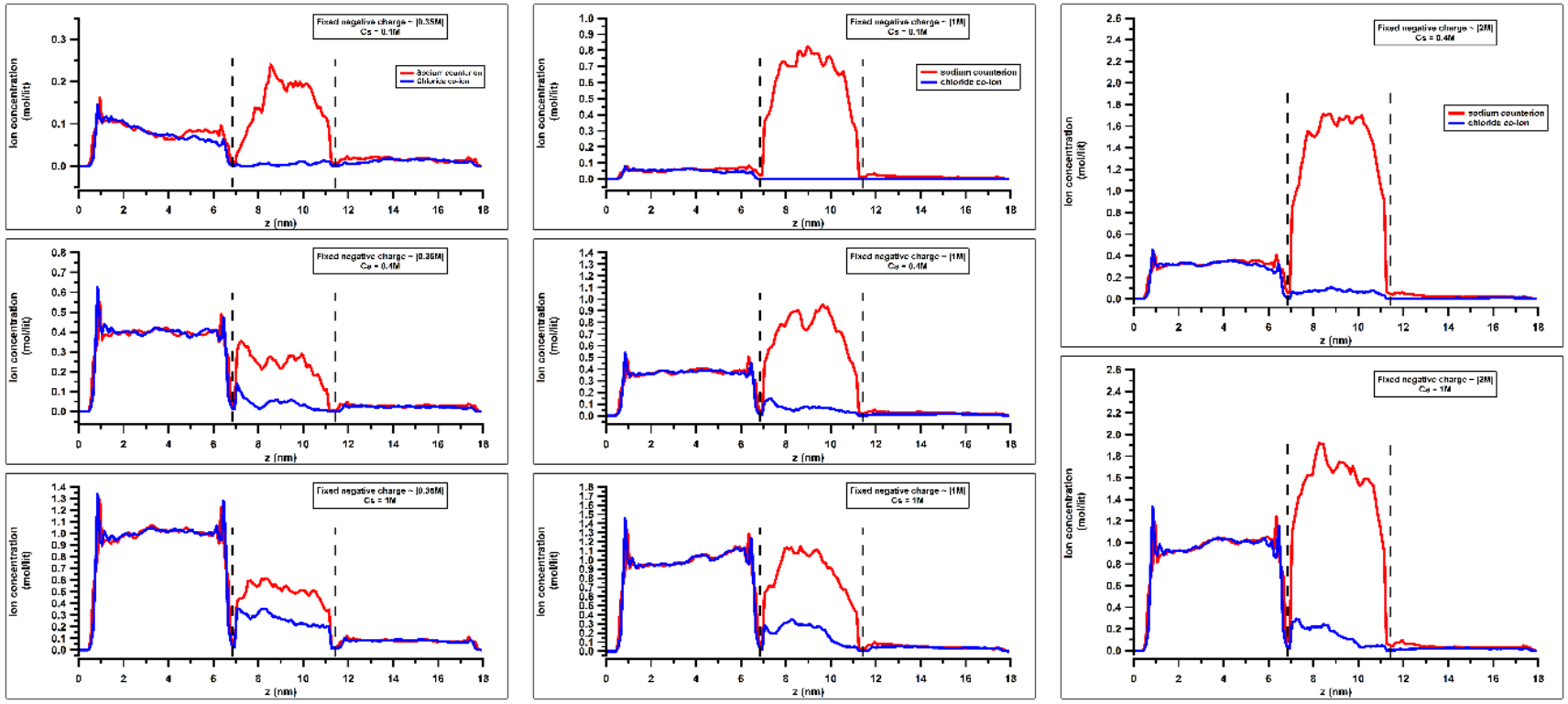

Figure 8-10: The axial concentration profiles for the various fixed-charge and external solution concentrations: *X* = 0.35 M (a), 1 M (b), and 2 M (c). The vertical dashed black lines serve as guides for the location of the graphene sheets.

concentration and low electrolyte flux. In order to attain high electrolyte rejection, the charge on the CNT must far exceed the strength of the high concentration reservoir.

At high external solution concentration, the electrostatic potential at the center decays to a very small value and we have found that we can correctly predict the electrolyte flux using the Nernst-Planck equation by inclusion of a partition coefficient for the co-ion that can be obtained from the MD concentration profile, the use of diffusion coefficients in the nanotube, and the diffusion potential. The partition coefficient implicitly takes into account the effect of the decayed electrostatic potential at the center of the nanotube.

We found a non-ideality for the case of low fixed-charge number where the ion flux is higher than the flux in the uncharged CNT. In the uncharged CNT, steric interactions cause low cation and anion partition coefficients, whereas in the case of the CNT with low fixed-charge number a higher amount of sodium counter-ions enter into the nanotube compared to the uncharged CNT owing to the electrostatic attraction to the negatively-charged CNT wall. Because of high ion-ion interactions inside the CNT, a greater number of chloride co-ions are attracted by the sodium counter-ions in the nanotube causing the co-ion occupancy to increase beyond its average value in the uncharged CNT. The higher number of co-ions in the lightly-charged nanotube results in a higher electrolyte flux and a worsening of the electrolyte rejection as compared to the uncharged CNT. In summary, this study has served as a demonstration of the controllability of ion flux by the modulation of the fixed-charges on the nanotube for different strengths of the high concentration reservoir.

Chapter 9. Electric field-driven ion transport through charged and uncharged single-walled carbon nanotubes

9.1 Introduction

We report the ion permeation trends obtained through a 3 nm diameter carbon nanotube (CNT) that connects two reservoirs, one containing a strong electrolyte at high concentration and the other containing water. We used field strengths that are an order of magnitude lower (one hundredth of a volt per nanometer) than those used in most studies of ion conduction that used larger electric fields (one tenth of a volt per nm)[207-210], which is greater than the dielectric breakdown voltage of water. The direction of the applied electric field is the same as the concentration gradient of the electrolyte and one may expect this to assist in cation transport by increasing the ion flux as compared to that of purely diffusive transfer; however, the trend for cation translocation events at long simulation times exhibits a slowdown after an initial spike. This slowdown in the number of ion permeation events is observed for all simulation systems regardless of the number of applied charges or the strength of the electric field. This retardation of the cation current with time is related to the development of an equilibrium potential arising out of a charge imbalance in the downstream reservoir that counterbalances the applied electric field, changing the initial field-driven ion migration into a primarily diffusive process. In the following sections, we describe the simulation method and theory and follow it up with a detailed analysis of the ion transfer phenomena under the scenario described herein.

9.2 Computational methods

The simulation setup is similar to the one used in the study for the diffusive transfer of ions where a carbon nanotube connects two bulk reservoirs containing sodium-chloride solutions of

unequal concentrations—see Figure 9-1. The CNT used in this study was 3 nm in diameter and 5 nm in length. The concentration of the electrolyte in compartment 1 was 1 M and compartment 2 contained pure TIP4P/2005 water. The reservoirs were bounded by rigid graphene walls. Ions could pass from one reservoir to the other only via the CNT. Three cases of negative fixed-charges on the tube were simulated (≈ 0.3 M, 1 M, and 2 M), which correspond to charge values of $5e^-$, $15e^-$, $30e^-$. The fixed-charges were calculated on the basis of the aqueous solution volume inside the nanotube and were uniformly distributed as partial charges on specific CNT atoms. An additional case where no charges were present on the tube was also considered as a control. An electric field was applied in the same direction as the concentration gradient. The electric field

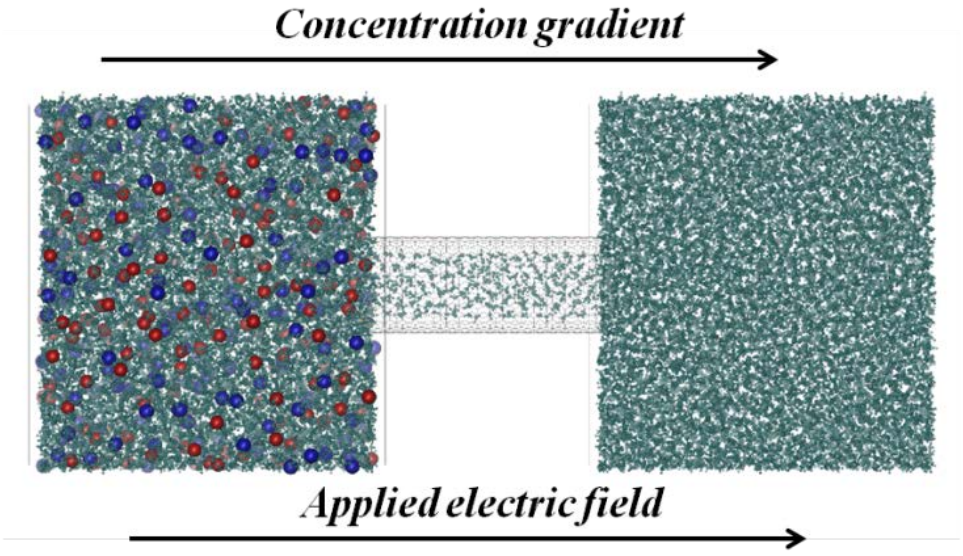

Figure 1

Figure 9-1: Schematic representation of the simulated system. The simulated particles are colored according to species: water molecules (cyan), sodium ions (red), chloride ions (blue), and carbon atoms (black).

strengths applied for each of the fixed-charge cases were 20 mV/nm, 40 mV/nm, 60 mV/nm, 80 mV/nm, and 100mV/nm. The total number of simulation cases thus generated was 20. Each system was equilibrated in the NVT ensemble for 1 ns followed by a 25 ns data collection phase. The MD simulation parameters are the same as those used for the previous case of diffusive transfer of ions and for the sake of brevity will not be repeated here.

9.3 Theory

Since the external solution concentration in the upstream reservoir is 1 M, the electric double layers ($\lambda = 0.3$ nm) that develop at the CNT entrance are expected to be thin compared to the tube diameter used in this study (3 nm). Ion transport is generally governed by the Nernst-Planck equation, which describes ion transport as a coupled process consisting of diffusion (concentration gradient), migration (electric field), and convection (pressure). In the absence of convection, the transport equation for the ions is

$$J_+ = -D^+ \frac{dC_+}{dx} - \frac{D^+ z_+ F}{RT} C_+ \frac{d\emptyset}{dx} \tag{9.1a}$$

$$J_- = -D^- \frac{dC_-}{dx} + \frac{D^- z_- F}{RT} C_- \frac{d\emptyset}{dx} \tag{9.1b}$$

If the electric field dominates the ion transport process, and assuming $\frac{d\emptyset}{dx} = \frac{\Delta\emptyset}{l} = constant$,

$$J_+ = -\frac{D^+ z_+ F}{RT} C_+ \frac{\Delta\emptyset}{l} \tag{9.2a}$$

$$J_- = \frac{D^- z_- F}{RT} C_- \frac{\Delta\emptyset}{l} \tag{9.2b}$$

$$D_+ = \frac{J_+ RT}{zFC} \frac{l}{\Delta\emptyset}; \tag{9.3a}$$

$$D_- = \frac{J_- RT}{zFC_-} \frac{l}{\Delta\emptyset} \tag{9.3b}$$

An applied electric field will induce a migration of sodium ions in the direction of the field and will propel the chloride ions in the opposite direction. Thus, initially, the net flux from the upstream to the downstream reservoir is promoted for sodium ions and retarded for chloride ions. By calculating the diffusion coefficient from the flux for sodium and chloride ions, it is apparent that the sodium diffusion coefficient is greater than that of chloride. This situation promotes large diffusion potentials that arise from charge separation, which act opposite to the applied electric field and reduce any further charge imbalance. This reduces the effective external electric field strength, which in turn retards the sodium ion transfer and tends to accelerate chloride ion transfer.

9.4 Results and discussion

The timescales associated with the MD simulations do not allow us to attain a steady-state transport process; however, they do permit a qualitative analysis of the transient transfer of ions from an upstream reservoir to a downstream reservoir through a CNT bridge under the combined effects of diffusion and migration. We contrast the process of diffusive transfer of ions under no external electric field (for which we observe a linear increase in the number of ions in the downstream reservoir) with the electro-migration process simulated here (where the increase in the number of ions in the downstream reservoir follows a non-linear trend for the timescales of observation).

In the presence of an electric field, the ion transport spikes initially and is followed by a slow permeation rate after the initial induction period. The induction times for the various fixed-charge cases are independent of the value of the applied electric field; these times are roughly shown by the dashed vertical lines in the Figure 9-2. The induction time is inversely proportional to the fixed-charge on the nanotube, with shorter induction times for tubes with greater fixed-

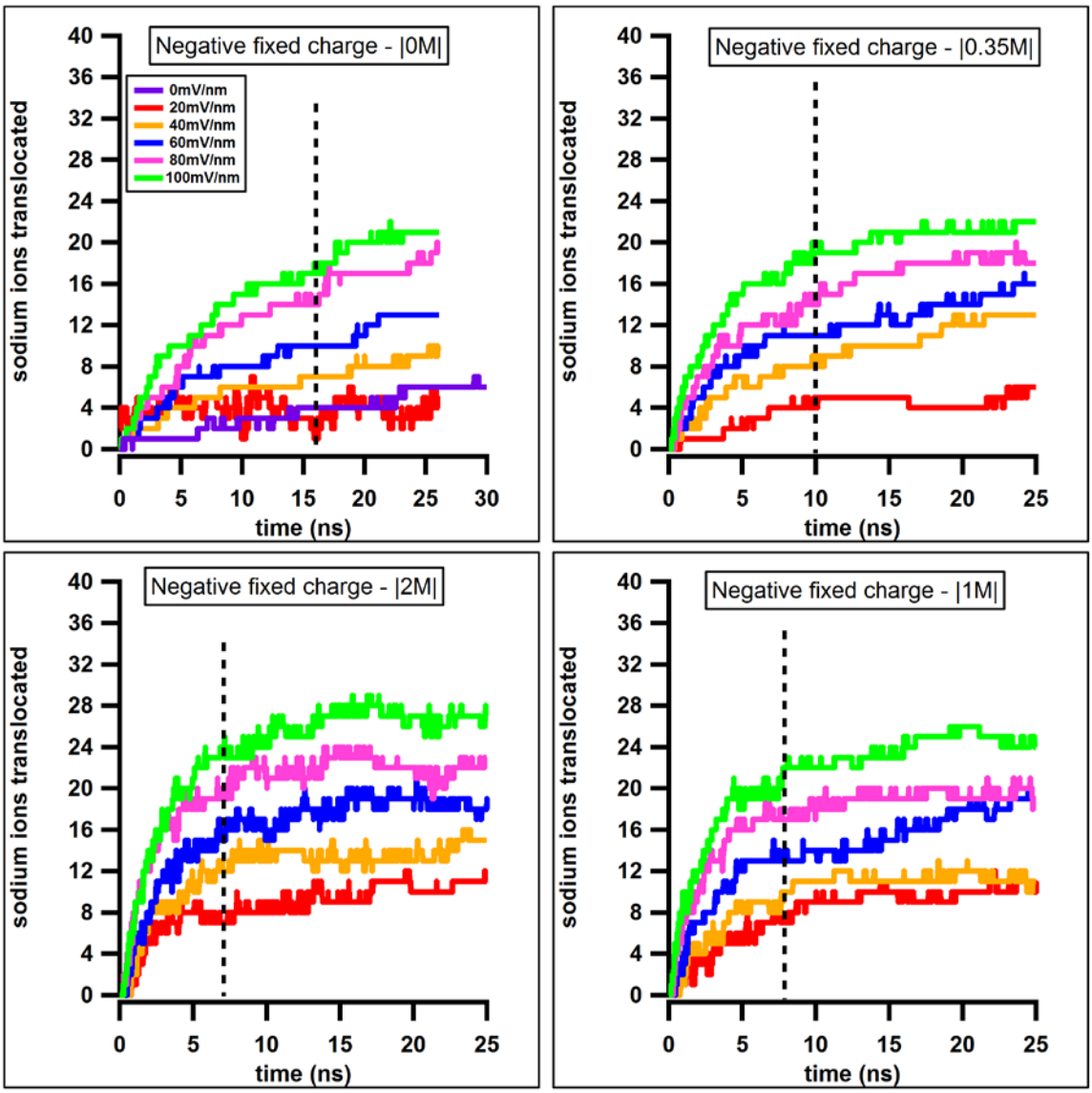

Figure 9-2: The number of sodium ions permeated from Reservoir 1 into Reservoir 2 for the various cases of negative fixed-charge on the (22,22) nanotube under the influence of an electric field and concentration gradient.

Panels clockwise from the upper left depict the number of sodium ions permeated from Reservoir 1 into Reservoir 2 for the various cases of negative fixed-charge on the nanotube corresponding to 0 M, 0.35 M, 1 M, and 2 M. Each case is simulated for six different field strengths: 0 mV/nm (purple), 20 mV/nm (red), 40 mV/nm (yellow), 60 mV/nm (blue), 80 mV/nm (pink), and 100 mV/nm (green).

charge and larger induction times for tubes with smaller fixed-charge. At the end of the induction period, the number of ions in reservoir 2 changes by less than 10% over the remainder of the simulation duration.

The observed current is obtained almost entirely from the transfer of cations. Tables 9-1 and 9-2 show the initial rapid cation transfer until the end of induction period followed by a very slow increase of ions in the second reservoir as the simulation progresses. (In a few cases, towards the end of recording time, the direction of cation transfer appears to reverse.) For the duration of observation, most of the cation transfer is achieved predominantly during the induction period. At the start of the simulation, the cations permeate as a result of the concentration gradient and the applied electric field, whereas the anions are completely rejected from the nanotube on account of the direction of the applied field. After a sufficient time (the 'induction time') has passed, the cations build up in the downstream reservoir, whereas the anions are mostly absent, causing a charge imbalance and loss of electroneutrality in compartment 2. This results in the downstream reservoir (i.e., compartment 2) becoming more positive with respect to compartment 1 and an electrical gradient develops for sodium ions in the opposite direction. This new electrical gradient that develops as a result of charge imbalance opposes the external electric field and, in the cases where fixed-charges are present on the tube, it also opposes the field developed by the fixed-charges. Such an electrical gradient counterbalances the applied electric field and the net transfer of sodium ions via migration stalls. This effectively forms an equilibrium potential or membrane potential. Thus the plateau in the trend for the number of sodium ions permeated indicates the approach towards an equilibrium potential for sodium and chloride ions that counterbalances the applied external electric field. Once the equilibrium potential is established, the transfer of cations and anions to the downstream reservoir can take place only via a diffusion process with the cations

Table 9-1: Number of cations in the downstream reservoir at different time intervals.

Fixed-charge	E (mV/nm)	$t = 5$ ns	$t = 10$ ns	$t = 15$ ns	$t = 20$ ns	$t = 25$ ns
0 M	**0**	1	3	4	4	6
0 M	**20**	4	1	3	4	4
	40	4	6	7	8	9
	60	6	8	10	11	13
	80	8	13	14	17	18
	100	10	15	17	20	21
0.35 M	**20**	2	4	5	4	6
	40	7	8	10	13	13
	60	9	11	13	14	16
	80	12	14	17	18	18
	100	15	19	21	21	22
1 M	**20**	5	9	10	10	11
	40	9	11	11	12	11
	60	12	14	15	18	19
	80	16	17	19	19	19
	100	18	22	23	26	24
2 M	**20**	8	8	9	10	11
	40	11	14	13	13	15
	60	14	15	18	19	18
	80	18	21	23	22	23
	100	21	25	28	27	27

Table 9-2: Number of cation permeation events in different time intervals. Note that C_t is the number of cations in the downstream reservoir at time *t*.

Fixed-charge	E (mV/nm)	$C_{t=5ns} - C_{t=0ns}$	$C_{t=10ns} - C_{t=5ns}$	$C_{t=15ns} - C_{t=10ns}$	$C_{t=20ns} - C_{t=15ns}$	$C_{t=25ns} - C_{t=20ns}$
0 M	**0**	1	2	1	0	2
0 M	**20**	4	-3	2	1	0
	40	4	2	1	1	1
	60	6	2	1	1	2
	80	8	5	1	3	1
	100	10	5	2	3	1
0.35 M	**20**	2	2	1	0	2
	40	7	1	2	3	0
	60	9	2	2	1	2
	80	12	2	3	1	0
	100	15	4	2	0	1
1 M	**20**	5	4	1	0	1
	40	9	2	0	1	-1
	60	12	2	1	3	1
	80	16	1	0	0	0
	100	18	4	1	3	-2
2 M	**20**	8	0	1	1	1
	40	11	3	-1	0	2
	60	14	1	3	1	-1
	80	18	3	2	-1	1
	100	21	4	3	-1	0

and anions travelling in pairs.

From Tables 9-3 and 9-4, it is evident that anion permeation starts during the later stage of data recording; i.e., after the equilibrium potential has been established. The chloride ions can transport against the electric field only via diffusion. As soon as more than one anion permeates through the nanotube to the downstream reservoir, we can expect the onset of a diffusive regime and a gradual decay of the migration process. A better understanding of this process can be achieved via Figure 9-2 for the case of the applied fixed-charge of 1 M and applied field strength of 60 mV/nm. The data show two distinct trends for ion permeation. First, there is an initial period from 0-7 ns where the cation permeation events rapidly increase and eventually plateau to set up the equilibrium or the reversal potential. Thereafter, ion transfer occurs via diffusion, as can be confirmed from the linear increase in the cation permeation events which occurs after the plateau region. These regions have two distinct slopes. If the simulation is extended to capture permeation events at long times, the plateau will merely appear as a hump with linear increase thereafter in the trend for the number of both species transferred from compartment 1 to 2. In the case where no charges are present on the tube and the field strength is low, the slope of this increase in the number of ions in compartment 2 will be more of less equal that which would be obtained in a regular diffusion process. Since diffusion is a slow process, if the simulation is extended to 100 ns, the diffusive trend will be clearly visible for the concentration gradient simulated here.

From Table 9-5, we can estimate the excess number of sodium ions that are required in reservoir 2 to initiate the equilibrium potential. At any given value of external electric field strength, the difference in the number of excess sodium ions in reservoir 2 obtained between the charged and the uncharged cases roughly corresponds to the values of the ions that diffuse into the

Table 9-3: Number of anions in the downstream reservoir at different time intervals.

Fixed-charge	E (mV/nm)	$t = 5$ ns	$t = 10$ ns	$t = 15$ ns	$t = 20$ ns	$t = 25$ ns
0 M	**0**	1	3	4	4	6
0 M	**20**	4	3	2	3	3
	40	0	0	0	0	1
	60	0	0	0	0	1
	80	0	0	0	2	3
	100	0	0	0	0	0
0.35 M	**20**	0	0	0	0	1
	40	0	0	0	3	3
	60	0	0	0	1	2
	80	0	0	0	0	1
	100	0	0	0	0	0
1 M	**20**	1	1	2	2	3
	40	0	0	0	0	0
	60	0	0	1	3	3
	80	0	0	0	0	1
	100	0	0	0	0	0
2 M	**20**	0	0	0	0	0
	40	0	0	0	0	0
	60	0	0	0	1	1
	80	0	0	1	1	1
	100	0	0	1	1	1

Table 9-4: Number of anion permeation events in different time intervals. A_t is the number of anions in the downstream reservoir at time *t*.

Fixed-charge	E (mV/nm)	$A_{t=5ns} - A_{t=0ns}$	$A_{t=10ns} - A_{t=5ns}$	$A_{t=15ns} - A_{t=10ns}$	$A_{t=20ns} - A_{t=15ns}$	$A_{t=25ns} - A_{t=20ns}$
0 M	**0**	1	2	1	0	2
0 M	**20**	4	-1	-1	1	1
	40	0	0	0	0	1
	60	0	0	0	0	1
	80	0	0	0	2	1
	100	0	0	0	0	0
0.35 M	**20**	0	0	0	0	1
	40	0	0	0	3	0
	60	0	0	0	1	1
	80	0	0	0	0	1
	100	0	0	0	0	0
1 M	**20**	1	0	1	0	1
	40	0	0	0	0	0
	60	0	0	1	2	0
	80	0	0	0	0	1
	100	0	0	0	0	0
2 M	**20**	0	0	0	0	0
	40	0	0	0	0	0
	60	0	0	0	1	0
	80	0	0	1	0	0
	100	0	0	1	0	0

Table 9-5: Difference in the number of cations and anions in Reservoir 2 in 25 ns.

Fixed-charge (M)	Electric field					
	0mV/nm	20mV/nm	40mV/nm	60mV/nm	80mv/nm	100mV/nm
0	0	1	8	12	15	21
0.35	1	5	10	14	17	22
1	3	8	11	16	18	24
2	6	11	15	17	22	26

downstream compartment when no external field is applied. This difference in the sodium ions required to set up the equilibrium potential between charged and uncharged cases is a consequence of the value of fixed-charge on the nanotube and this difference increases as the fixed-charge concentration on the tube increases. These values enable us to predict the equilibrium concentration of the reservoirs if the simulations were allowed to run for long durations. For instance, beginning with 280 ions (≈ 1 M) of each species in Reservoir 1 and for the case of 100 mV/nm of applied electric field, the initiation of the equilibrium potential requires the transfer of about 20 sodium ions. Thus, according to the equation for the equilibrium condition (Donnan equilibrium),

$$C_{NA,res1} \times C_{CL,res1} = C_{NA,res2} \times C_{CL,res2}$$

$$(280 - 20 - x) \times (280 - x) = (20 + x)(x) \tag{9.4}$$

Solving for x approximately gives the equilibrium number of ions in reservoir 1 as 130 (Na^+), 150 (Cl^-), and in reservoir 2 as 150 (Na^+), 130 (Cl^-). Hence the selectivity is established for the transfer of sodium ions over chloride ions, which is proportional to the magnitude of the membrane potential.

High charge separations give rise to high membrane potentials because a greater charge imbalance is required to counterbalance a larger applied electric field—see Figures 9-3a and b. Thus in the case of an external field strength of 100 mV/nm, compartment 2 has a higher number of sodium ions as compared to the case where the applied field strength is 40 mV/nm, resulting in a greater charge imbalance that is seen in Figure 9-3b and hence a greater membrane potential than that depicted in Figure 9-3a.

Figure 9-4 shows the ionic current, which is calculated by counting the number of ions in reservoir 2 at any instant (that is the number of ions permeated) and dividing it by the time that has elapsed since the beginning of the simulation until the instant at which the current is recorded.

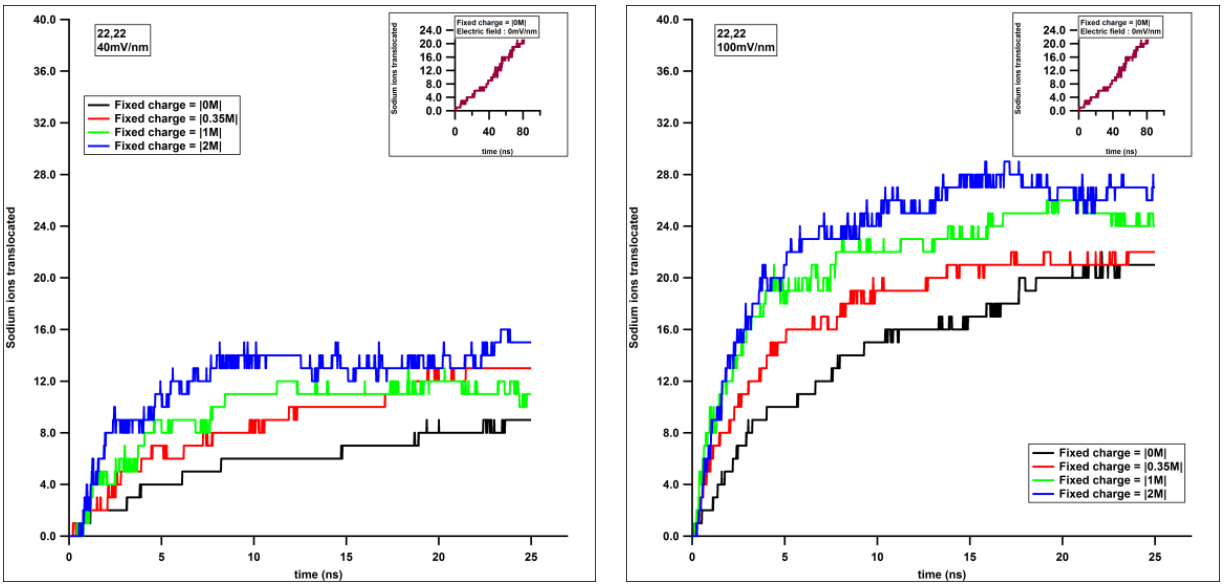

(a) **(b)**

Figure 9-3: : Sodium ions translocated from Reservoir 1 to 2 for all cases of fixed-charge at an external field of 40 mV/nm (a) and 100 mV/nm (b), respectively.

The insets show the ion permeation through the (22,22) nanotube in the absence of fixed-charges and applied fields.

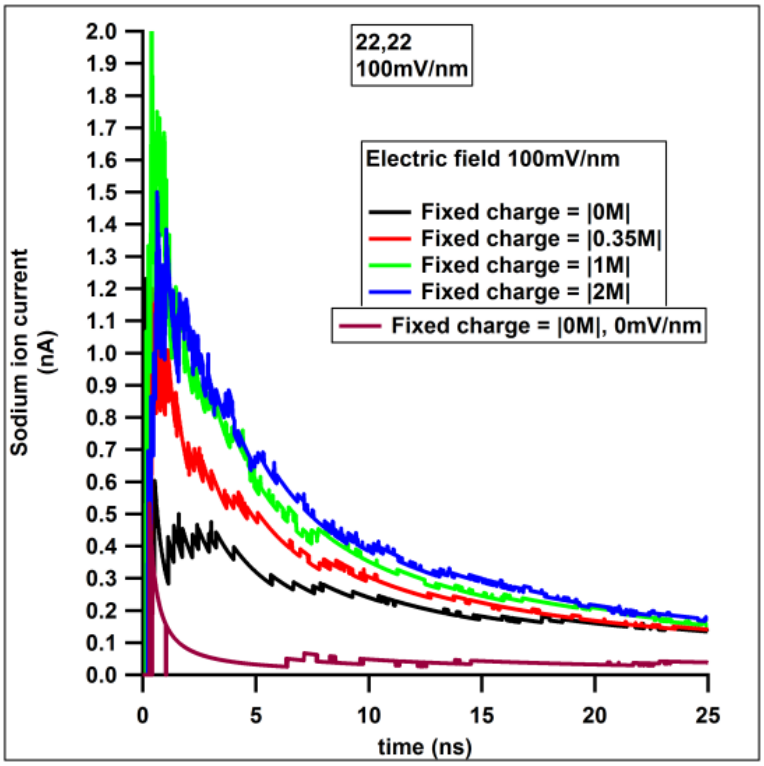

Figure 9-4: Sodium ion current vs. time.

It is obvious that the ion current at 100 mV/nm is greater than the current that would be obtained had the electric field been absent (i.e., from a purely diffusive transfer process). This current comes mainly from the initial ion migration events during the induction period.

The current that would be measured from the diffusive phase of the ion permeation (i.e., after the induction time) is shown in Figure 9-5. In this plot, the induction time is taken as the beginning of the simulation and the permeation events are counted thereafter for the current measurement. In this case, the ion currents closely resemble the values that would be obtained if no external fields were to be applied.

We extend the 25 ns simulation for the cases shown in Figures 9-6 a-c to 45 ns to view the electro-migration and diffusive regions with greater clarity. Figures 9-6 a-c show distinct time phases where ion permeation is dominated by the migration process at the beginning of the

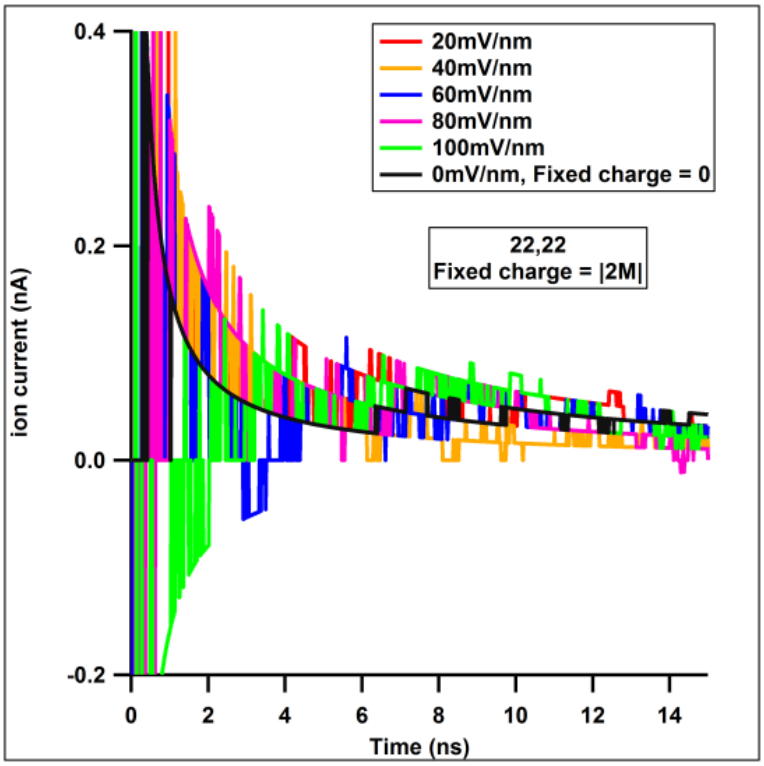

Figure 9-5: Sodium ion current vs. time (diffusive phase).

simulation and diffusion dominated after the equilibrium potential has been achieved. During the migration process, anion transfer to reservoir 2 is absent. In the absence of fixed-charges, diffusive regime has a steeper slope than when the tube has fixed-charges. In the diffusive regime, irrespective of the charge on the tube, the ions permeate in pairs maintaining charge neutrality of the ion transfer process. In the cases of tubes with fixed-charges, chloride ions are repelled by the fixed-charges on the nanotube and hence the chloride ion occupancy in the tube is low. The number of sodium and chloride ion pairs that can permeate is dependent on the chloride ion occupancy in the nanotube. Fewer chloride ions in the nanotube implies fewer sodium-chloride pairs diffusing into reservoir 2. Thus, at long times, one can expect a much slower ion transport process and hence a lower ion flux through tubes with higher number of fixed-charges.

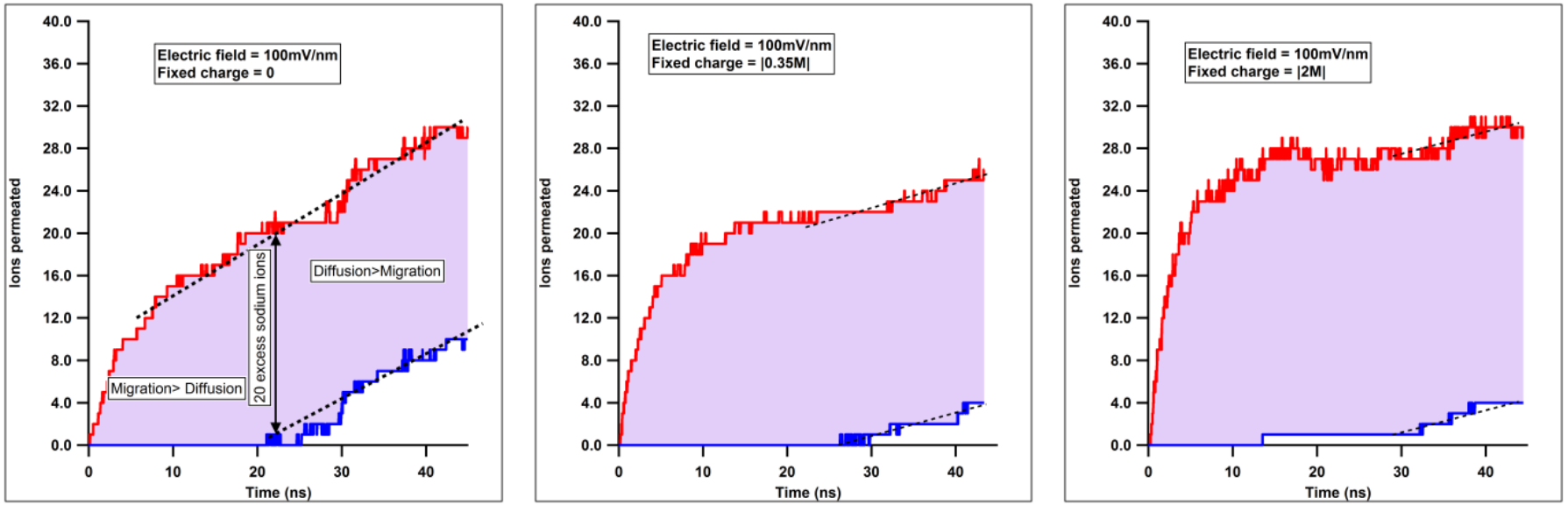

(a) **(b)** **(c)**

Figure 9-6: Ion permeation events vs. time at an applied field of 100 mV/nm for a CNT in which fixed-charges are absent (a), in which the fixed-charge is 0.35 M (b), and in which the fixed-charge is 1 M (c). Data for sodium ions are depicted in red whereas chlorine ion data are colored blue.

Axial concentration profiles

The average sodium and chloride ion axial concentration profiles obtained from the MD simulations for the last 15 ns (i.e., after the initial ion migration period) are shown in Figure 9-7. We do not observe concentration polarization at the entrance of the CNT for the electric field of 100 mV/nm and high external solution concentrations of 1 M. From previous experience, concentration polarization effects are important only at low external solution concentrations (100 mM). A gradient in concentration for sodium and chloride ions is witnessed in the case where no fixed-charges are applied on the tube. Since the concentration profiles are evaluated after the membrane potentials are established, the sodium and chloride ion concentrations in the nanotube in the absence of fixed-charges are equal despite the application of the external electric field. In the case where the tube possesses fixed-charges, the sodium counter-ion concentration is higher than the chloride concentration in the tube and remains more or less constant near the value of the applied fixed-charge with a slight gradient at end of the tube. The chloride ions in tubes with fixed-charges can migrate against the electric field only via diffusion; hence a concentration gradient for chloride is quite apparent inside the tube for all cases.

Current-voltage characteristics

We plot the ion current and conductivity vs. voltage (see Figure 9-8) for the first 15 ns of the simulations when the ion transport is dominated by the migration process. We find a linear increase in the ion current with voltage and the conductivity stays constant with voltage; this is typical of an ohmic process. At low voltages and in the case of the CNT with fixed-charges on the tube wall, the sodium ion current is a result of the higher rate of diffusion due to the attraction by the negative charge on the tube and the external electric field, which cause the high conductivity

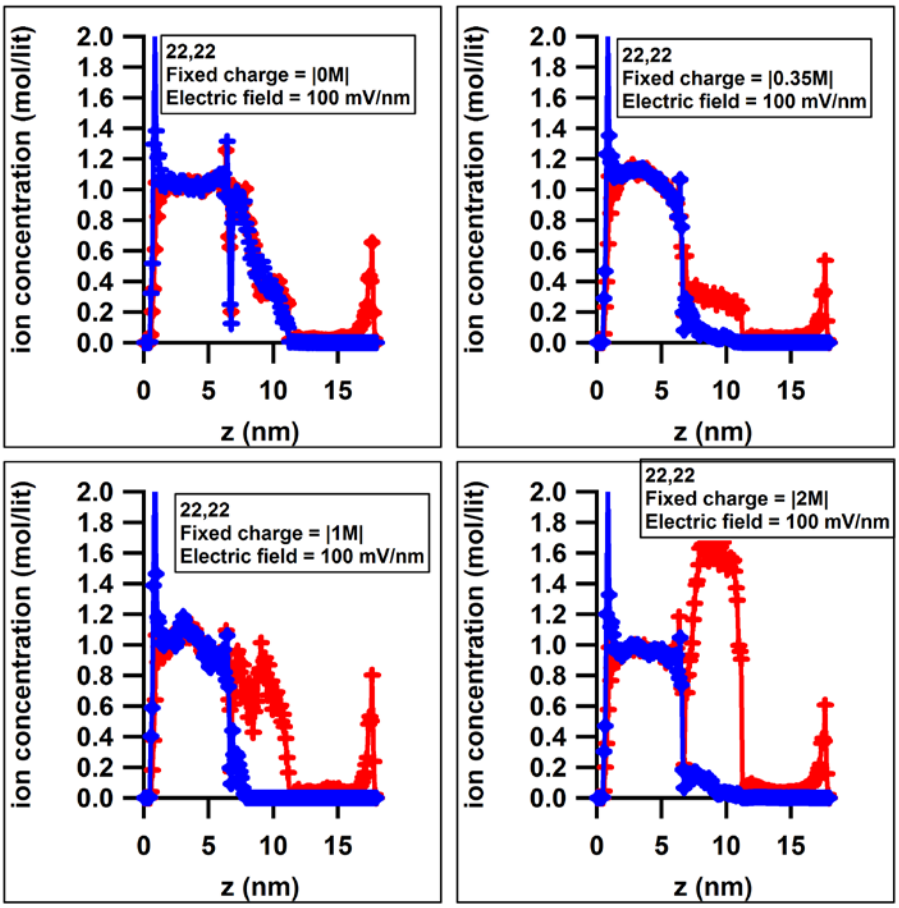

Figure 9-7: Ion concentration profiles in the axial direction. Sodium data is colored red, whereas chloride ion data are blue.

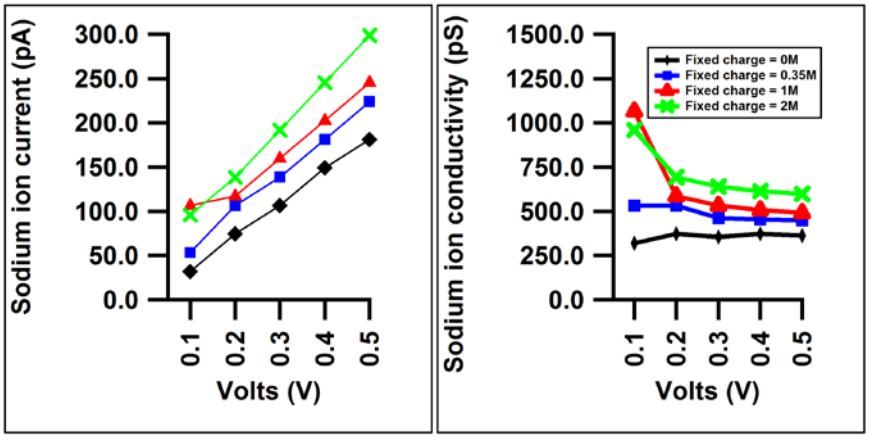

Figure 9-8: Sodium ion current and conductivity vs. voltage.

at the low applied voltages. At high applied field strengths, the contribution from diffusion is minimal as compared to that from migration, leading to a linear increase in current with voltage. The ion conductivity stays more or less constant at higher applied voltages and is a function of the fixed-charge on the tube, displaying increasing behavior with increasing fixed-charge number on the nanotube.

9.5 Conclusions

We have analyzed ion transport through carbon nanotubes under the influence of electric fields and have found that cation selectivity through a 3 nm diameter CNT increases to a greater extent with increasing electric field strengths and to a lesser extent with the magnitude of the negative fixed-charges on the tube. High equilibrium/depolarizing potentials are required to counterbalance the effects of high electric field and fixed-charge. This implies a greater charge imbalance will develop for the case of high electric fields and high fixed-charges before a sufficient equilibrium potential develops to halt any further migration of sodium ions.

The number of ions transferred to develop the equilibrium potential that counterbalances the applied electric field before the onset of the diffusive process is determined solely by the magnitude of the external electric field and of the fixed-charges on the tube and not by the imposed concentration gradient. Thus for any particular value of electric field, this results in a higher selectivity coefficient for cations and a higher rejection coefficient for anions when low concentration gradients are utilized, as compared to the case when the concentration gradients are high. The diffusive transport depends on the number of free ions (co-ions) in the nanotube which is governed by the magnitude of the fixed-charges (Donnan potential).

Chapter 10. Summary and perspective

In the last two decades, the exploration and revelation of their distinct properties (especially in terms of fluid structure under confinement) have caused 1-D and 2-D materials such as carbon nanotubes, graphene, and other nanoporous materials (such as graphene oxides, silica and boron nitride nanotubes) to gain prominence in the field of fluidics. For instance, in the case of fluids confined in a carbon nanotube, the restructuring of the encapsulated fluid leads to high solvent fluxes[23,110] and a steric rejection of solute, which could be exploited for biomimetic/biotechnological applications such as biosensors, field effect transistors for detection of protein binding[211], or in energy efficient desalination membranes[6]. While interest in the potential applications of the field of nanofluidics persists, it has also faced criticism with the prefix 'nano' becoming devalued through overuse[212] and some disappointment over the lack of commercial realization of the potential applications. However, only rigorous research geared towards unravelling the various coupled effects of surface interactions, charge interactions, and molecular component size can help accelerate the pace of development of novel nanofluidics devices or, at the very least, improve our understanding of fundamental nanoscale transport phenomena. In this dissertation, an effort was made to extend the current understanding of water and ion transport phenomena through carbon nanotubes for some representative cases by using molecular dynamics simulation. This study contains a thorough account of the structure, dynamics, energetics, and transport rates for water and ions that were obtained as functions of diameter, fixed-charge magnitudes and charge sign, external solution concentration, and electric field strength. The results of our studies were described in Chapters 4 through 9.

In **Chapter 4, "The general features of the structure and dynamics of water in single-walled carbon nanotubes"**, we investigated the structure, dynamics, and permeation rates of

water under confinement and compared our results with those from existing studies. Similar to the reports of previous simulation and experimental studies, we found that water assumes a layered structure under confinement. In larger diameter tubes (2.5-3 nm), it was found that layering in water structure is found mainly near the wall of the tubes whereas the fluid at the center of the tube resembles a more bulk-like structure. We observed anomalous dynamics in the (8,8) CNT, which can be attributed to the ice-like structure of water within the nanotube causing reduced mobility. The diffusion of water in CNTs is anisotropic as the molecular motion is severely restricted in the radial direction as compared to the axial direction. Water in a tube with chirality R > 10 follows clear Fickian diffusion; the mean-squared displacement plots for water in the (6,6) tube (which can only accommodate a single file of water) and in the (8,8) tube (where water assumes a square net-like structure) show apparently Fickian behavior for long time intervals and sub-diffusive behavior at short times. The axial diffusion coefficient of water is found to be slightly enhanced at the walls as compared to the center of the nanotube, owing to the reduced interaction between the CNT-water at the wall and the lower number of hydrogen bonds. We found a reduced number of hydrogen bonds of water under confinement in the nanotube as compared to those found in bulk water, but the hydrogen bonds have long lifetimes. A study of the permeation events in the (6,6) tube reveals the unidirectional bursts that were first observed by Hummer et al.[19] A comparison of the water permeation events with the controlled-time random walk (CTRW) model of Berezhkovskii et al.[20] was also shown. This study was used as validation of our method and model that was subsequently used to conduct comprehensive studies, mainly of ion transport through carbon nanotubes.

In **Chapter 5, "Ion uptake and the associated structure and dynamics of electrolytes in charged sub-3 nm carbon nanotubes"**, we obtained preliminary results of the influence of

electrostatics on the ion sorption trends in charged carbon nanotubes. Similar to the observations of Fornasiero et al.[51], these ion sorption isotherms bore similarity to the Donnan co-ion sorption trends. The results of this study served as a foundation allowing us to delve into a deeper investigation of the Donnan co-ion exclusion phenomena that was described in Chapter 6. We have also detailed the charge-related modifications in the structure of ions, the hydrogen bonding of water, and the diffusion coefficients of water. We found strikingly higher numbers of hydrogen bonds per water molecule and correspondingly lower diffusion coefficients of water in the positively-charged tubes as compared to the negatively-charged tubes. This demonstrated the ion specific structure making and breaking properties of sodium and chloride ions.

In **Chapter 6, "Pseudosteady-state diffusive transport of ions through carbon nanotubes",** we studied the passive transport of ions via diffusion across uncharged nanotubes using long time-scale molecular dynamics (MD) and have ascertained the rate of transport of ions as a function of CNT diameter. We were able to attain a steady-state diffusive flux over the duration of the MD simulation and we have demonstrated the power of MD as an alternative method to study nanoscale transport phenomena. The steady-state flux obtained from MD were contrasted against the result of Fick's law by neglecting the presence of a diffusive or liquid junction potential in the Nernst-Planck equation. The passive transport rates of ions obtained from MD are lower than those predicted by Fick's law. The rate of ion transport through nanotubes did not only depend on the magnitude of the concentration gradient imposed, but also depended on the permeability or the partition coefficients of ions and the modification of their diffusion coefficients in the nanotube. The partition coefficients and diffusion coefficients were both functions of diameter of the nanotube, and as result we obtained a diameter-dependent flux, as opposed to the Fickian ion flux (which is diameter independent). This was the reason for the deviation observed

between our results for ion flux and the results of macroscopic Fick's law. We have additionally also provided results of the energy barriers associated with the transport of ions through nanotubes that were calculated using umbrella sampling and free energy perturbation methods, and structural modification of the ion hydration shell during translocation through the CNT. These simulations also helped reveal additional information, such as ion pairing during translocation, ion residence times, and hydrogen bond modifications.

Previous studies have suggested that ion exclusion through charged nanotubes followed a trend that closely resembled the one obtained from Donnan theory[51]. We thus measured the co-ion exclusion in uniformly-charged CNTs of different diameters bearing partial charges that were in contact with strong electrolytes of high concentration and compared the results with the predictions of Donnan theory. The results of this study were reported in **Chapter 7, "A molecular dynamics study of electrolyte exclusion in charged carbon nanotubes via steric and electrostatic interactions: A comparison with Donnan theory."** We have found that co-ion exclusion in nanotubes is higher than that predicted by Donnan theory mostly on account of the additional steric exclusion to the electrostatic exclusion via charge repulsion. Donnan theory provides an inadequate description of ion exclusion in charged CNTs, especially when the CNT is in contact with solutions of high concentration. This happens mostly because of three important factors: first, the actual potential over the pore is non-uniform as opposed to the Donnan assumption of a uniform pore potential. The potential inside the CNT at the center of the tube that is in contact with high solution concentrations is quite low and ions at the center are shielded from the wall potential. The resulting concentration of the ions in the center of the tube is driven predominantly by diffusion rather than via electrostatics. This implies a worsening of the Donnan co-ion exclusion trend; however, we found that the exclusion is actually higher, which has to do with the second factor;

i.e., of ions having finite sizes that show a diameter-dependent partitioning. Finally, ion–ion correlations lead to some very specific ordering inside the nanotubes and can cause deviations from the predicted ion concentrations. Correcting Donnan theory for the relevant pore potential only leads to the Poisson-Boltzmann equation, which is not as easy a starting point as Donnan theory. This study allowed us to understand how the predictive power of the continuum-based equation is affected by the underlying assumptions of the mean-field approach, which leads to significant deviations with the actual observed ion concentrations.

In **Chapter 8, "Electrolyte diffusion through uniformly charged carbon nanotubes",** we studied the passive transport rates of electrolyte diffusion through uniformly-charged carbon nanotubes bearing different fixed-charges and with different solution strengths in the high concentration reservoir. We contrasted the results to the rates of ion transport observed through uncharged tubes and mainly found that the steady-state flux varies inversely with the magnitude of the fixed-charge on the tube and is lower than the flux obtained through uncharged tubes. The transport rate is determined by the strength of the pore potential (the Donnan potential), which determines the extent to which co-ions (also known as free ions) are present in the tube. Through this study, we have demonstrated the controllability of ion flux via a modulation of the fixed-charges on the nanotube for different strengths of the external reservoir.

In **Chapter 9. "Electric field-driven ion transport through charged and uncharged single-walled carbon nanotubes",** we reported the electric field-driven ion permeation trends through a charged 3 nm CNT in contact with a reservoir containing strong electrolyte at a high concentration. One of the salient features of this study was the use of much lower and more realistic electric field strengths than the fields generally employed in prior MD studies to circumvent the issue of a limited timescale and drive transport. Using these low field strengths, we were able to

characterize the permeation process as being dominated by two different processes at two different stages of the simulation duration. Initially persisting for a few nanoseconds, we have a migration-driven ion transport (electric field-driven) where a large permeate flux of cations in the direction of the applied field is achieved while the anions are completely rejected. The excess cations collected in the low concentration reservoir causes a charge imbalance and generates a field that counterbalances the applied external field, thus eventually stalling the migration process and marking the onset of the diffusive transport. The diffusive transport phenomena through charged nanotubes used in the simulation, even under the influence of electric field, bears conceptual similarity to the transport described in Chapter 8; i.e., it is dependent on the Donnan potential and the number of co-ions in the nanotubes.

The treatment described in this dissertation is general and is applicable to study of transport through other nanoporous media. It is certainly hoped that this work stimulates continuing efforts at exploring and clarifying the nanoscale transport behavior of water and ions, not only in carbon nanotubes but also in other promising nanoporous materials, such boron nitride tubes (that have been reported to have water permeation rates even greater than those seen in carbon nanotubes), graphene-based pores, and graphene oxide/metal oxide frameworks.

Bibliography

1 Schoch, R. B., Han, J. & Renaud, P. Transport phenomena in nanofluidics. *Rev Mod Phys* **80**, 839 (2008).
2 Abgrall, P. & Nguyen, N. T. Nanofluidic Devices and Their Applications. *Analytical chemistry* **80**, 2326-2341, doi:10.1021/ac702296u (2008).
3 Foldvari, M. & Bagonluri, M. Carbon nanotubes as functional excipients for nanomedicines: II. Drug delivery and biocompatibility issues. *Nanomedicine: Nanotechnology, Biology and Medicine* **4**, 183-200 (2008).
4 Li, J. *et al.* Carbon nanotube nanoelectrode array for ultrasensitive DNA detection. *Nano letters* **3**, 597-602 (2003).
5 Shim, M., Shi Kam, N. W., Chen, R. J., Li, Y. & Dai, H. Functionalization of carbon nanotubes for biocompatibility and biomolecular recognition. *Nano letters* **2**, 285-288 (2002).
6 Corry, B. Designing carbon nanotube membranes for efficient water desalination. *The Journal of Physical Chemistry B* **112**, 1427-1434 (2008).
7 Wang, C. *et al.* Wafer-scale integration of sacrificial nanofluidic chips for detecting and manipulating single DNA molecules. **8**, 14243, doi:10.1038/ncomms14243 https://www.nature.com/articles/ncomms14243#supplementary-information (2017).
8 Weerakoon-Ratnayake, K. M., O'Neil, C. E., Uba, F. I. & Soper, S. A. Thermoplastic nanofluidic devices for biomedical applications. *Lab on a chip* **17**, 362-381, doi:10.1039/C6LC01173J (2017).
9 Tans, S. J., Verschueren, A. R. M. & Dekker, C. Room-temperature transistor based on a single carbon nanotube. *Nature* **393**, 49-52 (1998).
10 Qiu, C. *et al.* Scaling carbon nanotube complementary transistors to 5-nm gate lengths. *Science* **355**, 271-276, doi:10.1126/science.aaj1628 (2017).
11 Jensen, K., Weldon, J., Garcia, H. & Zettl, A. Nanotube Radio. *Nano letters* **7**, 3508-3511, doi:10.1021/nl0721113 (2007).
12 Nihey, F. (Google Patents, 2002).
13 Agre, P. *et al.* Aquaporin CHIP: the archetypal molecular water channel. *American Journal of Physiology - Renal Physiology* **265**, F463-F476 (1993).
14 Doyle, D. A. *et al.* The Structure of the Potassium Channel: Molecular Basis of K⁺ Conduction and Selectivity. *Science* **280**, 69-77, doi:10.1126/science.280.5360.69 (1998).
15 MacKinnon, R., Cohen, S. L., Kuo, A., Lee, A. & Chait, B. T. Structural Conservation in Prokaryotic and Eukaryotic Potassium Channels. *Science* **280**, 106-109, doi:10.1126/science.280.5360.106 (1998).
16 Hille, B. *Ion channels of excitable membranes*. Vol. 507 (Sinauer Sunderland, MA, 2001).
17 De Volder, M. F., Tawfick, S. H., Baughman, R. H. & Hart, A. J. Carbon nanotubes: present and future commercial applications. *Science* **339**, 535-539 (2013).
18 Dresselhaus, M. S., Dresselhaus, G., Eklund, P. & Rao, A. in *The Physics of Fullerene-Based and Fullerene-Related Materials* 331-379 (Springer, 2000).
19 Hummer, G., Rasaiah, J. C. & Noworyta, J. P. Water conduction through the hydrophobic channel of a carbon nanotube. *Nature* **414**, 188-190 (2001).
20 Berezhkovskii, A. & Hummer, G. Single-file transport of water molecules through a carbon nanotube. *Phys Rev Lett* **89**, 064503 (2002).
21 Kalra, A., Garde, S. & Hummer, G. Osmotic water transport through carbon nanotube membranes. *Proceedings of the National Academy of Sciences* **100**, 10175-10180 (2003).

22 Majumder, M., Chopra, N., Andrews, R. & Hinds, B. J. Nanoscale hydrodynamics: Enhanced flow in carbon nanotubes. *Nature* **438**, 44-44, doi:http://www.nature.com/nature/journal/v438/n7064/suppinfo/438044a_S1.html (2005).
23 Holt, J. K. *et al.* Fast mass transport through sub-2-nanometer carbon nanotubes. *Science* **312**, 1034-1037 (2006).
24 Thomas, J. A. & McGaughey, A. J. H. Reassessing Fast Water Transport Through Carbon Nanotubes. *Nano letters* **8**, 2788-2793, doi:10.1021/nl8013617 (2008).
25 Zhang, Y., Tunuguntla, R. H., Choi, P.-O. & Noy, A. Real-time dynamics of carbon nanotube porins in supported lipid membranes visualized by high-speed atomic force microscopy. *Philosophical Transactions of the Royal Society B: Biological Sciences* **372**, doi:10.1098/rstb.2016.0226 (2017).
26 Noy, A. *et al.* Nanofluidics in carbon nanotubes. *Nano Today* **2**, 22-29, doi:http://dx.doi.org/10.1016/S1748-0132(07)70170-6 (2007).
27 Hersam, M. C. Progress towards monodisperse single-walled carbon nanotubes. *Nature nanotechnology* **3**, 387-394 (2008).
28 Guzmán de Villoria, R., Hart, A. J. & Wardle, B. L. Continuous High-Yield Production of Vertically Aligned Carbon Nanotubes on 2D and 3D Substrates. *ACS nano* **5**, 4850-4857, doi:10.1021/nn2008645 (2011).
29 Raja Noor Amalina Raja, S., Mohd Asyadi, A. & Mohd Ambri, M. Highly efficient growth of vertically aligned carbon nanotubes on Fe–Ni based metal alloy foils for supercapacitors. *Advances in Natural Sciences: Nanoscience and Nanotechnology* **7**, 045016 (2016).
30 Koga, K., Gao, G. T., Tanaka, H. & Zeng, X. C. Formation of ordered ice nanotubes inside carbon nanotubes. *Nature* **412**, 802-805 (2001).
31 Agrawal, K. V., Shimizu, S., Drahushuk, L. W., Kilcoyne, D. & Strano, M. S. Observation of extreme phase transition temperatures of water confined inside isolated carbon nanotubes. *Nat Nano* **12**, 267-273, doi:10.1038/nnano.2016.254 http://www.nature.com/nnano/journal/v12/n3/abs/nnano.2016.254.html#supplementary-information (2017).
32 Gordillo, M. & Martı, J. Hydrogen bond structure of liquid water confined in nanotubes. *Chem Phys Lett* **329**, 341-345 (2000).
33 Dalla Bernardina, S. *et al.* Water in carbon nanotubes: the peculiar hydrogen bond network revealed by infrared spectroscopy. *Journal of the American Chemical Society* **138**, 10437-10443 (2016).
34 Byl, O. *et al.* Unusual Hydrogen Bonding in Water-Filled Carbon Nanotubes. *Journal of the American Chemical Society* **128**, 12090-12097, doi:10.1021/ja057856u (2006).
35 Hanasaki, I. & Nakatani, A. Hydrogen bond dynamics and microscopic structure of confined water inside carbon nanotubes. *The Journal of chemical physics* **124**, 174714, doi:10.1063/1.2194540 (2006).
36 Mashl, R. J., Joseph, S., Aluru, N. & Jakobsson, E. Anomalously immobilized water: a new water phase induced by confinement in nanotubes. *Nano letters* **3**, 589-592 (2003).
37 Zhang, H., Ye, H., Zheng, Y. & Zhang, Z. Prediction of the viscosity of water confined in carbon nanotubes. *Microfluid Nanofluid* **10**, 403-414, doi:10.1007/s10404-010-0678-0 (2011).
38 Dellago, C., Naor, M. M. & Hummer, G. Proton transport through water-filled carbon nanotubes. *Phys Rev Lett* **90**, 105902 (2003).

39 Peter, C. & Hummer, G. Ion Transport through Membrane-Spanning Nanopores Studied by Molecular Dynamics Simulations and Continuum Electrostatics Calculations. *Biophysical journal* **89**, 2222-2234, doi:10.1529/biophysj.105.065946 (2005).
40 Lodish, H. *et al.* Intracellular ion environment and membrane electric potential. (2000).
41 Galama, A. *et al.* On the origin of the membrane potential arising across densely charged ion exchange membranes: How well does the Teorell-Meyer-Sievers theory work? *Journal of Membrane Science and Research* (2015).
42 Eisenberg, B. Permeation as a diffusion process. *arXiv preprint arXiv:0807.0721* (2008).
43 Bocquet, L. & Charlaix, E. Nanofluidics, from bulk to interfaces. *Chemical Society reviews* **39**, 1073-1095, doi:10.1039/b909366b (2010).
44 Andelman, D. Electrostatic properties of membranes: the Poisson-Boltzmann theory. *Handbook of biological physics* **1**, 603-642 (1995).
45 Vlachy, V. & Prausnitz, J. M. Donnan equilibrium: hypernetted-chain study of one-component and multicomponent models for aqueous polyelectrolyte solutions. *The Journal of Physical Chemistry* **96**, 6465-6469, doi:10.1021/j100194a066 (1992).
46 Vlachy, V. Ionic effects beyond Poisson-Boltzmann theory. *Annual review of physical chemistry* **50**, 145-165 (1999).
47 Donnan, F. G. Theorie der Membrangleichgewichte und Membranpotentiale bei Vorhandensein von nicht dialysierenden Elektrolyten. Ein Beitrag zur physikalisch-chemischen Physiologie. *Berichte der Bunsengesellschaft für physikalische Chemie* **17**, 572-581 (1911).
48 Donnan, F. G. The theory of membrane equilibria. *Chemical reviews* **1**, 73-90 (1924).
49 Dähnert, K. & Huster, D. Comparison of the Poisson–Boltzmann Model and the Donnan Equilibrium of a Polyelectrolyte in Salt Solution. *Journal of colloid and interface science* **215**, 131-139, doi:http://dx.doi.org/10.1006/jcis.1999.6238 (1999).
50 Galama, A. H., Post, J. W., Cohen Stuart, M. A. & Biesheuvel, P. M. Validity of the Boltzmann equation to describe Donnan equilibrium at the membrane–solution interface. *J Membrane Sci* **442**, 131-139, doi:http://dx.doi.org/10.1016/j.memsci.2013.04.022 (2013).
51 Fornasiero, F. *et al.* Ion exclusion by sub-2-nm carbon nanotube pores. *Proceedings of the National Academy of Sciences* **105**, 17250-17255 (2008).
52 Hoffmann, J. & Gillespie, D. Ion correlations in nanofluidic channels: effects of ion size, valence, and concentration on voltage-and pressure-driven currents. *Langmuir : the ACS journal of surfaces and colloids* **29**, 1303-1317 (2013).
53 Frenkel, D. & Smit, B. (Academic press, 2001).
54 Allen, M. P. & Tildesley, D. J. *Computer simulation of liquids*. (Clarendon Press, 1989).
55 Torrie, G. M. & Valleau, J. P. Nonphysical sampling distributions in Monte Carlo free-energy estimation: Umbrella sampling. *J Comput Phys* **23**, 187-199, doi:http://dx.doi.org/10.1016/0021-9991(77)90121-8 (1977).
56 Bennett, C. H. Efficient estimation of free energy differences from Monte Carlo data. *J Comput Phys* **22**, 245-268 (1976).
57 Hofmann, D. & Tocci, E. in *Membrane Operations: Innovative Separations and Transformations* (eds E. Drioli & L. Giorno) (Wiley, 2009).
58 van Gunsteren, W. F. & Berendsen, H. J. Computer simulation of molecular dynamics: Methodology, applications, and perspectives in chemistry. *Angewandte Chemie International Edition* **29**, 992-1023 (1990).

59 Meller, J. Molecular dynamics. *eLS* (2001).
60 Toghraee, R., Mashl, R. J., Lee, K. I., Jakobsson, E. & Ravaioli, U. Simulation of charge transport in ion channels and nanopores with anisotropic permittivity. *Journal of computational electronics* **8**, 98-109, doi:10.1007/s10825-009-0272-4 (2009).
61 Tieleman, D. P., Biggin, P. C., Smith, G. R. & Sansom, M. S. Simulation approaches to ion channel structure-function relationships. *Quarterly reviews of biophysics* **34**, 473-561 (2001).
62 Ercolessi, F. A molecular dynamics primer.
63 Karplus, M. & McCammon, J. A. Molecular dynamics simulations of biomolecules. *Nat Struct Mol Biol* **9**, 646-652 (2002).
64 Gong, X. *et al.* A charge-driven molecular water pump. *Nature nanotechnology* **2**, 709-712 (2007).
65 Wong-ekkabut, J., Miettinen, M. S., Dias, C. & Karttunen, M. Static charges cannot drive a continuous flow of water molecules through a carbon nanotube. *Nat Nano* **5**, 555-557 (2010).
66 Wong-ekkabut, J. & Karttunen, M. The good, the bad and the user in soft matter simulations. *Biochimica et Biophysica Acta (BBA)-Biomembranes* **1858**, 2529-2538 (2016).
67 Darden, T., York, D. & Pedersen, L. Particle mesh Ewald: An N· log (N) method for Ewald sums in large systems. *The Journal of chemical physics* **98**, 10089-10092 (1993).
68 Cheatham, T. I., Miller, J., Fox, T., Darden, T. & Kollman, P. Molecular dynamics simulations on solvated biomolecular systems: the particle mesh Ewald method leads to stable trajectories of DNA, RNA, and proteins. *Journal of the American Chemical Society* **117**, 4193-4194 (1995).
69 Varma, S. & Rempe, S. B. Coordination numbers of alkali metal ions in aqueous solutions. *Biophys Chem* **124**, 192-199 (2006).
70 van der Spoel, D., van Maaren, P. J., Larsson, P. & Tîmneanu, N. Thermodynamics of Hydrogen Bonding in Hydrophilic and Hydrophobic Media. *The Journal of Physical Chemistry B* **110**, 4393-4398, doi:10.1021/jp0572535 (2006).
71 Prada-Gracia, D., Shevchuk, R. & Rao, F. The quest for self-consistency in hydrogen bond definitions. *The Journal of chemical physics* **139**, 084501, doi:10.1063/1.4818885 (2013).
72 Tay, K. A. & Bresme, F. Kinetics of hydrogen-bond rearrangements in bulk water. *Physical Chemistry Chemical Physics* **11**, 409-415, doi:10.1039/B813896F (2009).
73 Luzar, A. & Chandler, D. Hydrogen-bond kinetics in liquid water. *Nature* **379**, 55 (1996).
74 Sheu, S.-Y., Yang, D.-Y., Selzle, H. & Schlag, E. Energetics of hydrogen bonds in peptides. *Proceedings of the National Academy of Sciences* **100**, 12683-12687 (2003).
75 Ren, H. *et al.* Interfacial structure and wetting properties of water droplets on graphene under a static electric field. *Physical chemistry chemical physics : PCCP* **17**, 23460-23467, doi:10.1039/c5cp04205d (2015).
76 Smart, O. S., Goodfellow, J. M. & Wallace, B. A. The pore dimensions of gramicidin A. *Biophysical journal* **65**, 2455-2460, doi:http://dx.doi.org/10.1016/S0006-3495(93)81293-1 (1993).
77 Zhao, G. *et al.* Structure and properties of water film adsorbed on mica surfaces. *The Journal of chemical physics* **143**, 104705, doi:10.1063/1.4930274 (2015).

78 Radmer, R. J. & Kollman, P. A. Free energy calculation methods: a theoretical and empirical comparison of numerical errors and a new method qualitative estimates of free energy changes. *J Comput Chem* **18**, 902-919 (1997).
79 Asthagiri, D. & Bashford, D. Continuum and Atomistic Modeling of Ion Partitioning into a Peptide Nanotube. *Biophysical journal* **82**, 1176-1189, doi:https://doi.org/10.1016/S0006-3495(02)75475-1 (2002).
80 Pronk, S. *et al.* GROMACS 4.5: a high-throughput and highly parallel open source molecular simulation toolkit. *Bioinformatics* **29**, 845-854, doi:10.1093/bioinformatics/btt055 (2013).
81 Zhang, X. *et al.* Crystal structure of an orthologue of the NaChBac voltage-gated sodium channel. *Nature* **486**, 130-134, doi:10.1038/nature11054 (2012).
82 Payandeh, J., Gamal El-Din, T. M., Scheuer, T., Zheng, N. & Catterall, W. A. Crystal structure of a voltage-gated sodium channel in two potentially inactivated states. *Nature* **486**, 135-139, doi:10.1038/nature11077 (2012).
83 Lou, K. L. *et al.* Structural and functional characterization of OmpF porin mutants selected for larger pore size. I. Crystallographic analysis. *The Journal of biological chemistry* **271**, 20669-20675 (1996).
84 Moldenhauer, H., Diaz-Franulic, I., Gonzalez-Nilo, F. & Naranjo, D. Effective pore size and radius of capture for K(+) ions in K-channels. *Sci Rep* **6**, 19893, doi:10.1038/srep19893 (2016).
85 Unwin, N. Refined structure of the nicotinic acetylcholine receptor at 4A resolution. *Journal of molecular biology* **346**, 967-989, doi:10.1016/j.jmb.2004.12.031 (2005).
86 Christ, C. D., Mark, A. E. & van Gunsteren, W. F. Feature Article Basic Ingredients of Free Energy Calculations: A Review. *J Comput Chem* **31**, 1569-1582, doi:10.1002/jcc.21450 (2010).
87 Kumar, S., Rosenberg, J. M., Bouzida, D., Swendsen, R. H. & Kollman, P. A. THE weighted histogram analysis method for free-energy calculations on biomolecules. I. The method. *J Comput Chem* **13**, 1011-1021, doi:10.1002/jcc.540130812 (1992).
88 Marrink, S. J. & Berendsen, H. J. C. Simulation of Water Transport through a Lipid-Membrane. *J Phys Chem-Us* **98**, 4155-4168, doi:Doi 10.1021/J100066a040 (1994).
89 Roux, B. & Karplus, M. Ion transport in a gramicidin-like channel: dynamics and mobility. *The Journal of Physical Chemistry* **95**, 4856-4868, doi:10.1021/j100165a049 (1991).
90 Vorobyov, I. *et al.* Ion-Induced Defect Permeation of Lipid Membranes. *Biophysical journal* **106**, 586-597, doi:10.1016/j.bpj.2013.12.027 (2014).
91 Iijima, S. Helical microtubules of graphitic carbon. *Nature* **354**, 56-58 (1991).
92 Tersoff, J. & Ruoff, R. Structural properties of a carbon-nanotube crystal. *Phys Rev Lett* **73**, 676 (1994).
93 Bacsa, W. *et al.* Aligned carbon nanotube films: production and optical and electronic properties. *Science* **268**, 845-847 (1995).
94 Ruoff, R. S. & Lorents, D. C. Mechanical and thermal properties of carbon nanotubes. *carbon* **33**, 925-930 (1995).
95 José-Yacamán, M., Miki-Yoshida, M., Rendon, L. & Santiesteban, J. Catalytic growth of carbon microtubules with fullerene structure. *Appl Phys Lett* **62**, 202-204 (1993).
96 Guo, T. *et al.* Self-assembly of tubular fullerenes. *The Journal of Physical Chemistry* **99**, 10694-10697 (1995).
97 Ebbesen, T. W. Carbon nanotubes. *Annual review of materials science* **24**, 235-264 (1994).

98 Wilder, J. W., Venema, L. C., Rinzler, A. G., Smalley, R. E. & Dekker, C. Electronic structure of atomically resolved carbon nanotubes. *Nature* **391**, 59-62 (1998).
99 Sanvito, S., Kwon, Y.-K., Tománek, D. & Lambert, C. J. Fractional quantum conductance in carbon nanotubes. *Phys Rev Lett* **84**, 1974 (2000).
100 Hone, J., Whitney, M., Piskoti, C. & Zettl, A. Thermal conductivity of single-walled carbon nanotubes. *Phys Rev B* **59**, R2514 (1999).
101 Dekker, C. Carbon nanotubes as molecular quantum wires. *Physics today* **52**, 22-30 (1999).
102 Sansom, M. S. P. & Biggin, P. C. Biophysics: Water at the nanoscale. *Nature* **414**, 156-159 (2001).
103 Jing-Yuan, L., Zai-Xing, Y., Hai-Ping, F., Ru-Hong, Z. & Xiao-Wei, T. Effect of the carbon-nanotube length on water permeability. *Chinese Physics Letters* **24**, 2710 (2007).
104 Su, J. & Guo, H. Effect of Nanochannel Dimension on the Transport of Water Molecules. *The Journal of Physical Chemistry B* **116**, 5925-5932, doi:10.1021/jp211650s (2012).
105 Walther, J. H., Jaffe, R., Halicioglu, T. & Koumoutsakos, P. Carbon nanotubes in water: structural characteristics and energetics. *The Journal of Physical Chemistry B* **105**, 9980-9987 (2001).
106 Werder, T. *et al.* Molecular dynamics simulation of contact angles of water droplets in carbon nanotubes. *Nano letters* **1**, 697-702 (2001).
107 Pascal, T. A., Goddard, W. A. & Jung, Y. Entropy and the driving force for the filling of carbon nanotubes with water. *Proceedings of the National Academy of Sciences of the United States of America* **108**, 11794-11798, doi:10.1073/pnas.1108073108 (2011).
108 Mashl, R. J., Joseph, S., Aluru, N. R. & Jakobsson, E. Anomalously Immobilized Water: A New Water Phase Induced by Confinement in Nanotubes. *Nano letters* **3**, 589-592, doi:10.1021/nl0340226 (2003).
109 Zhu, F. & Schulten, K. Water and proton conduction through carbon nanotubes as models for biological channels. *Biophysical journal* **85**, 236-244 (2003).
110 Joseph, S. & Aluru, N. R. Why Are Carbon Nanotubes Fast Transporters of Water? *Nano letters* **8**, 452-458, doi:10.1021/nl072385q (2008).
111 Thomas, J. A. & McGaughey, A. J. Reassessing fast water transport through carbon nanotubes. *Nano letters* **8**, 2788-2793 (2008).
112 Striolo, A. The Mechanism of Water Diffusion in Narrow Carbon Nanotubes. *Nano letters* **6**, 633-639, doi:10.1021/nl052254u (2006).
113 Baum, R. M. Nurturing nanotubes. *Chem Eng News* **75**, 39-41, doi:DOI 10.1021/cen-v075n026.p039 (1997).
114 Sun, L. & Crooks, R. M. Single carbon nanotube membranes: a well-defined model for studying mass transport through nanoporous materials. *Journal of the American Chemical Society* **122**, 12340-12345 (2000).
115 Fan, S. S. *et al.* Self-oriented regular arrays of carbon nanotubes and their field emission properties. *Science* **283**, 512-514, doi:DOI 10.1126/science.283.5401.512 (1999).
116 Schlittler, R. R. *et al.* Single crystals of single-walled carbon nanotubes formed by self-assembly. *Science* **292**, 1136-1139, doi:DOI 10.1126/science.1057823 (2001).
117 Li, W. Z. *et al.* Large-scale synthesis of aligned carbon nanotubes. *Science* **274**, 1701-1703, doi:DOI 10.1126/science.274.5293.1701 (1996).
118 Ren, Z. F. *et al.* Synthesis of large arrays of well-aligned carbon nanotubes on glass. *Science* **282**, 1105-1107, doi:DOI 10.1126/science.282.5391.1105 (1998).

119 Miller, S. A., Young, V. Y. & Martin, C. R. Electroosmotic Flow in Template-Prepared Carbon Nanotube Membranes. *Journal of the American Chemical Society* **123**, 12335-12342, doi:10.1021/ja011926p (2001).
120 Sahu, S., Di Ventra, M. & Zwolak, M. Dehydration as a universal mechanism for ion selectivity in graphene and other atomically thin pores. *arXiv preprint arXiv:1605.03134* (2016).
121 Hinds, B. J. *et al.* Aligned Multiwalled Carbon Nanotube Membranes. *Science* **303**, 62-65, doi:10.1126/science.1092048 (2004).
122 Daiguji, H., Yang, P. & Majumdar, A. Ion Transport in Nanofluidic Channels. *Nano letters* **4**, 137-142, doi:10.1021/nl0348185 (2004).
123 Qiao, R. & Aluru, N. R. Atypical Dependence of Electroosmotic Transport on Surface Charge in a Single-wall Carbon Nanotube. *Nano letters* **3**, 1013-1017, doi:10.1021/nl034236n (2003).
124 Yeh, I.-C. & Hummer, G. Nucleic acid transport through carbon nanotube membranes. *Proceedings of the National Academy of Sciences of the United States of America* **101**, 12177-12182, doi:10.1073/pnas.0402699101 (2004).
125 Gao, H., Kong, Y., Cui, D. & Ozkan, C. S. Spontaneous Insertion of DNA Oligonucleotides into Carbon Nanotubes. *Nano letters* **3**, 471-473, doi:10.1021/nl025967a (2003).
126 Ito, T., Sun, L. & Crooks, R. M. Observation of DNA transport through a single carbon nanotube channel using fluorescence microscopy. *Chemical communications*, 1482-1483, doi:10.1039/B302511J (2003).
127 Jae Hyun, P., Susan, B. S. & Aluru, N. R. Ion separation using a Y-junction carbon nanotube. *Nanotechnology* **17**, 895 (2006).
128 Wander, M. C. F. & Shuford, K. L. Alkali halide interfacial behavior in a sequence of charged slit pores. *Abstr Pap Am Chem S* **242** (2011).
129 Plecis, A., Schoch, R. B. & Renaud, P. Ionic transport phenomena in nanofluidics: experimental and theoretical study of the exclusion-enrichment effect on a chip. *Nano letters* **5**, 1147-1155, doi:10.1021/nl050265h (2005).
130 Liu, H. *et al.* Translocation of Single-Stranded DNA Through Single-Walled Carbon Nanotubes. *Science* **327**, 64-67, doi:10.1126/science.1181799 (2010).
131 Choi, W. *et al.* Diameter-dependent ion transport through the interior of isolated single-walled carbon nanotubes. **4**, 2397, doi:10.1038/ncomms3397
https://www.nature.com/articles/ncomms3397#supplementary-information (2013).
132 Secchi, E., Nigues, A., Jubin, L., Siria, A. & Bocquet, L. Scaling Behavior for Ionic Transport and its Fluctuations in Individual Carbon Nanotubes. *Phys Rev Lett* **116**, 154501, doi:10.1103/PhysRevLett.116.154501 (2016).
133 Amiri, H., Shepard, K. L., Nuckolls, C. & Hernández Sánchez, R. Single-Walled Carbon Nanotubes: Mimics of Biological Ion Channels. *Nano letters* **17**, 1204-1211, doi:10.1021/acs.nanolett.6b04967 (2017).
134 Gong, X., Li, J., Xu, K., Wang, J. & Yang, H. A Controllable Molecular Sieve for Na+ and K+ Ions. *Journal of the American Chemical Society* **132**, 1873-1877, doi:10.1021/ja905753p (2010).
135 Yang, L. & Garde, S. Modeling the selective partitioning of cations into negatively charged nanopores in water. *The Journal of chemical physics* **126**, 084706, doi:doi:http://dx.doi.org/10.1063/1.2464083 (2007).

136 Dzubiella, J. & Hansen, J.-P. Electric-field-controlled water and ion permeation of a hydrophobic nanopore. *The Journal of chemical physics* **122**, 234706, doi:doi:http://dx.doi.org/10.1063/1.1927514 (2005).
137 Tang, Y. W., Chan, K.-Y. & Szalai, I. Structural and Transport Properties of an SPC/E Electrolyte in a Nanopore. *The Journal of Physical Chemistry B* **108**, 18204-18213, doi:10.1021/jp0465985 (2004).
138 Murad, S. The role of external electric fields in enhancing ion mobility, drift velocity, and drift–diffusion rates in aqueous electrolyte solutions. *The Journal of chemical physics* **134**, 114504, doi:doi:http://dx.doi.org/10.1063/1.3565478 (2011).
139 Shao, Q. *et al.* Anomalous Hydration Shell Order of Na+ and K+ inside Carbon Nanotubes. *Nano letters* **9**, 989-994, doi:10.1021/nl803044k (2009).
140 de Groot, B. L. & Grubmüller, H. Water permeation across biological membranes: mechanism and dynamics of aquaporin-1 and GlpF. *Science* **294**, 2353-2357 (2001).
141 Joseph, S. & Aluru, N. Why are carbon nanotubes fast transporters of water? *Nano letters* **8**, 452-458 (2008).
142 Alexiadis, A. & Kassinos, S. Molecular simulation of water in carbon nanotubes. *Chemical reviews* **108**, 5014-5034 (2008).
143 Huang, L.-L. *et al.* Molecular dynamics simulation study of the structural characteristics of water molecules confined in functionalized carbon nanotubes. *The Journal of Physical Chemistry B* **110**, 25761-25768 (2006).
144 Perez-Hernandez, G. & Schmidt, B. Anisotropy of the water-carbon interaction: molecular simulations of water in low-diameter carbon nanotubes. *Physical Chemistry Chemical Physics* **15**, 4995-5006, doi:10.1039/C3CP44278K (2013).
145 Bushuev, Y., Davletbaeva, S. & Muguet, F. F. Hydration Simulations of a Carbon Nanotube, immersed in Water, according to the 3-Attractor Water Model. *Sensors (Basel, Switzerland)* **5**, 139-147 (2005).
146 Sadeghi, M. & Parsafar, G. Toward an equation of state for water inside carbon nanotubes. *The Journal of Physical Chemistry B* **116**, 4943-4951 (2012).
147 Maniwa, Y. *et al.* Phase Transition in Confined Water Inside Carbon Nanotubes. *Journal of the Physical Society of Japan* **71**, 2863-2866, doi:10.1143/jpsj.71.2863 (2002).
148 Naguib, N. *et al.* Observation of Water Confined in Nanometer Channels of Closed Carbon Nanotubes. *Nano letters* **4**, 2237-2243, doi:10.1021/nl0484907 (2004).
149 Kolesnikov, A. I. *et al.* Anomalously Soft Dynamics of Water in a Nanotube: A Revelation of Nanoscale Confinement. *Phys Rev Lett* **93**, 035503 (2004).
150 Robinson, G. W. *Water in biology, chemistry, and physics : experimental overviews and computational methodologies*. (World Scientific, 1996).
151 Bussi, G., Donadio, D. & Parrinello, M. COMP 8-Canonical sampling through velocity rescaling. *Abstr Pap Am Chem S* **234** (2007).
152 Wang, J., Zhu, Y., Zhou, J. & Lu, X.-H. Diameter and helicity effects on static properties of water molecules confined in carbon nanotubes. *Physical Chemistry Chemical Physics* **6**, 829-835, doi:10.1039/B313307A (2004).
153 Alexiadis, A. & Kassinos, S. Self-diffusivity, hydrogen bonding and density of different water models in carbon nanotubes. *Mol Simulat* **34**, 671-678, doi:10.1080/08927020802073057 (2008).
154 Abascal, J. L. F. & Vega, C. A general purpose model for the condensed phases of water: TIP4P/2005. *The Journal of chemical physics* **123**, 234505, doi:10.1063/1.2121687 (2005).

155 Mukherjee, B., Maiti, P. K., Dasgupta, C. & Sood, A. Strong correlations and Fickian water diffusion in narrow carbon nanotubes. *The Journal of chemical physics* **126**, 124704 (2007).
156 Mukherjee, B., Maiti, P. K., Dasgupta, C. & Sood, A. Single-file diffusion of water inside narrow carbon nanorings. *ACS nano* **4**, 985-991 (2010).
157 Min, K., Farimani, A. B. & Aluru, N. R. Mechanically modulated electronic properties of water-filled fullerenes. *Mrs Commun* **5**, 305-310, doi:10.1557/mrc.2015.22 (2015).
158 Heiranian, M., Farimani, A. B. & Aluru, N. R. Water desalination with a single-layer MoS2 nanopore. *Nat Commun* **6**, doi:Artn 8616
10.1038/Ncomms9616 (2015).
159 Eisenberg, D. S. & Kauzmann, W. *The Structure and Properties of Water*. (Oxford University Press, 1969).
160 Venkatesan, G. A. *et al.* Adsorption Kinetics Dictate Mono layer Self-Assembly for Both Lipid-In and Lipid-Out Approaches to Droplet Interface Bilayer Formation. *Langmuir : the ACS journal of surfaces and colloids* **31**, 12883-12893, doi:10.1021/acs.langmuir.5b02293 (2015).
161 Liu, Y.-C. *et al.* Diffusion dynamics of water controlled by topology of potential energy surface inside carbon nanotubes. *Phys Rev B* **77**, 125438 (2008).
162 Farimani, A. B. & Aluru, N. R. Spatial Diffusion of Water in Carbon Nanotubes: From Fickian to Ballistic Motion. *Journal of Physical Chemistry B* **115**, 12145-12149, doi:10.1021/jp205877b (2011).
163 Zhu, F. & Schulten, K. Water and proton conduction through carbon nanotubes as models for biological channels. *Biophysical journal* **85**, 236-244, doi:10.1016/S0006-3495(03)74469-5 (2003).
164 Galama, A. H., Post, J. W., Stuart, M. A. C. & Biesheuvel, P. M. Validity of the Boltzmann equation to describe Donnan equilibrium at the membrane-solution interface. *J Membrane Sci* **442**, 131-139, doi:10.1016/j.memsci.2013.04.022 (2013).
165 Kamcev, J. *et al.* Partitioning of mobile ions between ion exchange polymers and aqueous salt solutions: importance of counter-ion condensation. *Physical Chemistry Chemical Physics* **18**, 6021-6031, doi:10.1039/c5cp06747b (2016).
166 Malani, A., Ayappa, K. & Murad, S. Effect of confinement on the hydration and solubility of NaCl in water. *Chem Phys Lett* **431**, 88-93 (2006).
167 Calixte, E. I., Samoylova, O. N. & Shuford, K. L. Confinement and surface effects of aqueous solutions within charged carbon nanotubes. *Physical Chemistry Chemical Physics* **18**, 12204-12212, doi:10.1039/C5CP04446D (2016).
168 Li, H. *et al.* Electrosorptive desalination by carbon nanotubes and nanofibres electrodes and ion-exchange membranes. *Water research* **42**, 4923-4928 (2008).
169 Tofighy, M. A. & Mohammadi, T. Adsorption of divalent heavy metal ions from water using carbon nanotube sheets. *Journal of Hazardous Materials* **185**, 140-147 (2011).
170 Zhang, L., Li, T., Li, B., Li, J. & Wang, E. Carbon nanotube–DNA hybrid fluorescent sensor for sensitive and selective detection of mercury (II) ion. *Chemical communications* **46**, 1476-1478 (2010).
171 Wanunu, M. *et al.* Rapid electronic detection of probe-specific microRNAs using thin nanopore sensors. *Nature nanotechnology* **5**, 807-814 (2010).
172 Mir, M., Homs, A. & Samitier, J. Integrated electrochemical DNA biosensors for lab-on-a-chip devices. *Electrophoresis* **30**, 3386-3397 (2009).

173 Nam, S.-W., Rooks, M. J., Kim, K.-B. & Rossnagel, S. M. Ionic field effect transistors with sub-10 nm multiple nanopores. *Nano letters* **9**, 2044-2048 (2009).
174 Kim, J., Kim, S. J. & Kim, D.-K. Energy harvesting from salinity gradient by reverse electrodialysis with anodic alumina nanopores. *Energy* **51**, 413-421 (2013).
175 Khavrutskii, I. V., Gorfe, A. A., Lu, B. & McCammon, J. A. Free Energy for the Permeation of Na+ and Cl− Ions and Their Ion-Pair through a Zwitterionic Dimyristoyl Phosphatidylcholine Lipid Bilayer by Umbrella Integration with Harmonic Fourier Beads. *Journal of the American Chemical Society* **131**, 1706-1716, doi:10.1021/ja8081704 (2009).
176 Daiguji, H. Ion transport in nanofluidic channels. *Chemical Society reviews* **39**, 901-911 (2010).
177 Bocquet, L. & Charlaix, E. Nanofluidics, from bulk to interfaces. *Chemical Society reviews* **39**, 1073-1095 (2010).
178 Guo, S., Meshot, E. R., Kuykendall, T., Cabrini, S. & Fornasiero, F. Nanofluidic Transport through Isolated Carbon Nanotube Channels: Advances, Controversies, and Challenges. *Advanced materials* **27**, 5726-5737, doi:10.1002/adma.201500372 (2015).
179 Kalra, A., Garde, S. & Hummer, G. Osmotic water transport through carbon nanotube membranes. *Proceedings of the National Academy of Sciences of the United States of America* **100**, 10175-10180, doi:10.1073/pnas.1633354100 (2003).
180 Paineau, E. *et al.* X-ray scattering determination of the structure of water during carbon nanotube filling. *Nano letters* **13**, 1751-1756 (2013).
181 Allen, T. W., Andersen, O. S. & Roux, B. Energetics of ion conduction through the gramicidin channel. *Proceedings of the National Academy of Sciences* **101**, 117-122 (2004).
182 Thomas, M. & Corry, B. A computational assessment of the permeability and salt rejection of carbon nanotube membranes and their application to water desalination. *Phil. Trans. R. Soc. A* **374**, 20150020 (2016).
183 Beu, T. A. Molecular dynamics simulations of ion transport through carbon nanotubes. III. Influence of the nanotube radius, solute concentration, and applied electric fields on the transport properties. *The Journal of chemical physics* **135**, 044516 (2011).
184 Ozcan, A., Perego, C., Salvalaglio, M., Parrinello, M. & Yazaydin, O. Concentration gradient driven molecular dynamics: a new method for simulations of membrane permeation and separation. *Chem Sci* **8**, 3858-3865 (2017).
185 Heffelfinger, G. S. & Swol, F. v. Diffusion in Lennard-Jones fluids using dual control volume grand canonical molecular dynamics simulation (DCV-GCMD). *The Journal of chemical physics* **100**, 7548-7552, doi:10.1063/1.466849 (1994).
186 Kutzner, C., Grubmüller, H., de Groot, Bert L. & Zachariae, U. Computational Electrophysiology: The Molecular Dynamics of Ion Channel Permeation and Selectivity in Atomistic Detail. *Biophysical journal* **101**, 809-817, doi:10.1016/j.bpj.2011.06.010 (2011).
187 Marrink, S. J. & Berendsen, H. J. C. Simulation of Water Transport through a Lipid-Membrane. *Abstr Pap Am Chem S* **203**, 620-POLY (1992).
188 Zwolinski, B. J., Eyring, H. & Reese, C. E. Diffusion and Membrane Permeability. *The Journal of Physical Chemistry* **53**, 1426-1453 (1949).
189 Lakshminarayanaiah, N. Transport phenomena in membranes. (1969).
190 Helfferich, F. G. *Ion exchange*. (Courier Corporation, 1962).

191 Deen, W. M. *Analysis of Transport Phenomena, Topics in Chemical Engineering*. Vol. 3 (Oxford University Press, New York, 1998).
192 Klimovich, P. V., Shirts, M. R. & Mobley, D. L. Guidelines for the analysis of free energy calculations. *J Comput Aided Mol Des* **29**, 397-411, doi:10.1007/s10822-015-9840-9 (2015).
193 Pohorille, A., Jarzynski, C. & Chipot, C. Good practices in free-energy calculations. *The journal of physical chemistry. B* **114**, 10235-10253, doi:10.1021/jp102971x (2010).
194 Grossfield, A. WHAM: the weighted histogram analysis method. *version* **2**, 06 (2012).
195 Liu, H., Dai, S. & Jiang, D.-e. Molecular Dynamics Simulation of Anion Effect on Solubility, Diffusivity, and Permeability of Carbon Dioxide in Ionic Liquids. *Ind Eng Chem Res* **53**, 10485-10490, doi:10.1021/ie501501k (2014).
196 Payandeh, J., Scheuer, T., Zheng, N. & Catterall, W. A. The crystal structure of a voltage-gated sodium channel. *Nature* **475**, 353-358, doi:10.1038/nature10238 (2011).
197 McCleskey, E. & Almers, W. The Ca channel in skeletal muscle is a large pore. *Proceedings of the National Academy of Sciences* **82**, 7149-7153 (1985).
198 Saint, N. *et al.* Structural and functional characterization of OmpF porin mutants selected for larger pore size. II. Functional characterization. *The Journal of biological chemistry* **271**, 20676-20680 (1996).
199 Karger, J. & Ruthven, D. M. Diffusion in nanoporous materials: fundamental principles, insights and challenges. *New J Chem* **40**, 4027-4048, doi:10.1039/C5NJ02836A (2016).
200 Kong, J. *et al.* Temperature dependence of ion diffusion coefficients in NaCl electrolyte confined within graphene nanochannels. *Physical Chemistry Chemical Physics* **19**, 7678-7688, doi:10.1039/C6CP08752C (2017).
201 Kalluri, R. K., Konatham, D. & Striolo, A. Aqueous NaCl Solutions within Charged Carbon-Slit Pores: Partition Coefficients and Density Distributions from Molecular Dynamics Simulations. *The Journal of Physical Chemistry C* **115**, 13786-13795, doi:10.1021/jp203086x (2011).
202 Joseph, S., Mashl, R. J., Jakobsson, E. & Aluru, N. R. Electrolytic Transport in Modified Carbon Nanotubes. *Nano letters* **3**, 1399-1403, doi:10.1021/nl0346326 (2003).
203 Hummer, G., Pratt, L. R. & Garcia, A. E. Free energy of ionic hydration. *The Journal of Physical Chemistry* **100**, 1206-1215 (1996).
204 Grossfield, A., Ren, P. & Ponder, J. W. Ion Solvation Thermodynamics from Simulation with a Polarizable Force Field. *Journal of the American Chemical Society* **125**, 15671-15682, doi:10.1021/ja037005r (2003).
205 Strathmann, H. in *Ullmann's Encyclopedia of Industrial Chemistry* (Wiley-VCH Verlag GmbH & Co. KGaA, 2000).
206 Fedorov, M. V. & Kornyshev, A. A. Towards understanding the structure and capacitance of electrical double layer in ionic liquids. *Electrochim Acta* **53**, 6835-6840, doi:10.1016/j.electacta.2008.02.065 (2008).
207 Gurtovenko, A. A. & Vattulainen, I. Pore Formation Coupled to Ion Transport through Lipid Membranes as Induced by Transmembrane Ionic Charge Imbalance: Atomistic Molecular Dynamics Study. *Journal of the American Chemical Society* **127**, 17570-17571, doi:10.1021/ja053129n (2005).
208 Tieleman, D. P., Leontiadou, H., Mark, A. E. & Marrink, S.-J. Simulation of Pore Formation in Lipid Bilayers by Mechanical Stress and Electric Fields. *Journal of the American Chemical Society* **125**, 6382-6383, doi:10.1021/ja029504i (2003).

209 Tarek, M. Membrane Electroporation: A Molecular Dynamics Simulation. *Biophysical journal* **88**, 4045-4053, doi:http://dx.doi.org/10.1529/biophysj.104.050617 (2005).
210 Beu, T. A. Molecular dynamics simulations of ion transport through carbon nanotubes. I. Influence of geometry, ion specificity, and many-body interactions. *The Journal of chemical physics* **132**, 164513, doi:10.1063/1.3387972 (2010).
211 Wenrong, Y., Pall, T., Gooding, J. J., Simon, P. R. & Filip, B. Carbon nanotubes for biological and biomedical applications. *Nanotechnology* **18**, 412001 (2007).
212 Maier, J. Nanoionics: ion transport and electrochemical storage in confined systems. *Nat Mater* **4**, 805-815 (2005).

Vita

Michelle Aranha comes from Mumbai, India. She received her Bachelor's degree in July 2008 from Marathwada University located in Aurangabad, India. She has experience in the Petrochemical sector from her employment (September 2008 - April 2012) as a Process Engineer in the Purified Terephthalic Acid Operations division at Reliance Industries Limited (India). She joined the Chemical and Biomolecular Engineering department at University of Tennessee, Knoxville as a graduate student on a Chancellor's Fellowship in August 2012. Michelle successfully defended her dissertation on the study of nanoscale water and ion transport through carbon nanotubes using molecular dynamics simulations in August 2017.